Complexes homo- et hétero- métallique 3d avec des ligands N- et N,O donneurs : Synthèse, structure et propriétés

Oleh Stetsiuk

UNIVERSITE MATIERE BRETAGNE MOLECULES LOIRE ET MATERIAUX

université angers

THESE DE DOCTORAT

DE L'UNIVERSITE D'ANGERS
COMUE UNIVERSITE BRETAGNE LOIRE

ECOLE DOCTORALE N° 596
Matière, Molécules, Matériaux
Spécialité : *Chimie des matériaux*

Oleh STETSIUK

Homo- and Heterometallic 3d-Metal Complexes with N- and N,O-donor Ligands: Synthesis, Structure and Properties

Thèse en cotutelle «université d'Angers et université de Kiev»

Thèse présentée et soutenue à Kiev, le 10/12/2018

Unité de recherche : ***Laboratoire MOLTECH-Anjou (UMR 6200), Angers, France; Faculté de Chimie, Université de Kiev, Ukraine.***

Thèse N° : 153491

Composition du Jury

Rapporteurs :

Pr. Marius Andruh	Professeur	*Université de Bucarest*	(Romania)
Dr. Sergey Kolotilov	Leading researcher	*Institut de chimie physique de NAS*	(Ukraine)

Examinateurs :

Pr. Nicolas Mercier	Professeur,	*Université d'Angers*	(France)
Dr. Svitlana Petrusenko	Senior researcher	*Université de Kiev*	(Ukraine)

Directeurs de Thèse :

Dr. Narcis Avarvari	Directeur de Recherches	*Université d'Angers*	(France)
Pr. Vladimir Kokozay	Professeur,	*Université de Kiev*	(Ukraine)

Co-directeur de Thèse :

Dr. Abdelkrim El-Ghayoury	Maître de Conférences, HDR	*Université d'Angers*	(France)

Acknowledgment

This work has been done in the Moltech-Anjou laboratory (University of Angers) and in the Faculty of Chemistry of the National University of Kiev, under the double supervision of prof. Vladimir Kokozay (Kiev), Abdelkrim El-Ghayoury and Narcis Avarvari (Angers) according to the agreement of the joined thesis.

First of all I would like to adress my thanks to the members of the jury who did me the honor of evaluate this work. The reviewers, Dr. **Sergey Kolotilov** (Institut of physical chemistry NAS of Ukraine) and Pr. **Marius Andruh** (University of Bucharest). The examiners, Dr. **Svitlana Petrusenko** (University of Kiev) and Pr. **Nicolas Mercier** (University of Angers).

I would like to thank Prof. **Marc Salle**, the director of the Moltech-Anjou laboratory, for having accepted me in the laboratory. Also, I am very grateful to all my supervisors **Abdelkrim El-Ghayoury** and **Narcis Avarvari** who helped me a lot during all my stay in Angers and have found the time to help me with my articles, and Prof. **Vladimir Kokozay** and **Svitlana Petrusenko**, who were taking care of my work in Kiev.

Special thanks to **Cecile Meziere** for her kindness and preciseness during the work and for her help and our conversation in the laboratory; to **Magali Allain** for her strong background in the X-ray analyses and for her help for some of my structures; to **Valérie Bonnin** for the elemental analysis; to **Sonia Ouledkraim** and **Ingrid Freuze** for the mas-spectroscopymass spectrometry analyses.

I am very grateful to all Ukrainian people, our “Ukrainian team”, who were with me during these years: **Serhii Krykun**, **Nataliya Plyuta**, **Maxim Dekhtiarenko**, **Oksana Toma**, **Bohdan Kulyk** and all the master students for their humor, patience and the small piece of Ukraine in France. Thanks to my friends in France **Nabil Mroweh** for all his support, to **Yohan Chéret** for his jokes and patience about my jokes, to **Suchithra Ashoka Sahadevan** for her talkativeness (not all the time about the work) and to **Marwa Bel Haj Salah** for her innocent character and readiness to help all the time. Further I want to thank bonita **Cristina Oliveras** for her tortilla and to **Maurizio Mastropasqua Talamo** for his lasagna and especially for his strong surname. Thanks to **Kévin Martin** for his helpful advises in organic synthesis and also, I would like to mention **Awatef Ayadi** and say thank you for your help in organic synthesis at the beginning of my work in Angers.

Special thanks to prof. **Zoia Voitenko** for helping me to get funding for this position and to the French Embassy in Ukraine for the financial support of my work.

I would like also to thank everyone at the Moltech-Anjou laboratory and to all collaborators for their proper contribution to my work.

Content

Acronyms

dmf – Dimethylformamide
dmso – Dimethylsulfoxide
ACN – Acetonitrile
DCM – Dichloromethane
MST – Molecular structure type
OAc^- – Acetate anion
H_2L^1 – 2-(((2-hydroxyethyl)imino)methyl)phenol
H_3L^2 – 2-((2-hydroxybenzylidene)amino)-2-methylpropane-1,3-diol
H_4L^3 – 2-((2-hydroxybenzylidene)amino)-2-(hydroxymethyl)propane-1,3-diol
H_3L^4 – 3-((2-hydroxybenzylidene)amino)propane-1,2-diol
H_2L^5 – 4-bromo-2-(((2-hydroxyethyl)imino)methyl)phenol
H_3L^6 – 2-((5-bromo-2-hydroxybenzylidene)amino)-2-methylpropane-1,3-diol
H_4L^7 – 2-((5-bromo-2-hydroxybenzylidene)amino)-2-(hydroxymethyl)propane-1,3-diol
H_2L^8 – 2-(((2-hydroxyethyl)imino)methyl)-4-nitrophenol
H_3L^9 – 2-((2-hydroxy-5-nitrobenzylidene)amino)-2-methylpropane-1,3-diol
H_4L^{10} – 2-(hydroxymethyl)-2-(((2-hydroxynaphthalen-1-yl)methylene)amino) propane-1,3-diol
H_4L^{11} – 2-((2-hydroxy-5-nitrobenzylidene)amino)-2-(hydroxymethyl)propane-1,3-diol
H_2L^{12} – 4-([2,2'-bi(1,3-dithiolylidene)]-4-yl)-2-(((2-hydroxyethyl)imino)methyl) phenol
H_2L^{13} – 3,3'-((4,5-bis(((E)-2-hydroxybenzylidene)amino)-1,2-phenylene)bis (sulfanediyl))dipropanenitrile
HL^{14} – 6-chloro-N-(pyridin-2-ylmethyl)-1,2,4,5-tetrazin-3-amine
H_2L^{15} – N^3,N^6-bis(pyridin-2-ylmethyl)-1,2,4,5-tetrazine-3,6-diamine
CV – cyclic voltammogram
SMM – single molecule magnet
IR – Infrared
EPR – Electron paramagnetic resonance
NMR – Nuclear magnetic resonance
BVS – Bond valence sum
CDS – Chemical structural database
TON – Turnover number
PVB – Polyvinil butyral
PCF – Polymer composite films
TTF-Sal – 5-(tetrathiafulvalenyl)-2-hydroxybenzaldehyde
TTF – Tetrathiafulvalene
PPh_4^+ – Tetraphenylphisphinium cation
TBA^+ – Tetrabuthylammonium cation
LUMO – Lowest unoccupied molecular orbital
HOMO – Highest occupied molecular orbital
SOMO – Singly occupied molecular orbital
$Hfac^-$ – Hexafluoroacetylacetonate anion
TTZ – Tetrazine
DFT – Density functional theory
DC – direct current
AC – alternative current

Liste of complexes obtained

Heterometalllic Mn/Cu and Co/Cu complexes with Schiff base ligands	
1	$[Cu_3Mn(L^1)_4(CH_3OH)_3]I_3$
2	$[Cu_3Mn(L^1)_4(CH_3OH)_3(H_2O)]NCS\cdot H_2O$
3	$[Cu_3Mn(L^1)_4(CH_3OH)(H_2O)_{2.55}]Br\cdot 0.45H_2O$
4	$[Cu_3Mn(L^1)_4(H_2O)_{3.4}]BF_4\cdot 0.6H_2O$
5	$[Cu^{II}_3Mn^{III}(L^1)_4(CH_3OH)_3]_2[Mn^{II}(NCS)_4]\cdot 2CH_3OH$
6	$[Co^{II}Co^{III}Cu^{II}_2(L^1)_3(ea)(NCS)_2(H_2O)]$
Heterometalllic Mn/Co complexes with Schiff base ligands	
7	$[Co_2Mn_2(HL^3)_4(dmf)_2]\cdot 6H_2O$
8	$[Co_2Mn_2(HL^7)_4(dmf)_2]\cdot dmf\cdot H_2O$
9	$[Co_2Mn_2(HL^{11})_4(dmf)_2]\cdot dmf\cdot 3H_2O$
10	$[Co_2Mn_2(HL^{10})_4(dmf)(H_2O)]\cdot 2dmf\cdot 2H_2O$
11	$[Co_2Mn_2(L^6)_4(dmf)_2]\cdot 2dmf$
12	$[Co_2Mn_2(L^9)_4(dmf)_2]\cdot 2dmf\cdot 7H_2O$
13	$[Co^{III}_2Mn^{II}_2Mn^{III}_2(L^4)_4Cl_2(\mu_3\text{-}OH)_2(dmf)_4]\cdot 2dmf$
Dithiolene Schiff base complexes	
14	$[CuL^{13}]\cdot 0{,}5CH_3OH$
15	$[TBA]_2[\{Ni(L^{13})_2\}_2Ni]\cdot 6CH_2Cl_2$
16	$[TBA]_2[\{Cu(L^{13})_2\}_2Cu]\cdot 5CH_2Cl_2$
17	$[PPh_4][\{Ni(L^{13})_2\}_2Ni]\cdot 4CH_2Cl_2$
18	$[PPh_4][\{Cu(L^{13})_2\}_2Cu]\cdot 4CH_2Cl_2$
19	$[TBA]_2[\{Cu(L^{13})_2\}_2Ni]_2\cdot 2CH_2Cl_2$
Tetrazine based complexes	
20	$[Cu(Hfac)_2(HL^{14})]$
21	$[Cu_2(\mu_2\text{-}Cl)(L^{14})_2]$
22	$[Cu_2(CF_3SO_3)(L^{14})_2]$
23	$[CuCl_2(HL^{14})_2]\cdot 2CH_3CN$
24	$[Cu(Hfac)_2(H_2L^{15})]$
25	$[Ni(Hfac)_2(H_2L^{15})]$
26	$[Co(Hfac)_2(H_2L^{15})]\cdot CH_3CN$
27	$[\{Cu(Hfac)_2\}_2(H_2L^{15})]\cdot 2CH_3OH$
28	$[\{Ni(Hfac)_2\}_2(H_2L^{15})]\cdot 2CH_3CN$
29	$\{[Co(Hfac)_2(H_2L^{15})]\cdot[Co(Hfac)_2(CH_3OH)_2]\}_n$
TTF-based compounds	
$[Cu(HL^{12})_2]_n$	
$(TTF\text{-}Sal)_2PF_6$	
$(TTF\text{-}Sal)_2AsF_6$	

General introduction

This thesis is devoted to the synthesis of homo- and heterometallic complexes with Schiff base ligands and tetrazine based molecules, investigation of their structure, physico-chemical and functional properties.

In the first chapter the two main approaches to the synthesis of complexes were given. The main MSTs for Mn/Cu, Mn/Co heterometallic complexes with the Schiff base ligands have been described. The basic types of electroactive ligands, such as TTF-, dithiolene- and tetrazine-based ligands together with the proper examples of their complexes were discussed.

The second chapter is devoted to the "direct synthesis" of heterometallic Mn/Cu and Mn/Co complexes with the "classical" Schiff base ligands, derivatives of salicylaldehyde and aminoalcohols. The structural diversity of MSTs of polynuclear complexes together with the magnetic and catalytic measurements complete this chapter.

The third chapter describes the electroactive Schiff base molecule, functionalized by the TTF moiety and its coordination properties. The series of radical cation salts have been obtained and fully characterized.

The fourth chapter is devoted to dithiolene Schiff base complexes. The synthesis of an unprecendented Schiff base ligand, containing N_2O_2-chelating pocket and thiopropanenitrile groups, was described. Trinuclear homometallic dithiolene complexes together with the hexanuclear heterometallic Cu/Ni compound were discussed. The investigation of the physical properties of the complexes complete this chapter.

The fifth chapter describes the tetrazine based complexes. The main advantages of the TTZ-ring were discussed. Two new ligands, derivatives of TTZ and picolylamine, were obtained and characterized. Series of mono- and binuclear 3*d*-metal complexes and investigation of their properties were described.

The general conclusions summarize this thesis.

This manuscript includes three appendixes. Appendix 1 contains the main crystallographic parameters of all compounds described in this work. Appendix 2 describes all synthetic procedures for the new ligands and complexes. Appendix 3 includes the selected bond lengths and angles of the compounds obtained.

CHAPTER I

INTRODUCTION

1.1. The main approaches of the synthesis of homo- and heterometallic complexes.

Progress is the process of gradually improving or getting nearer to achieving or completing something[1]. The peculiar progress of coordination chemistry can be considered as gradual changing of research area – from the simplest mononuclear to dimeric[2], polynuclear[3] and heterometallic complexes[4]. The main approaches of the synthesis of polynuclear compounds can be classified in two groups: i) the designed synthesis, where the "building blocks" find each other to assemble into a polynuclear architectures through metal-coordination[5]. ii) methods where the element of strict design is absent, referred to as serendipity. In contrast to designed assembly, ligands that display several different coordination modes have been used in combination with metal centers that can vary their coordination geometries. In the works of R. Winpenny[6] this method was named "serendipitous assembly".

The main advantage of the first approach is the possibility to predict the structure of the desired product. However, it should be noted, that foresight of the complex may be also a disadvantage of this method. Firstly, the probability of prediction reaches 100% in the very rare cases. Secondly, the predictability of the results restricts the areas of scientific research. In the case of approach (ii), the key role is played by the background and skills of the researcher, which drives the probability to get unexpected scientific results. However, the necessity to obtain a large variety of experimental work is required. The majority of coordination compounds can be obtained using both approaches, but it is unquestionably true that the polymetallic complexes with the most interesting physical properties have been made, at least initially, by accident. For example, the first single molecule magnet (SMM), $[Mn_{12}O_{12}(O_2CR)_{16}\text{-}(H_2O)_4]$ (R = CH_3 or Ph) was made accidentally from a reaction of permanganate with an Mn(III) triangle[7-8]. Nowadays it is still not possible to isolate the "building blocks", which would lead to the formation of the above mentioned SMM.

1.1.1. The "building blocks" approach.

The most investigated variation of this approach is the "brick and mortar method". The striking examples of this method are the formation of pseudo halide complexes. The $[M(CN)_6]^{n-}$ anions play the role of the "bricks", while metal ions or complex cations $[M'(L)]^{m+}$ serve as the "mortar" resulting in the formation of 3D insoluble analogues of Prussian blue[9-11]. Thus, Ohba and co-workers have described the synthesis of heterometallic Ni^{II}–M^{III} (M = Co, Cr) *1D* coordination polymers[12].

Utilization of the $[M(CN)_xL_y]^{n-}$ blocks, (M = Cr^{III}, $Fe^{II/III}$, Ru^{III}, Mo^{III}; L = chelate ligand; x = 2, 3, 4), leads to the formation of the complexes, which possess different dimensionality[13]. Figure 1.1 illustrated the products of the reaction of $[Cr(bipy)(CN)_4]^-$ with Mn(II) salts in presence of ligand (2,2′- bipy, N_3^-, $N(CN)_2^-$).

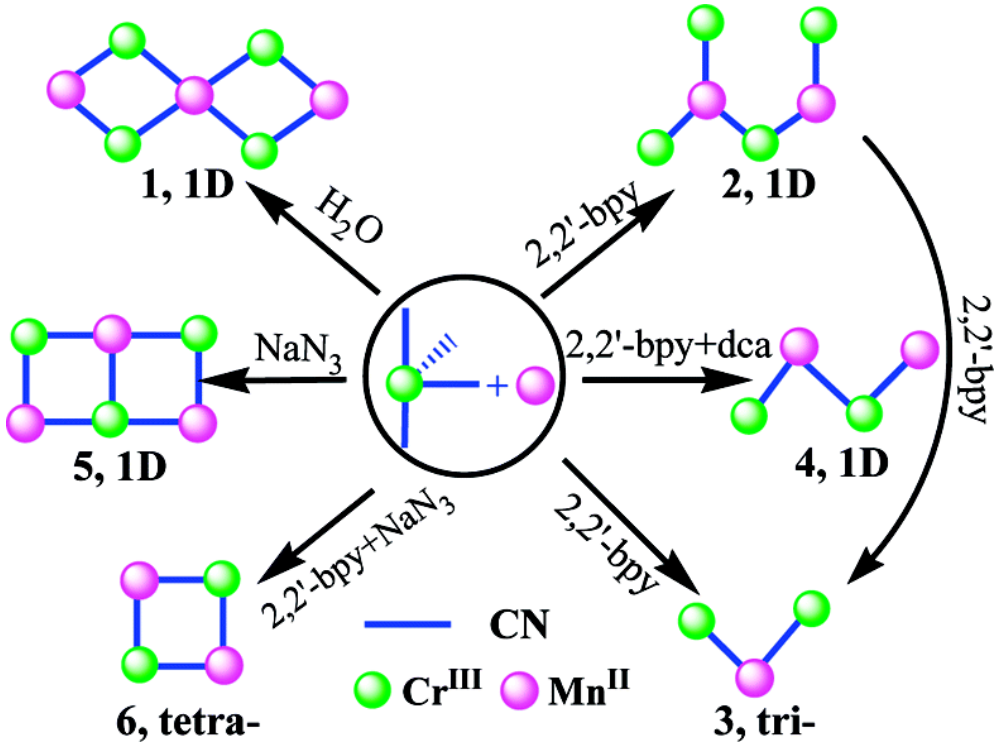

Figure 1.1. Synthesis of heterometallic complexes, starting from the $[Cr(bipy)(CN)_4]^-$ building block.

In 2002 Thompson described the influence of the ligand's nature on the nuclearity of desired complexes[14]. Thus, the authors used polydentate ligands due to their ability to form separated "coordination pockets". For example, heterocyclic 1,2-diazine ligands (pyridazine, phthalazine and thiadiazole fragments) can coordinate only two metal centers (Figure 1.2).

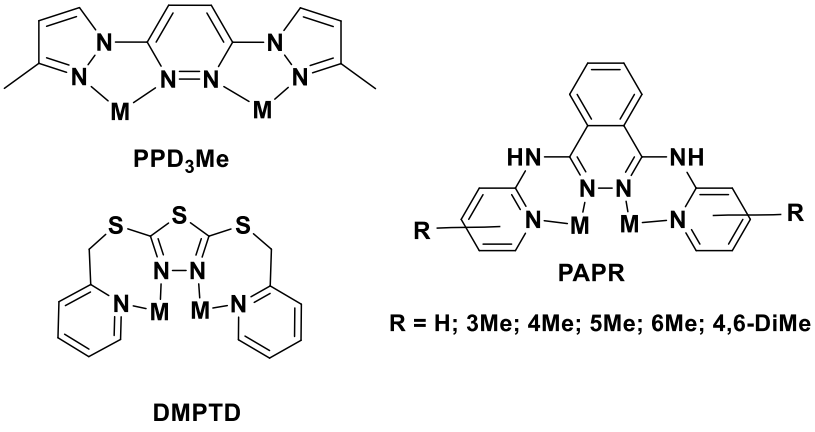

Figure 1.2. Coordination of the metal ions to the ligands which have pyridazine (PPD_3Me), phthalazine (PAPR) and thiadiazole (DMPTD) fragments.

1.1.2. Serendipitous assembly.

The definition of "assembly" can be given as the process of aggregation of the parts of a complex into the more complicate architecture[15]. In coordination chemistry, assembly can be

considered as the using of metal ions to controlling the organization of a supramolecular polynuclear structure. The majority of synthetic procedures of serendipitous assembly approach rely on creating a mismatch between the number of coordination sites available on a single metal ion and the donor atoms supplied by the ligand. The proper example is the work of Powell and Heath[16], where the authors have used a range of polycarboxylates (e.g. hydroxyethyliminodiacetic acid, $N(CH_2COOH)_2(CH_2CH_2OH)$) where the number of the donor atoms on the ligand makes it impossible to bind to a single metal ion. This has resulted in a series of $\{Fe_{17}\}$ and $\{Fe_{19}\}$ molecular cages, with an extension to the $\{Cu_{44}\}$ cage, produced more recently by Powell[17]. Murrie et al. have used citrate to produce $\{Ni_{21}\}$ cages[18] (Figure 1.3).

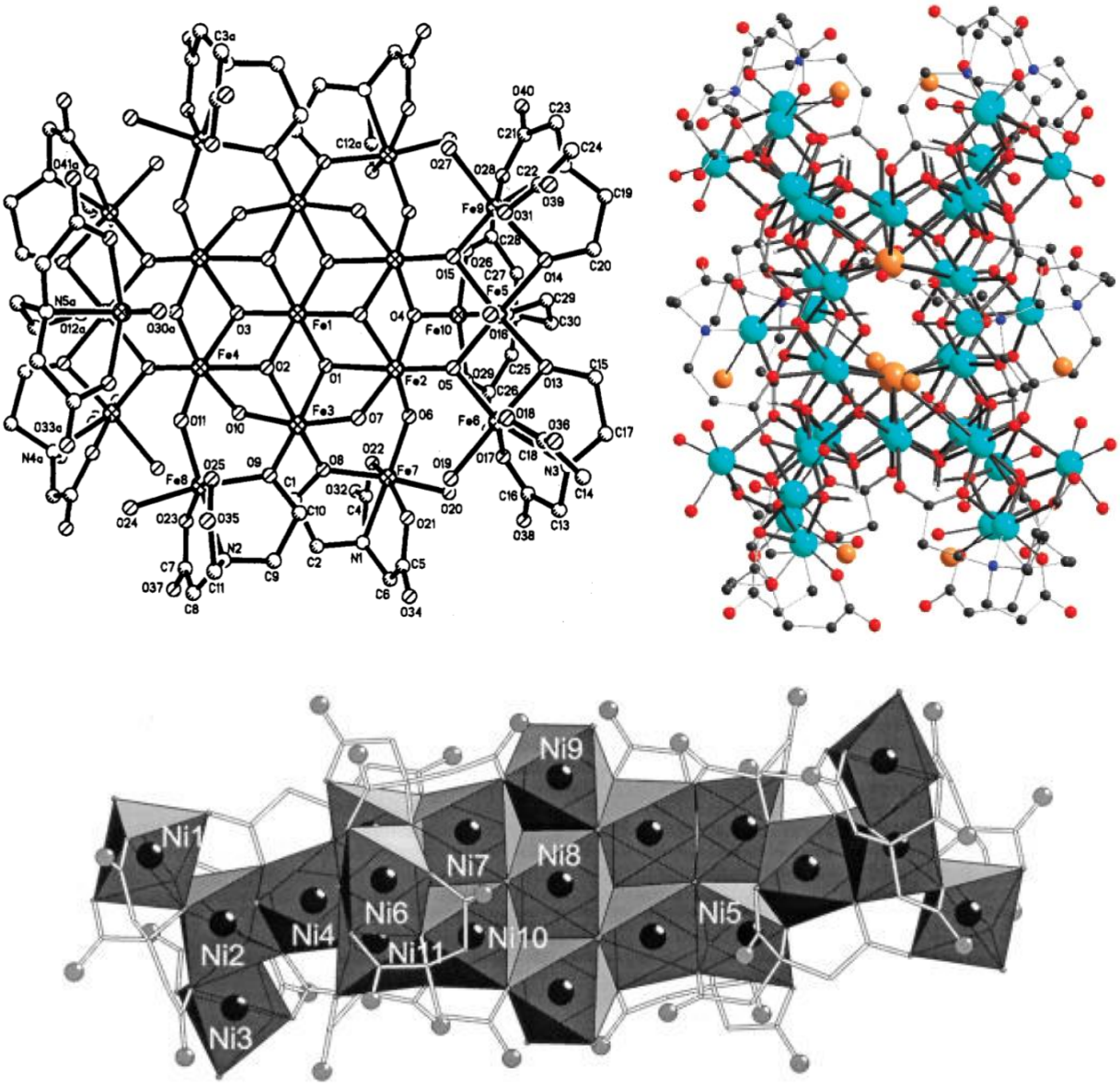

Figure 1.3. The crystal structures of $\{Fe_{19}\}$ (top, left), $\{Cu_{44}\}$ (top, right) and $\{Ni_{21}\}$ molecular cages.

Other examples of serendipitous assembly create the opposite mismatch, such as removing ligands from complexes resulted in coordinative unsaturation. If the $[Cr_3O(O_2CR)_6(H_2O)_3]X$

chromium carboxylate complexes (X = NO_3^- or OH^-), are heated to temperatures above 300 °C, it will lose either the terminally bounded water molecules or the carboxylic acid[19-21] (Figure 1.4).

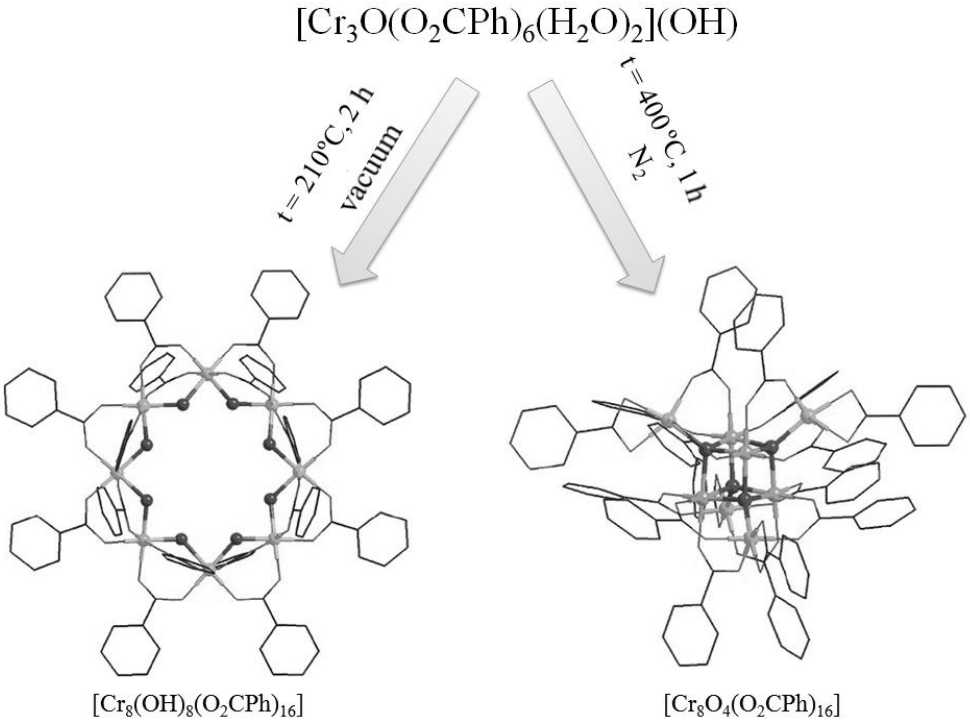

Figure 1.4. Example of serendipitous assembly $[Cr_3O(O_2CPh)_6(H_2O)_3](OH)$ due to the removing ligands.

In each case, vacant coordination sites of metal ion are formed, with the further interaction of complex particles resulted in the structure of higher nuclearity.

1.2. The basic molecular structure types (MSTs) of polynuclear complexes.

In 1990, Caulton and Hubert-Pfalzgraf, after considering of a large number of crystal structures, revealed that the variety of the molecular structures was based on a limited number of structural types[22-23]. The further analysis of the crystal structures of metal alkoxides, provided by Kessler[24] showed that the size and number of metal atoms and donor atoms have definitely more influence on the "choice" of the MSTs than their chemical nature. For example, in two different compounds $LiZr_2(O\textit{i}\text{-}Pr)_9(\textit{i}\text{-}PrOH)$[25] and $NaMo_2O_4(O\textit{i}\text{-}Pr)_5(\textit{i}\text{-}PrOH)$[26] the same trinuclear metallic fragments were observed. Kessler defines those metal-O species as molecular structure types (MSTs). Although in his work, he did not give a meaning to this term, the following definition can be considered as successful: molecular structure type is a set of topologically identical combinations of M_mX_n, where M – metal's ion, X – a bridging atom (donor atom of the ligand). The terminal donor atoms were not taken into account in this model, since the chemical nature of the metal ion influences more on their affinity to the former.

The crystal structures analysis of polynuclear complexes (general formula can be given as follows $M–(X–M)_n–X–M$, where *n* varies from 0 to 8; other restrictions are listed in the caption of

Figure 1.5) was performed by Nesterov in 2009[27]. As can be seen from Figure 1.5, the variety of polynuclear systems containing an even number of metal centers dominates over the odd numbers. An assumption that the compounds with the symmetric core M_mX_n are more stable than the respective asymmetric ones can be made. The ratio of the number of μ_n-X bridging atoms to the number of metal ions is also important (the higher is the better).

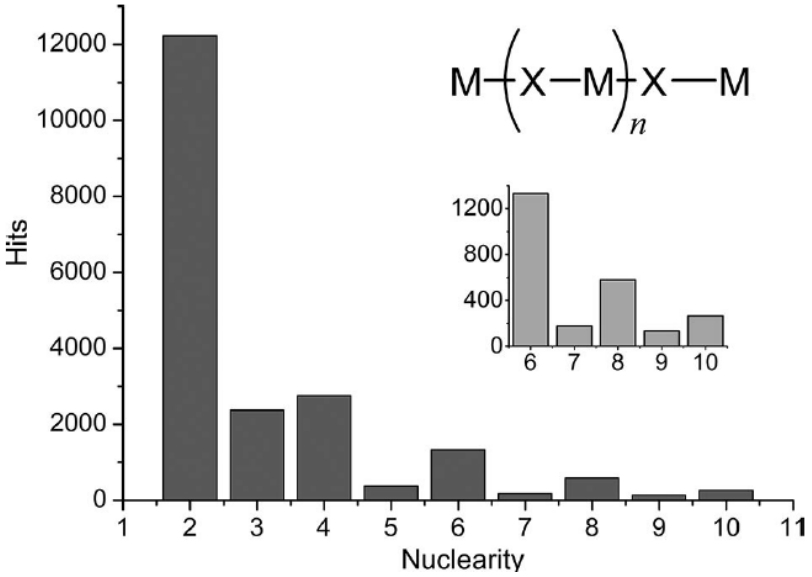

Figure 1.5. The dependence of the number of complexes on their nuclearity (for $0 \le n \le 8$, according to Cambridge Structural Database, CDS). The following restrictions were applied: the analysis was provided only for non-polymeric transition-metal (TR) compounds; the M–CO and M–CC fragments, as well as any non-TR atoms, were excluded. The inset illustrates the $n > 3$ area in details.

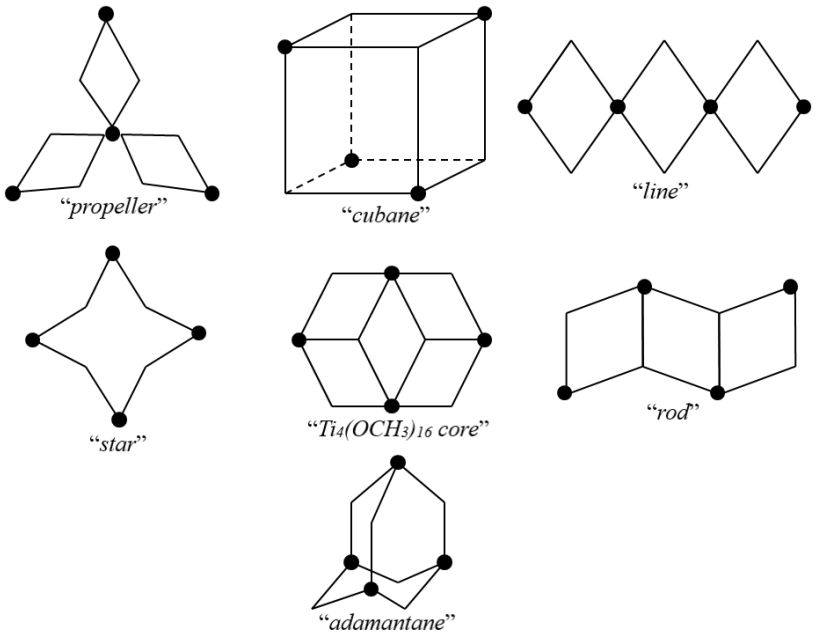

Figure 1.6. The main MSTs for tetranuclear complexes.

The majority of the polynuclear compounds ($m > 6$) can be considered as a combination of the simplest species ($m = 2 \div 5$). Since the variety of the MSTs of bi and trinuclear complexes is poor, we will focus mainly on the polynuclear species with m = 4, 6. The diagram on Figure 1.5 indicates that the tetranuclear compounds are the second prevalent (after dimers) among all multinuclear complexes.

The main MSTs can be distinguished as follows (Figure 1.6): "*propeller*", "*cubane*", "*line*", "*star*", "*divacant face-shared double cubane like the $Ti_4(OCH_3)_{16}$ core*", "*rod*", "*adamantane*".

The most widely spread MSTs are "*cubane*" (≈50 % among all tetranuclear structures) and "*$Ti_4(OCH_3)_{16}$ core*" (≈20 %).

According to CSD the hexanuclear compounds are the fourth prevalent among all polynuclear complexes with $(\mu\text{-X})_n$ (n = 1–4) bridged atom(s) between metal centers.

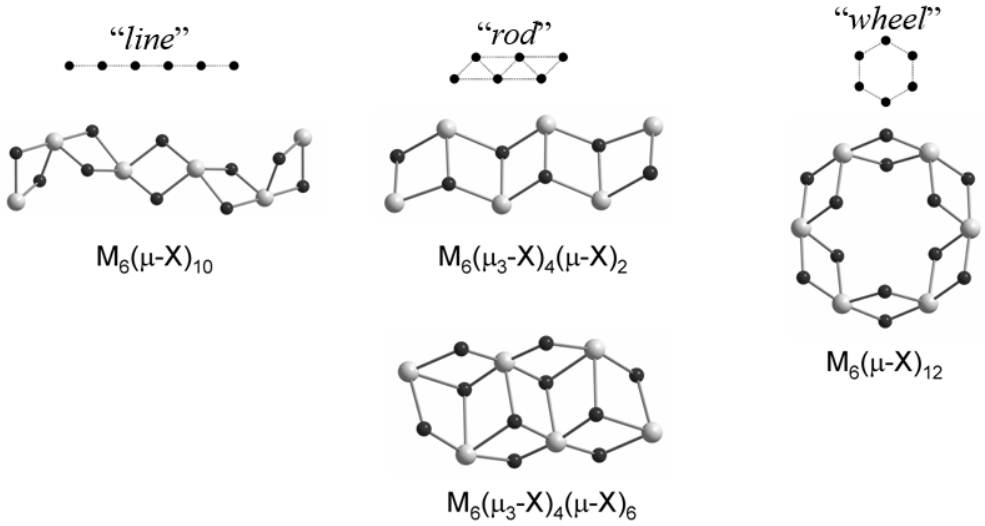

Figure 1.7. The main MSTs for hexanuclear complexes.

It should be noted that among all hexanuclear complexes the most common MST (Figure 1.7) is "wheel" (≈50 %).

1.3. Heterometallic Mn/Cu complexes.

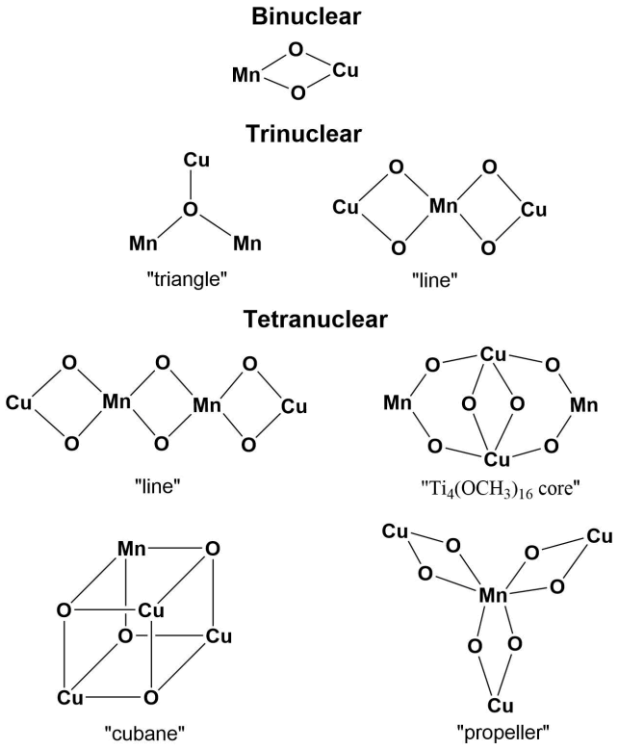

Figure 1.8. The main MSTs for the heterometallic Mn/Cu complexes.

The Cu/Mn metal's pair is among the most interesting combinations used for the construction of heterometallic compounds mainly because of the opportunity to show different stable oxidation states and particularly flexible coordination spheres of the metals. The latter allows the formation of complicated and specific architectures.

According to CSD around 400 heterometallic Mn/Cu complexes were described so far, with 25% among all Mn/Cu compounds containing at least one oxygen atom links the metal ions. The majority of these complexes contain Schiff

base molecules as ligands. The structural analysis for Mn/Cu complexes was performed and the main MSTs are shown in Figure 1.8.

Representative examples of binuclear Mn/Cu complexes are the series of compounds $[Mn^{III}Cu^{II}Cl(5\text{-Br-sap})_2(CH_3OH)]$ (**I1**), $[Mn^{III}Cu^{II}Cl(5\text{-Br-sap})_2(C_2H_5OH)]$ (**I2**) and $[Mn^{III}Cu^{II}Cl(5\text{-Cl-sap})_2(CH_3OH)]$ (**I3**), described by H. Oshio and co-workers[28-29]. The non-symmetrical Schiff base molecules, derivative of 5-bromo(chloro)-salicylaldehyde and propanolamine, were used as a ligand. The complexes obtained possessed similar crystal structures, shown in Figure 1.9 (left).

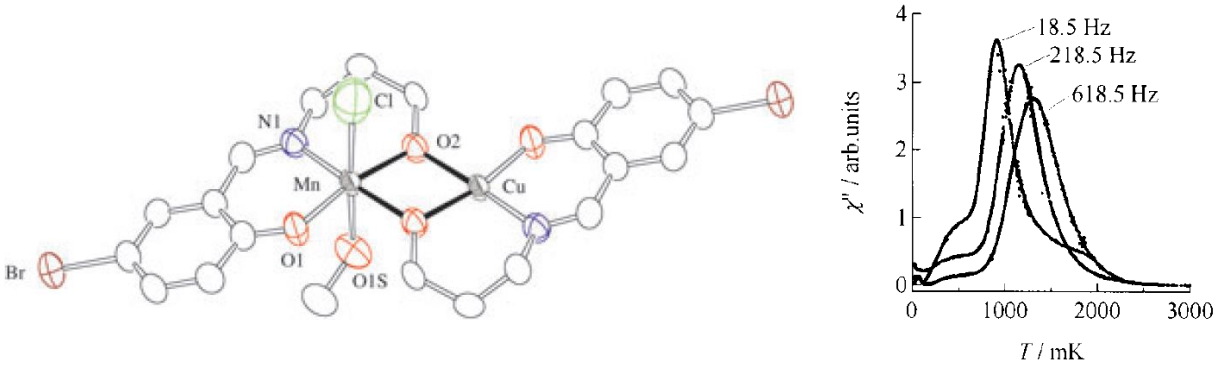

Figure 1.9. ORTEP diagram (left) of **I1** with 30 % probability and the plots of out-of-phase (χ_M'', right) ac magnetic susceptibility versus (T) in a 0.1 mT ac field oscillating at the indicated frequencies and with a zero dc field for **I1**.

In all complexes Mn^{III} and Cu^{II} ions were linked through O-atom from alkoxy groups of the Schiff base. The coordination environment around the Cu center is square planar within the O_3N donor set, while Mn^{III} ion adopts a distorted octahedral geometry. The equatorial sites formed by the O and N atoms of the ligands; methanol and chloride anion formed the apical position.

In the ac magnetic susceptibility measurements, frequency dependent out-of-phase (χ_M'') signals with peak maxima at 0.7–1.5 K was observed (Figure 1.9, right). The ac susceptibility data support that complexes **I1-I3** are single-molecule magnets (SMMs). Arrhenius plots for the χ_M'' peaks from 0.7–1.5 K gave the re-orientation energy barrier (ΔE) of 10.5 K with a pre-exponential factor of $8.2 \cdot 10^{-8}$ s for **I1**.

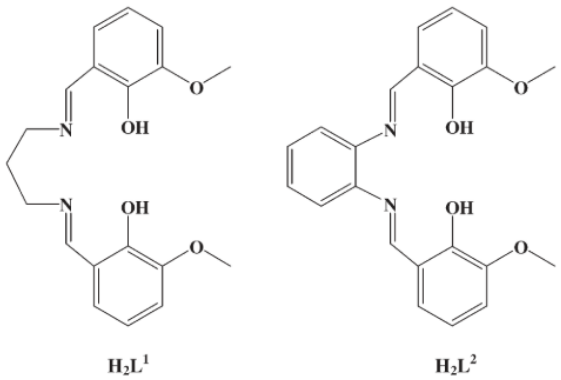

Figure 1.10. Molecular structures of the ligands.

The "building block" approach was applied by S. Mohanta[30]. The monometallic $[Cu^{II}L^1(H_2O)]$[31] and $[Cu^{II}L^2(H_2O)]$[32] complexes were used as a precursor in the synthesis of heterometallic aggregates with two 3-methoxysalicylaldehyde-diamine Schiff base compartmental ligands H_2L^1 and H_2L^2 (Figure 1.10). The binuclear $[Cu^{II}L^1Mn^{II}(H_2O)_3](ClO_4)_2$ (**I4**) and tetranuc-

lear [{$Cu^{II}L^2Mn^{II}(H_2O)(CH_3OH)_2$}{$Cu^{II}L^2$}$_2$]$(ClO_4)_2$·$CH_3OH$ (**I5**) compounds have been isolated and crystallographically characterized. In the dinuclear compound **I4** copper(II) center occupies the salen type N_2O_2 compartment, while the second metal ion (Mn^{II}) occupies the larger and open O_4 compartment (Figure 1.11).

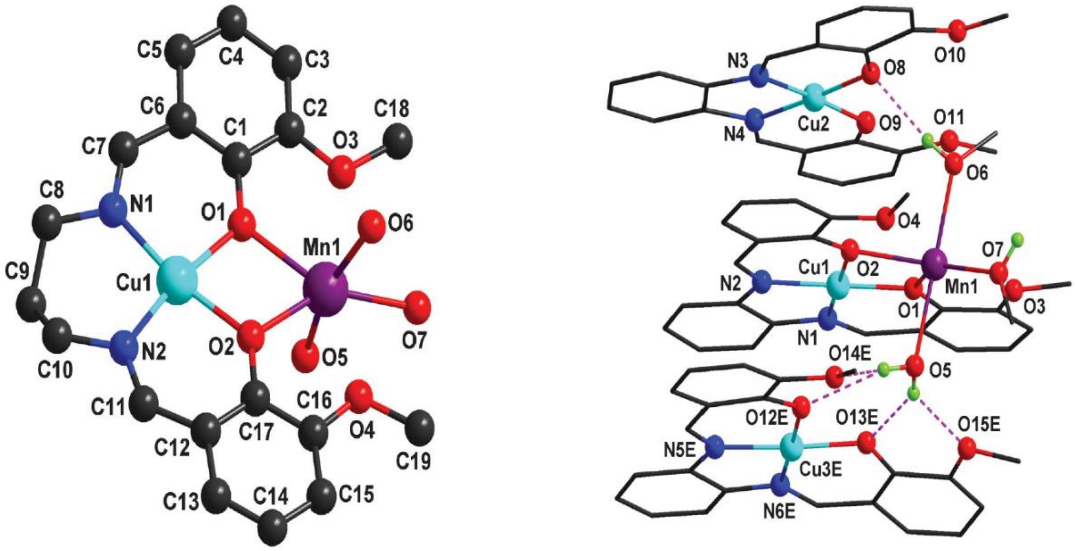

Figure 1.11. The crystal structures of **I4** (left) and **I5** (right).

The crystal structure of **I5** can be considered as a co-crystal, where the tetranuclear [{$Cu^{II}L^2Mn^{II}(H_2O)(MeOH)_2$}($Cu^{II}L^2$)$_2$]$^{2+}$ dication consists of one dinuclear diphenoxo-bridged [$Cu^{II}L^2Mn^{II}(H_2O)(MeOH)_2$]$^{2+}$ dication and two mononuclear [$Cu^{II}L^2$] neutral units. Interestingly, due to hydrogen bonds and π···π stacking interactions, the dinuclear [$Cu^{II}L^2Mn^{II}(H_2O)(MeOH)_2$]$^{2+}$ dication in **I5** was interlinked with two mononuclear [$Cu^{II}L^2$] moieties to form tetranuclear self-assemblies (Figure 1.12).

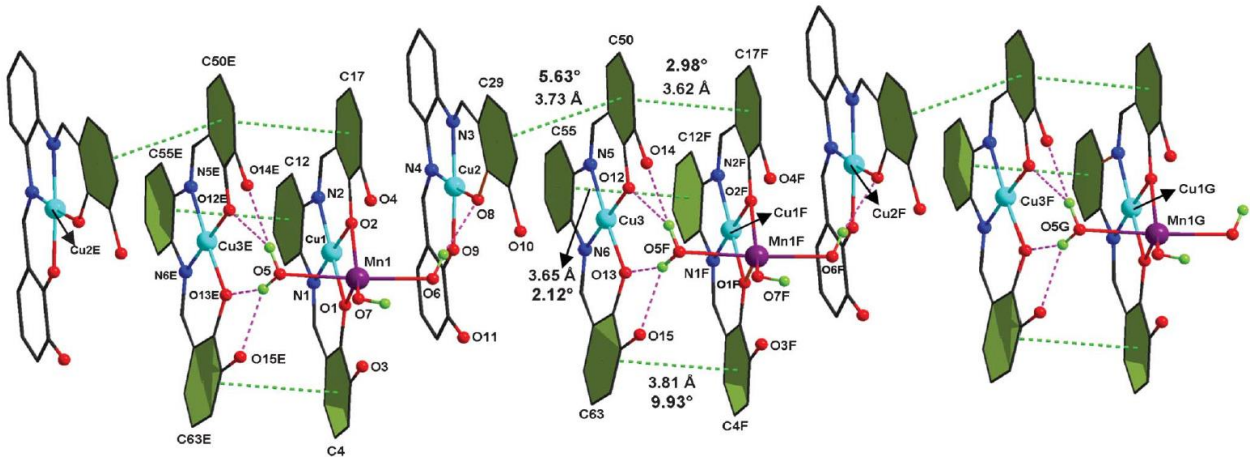

Figure 1.12. Perspective view of **I5** showing hydrogen bonding and π···π stacking interactions and one-dimensional self-assembly.

Magnetic properties of **I4** and **I5** have been studied, revealing moderate antiferromagnetic interactions (J = –29.1 and –15.9 cm^{-1} for **I4** and **I5**, respectively).

Another vivid example of the "building block" approach utilization is the series of heterotrinuclear Mn/Cu complexes, which have been prepared by A. Ghosh[33]. The Cu(II) complex of a dissymmetrically dicondensed Schiff base (H_2L= N-(2-hydroxyacetophenylidene)N′-salicylidene-1,3-propanediamine) has been used as metalloligand. The scheme of the synthesis of the heterometallic complexes **I6-I8** is shown in Figure 1.13. The magnetic properties of the **I6-I8** solids revealed antiferromagnetic exchange, as expected from bridging angles.

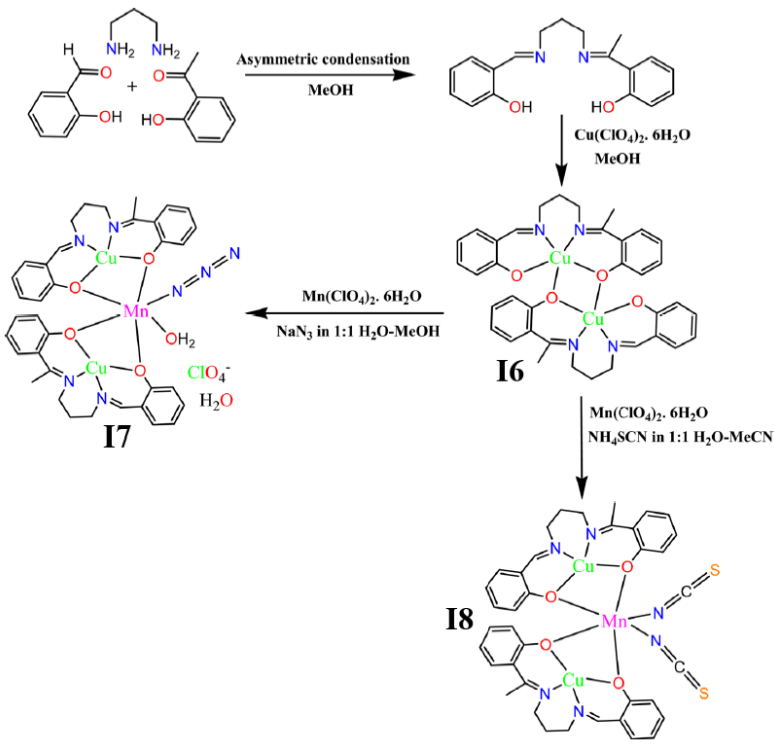

Figure 1.13. Syntheses of complexes **I6-I8**.

The catecholase like activity of the complexes was determined by the catalytic oxidation of 3,5-DiTertioButylCatechol (3,5- DTBC) (Figure 1.14).

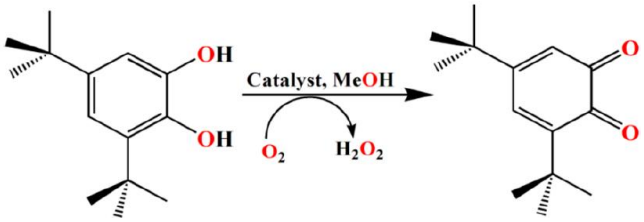

Figure 1.14. Catalytic Oxidation of 3,5-DTBC to 3,5-DTBQ in methanol.

The catalytic activity data of the complexes show that only complex **I7** with a labile coordinated water molecule at the Mn(II) center possesses very high catalytic activity toward catecholase. The catalytic conversions take place with the formation of hydrogen peroxide in catecholase like activities.

The MST "*star*" (Figures 1.6, 8), where the central metal ion is linked with the three terminal metal centers *via* six bridging donor atoms, is quite spread for the homo- and heterometallic complexes. However for the Mn/Cu there are only two reported compounds so far. The first example of star-shaped heterometallic $[\{CuL(H_2O)\}_2(CuL)Mn](ClO_4)_2$ (**I9**) complex was reported in 2012 by A. Ghosh[34]. In this case again the "building block" approach was successfully used. As a precursor for the synthesis of the tetranuclear aggregates, the [CuL] (where H_2L is the

tetradentate di-Schiff base derived from 1,3-propanediamine and 2-hydroxyacetophenone) complex has been used (Figure 1.15).

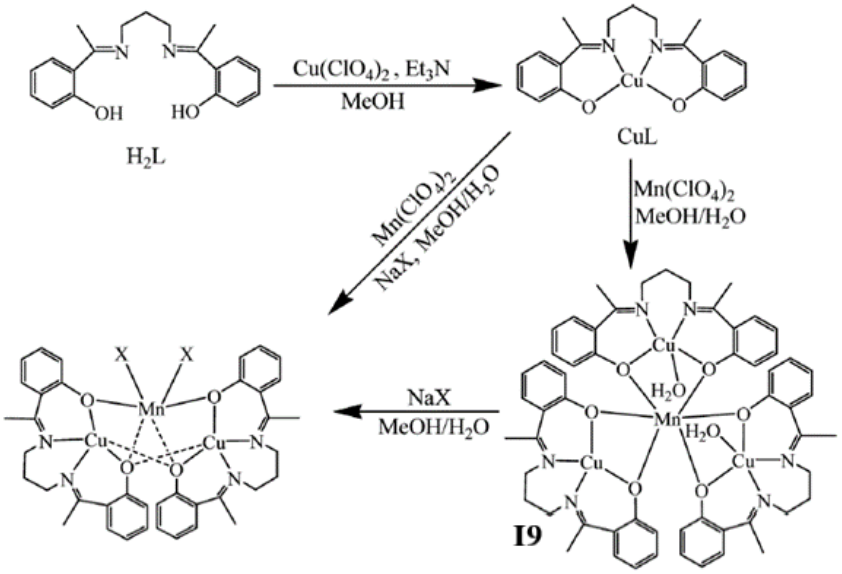

Figure 1.15. Synthetic route to complex **I9**.

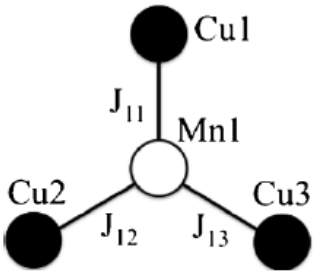

Figure 1.16. Magnetic exchange scheme in compound **I9**.

The magnetic data have been reconstructed by considering the following spin Hamiltonian $H = -[J_{11}S_{Mn}S_{Cu1} + J_{12}S_{Mn}S_{Cu2} + J_{13}S_{Mn}S_{Cu3}]$ (Figure 1.16) and clearly indicates antiferromagnetic interaction of medium size between metal ions (J_{11} = –41,2, J_{12} = –39,8 and J_{13} = –12,6 cm^{-1}).

The most common MSTs for tetranuclear complexes "*cubane*" and "*divacant face-shared double cubane like the $Ti_4(OCH_3)_{16}$ core*" (Figures 1.6, 8) for the Mn/Cu metal pair were described only in 2013[35] with Schiff base ligands, derivatives of salicylaldehyde and aminoalcohols (Figure 1.17). The higher flexibility of such kind of ligands (compared to the ones in Figures 1.10, 13, 15) drives the opportunity for synthesis of compounds with "unexpected"

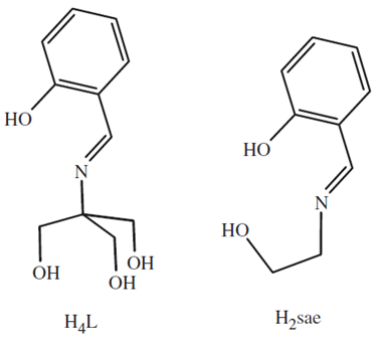

Figure 1.17. Schiff base ligands

crystal structure. The reaction of zero-valent metal's powder with transition metal salts and aminoalcohols has proved the effective way for the preparation of heterometallic aggregates[36-37], especially Mn^{III}–Cu^{II} clusters[38]. Various aminoalcohols such as triethanolamine (H_3tea) and diethanolamine (H_2dea) act as proton donating agents[36] for oxidation of copper or other transition metal ions in air and also as multidentate ligands that can assemble various metal centers into heterometallic clusters[36-37]. Accordingly, two multidentate Schiff-base ligands were prepared

in situ and reacted with zero-valent copper and manganese nitrates, leading to isolation of two new tetranuclear heterometallic $[Mn^{III}_2Cu^{II}_2(H_2L)_4](NO_3)_2{\cdot}2CH_3OH$ (**I10**) and $[Mn^{III}Cu^{II}_3(sae)_4(CH_3OH)(H_2O)_3](NO_3){\cdot}CH_3OH$ (**I11**) complexes (Figure 1.18).

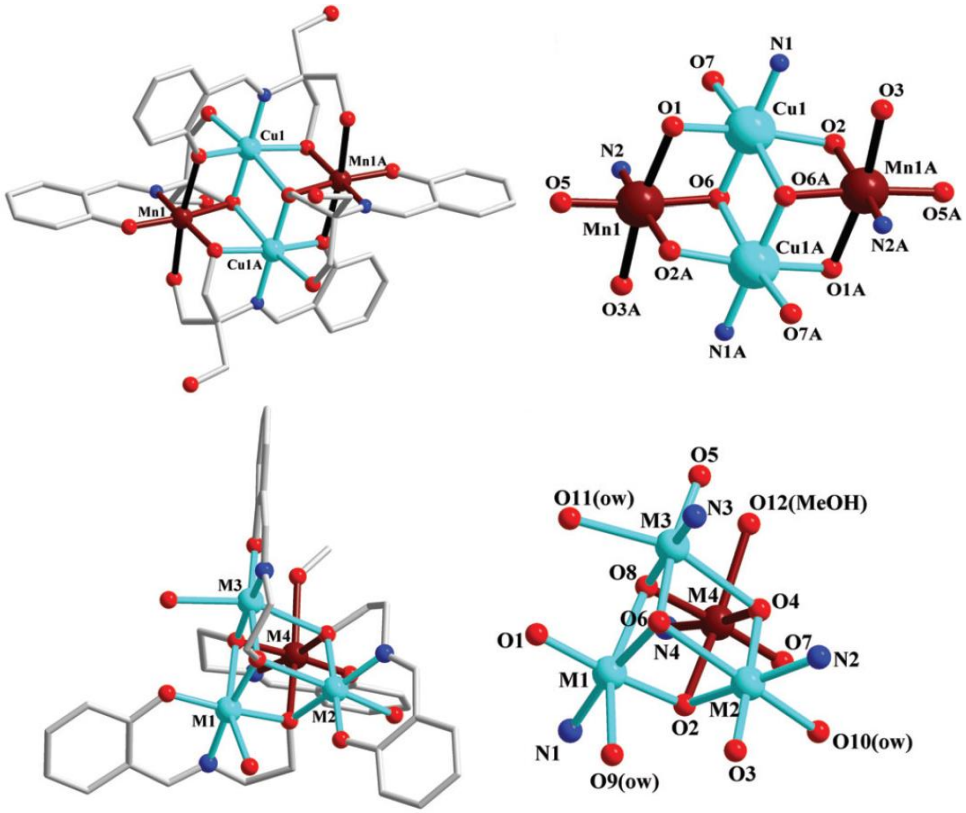

Figure 1.18. Ball-and-stick view of the cationic cluster of **I10** (top, left) and **I11** (bottom, left); the tetranuclear core together with the coordination modes of Cu and Mn centers of **I10** (top, right) and **I11** (bottom, right).

The magnetic properties of the **I10, I11** revealed antiferromagnetic exchange between the metal centers.

Note, that high nuclear heterometallic Mn/Cu complexes (M_mX_n, m > 10) are not common. Thus only 6 examples, with aminoalcohols and Schiff base ligands, were described so far. One of the most significant high nuclear compounds was the 45 nuclear Mn/Cu complex, reported in 2007 by D. N. Hendrickson[38]. Its formation can be described by the following scheme:

$$Cu^0 + Mn(OAc)_2 + H_3Tea + O_2 + dmf \rightarrow [Cu_{17}Mn_{28}(Tea)_{12}(HCO_2)_6(H_2O)_4]{\cdot}36H_2O$$

This giant heterometallic $\{Cu^{I}_{17}Cu^{II}_{13}Mn^{II}_4Mn^{III}_{12}Mn^{IV}_{12}\}$ cluster is unprecedented with five metal oxidation states.

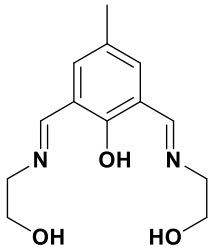

Figure 1.18. Schiff base ligand (H_3bemp).

The only two examples of high nuclear heterometallic Mn/Cu complexes with Schiff base ligand were reported in 2007 by H. Oshio[39]. Thus the reaction of tetradentate Schiff base ligand (H_3bemp, Figure 1.18) with manganese and copper nitrates in a 1:2:2/3 ratio

afforded the heterometallic mixed valence cluster $[Mn^{III}_8Mn^{IV}_6Cu^{II}_4Cu^{II}_8O_{16}(OMe)_4(OAc)_4(NO_3)_2(bemp)_4(H_2O)_{10}](NO_3)_2{\cdot}8H_2O$ (**I12**), while the reaction with a 1:2:2 ratio yielded the different compound $[Mn^{III}_6Cu^{II}_{10}O_8(OH)_2(OAc)_8(bemp)_2(Hbemp)_2](NO_3)_2{\cdot}14H_2O$ (**I13**). The crystal structures of obtained compounds are based on icosahedral $\{Mn_8^{III}Mn^{IV}_4Cu^{II}_8O_{16}\}$ (**I12**) and 16 nuclear $\{Mn_6^{III}Cu^{II}_{10}O_{22}\}$ (**I13**) fragments (Figure 1.19)

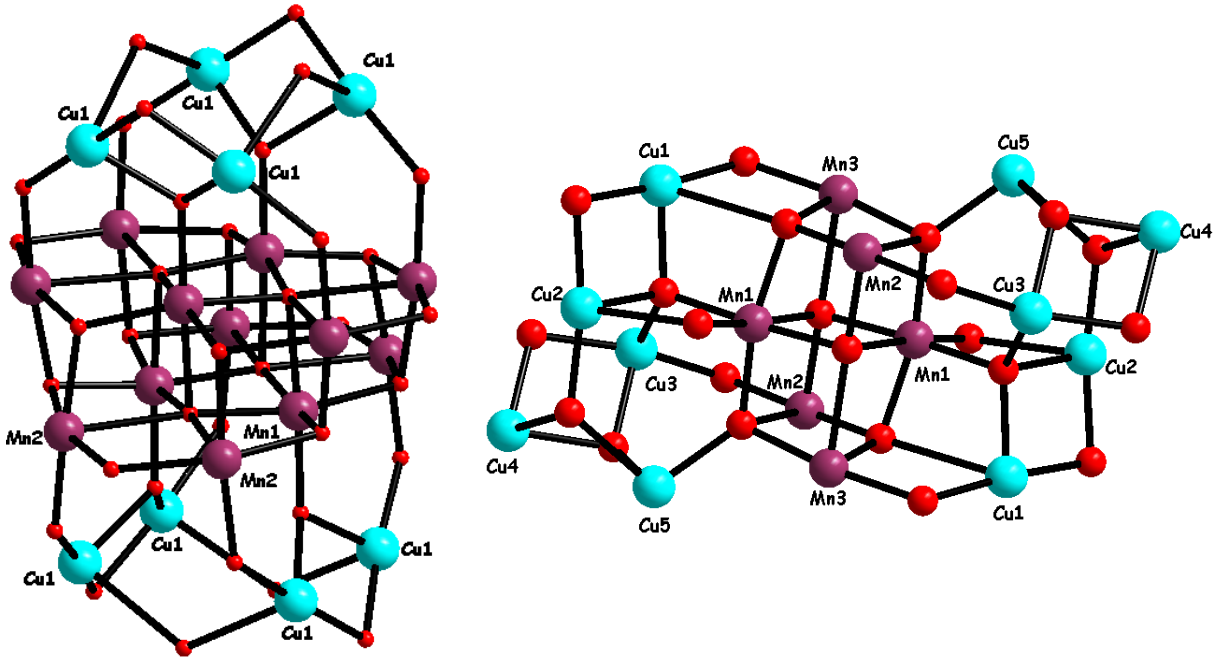

Figure 1.19. The crystal structures of $\{Mn_8^{III}Mn^{IV}_4Cu^{II}_8O_{16}\}$ (**I12**, left) and $\{Mn_6^{III}Cu^{II}_{10}O_{22}\}$ (**I13**, right) fragments.

Magnetochemical studies revealed the dominant antiferromagnetic interaction between metal centers.

The present analysis of the heterometallic Mn/Cu complexes shows the most of them were obtained using the designed synthesis or the "building blocks" approach. Only far fewer examples were isolated when the "serendipitous assembly" method was applied. This observation drives the new perspective direction in the synthesis of Mn/Cu compounds with the non-symmetrical Schiff base ligands, derivative of salicylaldehyde and aminoalcohols.

1.4. Heterometallic Mn/Co complexes.

The Mn/Co metal's pair, besides the opportunity to show different stable oxidation states and to form polynuclear architectures, is interesting thanks to the magnetic properties of these ions[40]. On the other hand, the multimetallic Mn/Co active sites are found in enzymes that catalyze vital processes such as photosynthesis, nitrogen fixation, and carbon dioxide reduction[41-43]. According to CSD around 230 heterometallic Mn/Co complexes were described so far and only forty-three among all Mn/Co compounds contain at least one bridging oxygen atom. The similar

structural analysis as for Mn/Cu complexes has been done also for Mn/Co derivative. The main MSTs are shown in Figure 1.20.

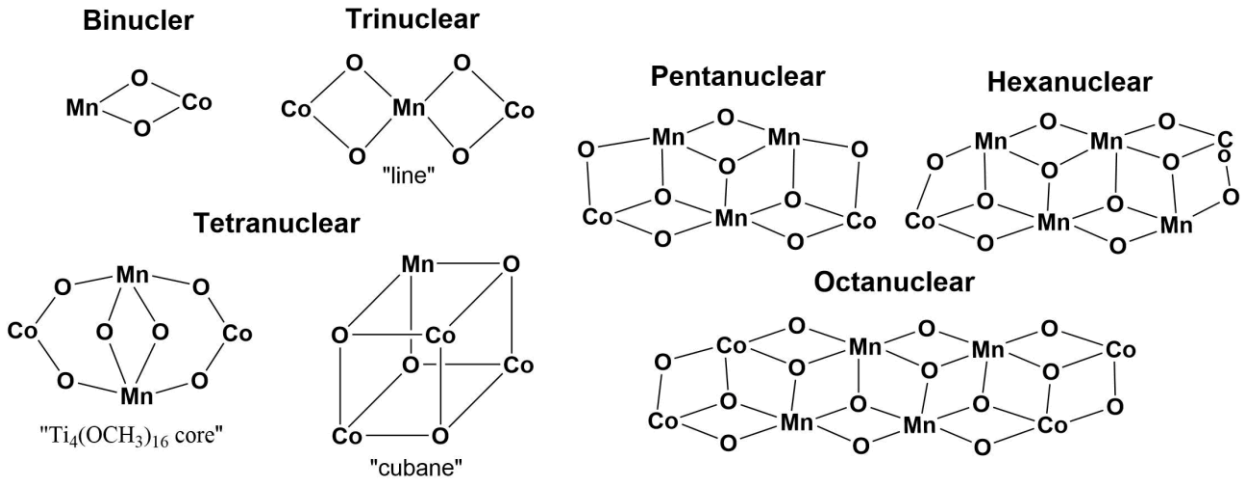

Figure 1.20. The main MSTs for the heterometallic Mn/Co complexes.

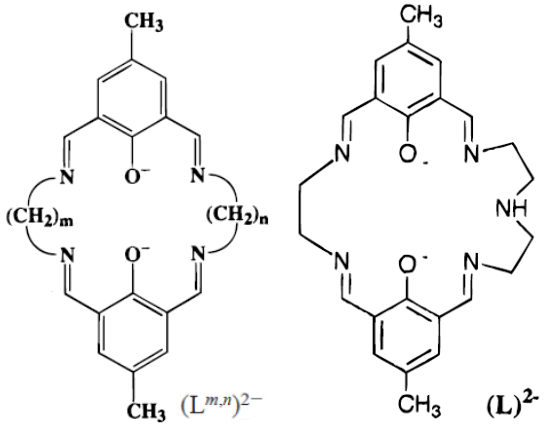

Figure 1.21. Macrocyclic Schiff base ligands.

The first examples of binuclear Mn/Co compounds were described in 1997 and 1999 by H. Okawa,[44-45] in which macrocyclic Schiff base ligands were used (Figure 1.21). The resulting $[CoMn(L^{2,3})(OAc)]ClO_4 \cdot dmf$ (**I14**) and $[CoMn(L^{2,4})(OAc)]ClO_4$ (**I15**) heterometallic complexes based on the $\mathbf{(L^{m,n})^{2-}}$ ligands are isostructural, while the $[CoMn(L)(OAc)]ClO_4$ (**I16**) and $[CoMn(L)(NCS)]ClO_4$ (**I17**) compounds with $\mathbf{(L)^{2-}}$ just exhibit similar structural features.

Series of trinuclear $[Co_2Mn(\mu\text{-}salenph)_2(\mu\text{-}OAc)_2]$ (**I18**) and $[Co_2Mn(\mu\text{-}salenph)_2(\mu\text{-}Cl)_2]$ (**I19**), where salenph – *N*,*N*^{0}-phenylenebis(salicylideniminato) complexes have been obtained by solvothermal reaction between [Co(salenph)] and the corresponding manganese(II) salts in ethanol[46] . The scheme of the synthesis is shown in Figure 1.22.

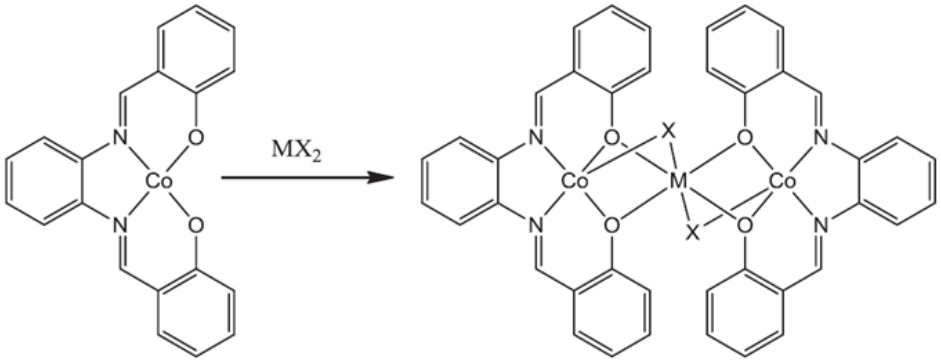

Figure 1.22. The scheme of the synthesis of **I18** and **I19** (X = OAc^-, Cl^-).

For both complexes the magnetic susceptibility data indicate that the terminal cobalt (II) ions are in a low spin state, while the central manganese (II) ion possesses the high spin state. The superexchange between these atoms takes place through the bridging oxygen atoms leading to a ferromagnetic interaction (Figure 1.23).

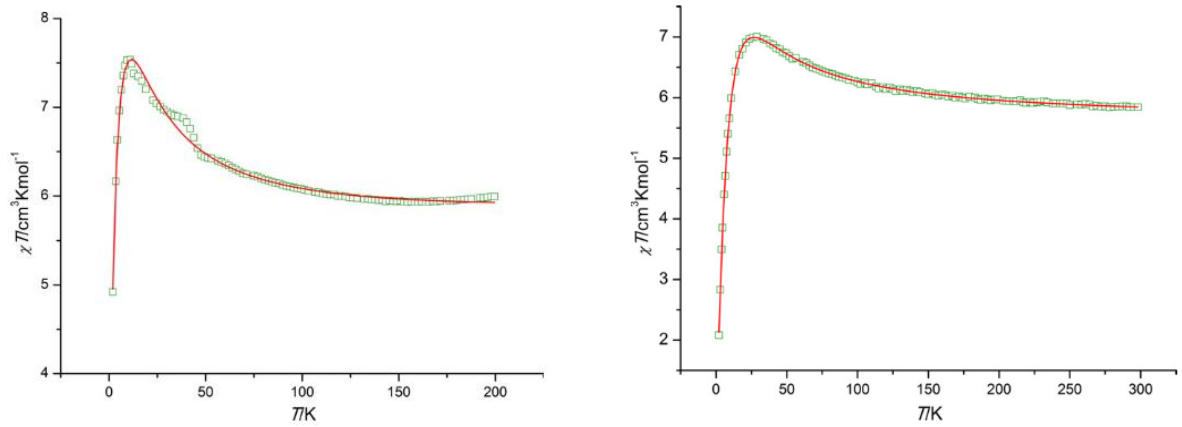

Figure 1.23. Temperature dependence of χT for **I18** (left) and **I19** (right).

The best fits were obtained as follows g = 2.89(1), J = 11.0(4) cm^{-1}, for **I18** and g = 2.13(1), J = 13.6(8) cm^{-1} for **I19**. Like many heteronuclear derivatives, the trinuclear complexes **I18** and **I19** can be used as single-source precursors for the formation of mixed oxides of nanometric size. Thermal stability investigation revealed that these *salen* based complexes started to decompose above 300 °C leading to the expected spinel Co_2MnO_4 where the same metal ratio as in their parent complexes was observed.

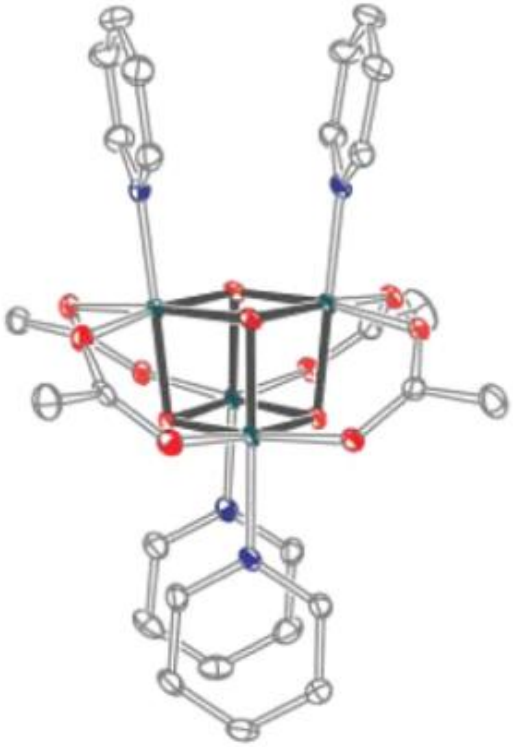

Figure 1.24. The crystal structure of $[Co_4O_4(OAc)_4py_4]$.

It is well known that cobalt oxide materials CoO_x are among the most promising catalysts for water oxidation, due to their robust structures, inherent activity, and most importantly, the abundance of cobalt in the earth's crust[47-49]. But the low solubility of such kind of materials in water makes the mechanistic studies of the cobalt containing catalysts difficult for investigation. Therefore Co-containing complexes were chosen as a model for investigation of water oxidation catalysts (WOCs) mechanism. One of the first research dedicated to this problem was described in 2015 by T. D. Tilley[50]. The cobalt containing $[Co_4O_4]$ oxide cubane cluster,

obtained by Beattie in *1998*[51] (Figure 1.24), was used as a model for WOC mechanism's investigation. The investigations involved a combination of electrochemistry, stoichiometric reactivity, spectroscopy, and kinetic experiments to observe and identify many key intermediates and reaction steps of catalyzed water oxidation involving the $[Co^{III}_4]$ cubane. Kinetic studies show an unusual mechanism involving the formation of a formal $[Co^{III}_3Co^{V}]$ or $[Co^{III}_2Co^{IV}_2]$ intermediate prior to O_2 release. Taken together, these data may provide a basis for the rational design of more efficient and robust cobalt-based catalysts.

As a continuation of this research the series of heterometallic complexes, possessing the $[MnCo_3O_4]$ cubane-like core was described[52]. These $[MnCo_3O_4]$ clusters may be regarded as Mn-doped versions of the $[Co_4O_4]$ catalyst[50], and may serve as useful models for Mn-doped CoO_x (Figure 1.25). $[MnCo_3O_4]$-based clusters are ligated by simple air- and water stable carboxylate and pyridine ligands, and ligand exchange reactions allow systematic modifications of the Mn coordination sphere.

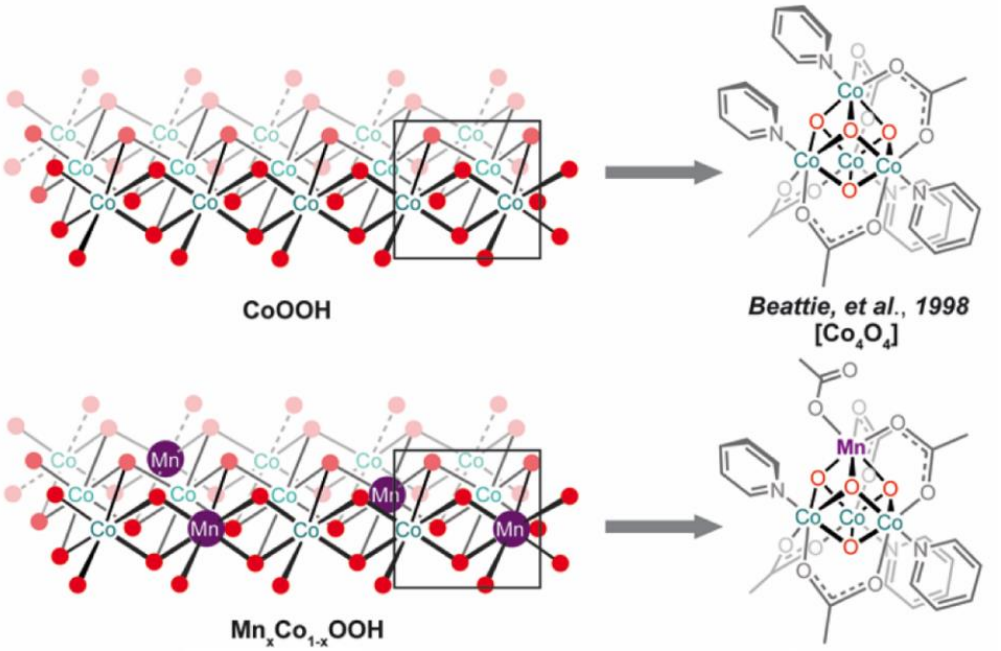

Figure 1.25. Comparison of models for cobalt oxyhydroxide and manganese-doped-cobalt oxyhydroxide.

The reaction of 3 equivalents of cobalt(II) acetate tetrahydrate with potassium permanganate in the presence of pyridine yielded the heterometallic tetranuclear cluster $[MnCo_3O_4(OAc)_5py_3]$ (**1-OAc**) (Figure 1.26). It should be noted that **1-OAc** was soluble and stable in water and organic solvents such as DCM, ACN, and CH_3OH.

The reaction of **1-OAc** with oxalyl chloride resulted in **1-Cl**. The **1-Cl** chloride derivative can be used as a starting point for further ligand substitutions *via* precipitation of metal chloride salts. For example, exchange for nitrate (NO_3^-) upon reaction of 1-Cl with silver nitrate afforded **1-NO$_3$** (Figure 1.26). On the other hand, the strong toluenesulfonic acid (HOTs) acid reacted with 1-OAc by way of exchange of an acetate ligand for tosylate (OTs) to generate **1-OTs**.

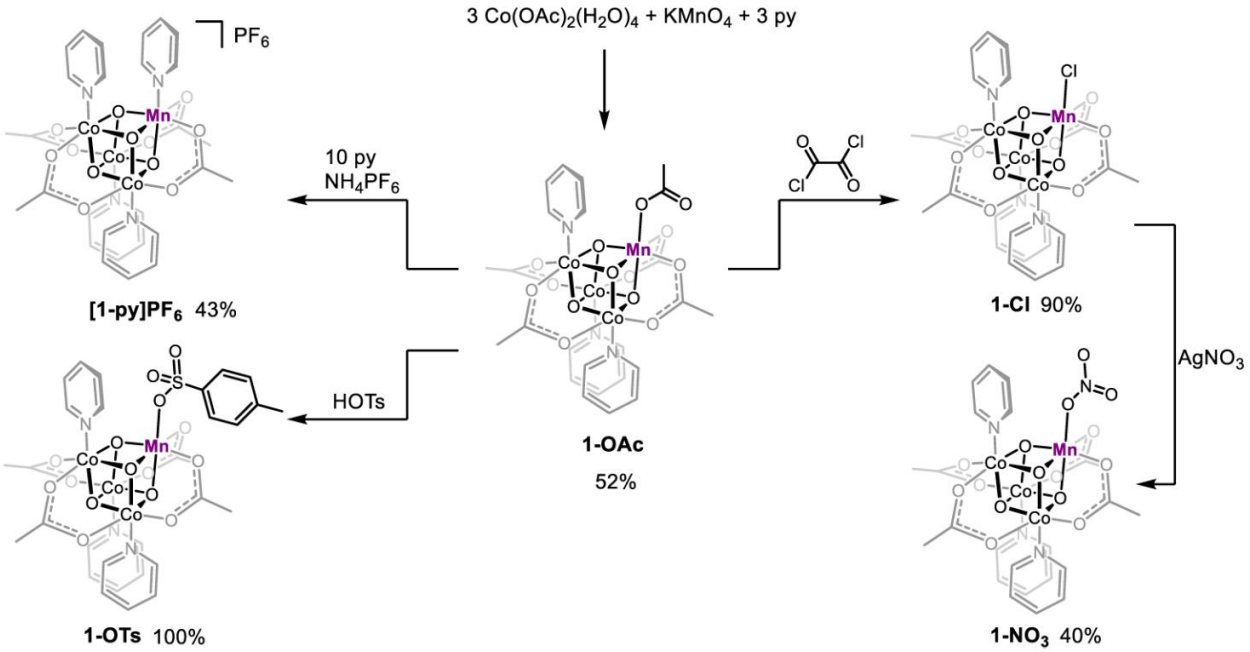

Figure 1.26. Synthesis of $[MnCo_3O_4]$ cubane complexes.

And finally, heating an aqueous solution of **1-OAc** with an excess of pyridine in the presence of hexafluorophosphate anion (PF_6^-), the $[Co_3MnO_4(OAc)_4py_4]PF_6$ (**[1py]PF$_6$**) complex has been isolated.

The latest investigation reported in 2018 by T. D. Tilley[53] showed that the cobalt(II), quantitatively added to the heterometallic Mn/Co cubane $[MnCo_3O_4(OAc)_5(py)_3]$ (**1-OAc**) complex in the presence of acetate and nitrate, yielded the pentametallic "dangler" complex $[MnCo_4O_4(OAc)_6(NO_3)(py)_3]$ (**2**) (Figure 1.27, left).

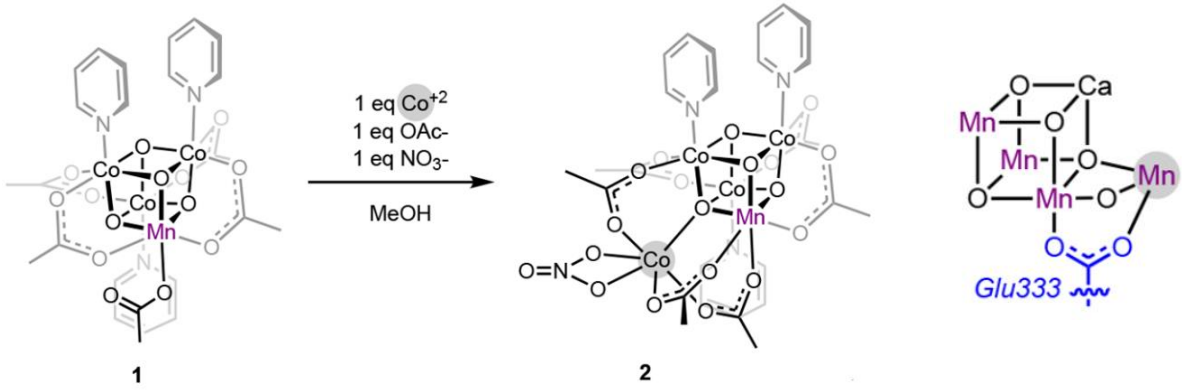

Figure 1.27. Synthetic strategy for a "Dangler" complex **2** (left) and OEC core (right).

The structure of complex **2** reminiscent of photosystem II's oxygen-evolving center, and is a very rare example of a transition metal "dangler" complex. OEC is a peculiar cofactor, which can be also considered as a complex with a "dangling" Mn ion[54] (Figure 1.27, right).

The only few examples of high nuclear Co/Mn complexes (M_mX_n, $m > 5$) were reported in 2012 by K. S. Murray[55]. Complexes of different nuclearity were obtained by using aminoalcohols as the ligands (Figure 1.28). In the case of manganese nitrate as a precursor, the two heterometallic

pentanuclear **I21**, **I23** were isolated. Both compounds are based on the mixed valence metal core ($\{Mn^{II}Mn^{III}{}_2Co^{III}{}_2O_8\}$ for **I21**, while the $\{Mn_2{}^{II}Mn^{III}Co^{III}{}_2O_8\}$ cluster for **I23**). Magnetochemical data revealed the presence of antiferromagnetic interactions between Mn ions in **I21** and **I23**. For the latter the ferromagnetic exchange was detected between Mn^{II} and Mn^{III} ions.

The reaction of manganese (II) acetate with cobalt tetrafluoroborate resulted in the octanuclear complex **I20** (Figure 1.28). The main structural unit of the compound obtained is the $\{Mn^{III}{}_4Co^{II}{}_2Co^{III}{}_2O_{12}\}$ mixed valence fragment. Here the Co ions possess several different oxidation states.

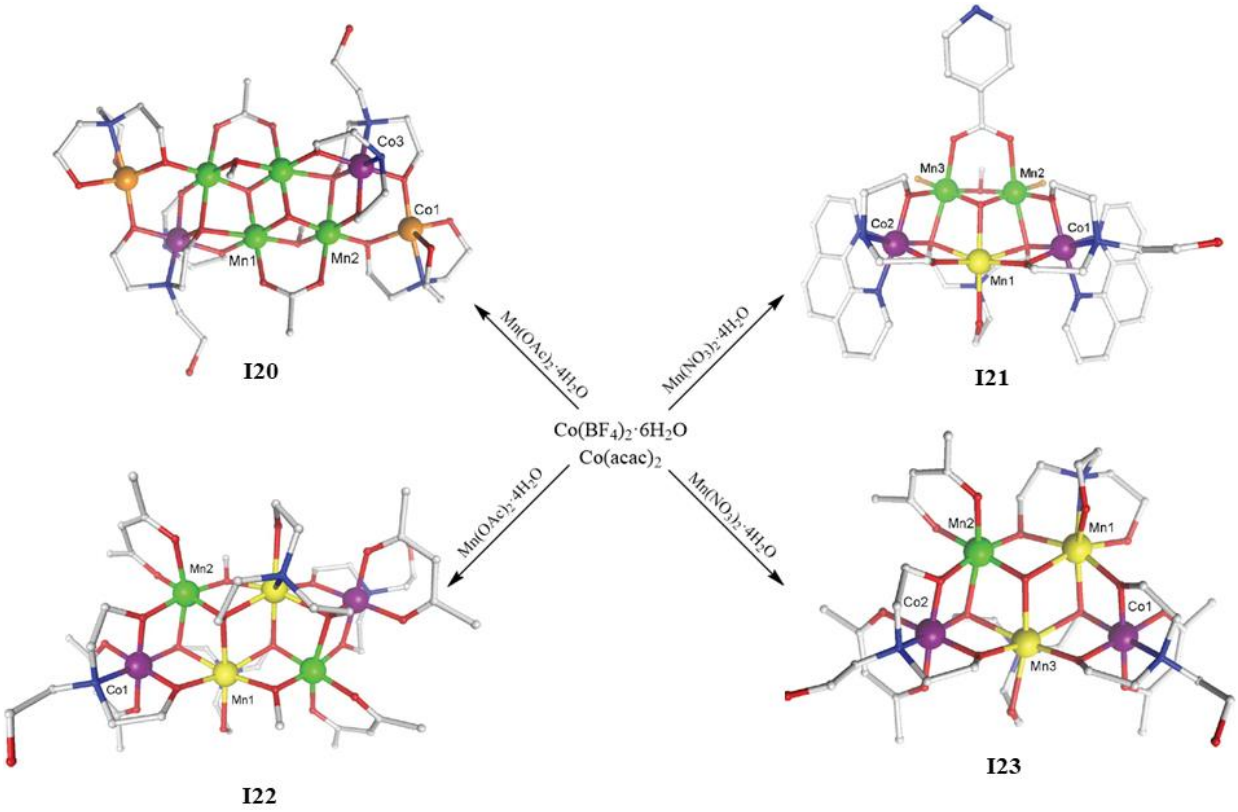

Figure 1.28. The synthesis of **I20-I23**. Mn^{III} green, Mn^{II} yellow.

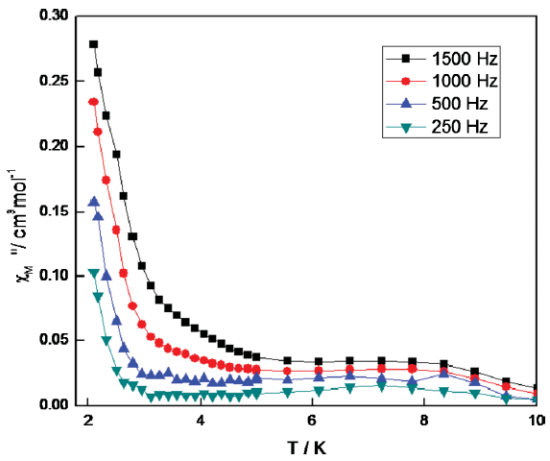

Figure 1.29. Plots of the out-of-phase AC susceptibilities χM″ vs. T (2–10 K) for **I21** frequencies shown. The solid lines just join the points.

Frequency-dependent AC out-of-phase susceptibilities, in the temperature range 2–10 K, are indicative of the probable single molecule magnetism (SMM) in cluster **I21** (Figure 1.29).

The analysis of the heterometallic Mn/Co complexes revealed that such compounds may exhibit different useful properties from magnetism to catalytic activity. The prominent examples of $[MnCo_3O_4]$

cubane systems represent a new class of easily prepared, versatile, and redox-active oxide clusters that should contribute to the understanding of Mn-containing coordination clusters. Most of the Mn/Co heterometallic complexes, like the Mn/Cu derivative, were obtained using the "building blocks" approach, while the coordination chemistry of Mn/Co complexes with Schiff base ligands is not well investigated so far.

1.5. Electroactive ligands and complexes.

The synthesis and coordination chemistry of electroactive ligands leading to various electroactive metal complexes have been developed during the past two decades. Indeed, remarkable redox-active classes of compounds are represented by tetrathiafulvalene derivatives[56], dithiolene complexes[57] and tetrazine[58-59] which have been extensively studied in the search for multifunctional materials, exhibiting a variety of properties, arising from the nature of the ligands and respective metal ions. The previous sub-chapters described mainly the complexes with "classical" Schiff base ligands, obtained by a simple *in situ* condensation. As an extension of this work, our objective was devoted to the mentioned above redox-active molecules and the main aspects of their coordination chemistry.

1.5.1. Tetrathiafulvalene (TTF) based complexes.

Tetrathiafulvalene is an organosulfur compound with the empirical formula of $(C_2H_2S_2C)_2$. Its molecular and crystal structures[60] are illustrated in Figure 1.30.

Figure 1.30. Molecular (left) and crystal structures (right) of the TTF molecule.

The research investigation of this heterocyclic compound mainly contributed to the development of molecular electronics. The TTF molecule itself does not exhibit any remarkable electrical properties. However, the distinctive properties are associated with salts of its oxidized derivatives. Electrochemical measurements show that TTF can be oxidized twice reversibly[61] (Figure 1.31, 32).

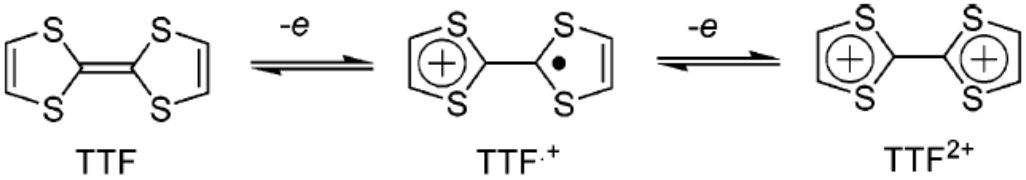

Figure 1.31. The oxidation steps of the TTF molecule.

The high electrical conductivity of TTF salts can be attributed to the following features of TTF: (i) planarity of the molecule, resulted in orbital overlap of its oxidized derivatives, (ii) high symmetry promotes charge delocalization, thereby minimizing coulombic repulsions (iii) the ability to undergo oxidation at mild potentials to give a stable radical cation.

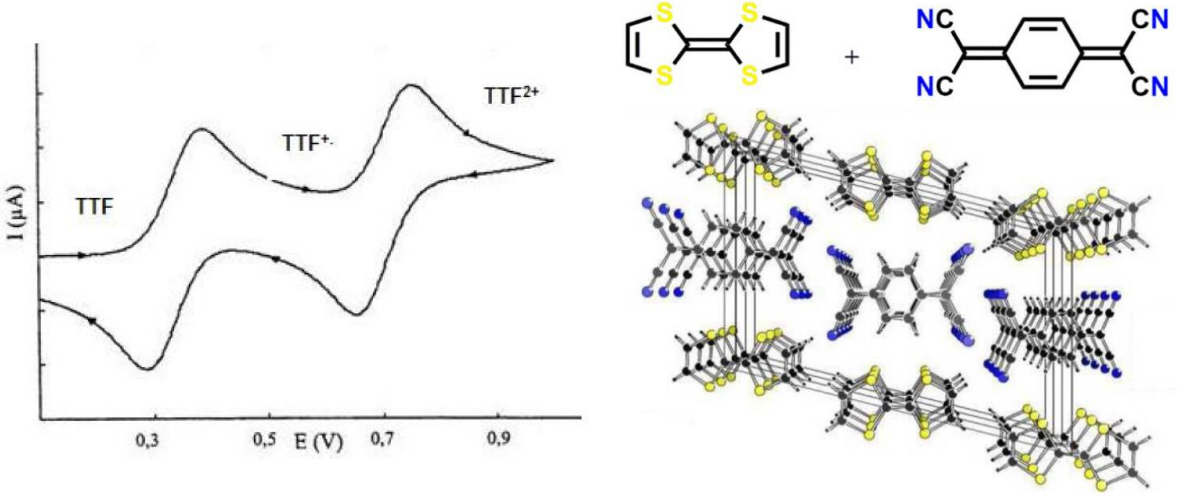

Figure 1.32. The cyclic voltammogram of TTF (10^{-3} M) in ACN, (V = 100 mV·s^{-1}, Bu_4NPF_6 (10^{-1} M) *vs.* Ag/AgCl, left) and the unit cell of the TTF-TCNQ charge transfer complex (right).

The stability of the oxidized TTF-species can be proved by CV, where the two oxidation waves at 0.34 V and 0.78 V were observed.

An extensive study of TTF and its derivative as the molecular conductors began in 1973, after charge transfer complex (Figure 1.32, right) of TTF (donor) and tetracyanoquinodimethane (TCNQ, acceptor) has been described by Cowan et al.[62]. As can be seen in Figure 1.32, the crystal structure of the TTF-TCNQ complex is remarkable because of the presence of separate stacks of donors and acceptors. The conductivity value at room temperature was $\sigma \approx 500$ S·cm^{-1}, which is close to the one found in classical metals. In fact, the compound obtained was the first example of an organic metal. However, a limitation of the conductivity in a single direction (in the stack direction) has been observed. This first result prompted the further research that has been devoted to TTF.

Thanks to the large variety of the properties of the TTF molecule, it became one of the main motifs for obtaining multifunctional materials. Figure 1.33 summarizes all the changes made on the TTF core.

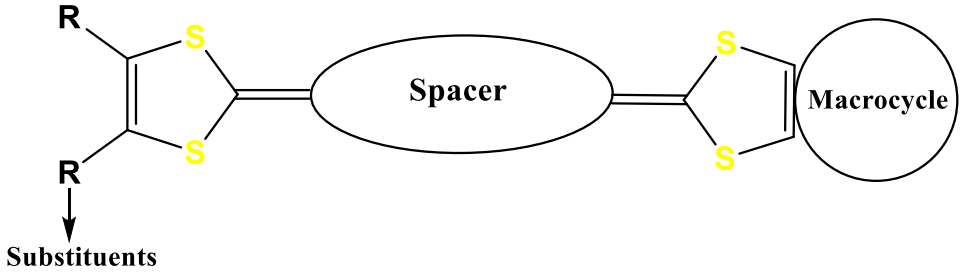

Figure 1.33. Structural modification of the TTF core.

One of the most prominent investigation in this direction is the TTF-based macrocyclic systems with a focus on their use in supramolecular host-guest recognition, as components in non-covalent electron transfer systems[63-69]. The following classes of TTF-based systems were described so far: TTF-calixpyrroles[70-71], exTTF macrocyclic systems[71], tetrathiafulvalene vinylogues (TTFVs)[71], TTF-hemicarcerand and TTF-carcerands[71].

Among the numerous TTF ligand systems investigated during last few decades those containing N, O donor atoms and 3d-metal ions are the most extensively studied so far. In 2009 N. Avarvari discussed in a review article the two synthetic strategies towards these electroactive ligands[56] (Figure 1.37).

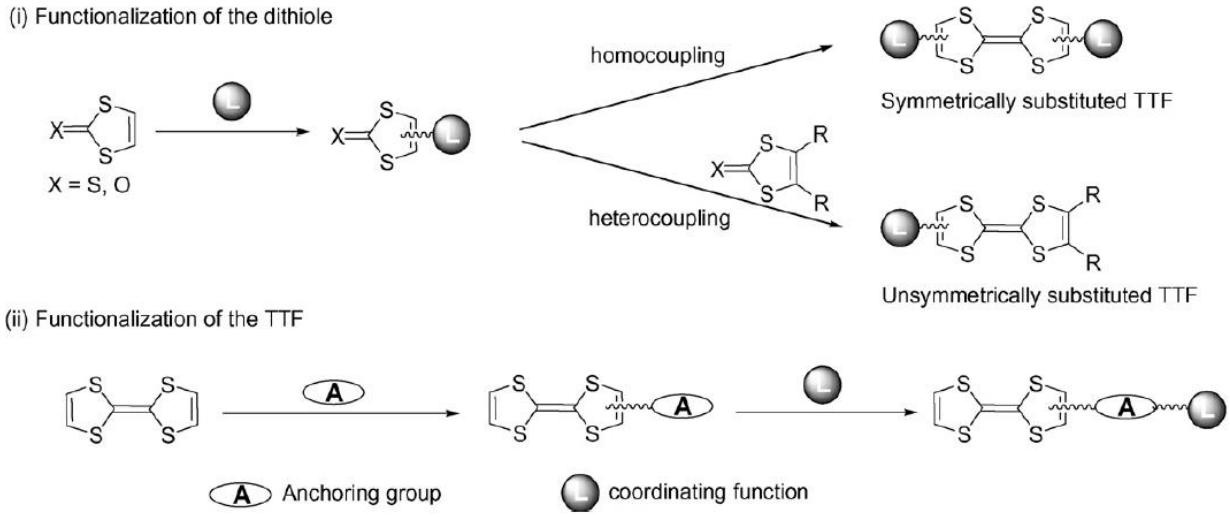

Figure 1.37. Two main synthetic approaches for the synthesis of N,O-TTF ligands[56].

The first strategy (i) is based on the functionalization of the dithiole unit by the coordination function, followed by its homo or heterocoupling to the symmetrical or non symmetrical substituted. The second approach (ii) is the modification of the previously formed donor moiety with a reactive group which will then serve as an anchorage for introducing the coordinating part on the TTFs. The respective examples of complexes with these functionalized TTF-based ligands will be given in chapter III of this manuscript.

1.5.2. Dithiolene metal complexes.

Metal dithiolene compounds can be considered as complexes containing unsaturated bidentate dithiolate ligand wherein the two donor atoms are sulfur. They can be either heteroleptic (contain an auxiliary ligand besides the dithiolate ligand) or homoleptic. The most representative examples of homoleptic compounds are the bis(dithiolenes)[72] and tris(dithiolenes)[73] metal complexes, whereas the most popular hetereleptic complexes are the metal diimine dithiolenes, developed by Eisenberg[74], and the cyclopentadienyl metal dithiolenes extensively investigated, among others, by Fourmigué[75] and Nishihara [76] (Figure 1.38).

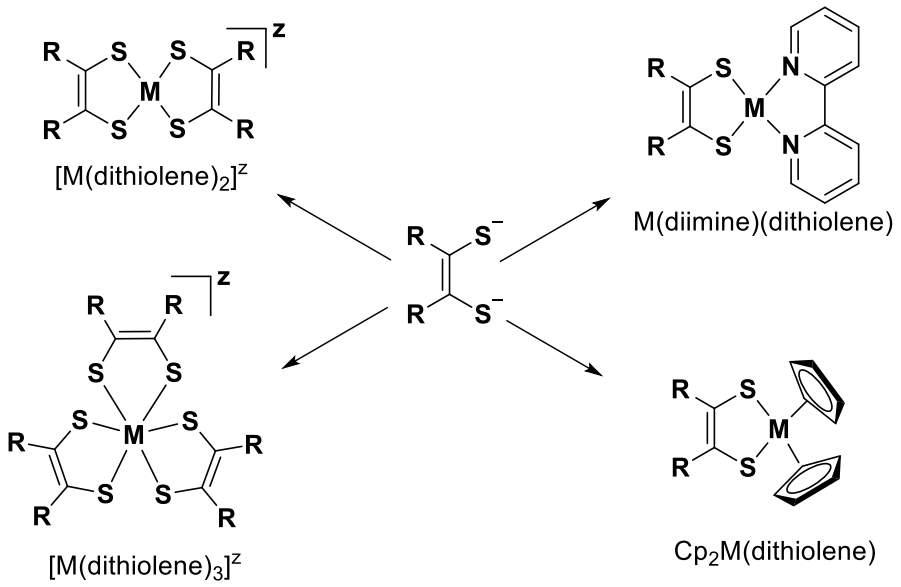

Figure 1.38. The most representative types of dithiolene complexes[77].

The wide interest of the dithiolene complexes is arised from the ‘‘non-innocent” character of these ligands[78]. Thus, a strong mixing of the ligand and metal contributions in the frontier orbitals, allow us to consider these complexes as a radical, what resulted in the unique properties which are increasingly relevant to fields including electrical and magnetic materials, non-linear optics, catalysis and bioinorganic chemistry[79-80].

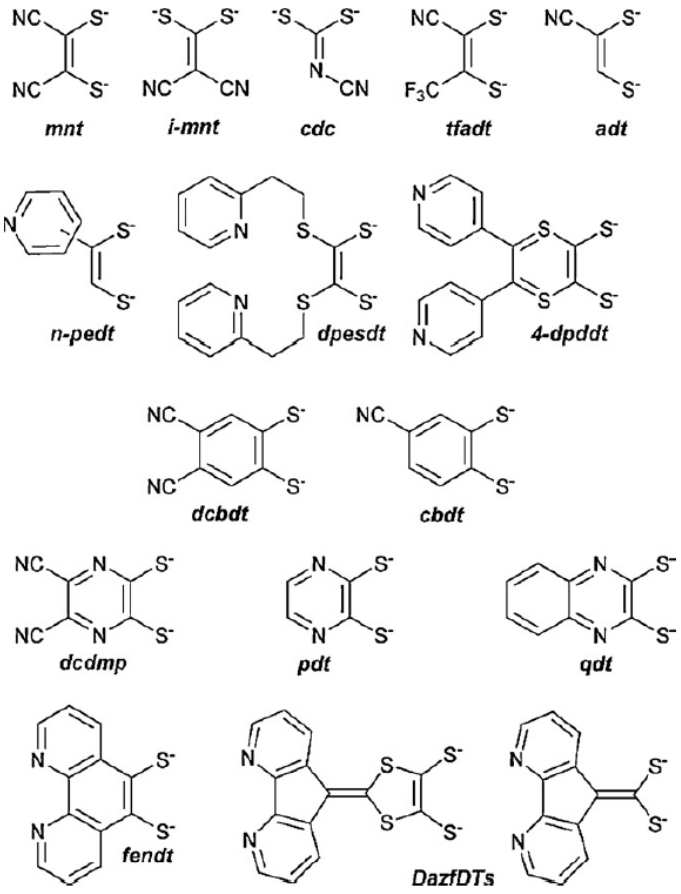

Figure 1.39. Dithiolene ligands containing N coordinating atoms.

However, the research interest nowadays is to functionalize the dithiolene ligands in order to have the opportunity to obtain the polynuclear compounds in which two or more metal centers coexist. One of the most promising approach to reach this goal is the incorporation of the additional donor atoms into the dithiolene ligand. Indeed, the dithiolene ligands containing N coordinating atoms can selectively bind different metal ions and act as bridging units in coordination architectures. Some of these types of ligands were discussed in 2009 by M. Almeida[81] (Figure 1.39). The complexes obtained with maleo-

nitriledithiolate (*mnt*) ligand are among the most popular from this family and probably one of the most investigated classes of dithiolene compounds[57, 72]. The first three ligands (*mnt, i-mnt, cdc*) were also the premier dithiolenes substituted with N coordinating groups.

One of the most representative complexes with the *mnt* ligand is a coordination polymeric material (Figure 1.40) based on Mn_4 clusters and a bisdithiolene complex, exhibiting SMM behavior at low temperatures, with a ground state total spin $S_T = 9$ and reasonable electronic conductivity 0.22 S/cm at room temperature, thus showing a semiconducting behavior with an activation energy of 136 meV[82].

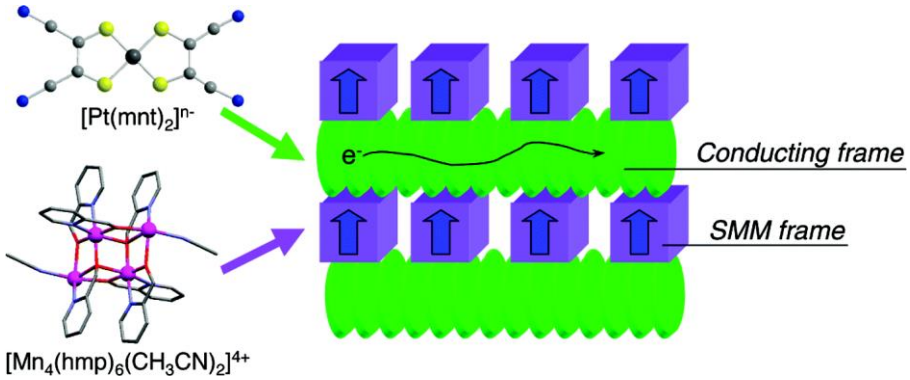

Figure 1.40. The representation of the $[\{Mn^{II}_2Mn^{III}_2(hmp)_6(CH_3CN)_2\}\{Pt(mnt)_2\}_4][Pt(mnt)_2]_2$ hybrid material, (hmp = 2-hydroxymethylpyridinate)[82].

The $[(CH_3CN)Ni(L)][Cu(mnt)_2]\cdot CH_3CN$ complex[83] can be considered as an isolated discrete heterometallic compound (L = tetrabenzo-[1,5,9,13]-tetra-azacyclohexadecine). This one contains one $[Cu(mnt)_2]^{2-}$ dianionic unit and the one $[Ni(L)]^{2+}$ dicationic fragment, linked *via* Ni–N covalent bond (Figure 1.41, left). Both Cu(II) and Ni(II) metal centers are paramagnetic, but they show some negligible magnetic interaction through the *mnt* bridge (Figure 1.41, right).

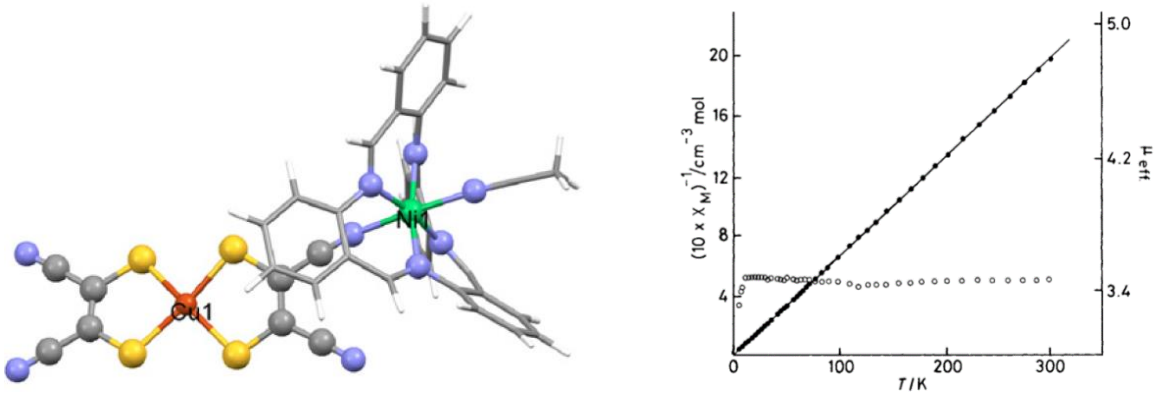

Figure 1.41. Crystal structure of the $[(CH_3CN)Ni(L)][Cu(mnt)_2]\cdot CH_3CN$ complex (left) and its temperature dependence of the reciprocal magnetic susceptibility $(\chi_M)^{-1}$ per molecule (•) and the effective magnetic moment per molecule (o), (right).

Pyrazine based dithiolene ligands *pdt*, *qdt* (Figure 1.39) represented only in few examples of Ni and Cu complexes[84-86] with alkaline metal ions such as Li^+, and Na^+. The side coordination in these compounds demonstrates a new branch in crystal engineering. However the possibility to coordinate other paramagnetic metal ions in these side positions has not yet been explored.

The functionalization of 1,10-phenanthroline in the 5th and 6th positions allowed the synthesis of 5,6-dithio-1,10-phenanthroline derivatives (*fendt*, Figure 1.39) which can be promising dithiolate ligand due to the combination of dithiolene and phenanthroline coordination units. Despite the functionality of such kind of ligand, only a few examples of homo- and heterometallic Ir- and Ru-based complexes were reported so far.

The series of dinuclear Ru/Ni, Ir/Ni, and Ir/Pt heteroleptic complexes with bridging phenanthroline-5,6-dithiolate ligands were reported in 2014[87]. The crystal structure of the Ru/Ni complexes $[(C_5H_5)(PPh_3)Ru(fendt)Ni(dppe)](PF_6)$ is illustrated in Figure 1.42.

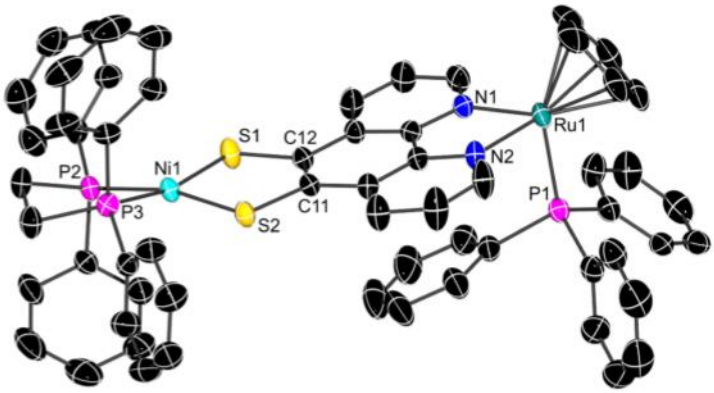

Figure 1.42. Crystal structure of the $[(C_5H_5)(PPh_3)Ru(fendt)Ni(dppe)]^+$ cation.

Lifetime measurements at room temperature, electrochemical investigations, together with the DFT calculations provide evidence for the efficient energy transfer from the Ru/Ir to the Ni complex moiety with a rate constant $k > 5 \cdot 10^9$ s^{-1}.

Other examples of homo- and heterometallic dithiolene based complexes will be given in chapter IV of this manuscript.

1.5.3. Tetrazine based complexes.

Tetrazine is a compound that consists of a six-membered aromatic ring containing four nitrogen atoms. The name tetrazine is used in the nomenclature of derivatives of this compound. Three core-ring isomers exist: 1,2,4,5-tetrazines, 1,2,3,4-tetrazines and 1,2,3,5-tetrazines, also known as *s*-tetrazines, *v*-tetrazines and *as*-tetrazines, respectively[88] (Figure 1.43).

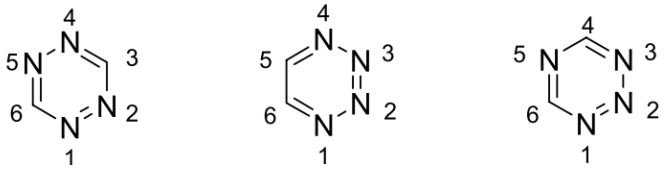

Figure 1.43. Numbering of the three possible isomers of tetrazine.

s-Tetrazines were employed successfully in several field of chemistry, starting from coordination chemistry[58] to the development of the explosive materials[89]. Only three main research direction in the field will be listed here: (1) Implication of tetrazines in the Diels-Alder

cycloaddition reactions to make new pyridazines[90]. It was particularly successfully employed in the synthesis of numerous natural products. (2) The high nitrogen content in these tetrazines allows them to be good candidate for application as explosive materials[91]. (3) Tetrazine based ligands for coordination chemistry[58-59].

CDS analysis of all *s*-tetrazine-containing molecules revealed ≈ 450 structures (≈ 250 among all are metal complexes). The close inspection of all these complexes allows us to propose the following classification of tetrazine based ligands (Figure 1.44).

First group of tetrazine based ligands mainly includes the symmetric dipyridyltetrazines (**T1–T5**), while the second one – is the symmetric dipyrimidyltetrazines (**T6**, **T7**). The last group contains the nonsymmetric ligands, which have two different substituents in 3rd and 6th position of the tetrazine ring (**T8–T12**).

Coordination chemistry of the first group of ligands is widely investigated. Thus, according to CSD, more than half of all tetrazine-based complexes are the compounds with the first group ligands, whereas the complexes based on the second and third groups of ligands are represented by fewer examples.

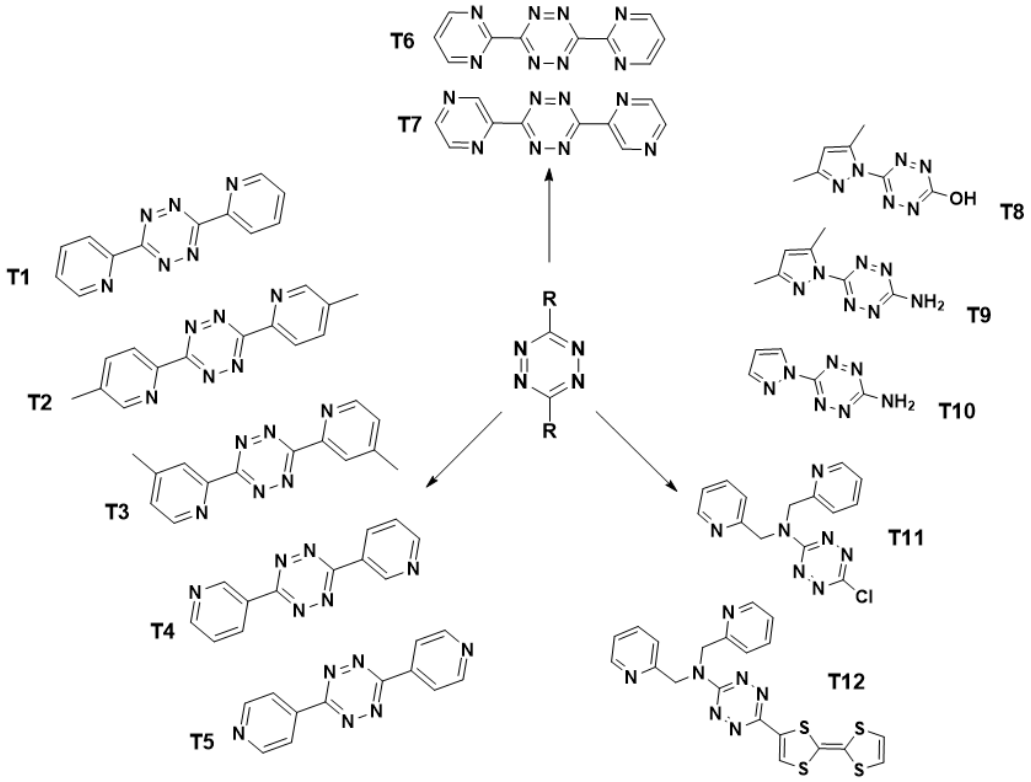

Figure 1.44. The classification proposed of the tetrazine based ligands.

In most cases the **T1** ligand was used for designing complexes which possess various topologies and architectures. The majority of the work in this direction was done by the group of K. Dunbar. The first publications[92-93] were devoted to the self-assembly of nickel complexes and to the investigation of the dependence of the complex architecture on the nature of the anion. Thus, the formation of the nickel complexes can be described by the following reaction schemes:

$$4[Ni(CH_3CN)_6][BF_4]_2 + 4\mathbf{T1} \xrightarrow{CH_3OH} [Ni_4(T1)_4(CH_3CN)_8][BF_4]_8 \quad (\mathbf{I24})$$

$$5[Ni(CH_3CN)_6][SbF_6]_2 + 5\mathbf{T1} \xrightarrow{CH_3CN} [Ni_5(T1)_5(CH_3CN)_{10}][SbF_5]_{10} \quad (\mathbf{I25})$$

X-ray analysis revealed that **I24** compound is the partially solvated molecular square $[Ni_4(bptz)_4(CH_3CN)_8][BF_4]_8 \cdot 4CH_3CN$ (Figure 1.45, left). The coordination environment of the nickel(II) ions is octahedral, with four of the coordination sites being occupied by two different **T1** chelate donors and the other two positions being capped by solvent molecules. The void space in the center of the square is about 4.6 Å in diameter which is an excellent size match for the tetrafluoroborate anion that resides in this cavity (Figure 1.45, right). The magnetochemical studies revealed that the unpaired electrons on the Ni^{II} ions are not magnetically communicating through the **T1** ligand and it does not rule out the possibility that metal ions with different magnetic orbitals will experience superexchange.

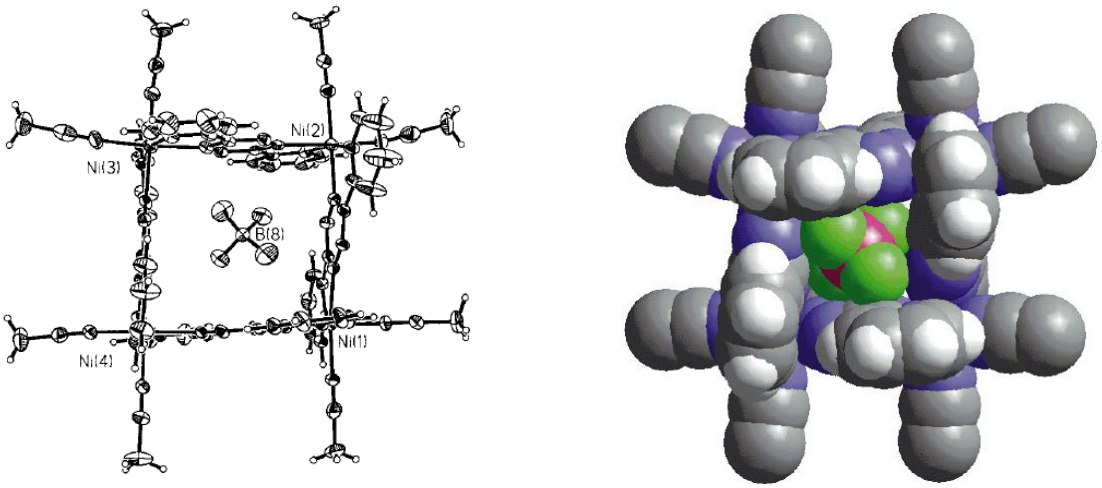

Figure 1.45. Crystal structure of the $[Ni_4(\mathbf{T1})_4(CH_3CN)_8]^{8+}$ cation (left); space-filling diagram of the molecular cation with the encapsulated $[BF_4]^-$ anion (right).

Influence of the anion on the crystal structure is nicely illustrated by the self-assembly formation of **I25**. Thus, the utilization the $[SbF_6]^-$ leads to the design of the molecular pentagon whose asymmetric unit is shown in Figure 1.46.

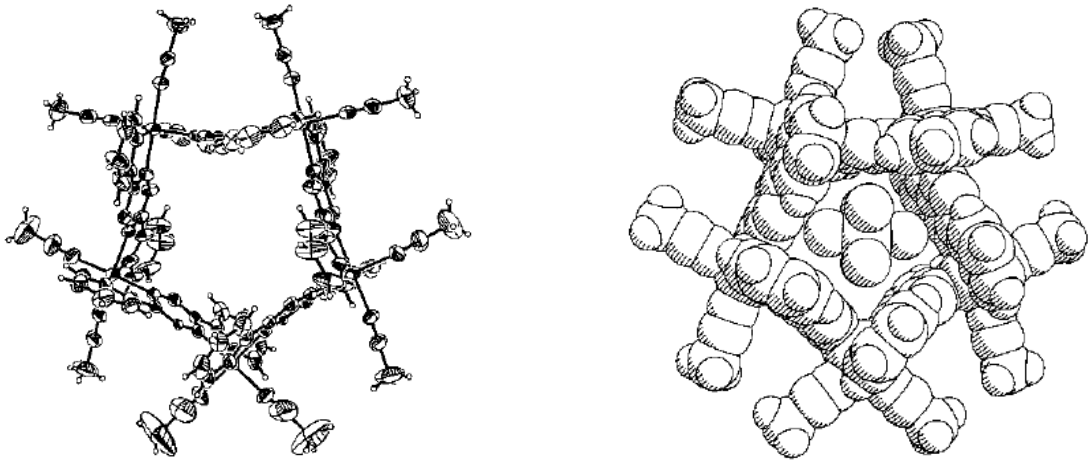

Figure 1.46. Crystal structure of the $[Ni_5(\mathbf{T1})_5(CH_3CN)_{10}]^{10+}$ cation (left); space-filling diagram of the molecular cation with the encapsulated $[SbF_6]^-$ anion (right).

The further comprehensive investigation of an anion templated self-assembly reaction of ligand **T1** was reported in 2005 by K. Dunbar[94]. The combined results of X-ray analysis, mass spectrometry, and NMR studies provide convincing evidence that the anions play a decisive role in the formation of a particular cyclic structure both in the solid state and in solution. The results described revealed that the smaller anions (BF_4^-, ClO_4^-) stabilize the molecular square structure, while the molecular pentagons are more suitable for the bulky SbF_6^- anion. The latter architecture can be reassembled onto the molecular square by the way of treatment with an excess of the BF_4^-, ClO_4^-, I^- anions (Figure 1.47), while the inverse transformation occurs under more rigorous conditions, in the presence of a large excess of the SbF_6^- anion.

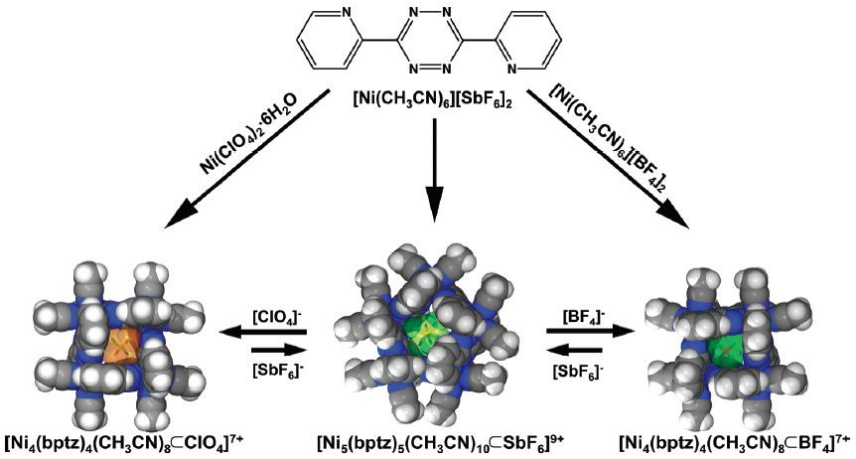

Figure 1.47. The structural assemblies of the Ni complexes in the presence of different anions.

It is well known that the tetrazines molecules, substituted by heteroatoms[59] can be reversibly reduced in organic solvents, because of their electron-deficient character, accepting one electron to give stable radical anion. This feature of tetrazine radical bridges have the added advantage of increasing the magnitude of the magnetic exchange coupling[95-100] which leads to higher blocking temperatures[101]. One of the first examples of such complexes containing tetrazine radical anion were the Co-compounds $[Co_3(\mathbf{T1})_3(dmb)_3]\cdot 2Ph\text{-}CH_3$ (**I26**) and $[Co_4(\mathbf{T1})_4(dmb)_4]\cdot 4CH_3CN$ (**I27**) (dmb – 1,3-diphenyl-1,3-propanedionate) reported in 2017[102].

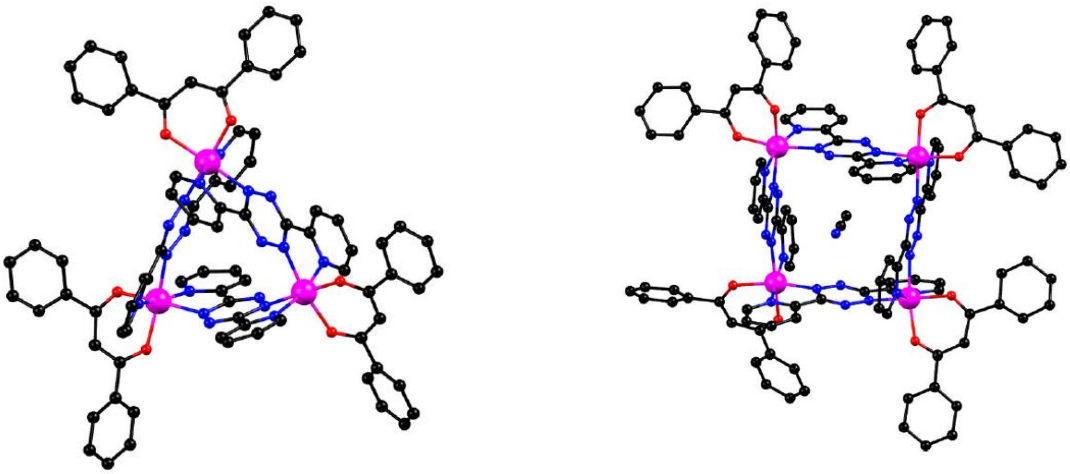

Figure 1.48. The crystal structures of **I26** (left) and **I27** (right). H atoms are omitted for clarity.

X-ray analysis showed that the **I26** complex can be considered as a molecular triangle, while **I27** is a molecular square, bearing a radical anion of the **T1** ligand (Figure 1.48).

Magnetic studies revealed strong antiferromagnetic Co···radical and weak ferromagnetic Co···Co exchanges with coupling constants of $J_{Co\cdots rad} = -67.5$ cm^{-1}, $J_{Co\cdots Co} = +6{,}0$ cm^{-1} and $J_{Co\cdots rad} = -66.8$ cm^{-1} , $J_{Co\cdots Co} = +9{,}2$ cm^{-1} for **I26** and **I27**, respectively.

Coordination chemistry of the **T5** ligand (Figure 1.44) is well investigated and the main advantage of this molecule is the presence on the N atom in the *para* position of the pyridine ring. This feature influences the crystal structures of desired complexes. Indeed, the majority of the compounds exhibit polymeric structures of different dimensionality. As examples the following complexes Mn(**T5**)$(N_3)_2]_n$ (**I28**), [Mn(**T5**)$_2(NCS)_2]_n$ (**I29**), [Mn(**T5**)$(PhCH_2COO)_2(H_2O)_2]_n$ (**I30**), [Mn_3(**T5**)$_2(PhCOO)_6]_n$ (**I31**) were described by A. Ghosh in 2013[103-104] (Figure 1.49).

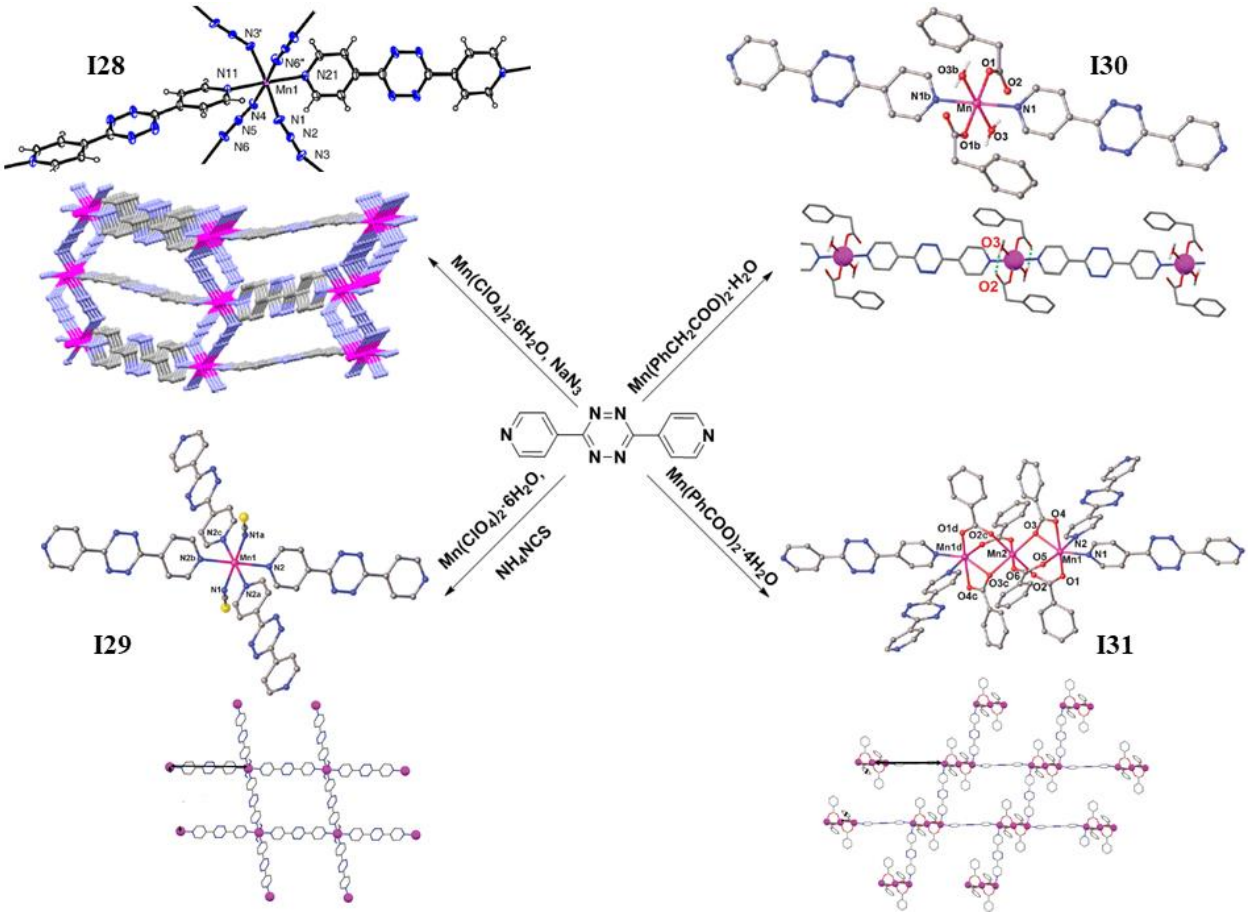

Figure 1.49. Scheme of the synthesis, crystal structures and the views of the polymeric grids of **I28-I31**.

Compounds **I29**, **I31** are examples of 2*D*-coordination polymers. In the structure of **I29** four bridging tetrazine ligands connect the Mn ion to four adjacent metals, thus forming a 2*D* (4,4) square-grid framework. In the case of **I30**, the bridging **T5** ligands connect Mn^{II} ions to generate a 1*D* coordination polymer. In the complex **I28** four nitrogen atoms from N_3^- neighbors *via* azido bridges, yield a 3*D* architecture. In **I31**, each trimanganese unit was connected to four adjacent trinuclear clusters, producing a 2*D* rhombohedral grid structure, as shown in Figure 1.49.

One of the first studies in the third group of tetrazine based ligands (see Figure 1.44) was the Stille coupling reaction between the 3,6-dichloro-1,2,4,5-tetrazine and TTF-$SnMe_3$ providing the TTF-TTZ-Cl (**I32**), (Figure 1.50, left) reported in 2013 by N. Avarvari and coworkers[105].

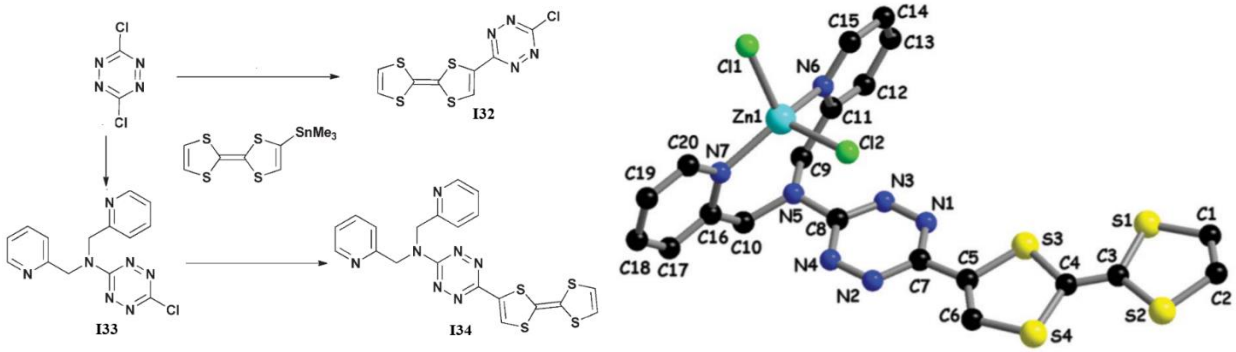

Figure 1.50. Synthesis of TTF-TTZ **1** and **3**. (left) and the molecular structure of (**I34**)–$ZnCl_2$ with the numbering scheme.

Attachment of the dipicolyl-amine chelating unit to the TTF-TTZ moiety affords a multifunctional ligand (**I34**), which allows the preparation of the (**I34**)-$ZnCl_2$ complex (Figure 1.50, right).

The analysis of the 1,2,4,5-tetrazine based complexes revealed that the mainly dipyridyltetrazines (group I) attracted growing interest for chemists, while the coordination chemistry of third group of ligands only began to develop. This observation makes non-symmetric ligands the promising candidates to be investigated.

References

1. collinsdictionary. https://www.collinsdictionary.com/dictionary/english/progress.
2. Cannon, R. D., *Nature* **1970,** *228*, 644.
3. Niel, V.; Milway, V. A.; Dawe, L. N.; Grove, H.; Tandon, S. S.; Abedin, T. S. M.; Kelly, T. L.; Spencer, E. C.; Howard, J. A. K.; Collins, J. L.; Miller, D. O.; Thompson, L. K., *Inorg. Chem.* **2008,** *47*, 176-189.
4. Melník, M.; Holloway Clive, E., Crystallographic and structural analysis of iron heterometallic hexa- and heptanuclear complexes. In *Reviews in Inorganic Chemistry*, 2011; Vol. 31, p 211.
5. Fujita, M.; Umemoto, K.; Yoshizawa, M.; Fujita, N.; Kusukawa, T.; Biradha, K., *Chem. Commun.* **2001,** *6*, 509-518.
6. Winpenny, R. E. P., *J. Chem. Soc., Dalton Trans.* **2002,** *1*, 1-10.
7. Sessoli, R.; Tsai, H. L.; Schake, A. R.; Wang, S.; Vincent, J. B.; Folting, K.; Gatteschi, D.; Christou, G.; Hendrickson, D. N., *J. Am. Chem. Soc.* **1993,** *115*, 1804-1816.
8. Lis, T., *Acta Crystallogr., Sect. B* **1980,** *36*, 2042-2046.
9. Ferlay, S.; Mallah, T.; Ouahès, R.; Veillet, P.; Verdaguer, M., *Nature* **1995,** *378*, 701.
10. Entley, W. R.; Girolami, G. S., *Science* **1995,** *268*, 397-400.
11. Sato, O.; Iyoda, T.; Fujishima, A.; Hashimoto, K., *Science* **1996,** *271*, 49-51.
12. Ohba, M.; Usuki, N.; Fukita, N.; Ōkawa, H., *Inorg. Chem.* **1998,** *37*, 3349-3354.
13. Zhang, Y.-Z.; Gao, S.; Wang, Z.-M.; Su, G.; Sun, H.-L.; Pan, F., *Inorg. Chem.* **2005,** *44*, 4534-4545.
14. Thompson, L. K., *Coord. Chem. Rev.* **2002,** *233-234*, 193-206.
15. dictionary.com. https://www.dictionary.com/browse/assembly.
16. Powell, A. K.; Heath, S. L.; Gatteschi, D.; Pardi, L.; Sessoli, R.; Spina, G.; Del Giallo, F.; Pieralli, F., *J. Am. Chem. Soc.* **1995,** *117*, 2491-2502.
17. Murugesu, M.; Clérac, R.; Anson, C. E.; Powell, A. K., *Inorg. Chem.* **2004,** *43*, 7269-7271.
18. Murrie, M.; Stoeckli-Evans, H.; Güdel, H. U., *Angew. Chem. Int. Ed.* **2001,** *40*, 1957-1960.
19. Murrie, M.; Parsons, S.; E. P. Winpenny, R.; M. Atkinson, I.; Benelli, C., *Chem. Commun.* **1999,** *3*, 285-286.
20. Murrie, M.; Parsons, S.; E. P. Winpenny, R.; E. Mabbs, F.; J. L. McInnes, E.; C. Wilson, C.; M. Smith, G., *Chem. Commun.* **1999,** *7*, 643-644.
21. Parsons, S.; Smith, A. A.; Winpenny, R. E. P., *Chem. Commun.* **2000,** *7*, 579-580.

22. Mehrotra, R. C.; Singh, A.; Tripathi, U. M., *Chem. Rev.* **1991,** *91*, 1287-1303.

23. Mehrotra, R. C.; Singh, A., *Polyhedron* **1998,** *17*, 689-704.

24. Turova, N. Y.; Turevskaya, E. P.; Kessler, V. G.; Yanovskaya, M. I., Crystal and Molecular Structures of Metal Alkoxides. In *The Chemistry of Metal Alkoxides*, Springer US: Boston, MA, 2002; pp 37-68.

25. Vaartstra, B. A.; Huffman, J. C.; Streib, W. E.; Caulton, K. G., *J. Chem. Soc., Chem. Commun.* **1990,** *24*, 1750-1751.

26. Turova, N. Y.; Kessler, V. G.; Kucheiko, S. I., *Polyhedron* **1991,** *10*, 2617-2628.

27. Nesterov, D. S.; Kokozay, V. N.; Skelton, B. W., *Eur. J. Inorg. Chem.* **2009,** *2009*, 5469-5473.

28. Oshio, H.; Nihei, M.; Yoshida, A.; Nojiri, H.; Nakano, M.; Yamaguchi, A.; Karaki, Y.; Ishimoto, H., *Chem. Eur. J.* **2005,** *11*, 843-848.

29. Nihei, M.; Yoshida, A.; Koizumi, S.; Oshio, H., *Polyhedron* **2007,** *26*, 1997-2007.

30. Biswas, A.; Mandal, L.; Mondal, S.; Lucas, C. R.; Mohanta, S., *CrystEngComm* **2013,** *15*, 5888-5897.

31. Wang, H., *Acta Crystallogr. Sect. Sect. E: Struct. Rep. Online* **2009,** *65*, m1490-m1490.

32. Biswas, A.; Mondal, S.; Mohanta, S., *J. Coord. Chem.* **2013,** *66*, 152-170.

33. Mahapatra, P.; Ghosh, S.; Giri, S.; Rane, V.; Kadam, R.; Drew, M. G. B.; Ghosh, A., *Inorg. Chem.* **2017,** *56*, 5105-5121.

34. Biswas, S.; Naiya, S.; Gómez-García, C. J.; Ghosh, A., *Dalton Trans.* **2012,** *41*, 462-473.

35. Wu, Q.; Shi, Q.; Li, Y.-G.; Wang, E.-B., *J. Coord. Chem.* **2008,** *61*, 3080-3091.

36. Makhankova, V. G.; Vassilyeva, O. Y.; Kokozay, V. N.; Skelton, B. W.; Reedijk, J.; Van Albada, G. A.; Sorace, L.; Gatteschi, D., *New J. Chem.* **2001,** *25*, 685-689.

37. Makhankova, Valeriya G.; Vassilyeva, Olga Y.; Kokozay, Volodymyr N.; Reedijk, J.; Albada, Gerard A. v.; Jezierska, J.; Skelton, Brian W., *Eur. J. Inorg. Chem.* **2002,** *2002*, 2163-2169.

38. Wang, W.-G.; Zhou, A.-J.; Zhang, W.-X.; Tong, M.-L.; Chen, X.-M.; Nakano, M.; Beedle, C. C.; Hendrickson, D. N., *J. Am. Chem. Soc.* **2007,** *129*, 1014-1015.

39. Yamashita, S.; Shiga, T.; Kurashina, M.; Nihei, M.; Nojiri, H.; Sawa, H.; Kakiuchi, T.; Oshio, H., *Inorg. Chem.* **2007,** *46*, 3810-3812.

40. Kahn, O., *Molecular Magnetism*. Wiley: 1993.

41. Yano, J.; Yachandra, V., *Chem. Rev.* **2014,** *114*, 4175-4205.

42. Hoffman, B. M.; Lukoyanov, D.; Yang, Z.-Y.; Dean, D. R.; Seefeldt, L. C., *Chem. Rev.* **2014,** *114*, 4041-4062.

43. Can, M.; Armstrong, F. A.; Ragsdale, S. W., *Chem. Rev.* **2014,** *114*, 4149-4174.

44. Furutachi, H.; Ōkawa, H., *Inorg. Chem.* **1997,** *36*, 3911-3918.

45. Kita, S.; Furutachi, H.; Ōkawa, H., *Inorg. Chem.* **1999,** *38*, 4038-4045.

46. Gutiérrez, A.; Perpiñán, M. F.; Sánchez, A. E.; Torralba, M. C.; Torres, M. R., *Polyhedron* **2012,** *44*, 165-173.

47. Kanan, M. W.; Nocera, D. G., *Science* **2008,** *321*, 1072-1075.

48. Jiao, F.; Frei, H., *Angew. Chem. Int. Ed.* **2009,** *48*, 1841-1844.

49. Esswein, A. J.; McMurdo, M. J.; Ross, P. N.; Bell, A. T.; Tilley, T. D., *The Journal of Physical Chemistry C* **2009,** *113*, 15068-15072.

50. Nguyen, A. I.; Ziegler, M. S.; Oña-Burgos, P.; Sturzbecher-Hohne, M.; Kim, W.; Bellone, D. E.; Tilley, T. D., *J. Am. Chem. Soc.* **2015,** *137*, 12865-12872.

51. Beattie, J. K.; Hambley, T. W.; Klepetko, J. A.; Masters, A. F.; Turner, P., *Polyhedron* **1998,** *17*, 1343-1354.

52. Nguyen, A. I.; Suess, D. L. M.; Darago, L. E.; Oyala, P. H.; Levine, D. S.; Ziegler, M. S.; Britt, R. D.; Tilley, T. D., *J. Am. Chem. Soc.* **2017,** *139*, 5579-5587.

53. Nguyen, A. I.; Darago, L. E.; Balcells, D.; Tilley, T. D., *J. Am. Chem. Soc.* **2018,** *140*, 9030-9033.

54. Rutherford, A. W.; Boussac, A., *Science* **2004,** *303*, 1782.

55. Langley, S. K.; Chilton, N. F.; Moubaraki, B.; Murray, K. S., *Dalton Trans.* **2012,** *41*, 1033-1046.

56. Lorcy, D.; Bellec, N.; Fourmigué, M.; Avarvari, N., *Coord. Chem. Rev.* **2009,** *253*, 1398-1438.

57. Kato, R., *Chem. Rev.* **2004,** *104*, 5319-5346.

58. Kaim, W., *Coord. Chem. Rev.* **2002,** *230*, 127-139.

59. Clavier, G.; Audebert, P., *Chem. Rev.* **2010,** *110*, 3299-3314.

60. Cooper, W. F.; Kenny, N. C.; Edmonds, J. W.; Nagel, A.; Wudl, F.; Coppens, P., *Journal of the Chemical Society D: Chemical Communications* **1971,** *16*, 889-890.

61. Bendikov, M.; Wudl, F.; Perepichka, D. F., *Chem. Rev.* **2004,** *104*, 4891-4946.

62. Ferraris, J.; Cowan, D. O.; Walatka, V.; Perlstein, J. H., *J. Am. Chem. Soc.* **1973,** *95*, 948-949.

63. Bivaud, S.; Goeb, S.; Croué, V.; Dron, P. I.; Allain, M.; Sallé, M., *J. Am. Chem. Soc.* **2013,** *135*, 10018-10021.

64. Dolder, S.; Liu, S.-X.; Le Derf, F.; Sallé, M.; Neels, A.; Decurtins, S., *Org. Lett.* **2007,** *9*, 3753-3756.

65. Balandier, J.-Y.; Chas, M.; Dron, P. I.; Goeb, S.; Canevet, D.; Belyasmine, A.; Allain, M.; Sallé, M., *The Journal of Organic Chemistry* **2010,** *75*, 1589-1599.

66. Bivaud, S.; Balandier, J.-Y.; Chas, M.; Allain, M.; Goeb, S.; Sallé, M., *J. Am. Chem. Soc.* **2012,** *134*, 11968-11970.

67. Vajpayee, V.; Bivaud, S.; Goeb, S.; Croué, V.; Allain, M.; Popp, B. V.; Garci, A.; Therrien, B.; Sallé, M., *Organometallics* **2014,** *33*, 1651-1658.

68. Bastien, G.; Dron, P. I.; Vincent, M.; Canevet, D.; Allain, M.; Goeb, S.; Sallé, M., *Org. Lett.* **2016,** *18*, 5856-5859.

69. Zhao, B.-T.; Blesa, M.-J.; Mercier, N.; Le Derf, F.; Sallé, M., *The Journal of Organic Chemistry* **2005,** *70*, 6254-6257.

70. Jana, A.; Ishida, M.; Park, J. S.; Bähring, S.; Jeppesen, J. O.; Sessler, J. L., *Chem. Rev.* **2017,** *117*, 2641-2710.

71. Jana, A.; Bähring, S.; Ishida, M.; Goeb, S.; Canevet, D.; Sallé, M.; Jeppesen, J. O.; Sessler, J. L., *Chem. Soc. Rev.* **2018,** *47*, 5614-5645.

72. Robertson, N.; Cronin, L., *Coord. Chem. Rev.* **2002,** *227*, 93-127.

73. Eisenberg, R., *Coord. Chem. Rev.* **2011,** *255*, 825-836.

74. Lazarides, T.; McCormick, T. M.; Wilson, K. C.; Lee, S.; McCamant, D. W.; Eisenberg, R., *J. Am. Chem. Soc.* **2011,** *133*, 350-364.

75. Fourmigué, M., *Acc. Chem. Res.* **2004,** *37*, 179-186.

76. Sakamoto, R.; Kambe, T.; Tsukada, S.; Takada, K.; Hoshiko, K.; Kitagawa, Y.; Okumura, M.; Nishihara, H., *Inorg. Chem.* **2013,** *52*, 7411-7416.

77. Pop, F.; Avarvari, N., *Coord. Chem. Rev.* **2017,** *346*, 20-31.

78. Eisenberg, R.; Gray, H. B., *Inorg. Chem.* **2011,** *50*, 9741-9751.

79. Kubo, K.; Shiga, T.; Yamamoto, T.; Tajima, A.; Moriwaki, T.; Ikemoto, Y.; Yamashita, M.; Sessini, E.; Mercuri, M. L.; Deplano, P.; Nakazawa, Y.; Kato, R., *Inorg. Chem.* **2011,** *50*, 9337-9344.

80. Kato, R., *Bull. Chem. Soc. Jpn.* **2014,** *87*, 355-374.

81. Rabaça, S.; Almeida, M., *Coord. Chem. Rev.* **2010,** *254*, 1493-1508.

82. Hiraga, H.; Miyasaka, H.; Nakata, K.; Kajiwara, T.; Takaishi, S.; Oshima, Y.; Nojiri, H.; Yamashita, M., *Inorg. Chem.* **2007,** *46*, 9661-9671.

83. Zhong, Z. J.; Matsumoto, N.; Ōkawa, H.; Kida, S., *J. Chem. Soc., Dalton Trans.* **1989,** *11*, 2095-2097.

84. Ribas, X.; Dias, J. C.; Morgado, J.; Wurst, K.; Molins, E.; Ruiz, E.; Almeida, M.; Veciana, J.; Rovira, C., *Chem. Eur. J.* **2004,** *10*, 1691-1704.

85. Ribas, X.; Maspoch, D.; Dias, J.; Morgado, J.; Almeida, M.; Wurst, K.; Vaughan, G.; Veciana, J.; Rovira, C., *CrystEngComm* **2004,** *6*, 589-592.

86. Ribas, X.; Dias, J. C.; Morgado, J.; Wurst, K.; Santos, I. C.; Almeida, M.; Vidal-Gancedo, J.; Veciana, J.; Rovira, C., *Inorg. Chem.* **2004,** *43*, 3631-3641.

87. Schallenberg, D.; Neubauer, A.; Erdmann, E.; Tänzler, M.; Villinger, A.; Lochbrunner, S.; Seidel, W. W., *Inorg. Chem.* **2014,** *53*, 8859-8873.

88. Alvarez-Builla, J.; Jose Vaquero, J.; Barluenga, J., Six-Membered Heterocycles: Triazines, Tetrazines and Other Polyaza Systems. In *Modern Heterocyclic Chemistry*, 2011; pp 1777-1844.

89. Chavez, D. E.; Hiskey, M. A.; Gilardi, R. D., *Org. Lett.* **2004,** *6*, 2889-2891.

90. Boger, D. L., *Chem. Rev.* **1986,** *86*, 781-793.

91. Talawar, M. B.; Sivabalan, R.; Senthilkumar, N.; Prabhu, G.; Asthana, S. N., *J. Hazard. Mater.* **2004,** *113*, 11-25.

92. Campos-Fernández, C. S.; Clérac, R.; Dunbar, K. R., *Angew. Chem. Int. Ed.* **1999,** *38*, 3477-3479.

93. Campos-Fernández, C. S.; Clérac, R.; Koomen, J. M.; Russell, D. H.; Dunbar, K. R., *J. Am. Chem. Soc.* **2001,** *123*, 773-774.

94. Campos-Fernández, C. S.; Schottel, B. L.; Chifotides, H. T.; Bera, J. K.; Bacsa, J.; Koomen, J. M.; Russell, D. H.; Dunbar, K. R., *J. Am. Chem. Soc.* **2005,** *127*, 12909-12923.

95. Rinehart, J. D.; Fang, M.; Evans, W. J.; Long, J. R., *Nature Chemistry* **2011,** *3*, 538.

96. Rinehart, J. D.; Fang, M.; Evans, W. J.; Long, J. R., *J. Am. Chem. Soc.* **2011,** *133*, 14236-14239.

97. Zhu, M.; Li, Y.-G.; Ma, Y.; Li, L.-C.; Liao, D.-Z., *Inorg. Chem.* **2013,** *52*, 12326-12328.

98. Fortier, S.; Le Roy, J. J.; Chen, C.-H.; Vieru, V.; Murugesu, M.; Chibotaru, L. F.; Mindiola, D. J.; Caulton, K. G., *J. Am. Chem. Soc.* **2013,** *135*, 14670-14678.

99. Wu, J.; MacDonald, D. J.; Clérac, R.; Jeon, I.-R.; Jennings, M.; Lough, A. J.; Britten, J.; Robertson, C.; Dube, P. A.; Preuss, K. E., *Inorg. Chem.* **2012,** *51*, 3827-3839.

100. Jeon, I.-R.; Park, J. G.; Xiao, D. J.; Harris, T. D., *J. Am. Chem. Soc.* **2013,** *135*, 16845-16848.

101. Demir, S.; Zadrozny, J. M.; Nippe, M.; Long, J. R., *J. Am. Chem. Soc.* **2012,** *134*, 18546-18549.

102. Alexandropoulos, D. I.; Dolinar, B. S.; Vignesh, K. R.; Dunbar, K. R., *J. Am. Chem. Soc.* **2017,** *139*, 11040-11043.

103. Seth, P.; Bauzá, A.; Frontera, A.; Massera, C.; Gamez, P.; Ghosh, A., *CrystEngComm* **2013,** *15*, 3031-3039.

104. Kar, P.; Drew, M. G. B.; Gómez-García, C. J.; Ghosh, A., *Inorg. Chem.* **2013,** *52*, 1640-1649.

105. Pop, F.; Ding, J.; Daku, L. M. L.; Hauser, A.; Avarvari, N., *RSC Advances* **2013,** *3*, 3218-3221.

CHAPTER II

HETEROMETALLIC COMPLEXES WITH SCHIFF BASE LIGANDS

2.1. Introduction.

The high-nuclearity heterometallic complexes represent an actively pursued topic in modern coordination chemistry. The presence of different metal cores can be responsible for a fascinating magnetic behavior, such as single molecule magnets (SMM), catalytic and biological activity of such compounds in various processes. Furthermore, high-nuclearity solids are also attractive from the crystallographic point of view because they are able to reveal a wide range of shapes and different manners of metal ions arrangement.

The analysis of all homo- and heterometallic polynuclear complexes, described in Chapter I, indicates that the tetranuclear complexes are the second prevalent polynuclear compounds. The most common molecular structure type (MST) of tetranuclear complexes is “cubane” (more than 55% of all examples). Such an abundance of cubane-complexes in nature, mainly as the key parts of metalloenzymes,[1-3] attract the constant and growing interest of chemists. Their specific architecture determines their unusual physico-chemical properties, which could be further used for the creation of new functional materials.

Earlier in our group, the syntheses of new polynuclear Fe-based complexes were reported. One of the most peculiar compounds is the hexanuclear $[Co_4Fe_2OSae_8]\cdot 4dmf\cdot H_2O$ complex (Sae - salicylidene-2-ethanolamine) illustrated in Figure 2.1.

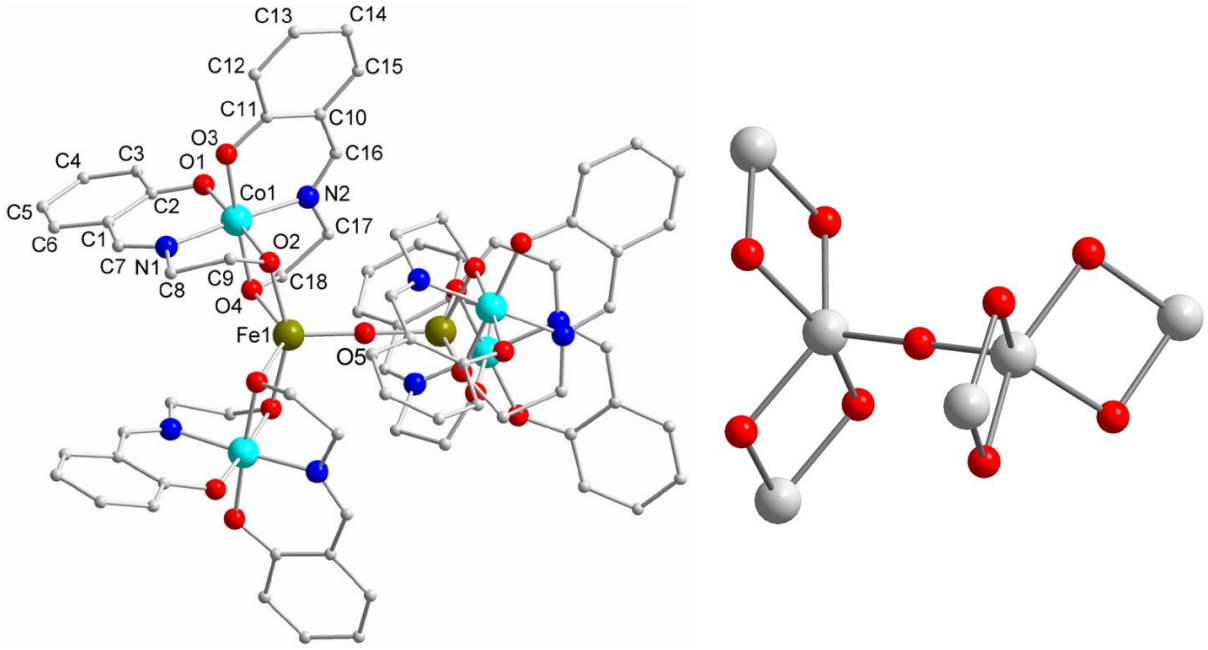

Figure 2.1. Crystal structure of $[Co_4Fe_2OSae_8]\cdot 4dmf\cdot H_2O$ with the atom numberings (left) and Ball-and-stick representation of the $M_6(\mu\text{-}X)_9$ MST (right).

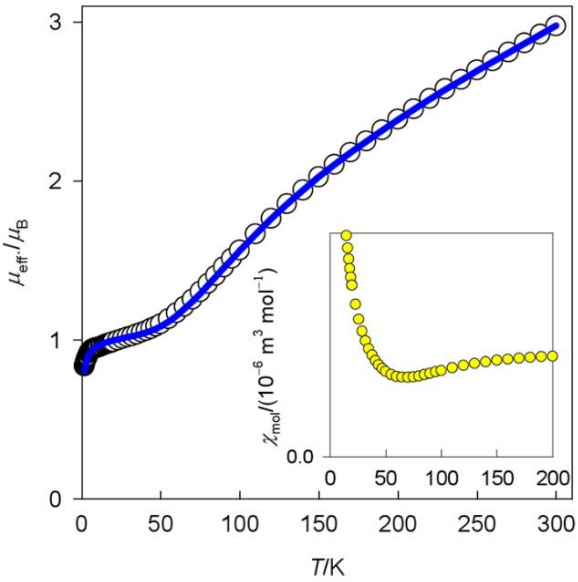

Figure 2.2. Temperature dependence of the effective magnetic moment for $[Co_4Fe_2OSae_8]\cdot 4dmf\cdot H_2O$

The structure of the complex shows the presence of two Fe(III) ions linked by a oxido-bridge. The peripheral cobalt(III) atoms are magnetically silent. This implies that a model of the exchange coupled Fe(III) pair could be explained through the following Hamiltonian:

$$\hat{H}^{iso} = -J(\vec{S}_A \cdot \vec{S}_B)\hbar^{-2} + \mu_B g_{iso} B(\hat{S}_{Az} + \hat{S}_{Bz})\hbar^{-1}$$

The fitting procedure (Figure 2.2) yielded the following set of magnetic parameters: $J/hc = -190\ cm^{-1}$, $g_{iso} = 2.008$.

The catalytic investigations disclosed an activity of $[Co_4Fe_2OSae_8]\cdot 4dmf\cdot H_2O$ toward oxidation of cycloalkanes with H_2O_2, under mild conditions. The most efficient system showed a turnover number (TON) of $3.57\cdot 10^3$ and $2.28\cdot 10^3$ for cyclooctane.

The set of cubane-like copper-based molecular catalysts for water oxidation $[(LGly\text{-}Cu)_4]$ and $[(LGlu\text{-}Cu)_4]$, were reported in *2018*[6] (Figure 2.3). The Cu_4O cubane core is structurally similar to the oxygen-evolving center Mn_4CaO_5 clusters in the photosystem II,[7] and show efficient electrocatalytic water oxidation activity with a turnover frequency (TOF) of 267 s^{-1} for $[(L_{Gly}\text{-}Cu)_4]$ at 1.70 V and 105 s^{-1} for $[(L_{Glu}\text{-}Cu)_4]$ at 1.56 V. The high performance may be attributed to the synergy and the successive two-electron transfer processes involved in the tetranuclear copper cubane centers. In situ EPR and Raman spectroscopy suggest the presence of high-valent Cu^{III} and $Cu^{III}O^*$ intermediates.

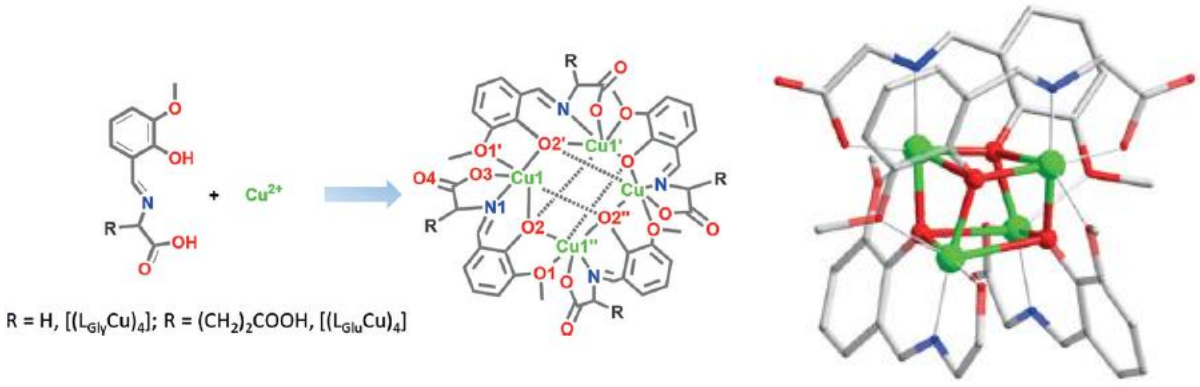

Figure 2.3. Synthesis of $[(L_{Gly}\text{-}Cu)_4]$ and $[(L_{Glu}\text{-}Cu)_4]$ (left) and the crystal structure of $[(L_{Gly}\text{-}Cu)_4]$ (right).

Multi-electron redox properties of 3*d* metals in cubane $\{M_4O_4\}$ cores might be favorable to activate catalytic cycles for water oxidation. Therewith we have been stimulated in the study of systems containing dissimilar 3*d* metals.

2.2. Tetranuclear cubane Mn(III)/Cu(II) and Co(II, III)/Cu(II) complexes

The "direct synthesis" approach has been chosen for the synthesis of heterometallic complexes. The main idea of this method is the utilization of zero-valent metals or their oxides as the starting materials for the synthesis.[8-9] The main advantage of this approach is the generation, *in situ*, of the different building blocks instead of a multi-steps synthesis. The systems **S** that were investigated during this work for the preparation of the different heterometallic complexes were:

$$\mathbf{Mn^0 - Cu^0 - mH_nL - solv} \qquad \mathbf{(S1)}$$

$$\mathbf{Mn^0 - CuX_2 - mH_nL - solv} \qquad \mathbf{(S2)}$$

$$\mathbf{MnX_2 - Cu^0 - mH_nL - solv} \qquad \mathbf{(S3)}$$

$$\mathbf{Mn^0 - Cu^0 - mH_nL - 2NH_4Y - solv} \qquad \mathbf{(S4)}$$

$$\mathbf{Mn^0 - Cu^0 - mH_nL - BA - 2NH_4Y - solv} \qquad \mathbf{(S5)}$$

X = Cl^-, OAc^-; Y = Cl^-, Br^-, I^-, SCN^-, OAc^-, BF_4^-, NO_3^-; m = 1-3; BA – basic agent (CaO, BaO); solv = dmf, dmso, ACN, CH_3OH; H_nL = general formula of Schiff base ligands (figure 2.4).

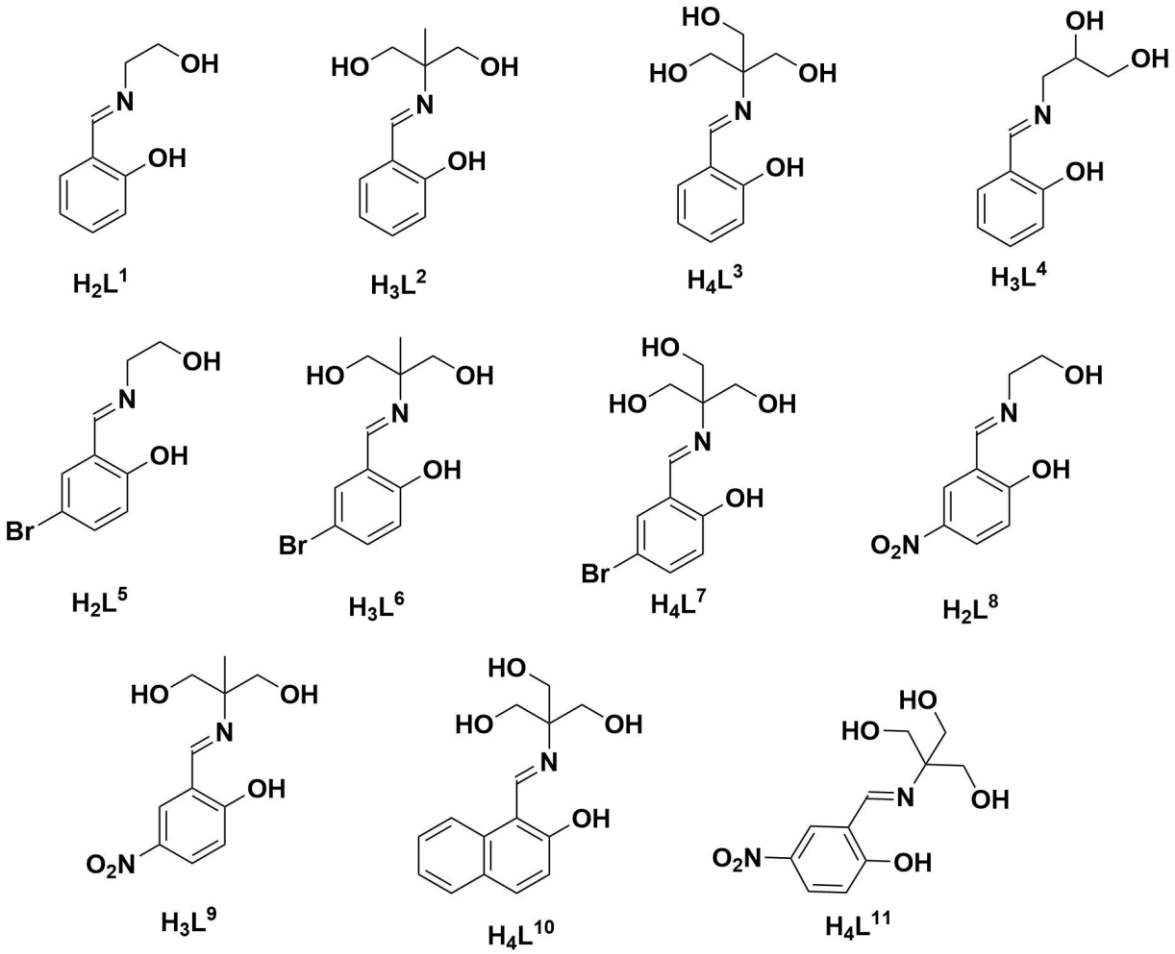

Figure 2.4. Schiff base ligands.

The system **S1** proved not to be suitable for the synthesis of heterometallic complexes due to the very slow dissolution of the metals powders. In fact, after 12 hours of reaction, no changes

in the reaction mixture were observed. We have therefore decided to replace one of the metal with its salts (systems **S2**, **S3**).

The monometallic complexes of copper $[Cu(HL^1)_2]$[10] and $[Cu_4(H_2L^3)_4]$[11] were isolated within the **S2** system in methanolic solutions, while the in case of system **S3** the manganese complexes $\{[Mn^{III}(HL^1)_2]Cl\}_n$[12] and $[Mn^{IV}(HL^2)_2]\cdot 2dmf$[13] were obtained from methanol and dmf solutions, respectively. It should be noted that the molar ratio Mn : Cu : H_nL does not influence the composition of the final products, but the dissolution of the metals significantly increased at an excess of ligand (ratio of 1:1:3 in comparison with 1:1:1). The utilization of solvents like dmso or ACN did not allow to obtain any crystalline compound, but only oil-like products.

As for **S1**, the use of the systems **S2** and **S3** did not allow the formation of heterometallic complexes and the possible reason is that under these conditions thermodynamically stable monometallic compounds were formed.

The next attempt to synthesize heterometallic complexes was the use of ammonia method for the direct synthesis[14]. One of its variations is the interaction of metal powders with a solution of a ligand in the presence of an ammonium salt (system **S4**). Once again, only monometallic copper complexes $[Cu_4(H_2L^3)_4]$ (**C1**), $[Cu_4(L^1)_4]\cdot 3H_2O$ (**C2**) and $[Cu(HL^1)_2]$ (**C3**) were isolated using this method. In this case, the molar ratio Cu : H_nL directly affects the composition of the isolated metal complexes. Each metal ion in **C1** and **C2** is coordinated by only one molecule of ligand forming the structure with final ratio metal: ligand = 1 : 1, while an excess of ligand (Cu : H_nL = 1 : 3) results in the formation of **C3**, where the copper center is coordinated by two molecules of ligand. Note that the use of dmf, dmso or ACN as solvent did not allow to isolate any crystalline products.

It is well known that the acidity of the solution can influence the complexation reactions. The introduction of the so-called basic agent (BA) in the reaction mixture reduces the acidity. As a consequence, it can change the coordination and chemical properties of ligand, in particular BA allows the deprotonation of the Schiff base. A modification of the system **S4** results in the system **S5** in which a reagent with basic properties has been introduced. Thus, by using the **S5** system, four new heterometallic Mn/Cu complexes have been isolated.

The general reactions can be written as follows:

$$4Mn^0 + 12Cu^0 + 16H_2L^1 + 12NH_4I + 11O_2 + 12CH_3OH \rightarrow 4\{[Cu_3Mn(L^1)_4(CH_3OH)_3]I_3\}\ (\mathbf{1}) + 12NH_3 + 22H_2O;$$

$$4Mn^0 + 12Cu^0 + 16H_2L^1 + 4NH_4NCS + 9O_2 + 12CH_3OH \rightarrow 4\{[Cu_3Mn(L^1)_4(CH_3OH)_3(H_2O)]NCS\cdot H_2O\}\ (\mathbf{2}) + 4NH_3 + 10H_2O;$$

$4Mn^0 + 12Cu^0 + 16H_2L^1 + 4NH_4Br + 9O_2 + 4CH_3OH \rightarrow$
$4\{[Cu_3Mn(L^1)_4(CH_3OH)(H_2O)_{2,55}]Br\cdot 0,45H_2O\}$ (**3**) $+ 4NH_3 + 6H_2O$;

$4Mn^0 + 12Cu^0 + 16H_2L^1 + 4NH_4BF_4 + 9O_2 \rightarrow$
$4\{[Cu_3Mn(L^1)_4(H_2O)_{3,4}]BF_4\cdot 0,6H_2O\}$ (**4**) $+ 4NH_3 + 2H_2O$;

The formation of I_3^- anion in complex **1** can be explained by the interaction of Cu^{2+} ions with NH_4I.

$$Cu^{+2} + 2NH_4I = Cu^+ + I_2 + 2NH_4^+$$

The product of that reaction, iodine, interacts with an excess of ammonium iodide, thus, forming I_3^-.

Note that a mixture of blue and brown crystals was obtained upon using the ligand H_4L^3. The X-ray analysis of the blue crystals revealed the formation of the already known monometallic copper(II) complex $[Cu_4(H_2L^3)_4]$[11], while the brown crystals were not suitable for further structural investigation.

The IR spectra of complexes **1–4** in the 4000–400 cm^{-1} range (Figure 2.5) confirmed the presence of the Schiff base ligands.

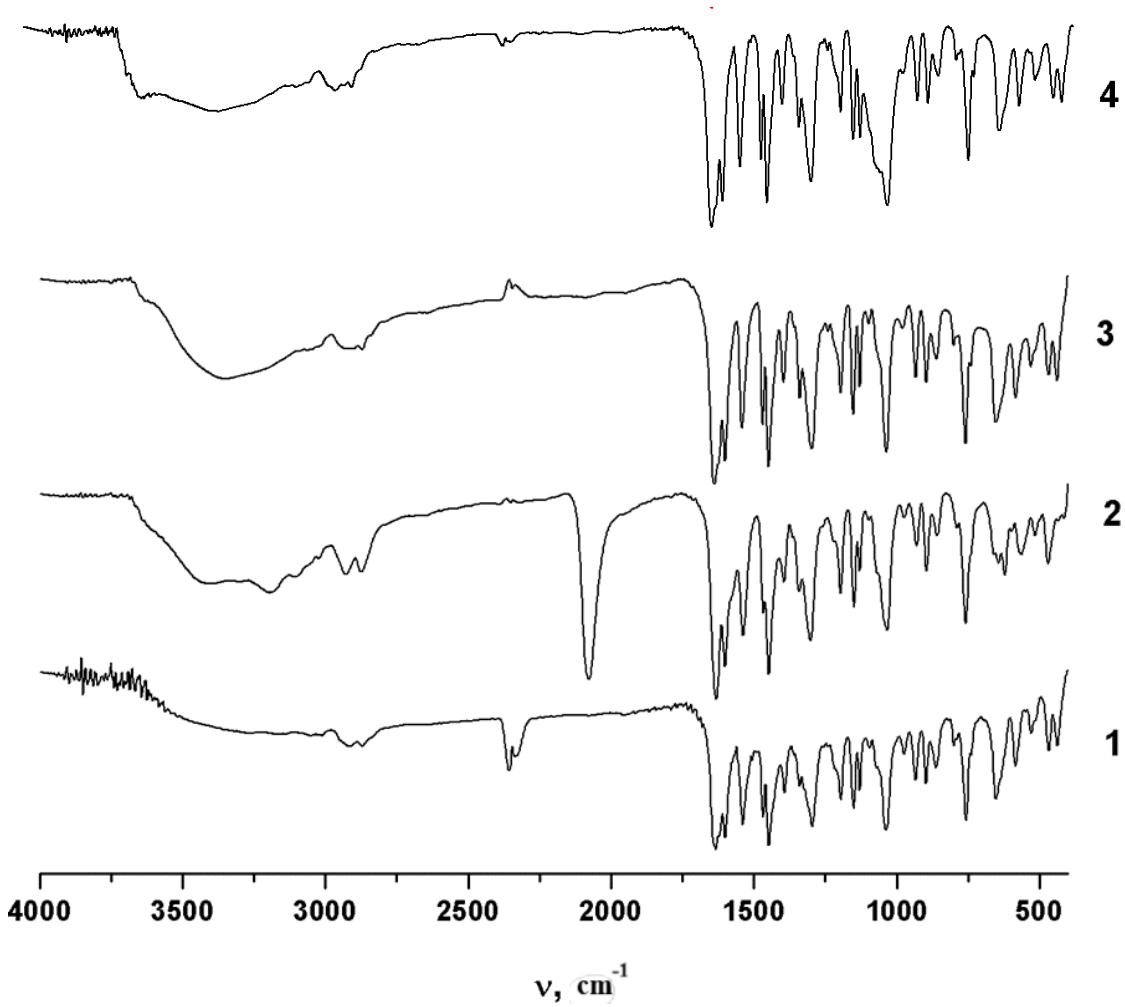

Figure 2.5. IR spectra of **1-4**.

The very strong bands at 1633 (**1**), 1631 (**2**), 1638 (**3**) and 1635 cm^{-1} (**4**) were assigned to the ν(C=N) stretching vibrations of the Schiff base ligands. The broad bands in the region of 3600–3100 cm^{-1} in the spectra of the four compounds are characteristic of the ν(O–H) frequencies of the CH_3OH or/and water molecules. The presence of the uncoordinated thiocyanate ion in **2** can be identified by the strong ν(C–N) absorption peak at 2056 cm^{-1} and the weak ν(C–S) vibration at 750 cm^{-1}. For all complexes in the regions 3050-3010 cm^{-1} and 2900-2890 cm^{-1}, there are absorption bands corresponding to the ν(C–H) of the aromatic ring and to the aliphatic C–H bonds, respectively.

2.2.1. The crystal structure of $[Cu_3Mn(L^1)_4(CH_3OH)_3]I_3$ ***(1)***, $[Cu_3Mn(L^1)_4(CH_3OH)_3(H_2O)]NCS{\cdot}H_2O$ ***(2)***, $[Cu_3Mn(L^1)_4(CH_3OH)(H_2O)_{2,55}]Br{\cdot}0,45H_2O$ ***(3)***, $[Cu_3Mn(L^1)4(H_2O)_{3,4}]BF_4{\cdot}0,6H_2O$ ***(4)***.

The X-ray analysis shows that the overall structural configurations of the heterometallic $Cu^{II}Mn^{III}$ complexes **1–4** are similar. All of them are based on the tetranuclear core $\{Cu_3Mn(\mu_3\text{-}O)_4\}$ (Figure 2.6), where the metal centers are linked through the μ_3-O bridges from the Schiff base ligands forming a cube-like core. The Schiff base precursors H_2L^1 are doubly deprotonated and show tridentate (N,O,O) coordination in the crystal structures of **1–4**.

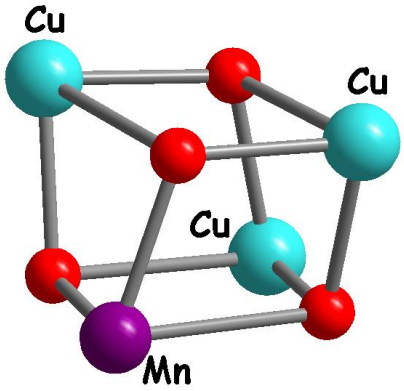

Figure 2.6. The ball-and-stick representation of the $\{Cu_3Mn(\mu_3\text{-}O)_4\}$molecular core in **1–4**.

The tetranuclear core $\{Cu_3Mn(\mu_3\text{-}O)_4\}$ belongs to the $\{M_4(\mu_3\text{-}X)_4\}$ (M = metal atom, X = bridging atom) molecular structure type (MST), obtained by excluding all non-bridging non-metal atoms of the structure. This MST, according to the CSD, dominates over all other tetranuclear MSTs, representing almost 30% of all described tetranuclear complexes.

Compound **1** contains three Cu(II) ions, two of them, Cu1 and Cu2, having distorted octahedral environments formed by oxygen and nitrogen atoms from the Schiff base ligands and oxygen atoms from the coordinated molecules of methanol (Figure 2.7 A). The coordination polyhedra around the Cu3 atom is square pyramidal within the O_4N donor set. The equatorial Cu–O(N) bond lengths vary from 1.901(2) to 1.992(2) Å, while the apical Cu–O distances range from 2.379(3) to 2.580(2) Å. The O–Cu–$O(N)_{cis}$ bond angles vary from 72.63(8)° to 109.52(9)°, while the O–Cu–$O(N)_{trans}$ angles span from 155.88(8) to 177.40(11)°.

The Mn(III) ion shows a distorted octahedral geometry with the $\{MnO_5N\}$ unit formed by the O and N atoms of the ligand and methanol in the coordination sphere of the metal, with the

equatorial Mn–O(N) distances varying from 1.8675(2) to 1.958(3) Å, while the apical Mn–O bond distances measure 2.320(3) and 2.411(2) Å. The *cis* and *trans* O–Mn–O(N) bond angles span from 75.26(8) to 101.81(9)° and from 159.06(9) to 176.71(11)°, respectively. The intermetallic M···M non-bonded distances within the metal core lie in the range of 3.115(1)–3.520(9) Å.

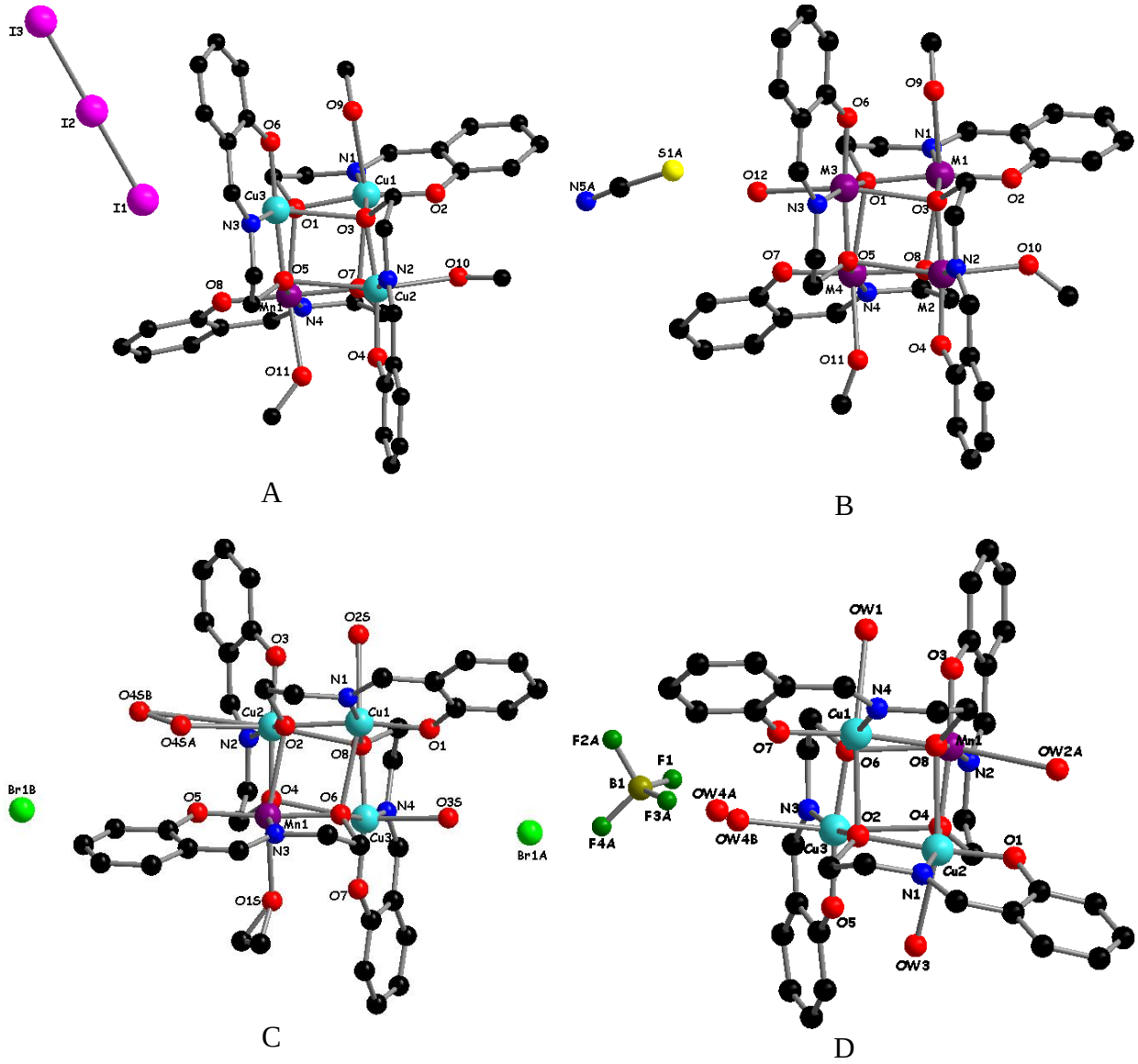

Figure 2.7. The crystal structure of **1-4** (A-D, respectively) with atom labeling. The hydrogen atoms were omitted for clarity.

Intramolecular O–H···O hydrogen bonds [d(O···O) vary from 2.672(8) to 2.691(12) Å, while the O–H···O bond angles range from 166.71(22) to 175.17(19)°] in the crystal structure of **1**, involving the oxygen atoms of the Schiff bases and the coordinated methanol molecules that further stabilize the overall tetranuclear structure of the complex.

In the crystal structures of complexes **2**, **3** and **4** all metal ions possess a distorted octahedral coordination environment (Figure 2.7, B-D). The equatorial O_3N donor set of each metal center is formed by oxygen and nitrogen atoms from the ligand with the M–O(N) bond lengths ranging from 1.862(5) to 1.986(3) Å. One of the axial oxygen atoms

belongs to the Schiff base while the second one belongs to the coordinated CH_3OH/H_2O molecule, with M–O bond distances ranging from 2.355(9) to 2.741(11) Å. For complex **2**, the positions of Cu and Mn ions were not distinguishable. Therefore, they were refined as mixed atoms with estimated partial contribution factors of 0.75 (Cu) and 0.25 (Mn). In the case of **3** and **4** a structural disorder of coordinated water molecules was observed. Particularly, atoms O4S in **3** and O4W in **4** are both disordered in such way that the Cu–O bond lengths float from 2.536(18) to 3.56(3) Å and from 2.45(2) to 3.055(12) Å, respectively. Therefore, the first part of each of those H_2O molecules can be treated as coordinated to Cu centers and the second part as non-coordinated one. This results in mixed O_5N (octahedral) / O_4N (square pyramidal) coordination environment of Cu2 in **3** and Cu3 in **4**. The $O–M–O(N)_{cis}$ bond angles in **2**–**4** range from 72.4(2)° to 112.96(16)° and the $O–M–O(N)_{trans}$ angles span from 155.29(15)° to 176.9(3)°. Systematic differences between bonds and angles involving Cu and Mn centers are negligible.

The M···M non-bonded distances within the metal core for complexes **2–4** vary in the 3.1040(18)–3.5242(7) Å range. Similar to **1**, the tetranuclear cubane-like cations in **2**–**4** are additionally stabilized by intramolecular O–H···O hydrogen bonds involving oxygen atoms from the ligands that act as acceptors and coordinated solvent molecules (methanol or water) as donors. In each of these compounds uncoordinated anions occupy cavities between closely packed bulky cations and are linked to them *via* non-directional electrostatic forces as well as intermolecular H-bonding.

The crystal structures of **1**–**4** are similar on one hand, but on the other hand, they drastically differ by the number and combinations of coordinated methanol and water molecules. In the case of **1**, only CH_3OH molecules are coordinated to the cubane metal core forming the *{$Cu_3Mn(\mu_3\text{-}O)_4$}{$(CH_3OH)_3$}* fragment (Figure 2.8).

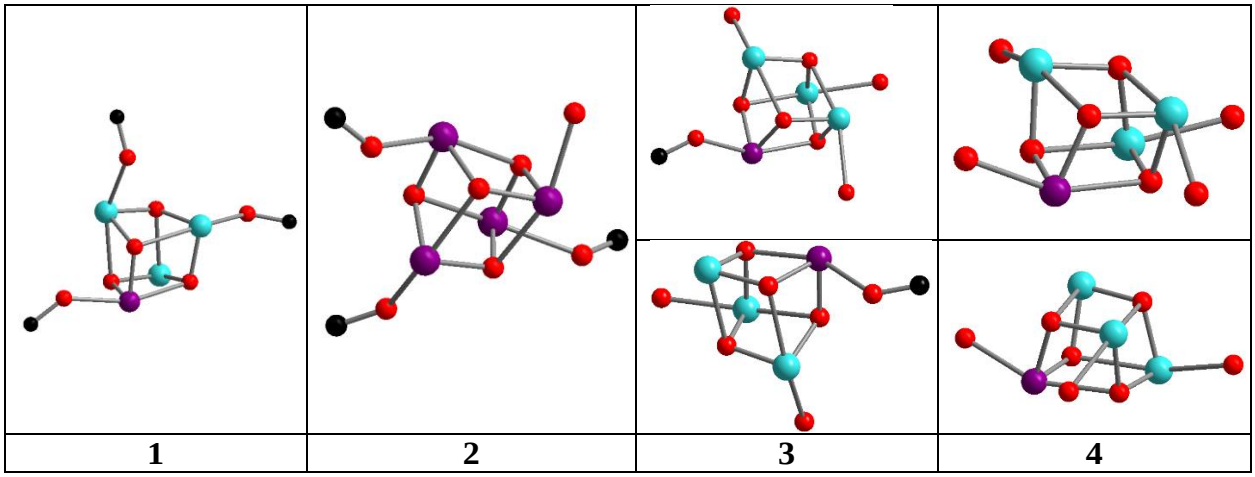

Figure 2.8. Ball-and-stick representations showing the coordination of the solvents to molecular cubane cores in complexes **1-4**.

Complex **2** shows coordination of four solvent molecules to the metal core with mixed-solvent CH_3OH_3/H_2O combination, while, due to the disorder, the formation of two mixed-solvent *{$Cu_3Mn(\mu_3\text{-}O)_4$}$(H_2O)_3(CH_3OH)$}* and *{$Cu_3Mn(\mu_3\text{-}O)_4$}$(H_2O)_2(CH_3OH)$}* fragments is observed in **3**. In the case of complex **4**, similarly to **1**, only one type of solvent molecules (water), is coordinated to the metal core.

*2.2.2. The crystal structure of $[Cu_3Mn(L^1)_4(CH_3OH)_3]_2[Mn(NCS)_4]\cdot 2CH_3OH$ (**5**) and $[Co^{II}Co^{III}Cu^{II}_2(L^1)_3(ea)(H_2O)(NCS)_2]$ (**6**)*

In order to investigate the possibility of using the monometallic complexes, which were formed as by-products in the above-mentioned reactions for the synthesis of heterometallic aggregates, the following systems were investigated:

MnX_2 – $Cu(HL^1)_2$ – NH_4SCN – solv **(S6)**

CoX_2 – $Cu(HL^1)_2$ – NH_4SCN – solv **(S7)**

X = Cl^-, CH_3COO^- (OAc^-); solv = dmf, dmso, ACN, CH_3OH; $Cu(HL^1)_2$ = the monometallic complex (figure 2.9)[15].

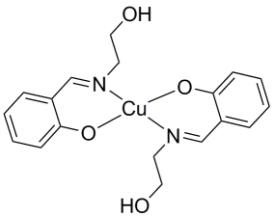

Figure 2.9. The formula of $Cu(HL^1)_2$.

The monometallic precursor $Cu(HL^1)_2$ has been chosen because of the presence of vacant axial positions in the copper atom.

Two new heterometallic complexes $[Cu_3Mn(L^1)_4(CH_3OH)_3]_2[Mn(NCS)_4]\cdot 2CH_3OH$ (**5**) and $[Co^{II}Co^{III}Cu_2(L^1)_3(ea)(NCS)_2(H_2O)]$ (**6**) were isolated using the conditions of **S6** and **S7** in methanol solutions. Compounds **5** and **6** were formed by the interaction of $Cu(HL^1)_2$ with manganese (cobalt) acetate and ammonium thiocyanate in the molar ratio $Cu(HL^1)_2$:$Mn(OAc)_2/Co(OAc)_2$:NH_4NCS = 1 : 1 : 2.

The following reaction scheme can explain the formation of **5**:

$$3Mn(OAc)_2 + 6Cu(HL^1)_2 + 4NH_4NCS + 0.5O_2 + 8CH_3OH \rightarrow$$
$$[Cu_3Mn(L^1)_4(CH_3OH)_3]_2[Mn(NCS)_4]\cdot 2CH_3OH + 4NH_4OAc + 2HOAc + 4H_2L^1 + H_2O.$$

The formation of **6** was accompanied by the formation of monometallic cobalt complex impurity $[Co(HL^1)(L^1)]\cdot CH_3OH\cdot H_2O$[16] (Figure 2.10).

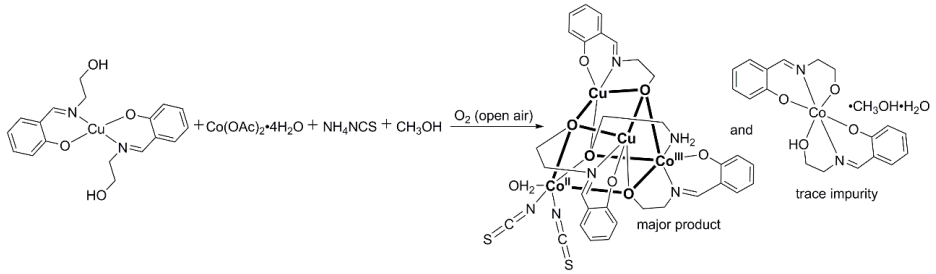

Figure 2.10. Synthetic route to complex **6**.

The deprotonated monoethanolamine fragment, which is part of the complex, is very likely formed as a result of the partial hydrolysis of the Schiff base ligand.

Utilization of manganese (cobalt) chloride as a metal source in **S6** and **S7** leads to the formation of the tetranuclear copper complex $[Cu_4(L^1)_4]\cdot 3H_2O$[17]. The use of solvents like dmf, dmso or ACN did not allow to isolate any crystalline products.

The IR spectra (Figure 2.11) show common features for both complexes. Thus, the intense peak at 2080 (**5**) та 2077 cm^{-1} (**6**) can be assigned to ν(C–N) vibration of the thiocyanate group coordinated through nitrogen atom[18]. The strong bands at 1620 (**5**) and 1636 cm^{-1} (**6**) are the ν(C=N) stretching vibrations of the Schiff base ligands. The broad bands in the region of 3600–3300 (**5**) and 3600–3150 cm^{-1} (**6**) are assigned as the ν(O–H) frequencies of the CH_3OH and water molecules. At 3050-3010 cm^{-1} and 2900-2890 cm^{-1}, there are absorption bands corresponding to the ν(C–H) of the aromatic ring and to the aliphatic C–H bonds for compounds **5** and **6**, respectively.

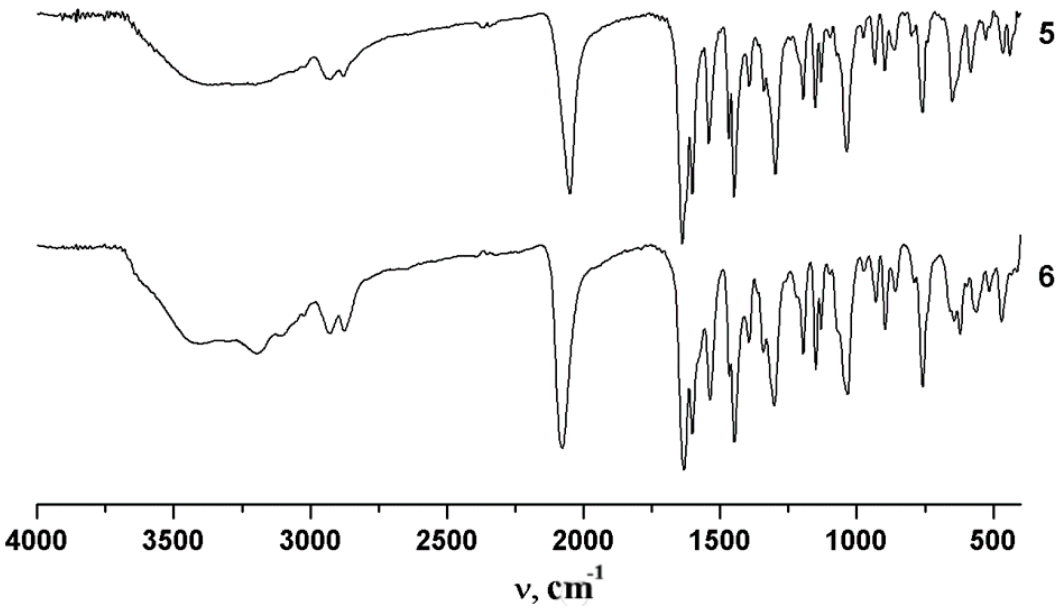

Figure 2.11. IR spectra of **5**, **6**.

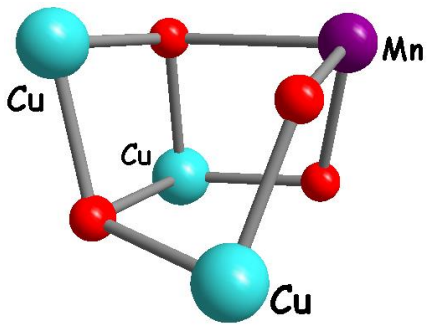

Figure 2.12. The ball-and-stick representation of the *{Cu₃Mn(μ-O)₂(μ₃-O)₂}* molecular core in complex **5**.

X-Ray investigation has been performed for compound **5**. It crystallizes in the triclinic system and consists of two independent heterometallic cations $[Cu_3Mn(L^1)_4(CH_3OH)_3]^{2+}$, that have a slightly different geometry, $[Mn(NCS)_4]^{2-}$ anion and two uncoordinated molecules of methanol. Both cations are based on the *{Cu₃Mn(μ-O)₂(μ₃-O)₂}* metal core which can be better described as the double open cube *{M₄(μ-X)₂(μ₃-X)₂}* (Figure 2.12.)

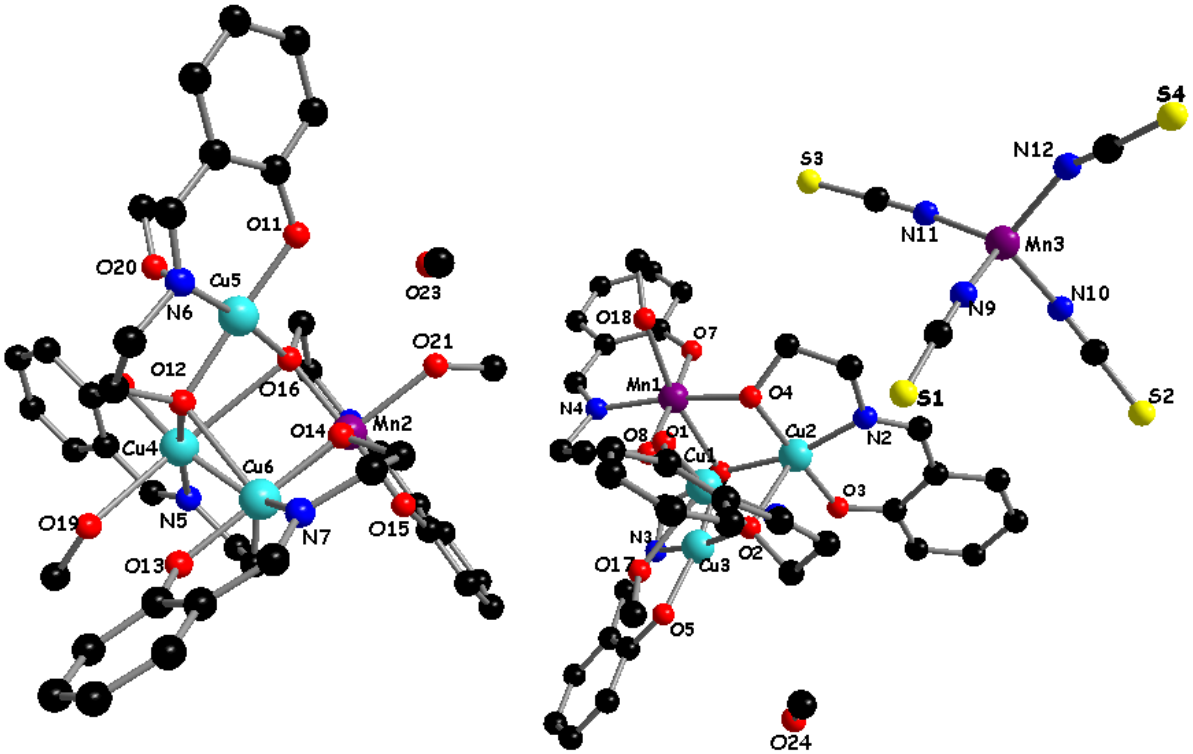

Figure 2.13. The crystal structure of **5** with atom labeling. The hydrogen atoms were omitted for clarity.

According to the CSD, only two complexes of this molecular structure type were described: $[(\mu_2\text{-}SC_6H_4NO_2)_2(\mu_3\text{-}SC_6H_4NO_2)_2(CuPPh_3)_4]$[19] and $[Li_3(tmeda)_2Cp^*TaS_3Cl]_2$(μ-tmeda), where tmeda = tetramethylethylenediamine, Cp* = C_5Me_5[20]. Hence, compound **5** represents the first example of a heterometallic transition 3*d*-metal complex with the *{M₄(μ-X)₂(μ₃-X)₂}* MST. The O atoms from the Schiff bases link the Cu and Mn centers in both double open cube-like cations, whereby two μ_3 [O2, O6] and two μ_2 bridge atoms [O4, O8] exist in one cation and two μ_3 [O10, O12] and two μ_2 bridge atoms [O14, O16] in the other one (Figure 2.13). All copper atoms in **5** have five-coordinated distorted square-pyramidal coordination environments, which in the case of Cu1, Cu3, Cu4, and Cu5 are formed by donor atoms of two Schiff base ligands and one coordinated molecule of methanol, while in the case of Cu2 and Cu6 they are formed exclusively by three deprotonated Schiff bases. The equatorial Cu–O(N) distances vary from 1.889(4) to 1.996(4) Å, while the apical Cu–O bond lengths lie in the 2.376(4)–2.504(5) range. The *cis* angles around the Cu atoms range from 73.39(15) to 124.94(17)° and the *trans* bond angles span from 158.44(19) to 179.13(16)°.

Both manganese ions of the cubane-like cations adopt a distorted octahedral geometry formed by the O and N atoms of the ligands and methanol with the Mn–O(N) distances varying from 1.857(4) to 2.331(4) Å. The *cis* and *trans* O–Mn–O(N) bond angles range from 76.60(14) to 102.76(16)° and from 165.12(16) to 173.75(16)°, respectively. The Mn3 atom from the $[Mn(NCS)_4]^{2-}$ anion has distorted tetrahedral coordination geometry with Mn–N bond lengths in the 2.020(6)–2.061(7) Å range and N–Mn–N bond angles ranging from 102.8(3)° to 118.4(3)°.

The intermetallic M···M non-bonded distances within both metal cores are in the range of 3.087(2)–3.608(2) Å. Similar to complexes **1–4**, the tetranuclear cations in **5** are reinforced by strong intramolecular O–H···O hydrogen bonds involving the oxygen atoms from Schiff bases and coordinated methanol molecules. Besides, each tetranuclear cation in **5** is H-bonded to the uncoordinated molecule of methanol that additionally stabilizes the overall double open cube-like metal cores.

X-ray diffraction analysis was performed for the heterometallic complex **6** and it was found that the compound crystallizes in the monoclinic system, space group $P2_1/n$, and consists of neutral tetranuclear cubane-like molecules with a $\{Co_2Cu_2O_4\}$ skeleton (Figure 2.14). All metal centers are bridged by four μ_3-O atoms of deprotonated hydroxyl groups from three Schiff base and one monoethanolamine ligands.

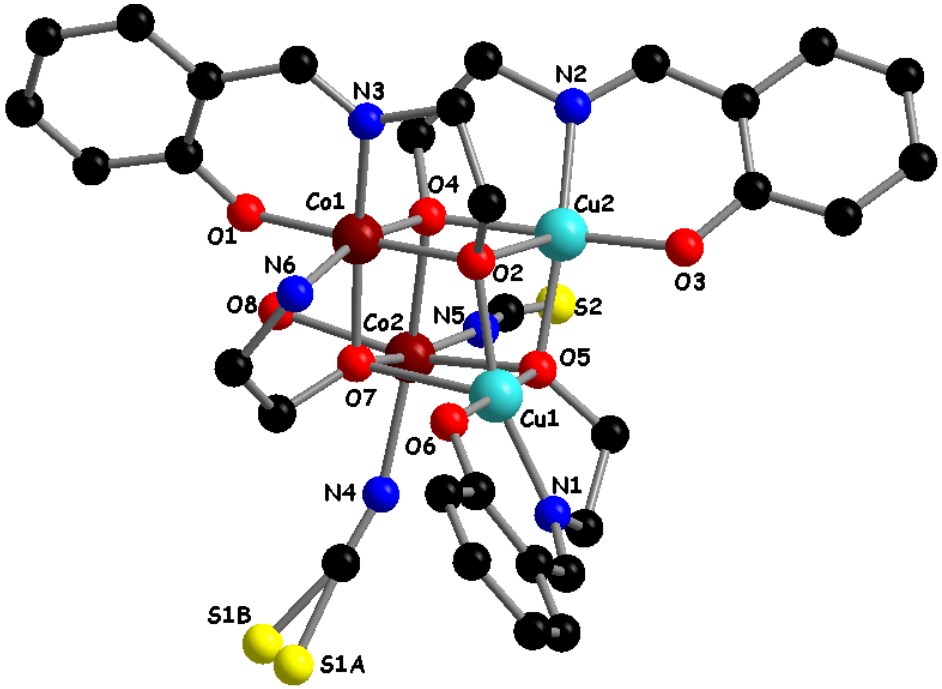

Figure 2.14. The crystal structure of **6** with atom labeling. Sulfur atom is disordered over two sites S1A and S1B with relative occupancies of 0.73/0.27, respectively (left).

The geometry of the coordination environment of both Cu(II) ions (CuO_4N fragments) can be described as square pyramidal (4+1). Thus, the equatorial Cu–O(N) bond distances range from 1.872(4) to 1.991(3) Å, while the apical Cu–O distances are 2.369(3) and 2.398(3) Å. The *cis* and *trans* (O–Cu–O(N)) angles are in the ranges 71.9(1)–118.6(1)° and 162.8(2)–176.4(2)°, respectively. The cobalt ions in the CoO_4N_2 units adopt a distorted octahedral geometry. The distortion of the coordination polyhedron is stronger in the case of Co2 (II) than in Co1 (III). The mean bond lengths amount to 2.145(4)/2.041(6) and 1.910(3)/1.910(5) Å for Co(II)–O/Co(II)–N and Co(III)–O/Co(III)–N, respectively, thus being in the normal range for Co containing

complexes described in literature[21]. The BVS (bond valence sum) analysis supports the correctness of the charge assignment giving the values: Co(II) = 2.01 and Co(III) = 3.28.

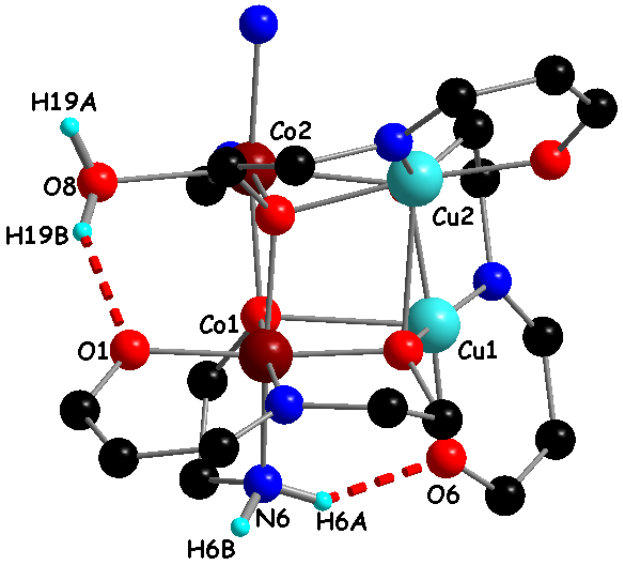

Figure 2.15. Intramolecular hydrogen bonds in the structure of **6**: OH···O [d(O(1)···O(8)) = 2.77 Å, ∠(O(1)–H(19B)–O(8)) = 145°] and NH···O [d(O(6)···N(6)) = 2.98 Å, ∠(N(6)–H(6A)–O(6)) = 142°] hydrogen bonds supporting the cubane core (right).

The closest M···M non-bonded distances within the core [3.067(5) – 3.309(5) Å] suggest that **6** could be considered as a metal cluster. The Co···Co distance [3.119(10) Å] is noticeably shorter than the one reported in the antiferromagnetic $\{Co_2Y_2\}$ cubane[22], while the Cu···Cu distance [3.0808(9) Å] is in a good agreement with ones found in related structures23. All hydrogen atoms from the coordinated water molecule and the NH2-group of monoethanolamine ligand take part in numerous H-bonds (Figure 2.15), thus providing a one-dimensional structure along the b axis (Figure 2.16).

Based on the CSD analysis, the systematization of cobalt-containing cubane complexes (Table 2.1) can be proposed.

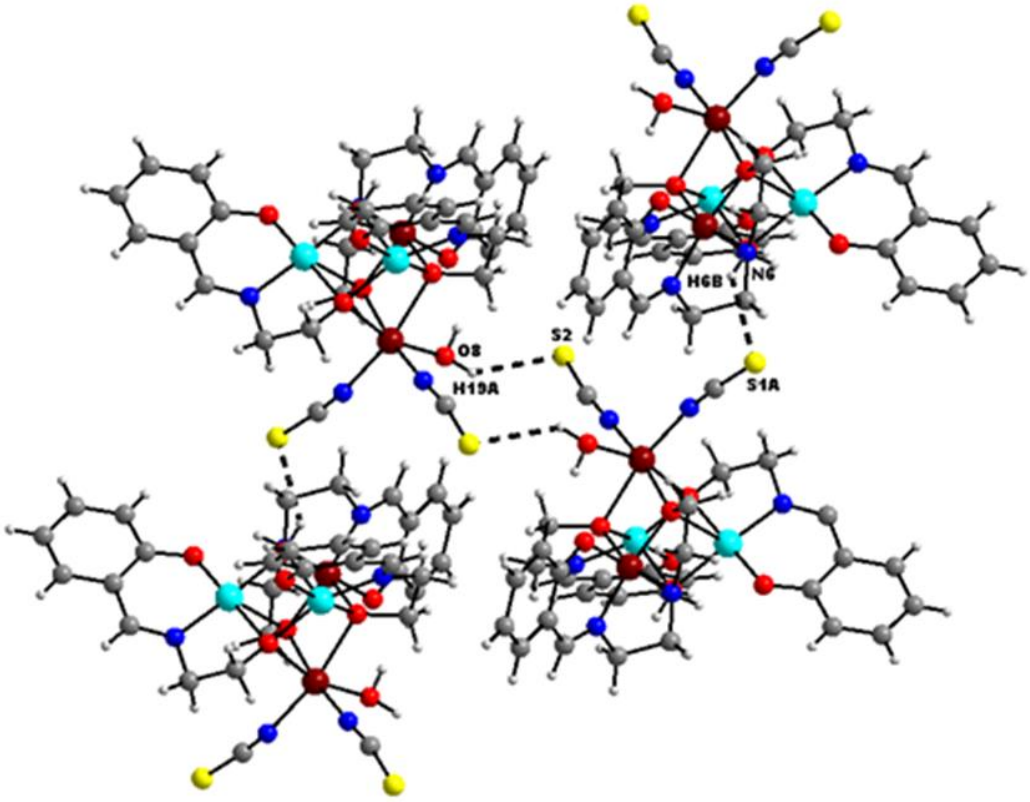

Figure 2.16. Intermolecular Hydrogen bonds in the structure of **6**: OH···S [d(S(2)···O(8)) = 3.27 Å, ∠(O(8)–H(19A)–S(2)) = 125°] and NH···S [d(N(6)··· S(1A)) = 3.35 Å, ∠(N(6)–H(6B)–S(1A)) = 137°] bonds.

Table 2.1. The main types and distribution of cobalt oxide tetranuclear cubane complexes according to CSD.

Homometallic $\{Co_4O_4\}$ *95 hits*	Heterometallic $\{Co_xM_yO_4\}$ *22 hits*		
	$\{Co_3MO_4\}$ *13 hits*	$\{Co_2M_2O_4\}$ *8 hits*	$\{CoM_3O_4\}$ *1 hit*
$\{Co^{II}{}_4O_4\}$ *70 hits*	$\{Co^{II}{}_3LnO_4\}$[24] *6 hits*	$\{Co^{II}{}_2Ln_2O_4\}$[25] *5 hits*	
$\{Co^{III}{}_4O_4\}$ *23 hits*	$\{Co^{III}{}_3MnO_4\}$[4] *5 hits*	$\{Co^{II}{}_2Ni_2O_4\}$[27] *1 hit*	$\{Co^{II}Cu_3O_4\}$[26] *1 hit*
$\{Co^{II}{}_2Co^{III}{}_2O_4\}$[28] *1 hit*	$\{Co^{III}{}_3NiO_4\}$[22] *1 hit*	$\{Co^{III}{}_2Ni_2O_4\}$[22] *1 hit*	
$\{Co^{III}{}_3Co^{IV}O_4\}$[29] *1 hit*	$\{Co^{III}{}_3ZnO_4\}$[22] *1 hit*	$\{Co^{II}Co^{III}Cu_2\}$[30] *complex **6***	

To summarize, the crystal structure of the complex **6** represents a new *{$Co^{II}Co^{III}M_2$}* type of cobalt-based oxide cubane complex according to the proposed classification.

2.3. Tetranuclear Co(III)/Mn(III) complexes with a chain like metal arrangement.

Based on the experimental data described above, the following system was investigated in order to obtain heterometallic Co/Mn complexes.

Mn^0 – CoX_2 – mH_nL – solv **(S8)**,

X = Cl^-, CH_3COO^-; m = 1–3; solv = dmf, dmso, ACN, CH_3OH; H_nL = general formula of Schiff base ligands (Figure 2.3).

The series of homo- and heterometallic complexes were isolated. Thus, molar ratio Mn : CoX_2 : ligand = 1 : 1 : 3 leads to the formation of six new Co/Mn complexes from dmf solution. The liquid diffusion of diethyl ether into the dmf was used to obtain single crystals of desired products. Different conditions, including different molar ratio of metals to ligands (1 : 1 : 1 and 1 : 1 : 2) were tested without success.

Using methanol as a solvent leads to the formation of the homometallic Co complexes $[Co(HL^1)(L^1)]\cdot CH_3OH\cdot H_2O$[16] and $[Co(HL^5)(L^5)]$[31], which have been previously described in the literature. These compounds are formed at molar ratios Mn : CoX_2 : ligand = 1 : 1 : 2 and 1 : 1 : 3. In case of using equimolar quantities the above mentioned complexes were not formed.

For verifying the influence of the experimental conditions on the composition of the products, the following system was investigated as well:

MnX_2 – Co^0 – mH_nL – solv (**S9**)

X = Cl^-, CH_3COO^-; m = 1–3; solv = dmf, dmso, ACN, CH_3OH; H_nL = general formula of Schiff base ligands (Figure 2.4).

The isolation of the same Co/Mn heterometallic complexes as in **S8** confirms that formation of these compounds is not affected by the composition of the precursors.

The formation of the complexes can be explained by the following equations:

$2Co^0 + 2Mn(OAc)_2{\cdot}4H_2O + 4H_4L^3 + 2O_2 + 2dmf \rightarrow$
$[Co_2Mn_2(HL^3)_4(dmf)_2]{\cdot}6H_2O$ (**7**) + 4HOAc+ $6H_2O$;

$2Co^0 + 2Mn(OAc)_2{\cdot}4H_2O + 4H_4L^7 + 2O_2 + 3dmf \rightarrow$
$[Co_2Mn_2(HL^7)_4(dmf)_2]{\cdot}dmf{\cdot}H_2O$ (**8**) + 4HOAc+ $11H_2O$;

$2Co^0 + 2Mn(OAc)_2{\cdot}4H_2O + 4H_4L^{11} + 2O_2 + 3dmf \rightarrow$
$[Co_2Mn_2(HL^{11})_4(dmf)_2]{\cdot}dmf{\cdot}3H_2O$ (**9**) + 4HOAc + $9H_2O$;

$2Co^0 + 2Mn(OAc)_2{\cdot}4H_2O + 4H_4L^{10} + 2O_2 + 3dmf \rightarrow$
$[Co_2Mn_2(HL^{10})_4(dmf)(H_2O)]{\cdot}2dmf{\cdot}2H_2O$ (**10**) + 4HOAc + $9H_2O$;

$2Co^0 + 2Mn(OAc)_2{\cdot}4H_2O + 4H_3L^6 + 2O_2 + 4dmf \rightarrow$
$[Co_2Mn_2(L^6)_4(dmf)_2]{\cdot}2dmf$ (**11**) + 4HOAc + $12H_2O$;

$2Co^0 + 2Mn(OAc)_2{\cdot}4H_2O + 4H_3L^9 + 2O_2 + 4dmf \rightarrow$
$[Co_2Mn_2(L^9)_4(dmf)_2]{\cdot}2dmf{\cdot}7H_2O$ (**12**) + 4HOAc + $5H_2O$;

In order to check the possibility of formation of heterometallic complexes under the conditions of ammonia method, the following systems were further investigated:

$Mn^0 – Co^0 – mH_nL – 2NH_4X – solv$ (S10)

$Mn^0 – Co^0 – mH_nL – BA – 2NH_4X – solv$ (S11)

$X = Cl^-, Br^-, I^-, SCN^-, OAc^-, BF_4^-, NO_3^-$; m = 1-3; BA – basic agent (CaO, BaO);

solv = dmf, dmso, ACN, CH_3OH; H_nL = general formula of Schiff base ligands (Figure 2.3).

However, the experimental conditions of these systems did not allow the formation of heterometallic complexes, unlike it was observed for Mn/Cu metal pairs.

From dmf solution only the homometallic Co complex was obtained and its composition was not determined due to the lack of single crystals formation. But the convincing argument about Co compound was the red color of the powder. The following complex $[Co(HL^1)(L^1)]{\cdot}CH_3OH{\cdot}H_2O$[16] has been isolated from a methanol solution. Dmso did not allow the formation of any products suitable for further investigations.

Figure 2.17 illustrates the IR spectra of the heterometallic Co(III)/Mn(III) compounds **7-12**, which are rather similar. The strong bands at 1645 cm^{-1} (**7**), 1648 cm^{-1} (**8**), 1646 cm^{-1} (**9**), 1644 cm^{-1} (**10**), 1655 cm^{-1} (**11**), 1660 cm^{-1} (**12**) can be assigned as the stretching vibrations ν(C=N) of Schiff base ligands.

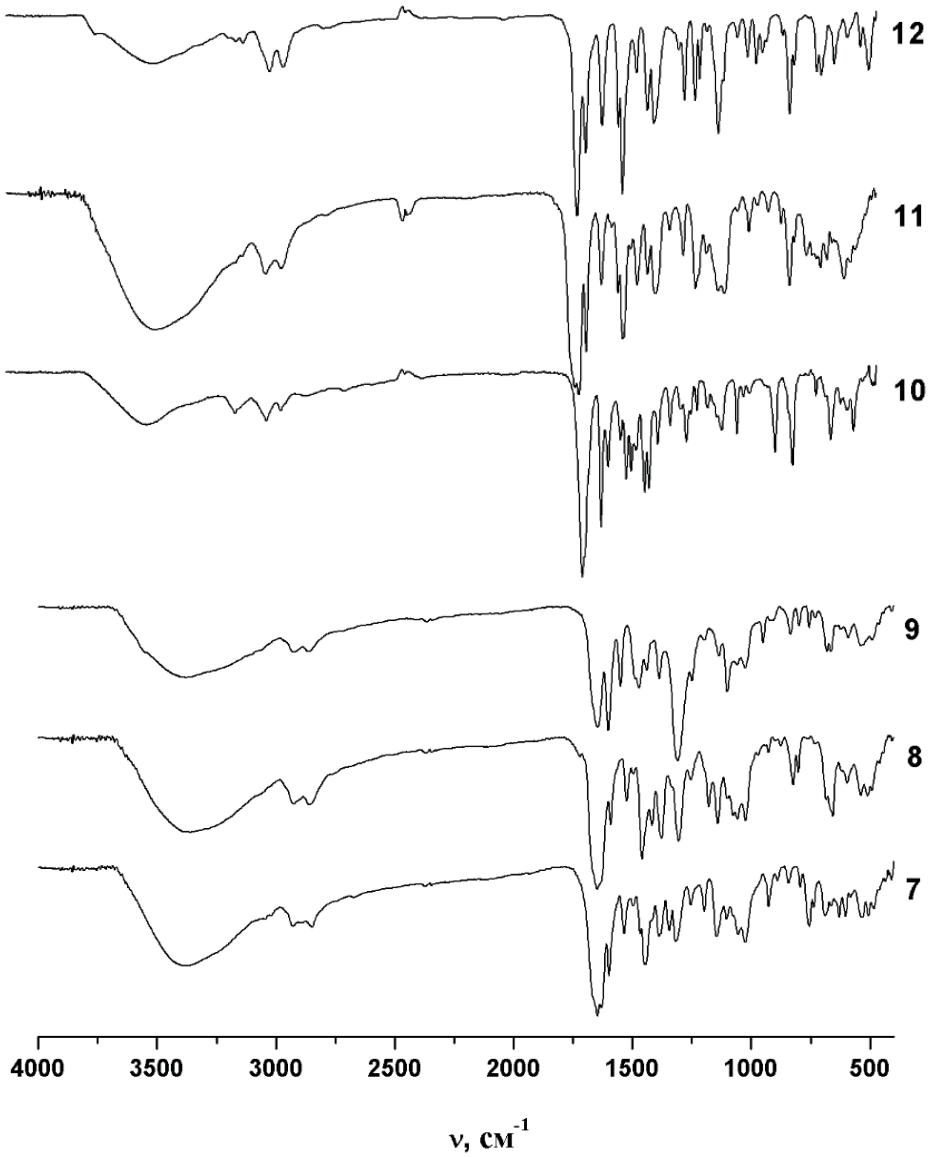

Figure 2.17. IR spectra of **7-12**.

The broad bands at 3500–3100 cm^{-1} show the presence of non-deprotonated OH-groups of the organic ligand and numerous hydrogen bonds in the crystal structure. At 3020-3010 cm^{-1} and 2900-2850 cm^{-1} there are absorption bands corresponding to the ν(C–H) of the aromatic ring and to the aliphatic C–H bonds[18].

2.3.1. The crystal structures of $[Co_2Mn_2(HL^3)_4(dmf)_2]\cdot 6H_2O$ ***(7)***, $[Co_2Mn_2(HL^7)_4(dmf)_2]\cdot dmf\cdot H_2O$ ***(8)***, $[Co_2Mn_2(HL^{11})_4(dmf)_2]\cdot dmf\cdot 3H_2O$ ***(9)***, $[Co_2Mn_2(HL^{10})_4(dmf)(H_2O)]\cdot 2dmf\cdot 2H_2O$ ***(10)***, $[Co_2Mn_2(L^6)_4(dmf)_2]\cdot 2dmf$ ***(11)*** *and* $[Co_2Mn_2(L^9)_4(dmf)_2]\cdot 2dmf\cdot 7H_2O$ ***(12)***

The X-Ray analysis reveals that the molecular structures of **7**-**12** are similar (Figure 2.18), based on the tetranuclear core $\{Co_2Mn_2(\mu\text{-}O)_6\}$ with the nonlinear Co···Mn···Mn'···Co' chain arrangement, where all metal pairs are connected by two O bridges from the deprotonated Schiff base ligands.

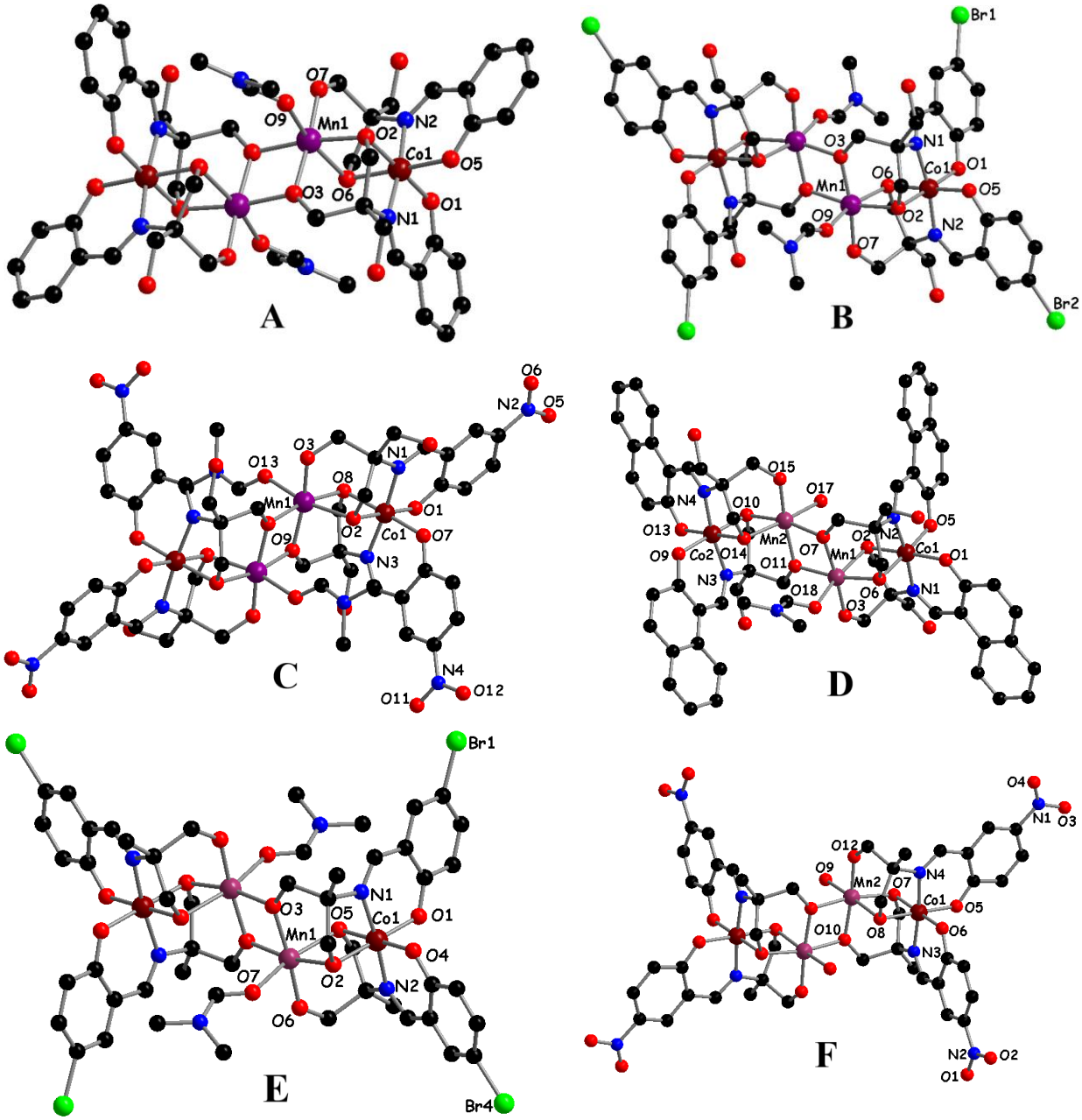

Figure 2.18. The crystal structure of **7-12** (A-F, respectively) with atom labeling. The hydrogen atoms were omitted for clarity.

The recurrent *{M₄(μ-X)₆}* (Figure 2.19) molecular structural type observed in complexes **7-12** is quite common and was widely described for many tetranuclear aggregates (*ca*. 350 hits) according to CSD, yet the present compounds are the first examples of heterometallic Mn^{III}/Co^{III} compounds with *{M₄(μ-X)₆}* MST.

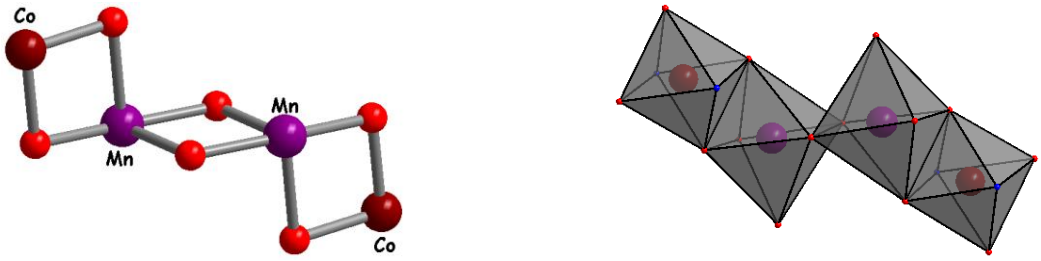

Figure 2.19. The ball-and-stick (left) and polyhedral (right) representations of the *{Co₂Mn₂(μ-O)₆}* molecular core in complexes **7-12**.

The crystal structures of all complexes (except **10**) are centrosymmetric with the inversion center located at the midpoint of the Mn_2O_2 unit and with all of the metal atoms lying in one plane. The presence of two different solvents (dmf and water), coordinated to the metal core in **10**, breaks the symmetry of the molecule, thus making the entire complex as an independent fragment.

Coordination environments of all cobalt(III) ions are formed by oxygen and nitrogen donor atoms of the Schiff base ligands, exclusively. Coordination sites of manganese(III) centers are occupied only by oxygen atoms from ligands and solvent molecules (dmf – for complexes **7-9**, **11**, **12** and dmf with H_2O – for **10**).

The cobalt and manganese ions display similar coordination polyhedra (distorted octahedra) comprised of four O and two N atoms (CoN_2O_4) and six O atoms (MnO_6) of two chelating tridentate ligands. The higher distortion observed for the octahedra of Mn is very likely due to the Jan-Teller effect (Table 2.2).

The unit cells of **7** and **12** contain large solvent-accessible voids (water and dmf molecules) along the *c* axis (V = 944 and 1457 $Å^3$, respectively).

The formation of complexes **7-12** can be understood if one considers the scheme presented in Figure 2.20 The literature search of the similar schemes gives few results of self-organization for heterometallic complexes of higher nuclearity[32-34].

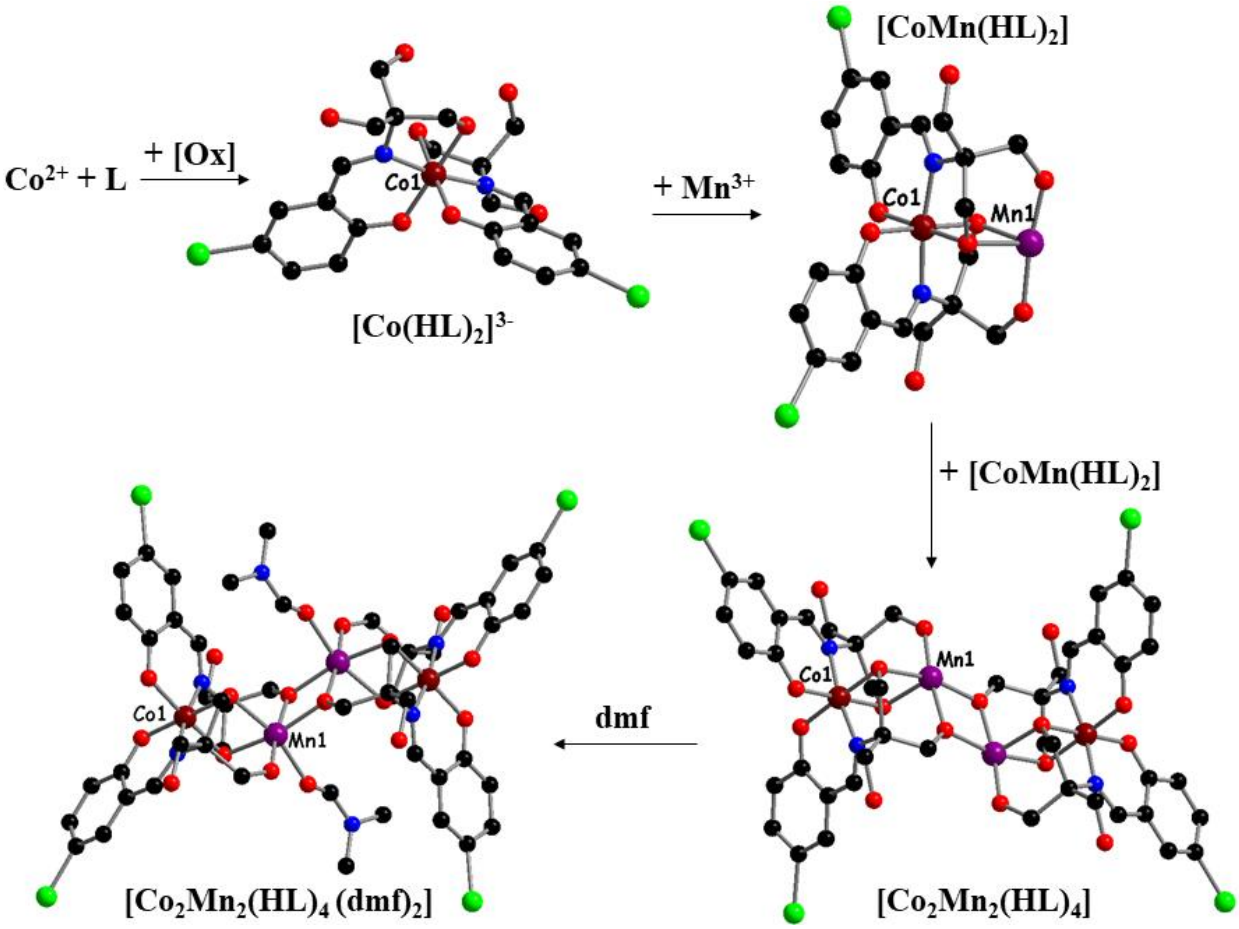

Figure 2.20. Proposed pathway for the formation of complexes **7-12**. As an example compound **8** was chosen.

Table 2.2. Selected Geometrical Parameters (Distances/Å and Angles/°) for **7**-**12**

Complex	**Co-O(N)**	**Mn-O**	***trans* O-Mn-O**	***trans* O-Co-O(N)**	***cis* O-Mn-O**	***cis* O-Co-O(N)**
7	1.8954(34)–1.9103(31)	1.8507(45)–2.2079(37)	164.070(141)–175.656(178)	173.766(212)–177.826(151)	79.339(150)–94.566(143)	84.821(173)–95.820(194)
8	1.8860(35)–1.9012(43)	1.8560(53)–2.1326(82)	164.275(229)–171.943(203)	171.684(178)–178.768(173)	75.445(169)–97.063(205)	83.974(178)–95.759(170)
9	1.8929(65)–1.9200(55)	1.8239(53)–2.1509(72)	163.897(231)–168.941(230)	174.752(261)–178.237(266)	74.996(213)–94.773(223)	84.186(222)–95.326(261)
10	1.8809(85)–1.9182(74)	1.8444(53)–2.1890(66)	167.323(310)–172.404(309)	172.160(339)–178.638(339)	74.825(259)–97.610(321)	83.839(388)–94.860(427)
11	1.8895(46)–1.9143(47)	1.8442(54)–2.1962(62)	162.458(226)–173.551(219)	174.134(220)–178.388(203)	77.285(197)–96.333(212)	84.829(211)–95.784(210)
12	1.8780(47)–1.9099(55)	1.8433(34)–2.1614(90)	168.580(168)–174.309(167)	174.309(167)–177.978(170)	78.045(188)–96.400(184)	85.245(183)–96.384(187)

The coordination mode of the Schiff base ligands to the Co center in compounds **7-12** leads to the formation of a $[Co^{III}(HL)_2]^{3-}$ unit with a quite typical N_2O_4 octahedral environment for Co(III) ions. The participation of Mn(III) in such a reaction is less probable. This is evidenced by the fact that Co powder dissolves much more slowly than $Mn(OAc)_2$. However, the formation of a $[Mn^{III}(HL)_2]^{3-}$ fragment was not observed. At the next step, free manganese(III) ions are coordinated to form a binuclear neutral $\{CoMn(HL)_2\}$ fragment, where the free sites in the coordination environment of manganese allow the further condensation reaction of two $\{CoMn(HL)_2\}$ blocks, providing the tetranuclear core of the isolated complexes. The molecules of dmf complete the coordination environment of the manganese atoms.

2.4. Hexanuclear complex $[Co_2Mn^{II}_2Mn^{III}_2(L^4)_4Cl_2(\mu_3\text{-}OH)_2(dmf)_4]\cdot 2dmf$ (13)

The reaction of cobalt powder with nonaqueous solutions which contain manganese chloride, triethylamine, and tridentate Schiff base ligand H_3L^4 (Figure 2.4) under open air condition during 4 hours leads to the formation of dark-brown mixtures. The new heterometallic Mn/Co complex $[Co_2Mn^{II}_2Mn^{III}_2(L^4)_4Cl_2(\mu_3\text{-}OH)_2(dmf)_4]\cdot 2dmf$ (**13**) was obtained using dmf as a solvent. The formation of the compound can be explained by the following scheme:

$$2Co + 4MnCl_2\cdot 4H_2O + 4H_3L^4 + 2O_2 + 6Et_3N + 6dmf \rightarrow$$
$$[Co_2Mn^{II}_2Mn^{III}_2(L^4)_4Cl_2(\mu_3\text{-}OH)_2(dmf)_4]\cdot 2dmf\ (\mathbf{13}) + 6Et_3N\cdot HCl + 18H_2O.$$

The IR spectrum shows the common features as for the other heterometallic complexes. Thus, the Schiff base molecule can be detected due to the presence of an intense band at 1632 cm^{-1}, which corresponds to the stretching vibrations ν(C=N) (Figure 2.21). Weak intense broad bands at 3100–2975 cm^{-1} and 2975–2840 cm^{-1} can be assigned as ν(C–H) of the aromatic ring and aliphatic C–H bonds, respectively. Dmf molecules have characteristic absorption bands, but in the case of complex **13** they completely coincide with the ones of the Schiff base ligand and therefore cannot be determined by IR spectroscopy.

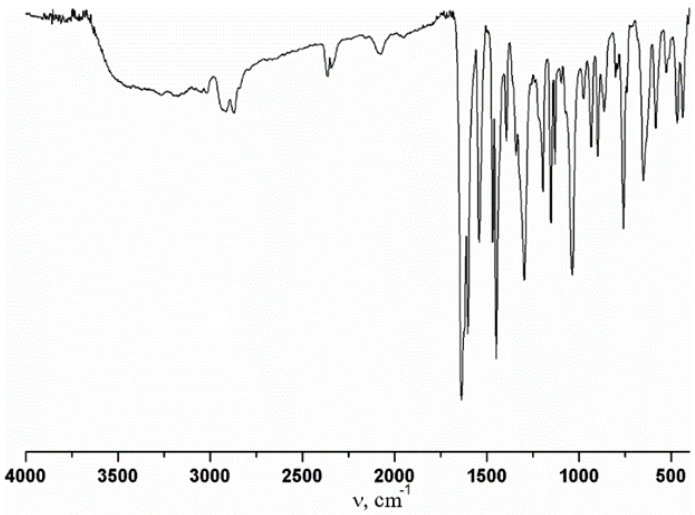

Figure 2.21. IR spectrum of **13**.

Compound **13** crystallizes in the monoclinic system, space group $P2_1/c$. The molecular structure of **13** is based on the hexanuclear core $\{Co^{III}_2Mn^{II}_2Mn^{III}_2(\mu_2\text{-}O)_8(\mu_3\text{-}OH)_2\}$, where all metal ions are linked through μ_2- and μ_3-O atoms from a deprotonated hydroxy group of the Schiff base ligand (figure 2.22).

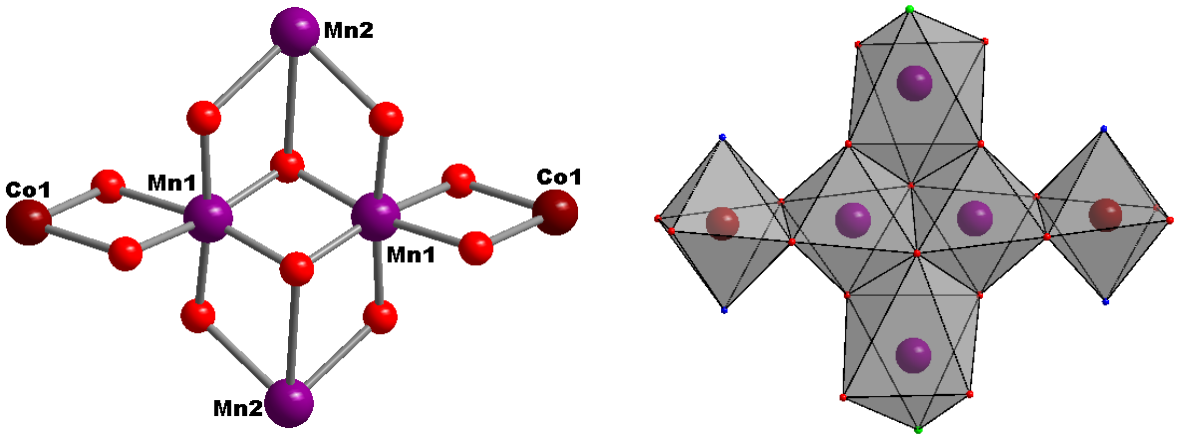

Figure 2.22. The ball-and-stick (left) and polyhedral (right) representations of the $\{Co^{III}_2Mn^{II}_2Mn^{III}_2(\mu_2\text{-}O)_8(\mu_3\text{-}O)_2\}$ molecular core in complex **13**.

According to CSD the only one example with the same MST was reported[35]. The complex $[HNEt_3][Ni_6L_4(\mu_3\text{-}OH)_2(\mu\text{-}OH_2)_2]\cdot 5CH_3CN\cdot 2.6H_2O$ (L – 2,2′,2″-nitrilotribenzoic acid) represents a very rare dicubane-like core. Thereby **13** is the first example of heterometallic complexes possessing $\{M_6(\mu\text{-}X)_8(\mu_3\text{-}X)_2\}$ MST.

The crystal structure of **13** is shown in Figure 2.23. Coordination environments of cobalt atoms are formed by oxygen and nitrogen donor atoms of the Schiff base ligands, while the manganese centers are coordinated only by oxygen atoms from ligands and solvent molecules, and chloride anions.

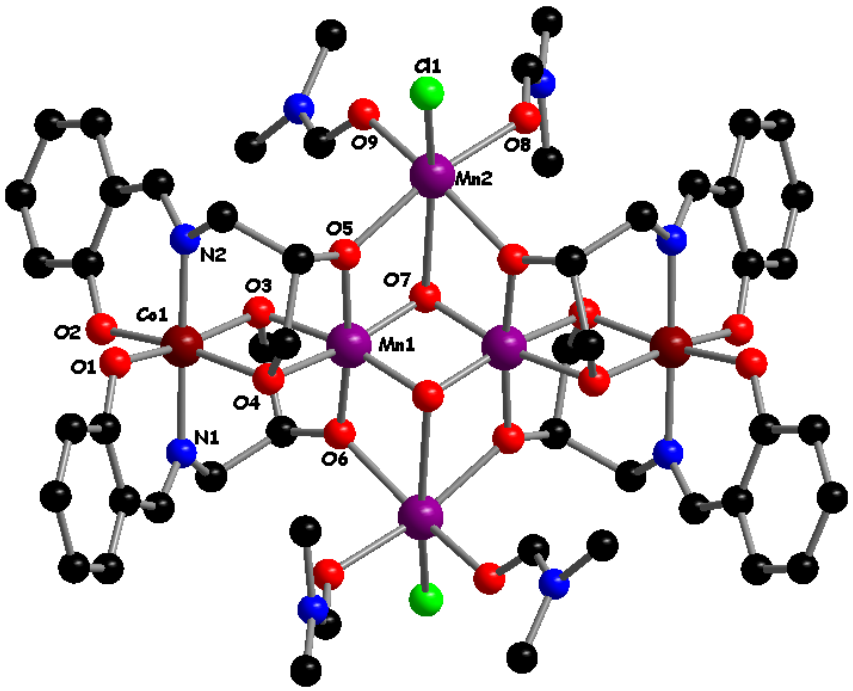

Figure. 2.23. The crystal structure of **13** with atom labeling. The hydrogen atoms were omitted for clarity.

Coordination polyhedra of each metal ion are distorted octahedra and for Co1 and Mn1, the degree of distortion being smaller than for Mn2 polyhedra. The bond lengths Co-(O)N are in the range 1.8775(14)–1.9478(16) Å and *cis*-/*trans*-angles are 83.505(60)–95.736(62)˚ and 168.547(59)–178.742(67)˚, respectively. In the case of manganese ions, the bond distances Mn-(O)Cl vary from 1.8435(13) to 2.4080(5) Å. C*is*- and *trans*- angles are in the range 65.650(45)–102.996(42)˚ and 152.490(57)–172.774(57)˚, respectively.

A careful inspection of the bond lengths between metal ions and donor atoms allows us to assign the charge +3 for cobalt, which is in good agreement with the polynuclear cobalt complexes described in literature[36-37]. The two crystallographically independent Mn atoms show different values of bond distances Mn–O. Thus, for Mn1 ion the charge +3 has been assigned, according to the literature sources[38-40], while Mn2 ion shows the typical bond lengths for Mn^{+2}. These results are supported by the bond valence sum (BVS) calculations. The final formula of complex **13** is $[Co_2Mn^{II}_2Mn^{III}_2(L^4)_4Cl_2(\mu_3\text{-}OH)_2(dmf)_4]\cdot 2dmf$.

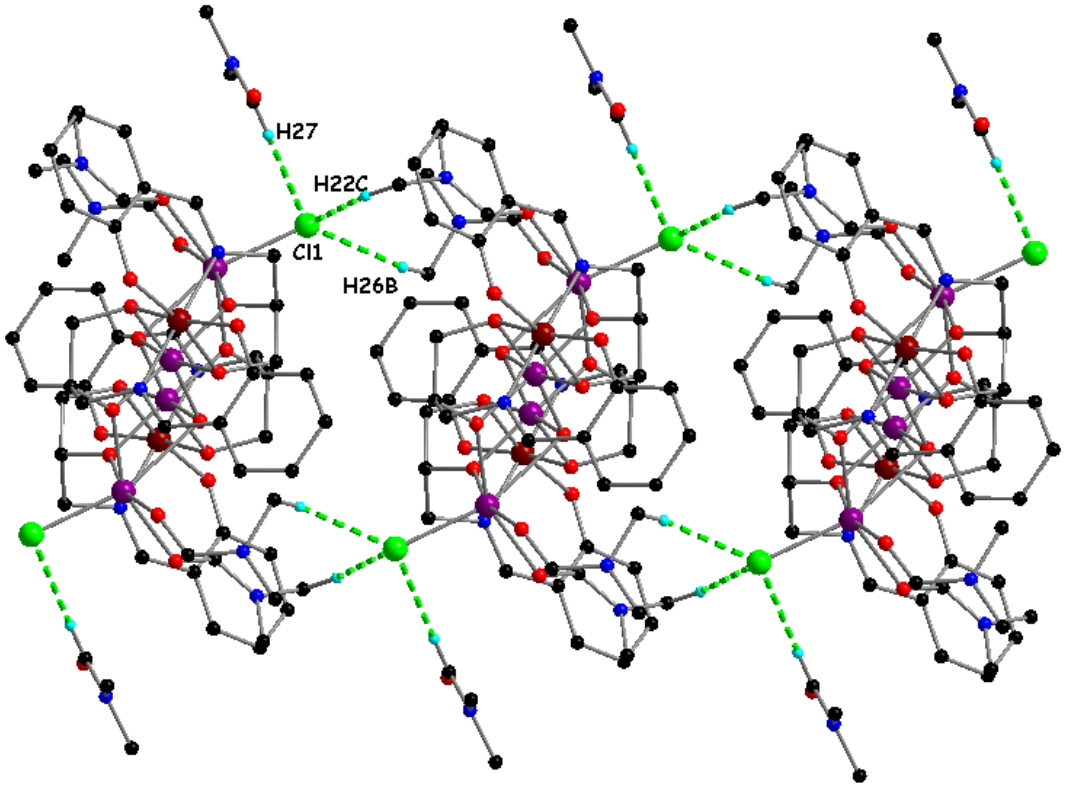

Figure 2.24. Hydrogen bonds in the crystal structure of compound **13**. Hydrogen atoms which are not involved in H bonding were omitted for clarity.

Numerous strong intermolecular hydrogen bonds C–H···Cl [d(C27···Cl1) = 3,75 Å, ∠(C27–H27–Cl1) = 167˚; d(C22···Cl1) = 3,66 Å, ∠(C22–H22C–Cl1) = 152˚; d(C26···Cl1) = 3,64 Å, ∠(C26–H26B–Cl1) = 158˚] between coordinated and uncoordinated dmf molecules and Cl^- anions were found. This fact allows us to describe the structure of **13** as one dimensional coordination polymer (Figure 2.24).

A possible pathway towards the formation of complex **13** is illustrated in Figure 2.25. It should be noted that the proposed mechanism is based on the literature sources where the self-assembly of polynuclear compounds was described.[32-34]

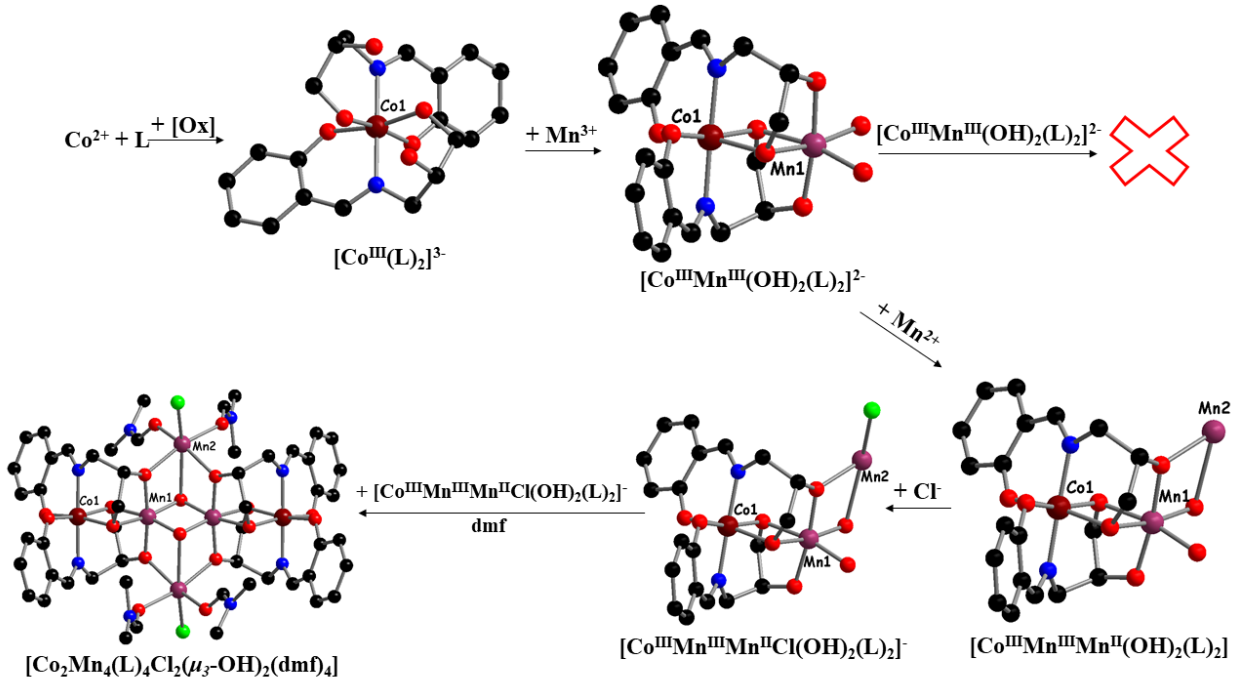

Figure 2.25. Proposed pathway for the formation of complex **13**.

The gradual dissolution of Co powder leads to the formation of a $[Co^{III}(L^4)_2]^{3-}$ unit. This step is similar to the one for the Mn/Co tetranuclear complexes **7-12**. The next step is the coordination of Mn(III) ions to this unit through the hydroxo-groups of the Schiff base ligand resulting in the formation of the heterometallic $[Co^{III}Mn^{III}(OH)_2(L^4)_2]^{2-}$ unit. The presence of OH^- can be explained upon the formation of water molecules during the Schiff base condensation. The further self-assembly of $[Co^{III}Mn^{III}(OH)_2(L^4)_2]^{2-}$ unit is less probable mainly due to the equality of charges and Coulomb repulsion forces. The next step could be the coordination of the second Mn(II) ion and formation of the trinuclear heterometallic $[Co^{III}Mn^{III}Mn^{II}(OH)_2(L^4)_2]$ fragment. The presence of vacant coordination sites creates the possibility for coordination of chloride anions providing the $[Co^{III}Mn^{III}Mn^{II}(OH)_2(Cl)(L^4)_2]^-$ unit. The further assembly of trinuclear units leads to the formation of the hexanuclear heterometallic core of complex **13**. The dmf molecules complete the coordination sphere of Mn ions and engage in the hydrogen bonds with chloride anions.

2.5. Magnetic properties

2.5.1. Heterometallic Cu^{II}_3/Mn^{III} cubane complexes.

The magnetic properties of complexes **1-5**, have been investigated in collaboration with R. Boca, University of SS Cyril and Methodius, Trnava, Slovakia.

The temperature dependence of the effective magnetic moment for complexes **1-4** is shown in Figure 2.26. The theoretical value of $\mu_{eff.}$ for a system with three copper and one manganese ions can be calculated with the formula $\mu_{eff.} = [3g_{Cu}^2S_{Cu}(S_{Cu} + 1) + g_{Mn}^2S_{Mn}(S_{Mn} + 1)]^{½}\mu B$ which amounts to 5.7 μB when all g = 2,0 (S_{Cu} = ½, S_{Mn} = 2). On cooling from room temperature, the effective magnetic moment for **1** gradually decreases from μ_{eff} = 5.54 μB to the value of 1.98 μB at T = 2.0 K. This feature indicates that an antiferromagnetic coupling among the magnetic centers occurs. Down to 2.0 K the molar magnetic susceptibility increases showing that S > 0 is the ground state. At a very low temperature, also some mononuclear fragments of the tetranuclear bulk complex might be present; the modeling of such paramagnetic impurities is rather problematic as they can contribute to the low temperature susceptibility data.

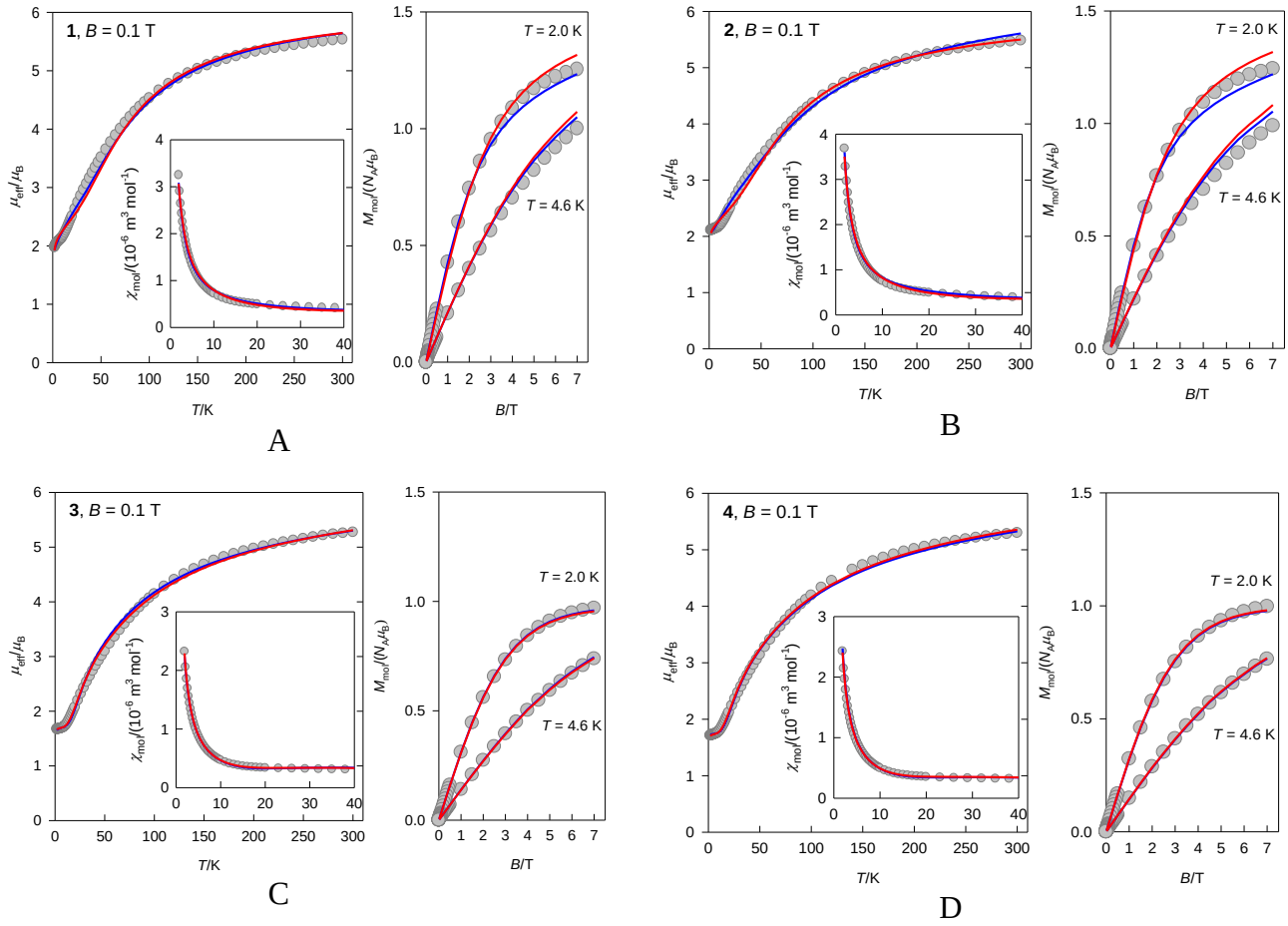

Figure 2.26. Magnetic functions for **1** (A), **2** (B), **3** (C) and **4** (D). Left – Effective magnetic moment, right magnetization per formula unit, inset – molar magnetic susceptibility (SI units). Solid lines – fitted: blue – fit-a, red – fit-b.

The molar magnetization per formula unit has the saturation limit $M_1 = M_{mol}/N_A\mu B = 3g_{Cu}S_{Cu} + g_{Mn}S_{Mn}$ which yields M_1 = 7 for S_{max} = 7/2. The measured magnetization shows a value of only M_1 = 1.2 at T = 2.0 K and B = 7 T. This small value is the fingerprint of a considerable antiferromagnetic exchange, eventually combined with single-ion zero-field splitting of the Mn(III) center.

The susceptibility and magnetization data were fitted simultaneously by applying an error functional $F = E(\chi) \times E(\mathrm{M})$ that accounts uniformly for the relative errors in susceptibility and magnetization. The calculated values have been reconstructed by considering the following spin Hamiltonian:

$$\begin{aligned}\hat{H}_a^{\mathrm{ex}} &= -[J_2(\vec{S}_{\mathrm{Mn}} \cdot \vec{S}_{\mathrm{Cu1}}) + J'_2(\vec{S}_{\mathrm{Cu2}} \cdot \vec{S}_{\mathrm{Cu3}})]\hbar^{-2} \\ &+ J_4[(\vec{S}_{\mathrm{Cu1}} \cdot \vec{S}_{\mathrm{Cu2}}) + (\vec{S}_{\mathrm{Cu1}} \cdot \vec{S}_{\mathrm{Cu3}}) + (\vec{S}_{\mathrm{Cu2}} \cdot \vec{S}_{\mathrm{Mn}}) + (\vec{S}_{\mathrm{Cu3}} \cdot \vec{S}_{\mathrm{Mn}})]\hbar^{-2} \\ &+ D_{\mathrm{Mn}}(\hat{S}^2_{\mathrm{Mn},z} - \hat{S}^2_{\mathrm{Mn}}/3)\hbar^{-2} \\ &+ \mu_{\mathrm{B}} B_a(g_{\mathrm{Mn}}\hat{S}_{\mathrm{Mn},a} + g_{\mathrm{Cu}}\hat{S}_{\mathrm{Cu1},a} + g_{\mathrm{Cu}}\hat{S}_{\mathrm{Cu2},a} + g_{\mathrm{Cu}}\hat{S}_{\mathrm{Cu3},a})\hbar^{-1}\end{aligned}$$

where the first term refers to the isotropic exchange, the second to the zero-field splitting, and the third to the Zeeman term. In the isotropic exchange part, several different coupling constants occur. The constants J_2 and J'_2 reflect the open angles between Mn–O–Cu1 (100°, 105°) and Cu2–O–Cu3 (101°, 104°) centers and they are expected to be negative (an antiferromagnetic exchange interaction). The remaining four interactions precede along the superexchange paths which involve pairs of acute and open angles so that a competition between ferromagnetic and antiferromagnetic interactions is expected: Mn–O–Cu2 (88°, 107°), Mn–O–Cu1 (91°, 106°), Cu1– O–Cu2 (87°, 108°), and Cu1–O–Cu3 (89°, 104°). Thus J_4 could be positive or negative, but less negative than J_2 and J'_2. During the fitting procedure, it was found that $J_2 = J'_2$ can be safely fixed.

The diagonalization of the above Hamiltonian produces a set of eigenvalues entering the partition function. Then the magnetic susceptibility and the magnetization are evaluated by using the formulae of the statistical thermodynamics. The susceptibility data were corrected for the molecular-field correction (zj) and the temperature-independent magnetism χ_{TIM} *via* $\chi_{\mathrm{corr}} = \chi_{\mathrm{mol}}/[1 - (zj)\chi_{\mathrm{mol}}] + \chi_{\mathrm{TIM}}$. The latter term accounts for the uncompensated underlying diamagnetism and the temperature-independent paramagnetism, along with the diamagnetic signal of the sample holder.

The final set of magnetic parameters for complexes **1-4** is listed in Table 2.3. In accordance with expectations, $g_{\mathrm{Mn}} < 2$ for the d^4 system and $g_{\mathrm{Cu}} > 2$ for the d^9 complex hold true.

Table 2.3. Calculated magnetic parameters for complexes **1-5**.

Compound	g_{Mn}	g_{Cu}	J_2/hc	J_4/hc	D_{Mn}/hc	$(zj)/hc$	χ_{TIM}	R(χ)/%	R(M)/%
1	1,859	2,313	–54,8	–27,0	–13,6	–0,075	+0,2	4,0	3,4
2	1,869	2,349	–54,8	–27,0	–14,4	–0,013	+14,4	3,5	4,3
3	1,988	2,009	–45,0	–37,5	–2,8	–0,079	+12,2	2,2	0,7
4	2,000	2,000	–52,5	–39,1	–2,5	~0	+15,0	1,9	1,0
5	1,851	2,178	–22,7	–11,6	–23,4	0,268	+40,0	2,5	3,3

Compound **5** consists of two [Cu_3Mn^{III}] cubes of the open type and one $[Mn^{II}(NCS)_4]^{2-}$ anion. The high-temperature limit of the effective magnetic moment is $\mu_{eff} = [6g_{Cu}^2S_{Mn}(S_{Mn}+1) + g_{Mn}'^2S_{Cu}(S_{Cu}+1) + 2g_{Mn}^2S_{Mn}'(S_{Mn}'+1)]^{1/2}\mu B$ which amounts to $10.34\mu B$ when all $g = 2.0$ (S_{Cu} = 1/2, S_{Mn} =2, $S_{Mn}' = 5/2$). At room temperature, however, μ_{eff} is much higher ($12.7\mu B$) owing to higher g-factors (Figure 2.27).

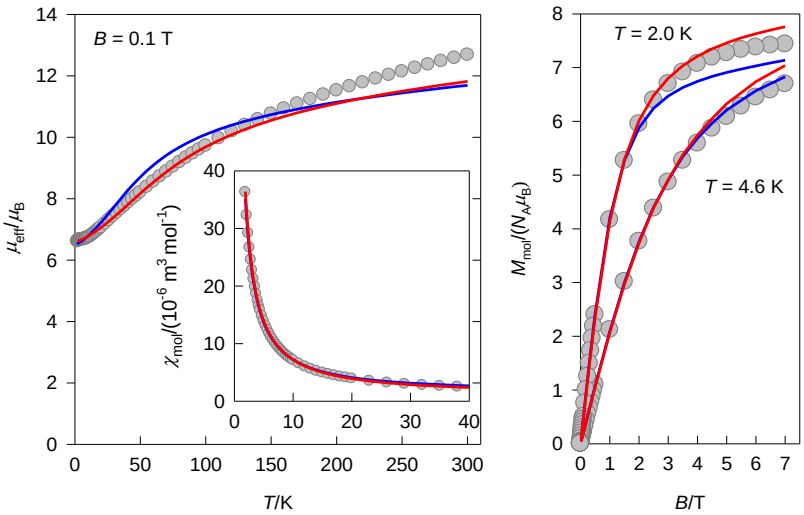

Figure 2.27. Magnetic functions for **5**. Left – Effective magnetic moment, right – magnetization per formula unit, inset – molar magnetic susceptibility (SI units). Solid lines – fitted: blue – fit-a, red – fit-b.

At the same time the magnetization per formula unit should saturate at $M_1 = 6g_{Cu}S_{Cu} + 2g_{Mn}S_{Mn} + g_{Mn}'S_{Mn}' = 19$ but its value at $T = 2.0$ K and $B = 7$ T is only $M_1 = 7.4$. This again confirms a dominating antiferromagnetic coupling along with sizable zero-field splitting. The data fitting for **5** is based upon the assumption that the formula unit contains 2/3 of the [Cu_3Mn^{III}] cube and 1/3 of the [Mn^{II}] complex ($S = 5/2$, $g = 2$). Thus the magnetic data were divided by a factor of 3, then fitted as before with a paramagnetic impurity of Mn^{II} ($x_{PI} = 1/3$) and the fitted data were back-transformed to the original scale by multiplying the calculated susceptibility and magnetization by a factor of 3. The final set of magnetic parameters is also listed in Table 2.3 and it is seen that the coupling constants for such an open structure system are much lower relative to compounds **1–4**.

2.5.2. Heterometallic Co^{III}_2/Mn^{III}_2 tetranuclear complexes.

The magnetic properties of complexes **7-9**, **11**, **12** have been investigated in collaboration with R. Boca, University of SS Cyril and Methodius, Trnava, Slovakia.

The effective magnetic moment for **7** at the room temperature adopts a value of $\mu_{eff} = 6.00\ \mu_B$ by considering two Mn(III) centres bearing $s = 2$ for which $\mu_{eff} = g[2s(s+1)]^{1/2} = 6.93\ \mu_B$ ($g = 2.0$). Upon cooling it decreases gradually (Figure 2.28) which is consistent with the exchange interaction of antiferromagnetic nature ($J < 0$). In such a case, however, it should drop to zero at low temperature which is not the case: at $T = 1.9$ K $\mu_{eff} = 1.34\ \mu_B$ and a maximum of the susceptibility curve is observed at $T \sim 2.8$ K.

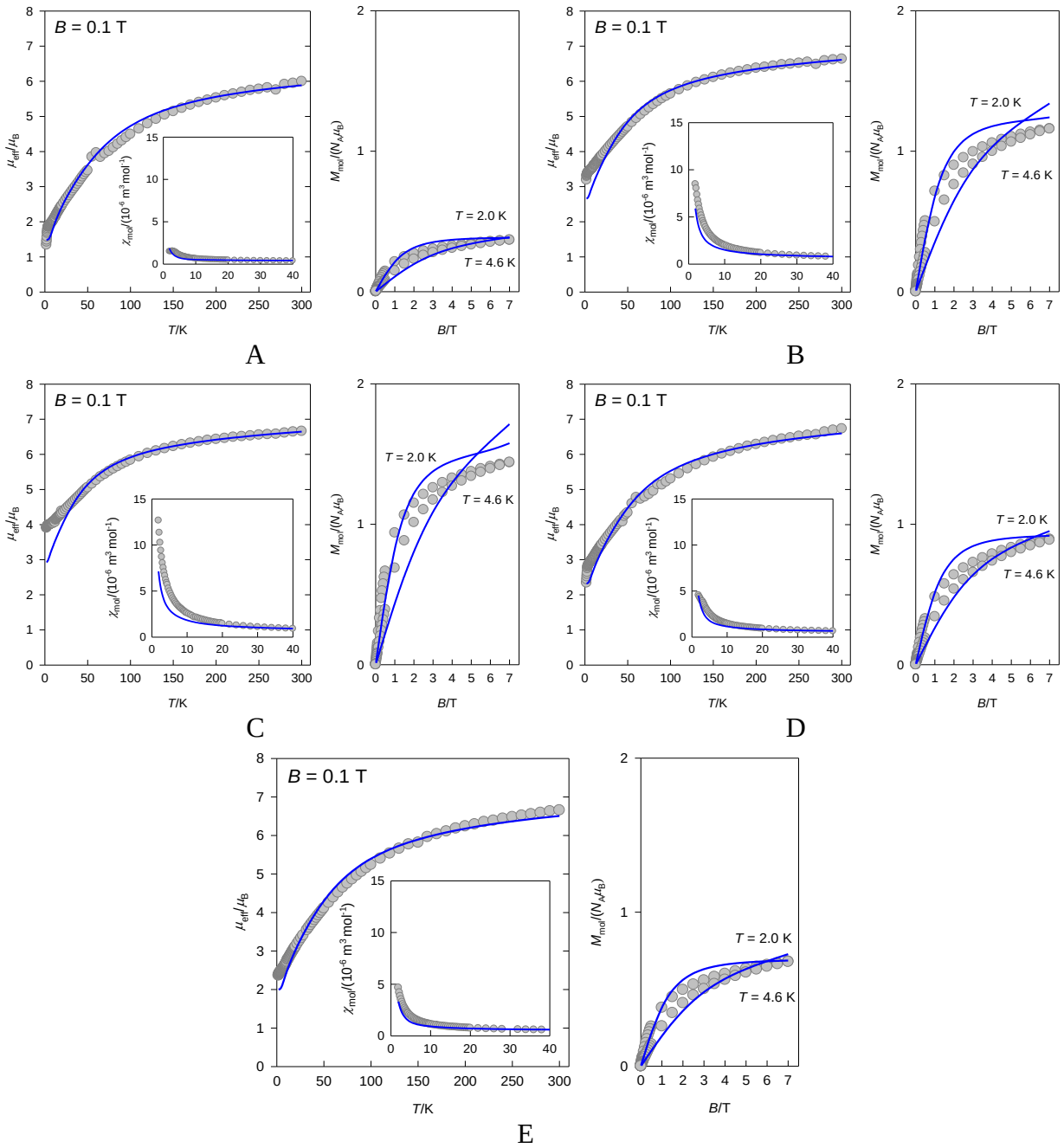

Figure 2.28. DC magnetic data for **7** (A), **8** (B), **9** (C), **11** (D), **12** (E). Left – effective magnetic moment (inset: molar magnetic susceptibility in SI units); right – magnetization per formula unit. Solid lines – fitted.

The experimental value of the magnetization per formula unit $M_1 = M_{mol}/N_A\mu_B$ saturates to $M_1 = 0.37$ at $T = 2.0$ K and $B = 7.0$ T which is far from the theoretical maximum value of $M_1(s) = g(2s) = 8$.

The fitting procedure was based upon the isotropic spin Hamiltonian appropriate to dinuclear systems:

$$\hat{H} = -J(\vec{S}_1 \cdot \vec{S}_2)\hbar^{-2} + \mu_B B g(\hat{S}_{z1} + \hat{S}_{z2})\hbar^{-1}$$

where the symbols adopt their usual meaning. The anisotropic term due to the zero-field splitting can be omitted in the case of sizable antiferromagnetic coupling. In such a case the ground state is

an isolated singlet, $S = 0$, and this is not affected (split) by the D-parameters. However, some additional correction can apply, such as the temperature-independent magnetism $\chi_{TIM} > 0$ and the presence of a mononuclear paramagnetic impurity with the mole fraction x_{PI}.. The retrieved magnetic parameters are listed in Table 2.4. The reconstructed magnetic functions are basically correct, however far from being perfect.

Table 2.4. Calculated magnetic parameters for complexes **7-9, 11, 12**.

Parameter	**7**	**8**	**9**	**11**	**12**
α**(Mn-O-Mn)/°**	100.66	101.96	102.71	104.55	105.00
J**/cm^{-1}**	-18.3	-15.3	-15.0	-12.1	-10.2
$\mu_{eff.}/\mu_B$	6.00	6.35	6.75	6.57	6.64
g	1.80	1.93	1.95	1.92	1.91
χ_{TIM} [a)]	10.5	20	20	20	20
x_{PI}	0.051	0.087	0.12	0.16	0.20
g_{PI}	[1.90]	[1.93]	[1.95]	[1.92]	[1.90]
$R(\chi)$	0.25	0.28	0.24	0.33	0.41
$R(M)$	0.10	0.83	0.093	0.11	0.13

[a)] In units of 10^{-9} m^3 mol^{-1} [SI].

Within the series of complexes **1** through **5** some trends are visible:

- The magnetization per formula unit saturates at $T = 2.0$ K and $B = 7.0$ T to $M_1 = 0.37$, 0.68, 0.89, 1.16 and 1.44; this trend indicates an increase of the exchange coupling constant from $J/hc = -18.3$ to -10.2 cm^{-1}. For **12** a second wave of the magnetization curve starts to be visible; it refers to the population of the $S = 2$ excited state.
- The effective magnetic moment at the room temperature taking adopts values of $\mu_{eff} = 6.00$, 6.35, 6.75, 6.57 and 6.64 μ_B.
- The value of the exchange coupling constant $J/hc = -18.3$, -15.3, -15.0, -12.1 and -10.2 cm^{-1} correlates with the Mn-O(R)-Mn bond angle $\alpha = 100.7$, 102.0, 102.7, 104.6 and 105.0°.

*2.5.3. Hexanuclear complex [$Co_2Mn^{II}_2Mn^{III}_2(L^4)_4Cl_2(\mu_3\text{-}OH)_2(dmf)_4]\cdot 2dmf$ (**13**).*

The magnetic properties of complex **13** have been investigated in collaboration with M. Julve and F. Lloret, University of Valencia, Spain.

The analysis of the magnetic data for compound **13** indicate a very small, if any, magnetic coupling between the two Mn(II) through the double hydroxo bridge and a quite weak ferromagnetic interaction between Mn(III) (dz^2 magnetic orbital) and Mn(II) ($d_{x^2-y^2}$ magnetic orbital) through the single oxygen atom as bridge (Figure 2.29).

The fitting procedure was based upon the following spin Hamiltonian for tetranuclear system:

$$H = -J(S_1S_2 + S_2S_3 + S_3S_4 + S_1S_4) - jS_2S_4 + D(S^2_{z2} + S^2_{z4} - 4) + \beta H[g_{Mn(III)}(S_2 + S_4) + g_{Mn(II)}(S_1 + S_3)]$$

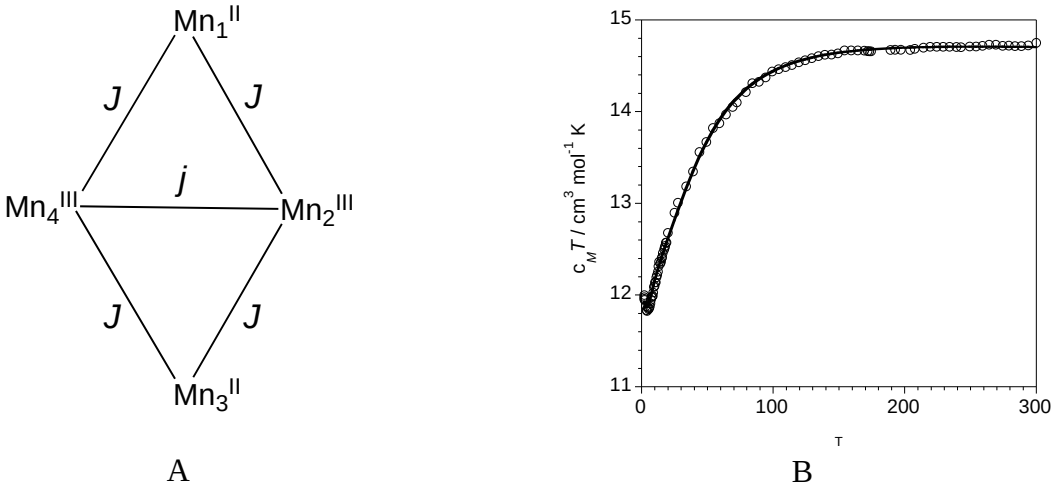

A B

Figure 2.29. Scheme of the magnetic interactions (A) and temperature dependence of the $\chi_M T$ product for 13 (o) experimental; (—) best-fit curve (B)

The best-fit parameters are J = +3.55(2) cm^{-1}, j = -15.1(1) cm^{-1}, $|D|$ = 3.92(2) cm^{-1}, $g_{Mn(II)}$ = 2.01, $g_{Mn(III)}$ = 1.98.

2.6. Light-driven water oxidation

The limited amount of hydrocarbon resources and the aggravation of the ecological situation due to the excessive consumption prompt us to find alternative sources of energy. The sun is the largest energy generator on Earth. That is why the use of solar energy is a logical alternative to exhaustive resources. Water occupies 2/3 of the area of the earth's crust thus being the best absorbent of sun energy. One of the ways for releasing and storing the solar energy is to turn it into chemical bonds, for example, when it is accumulated in H_2. This also solves the problem of the environmental factor, since hydrogen is a "green fuel".

Photocatalytic water oxidation is a long-term research devoted to the allocation and storage of the solar energy, which includes two half-reactions: the restoration of protons with hydrogen release and oxidation of water with further oxygen release. Nowadays the reduction process of the protons is well-developed. On the other hand, water oxidation itself remains an ineffective process. Its catalysts are insensitive to sunshine and require additional oxidants, such as oxone, $Ru(bipy)_3^{3+}$, etc. Therefore, it becomes quite clear that there is a problem to find more accessible oxidation catalysts for the photocatalytic water oxidation.

In nature, the reaction of water oxidation occurs due to the heterometallic Mn/Ca complex within the active $\{CaMn_4\}$ site of the photosystem II[7]. Unfortunately, manganese-containing complexes are not effective precursors of the photocatalytic decomposition of water, unlike other metals such as iridium[41] or ruthenium[42-43]. It should be noted that for the introduction of the

catalytic system into the technology of conversion of solar energy, the latter should contain cheap and affordable starting materials.

The catalytic reaction of water oxidation catalyst (WOC) can be represented by the following scheme (figure 2.30):

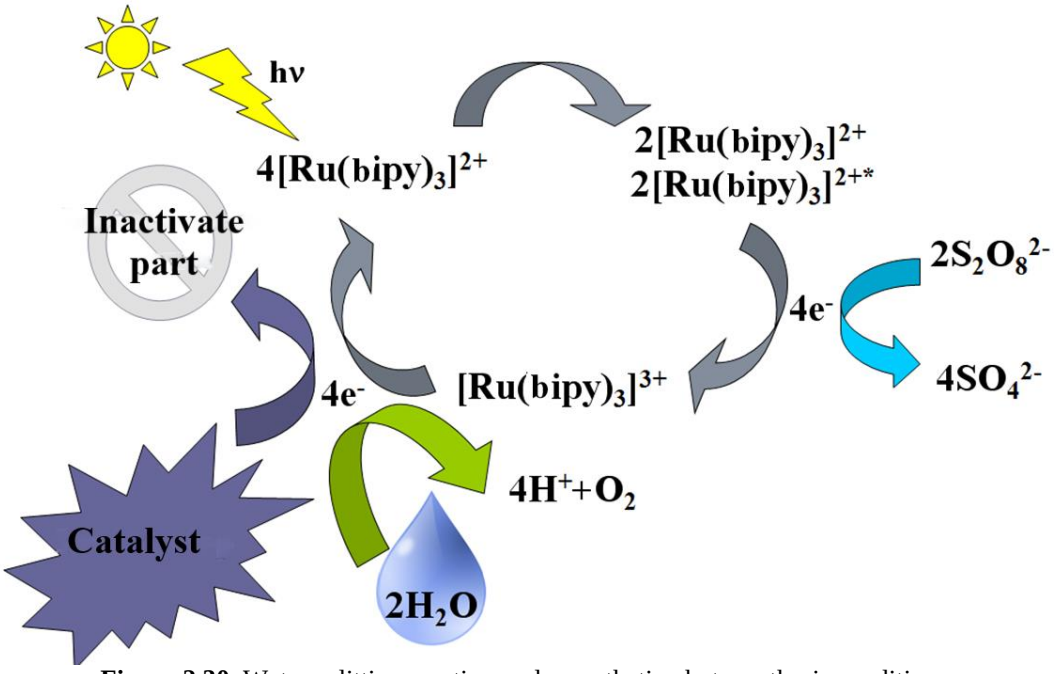

Figure 2.30. Water splitting reaction under synthetic photosynthesis condition.

The ruthenium complex $[Ru(bipy)_3]^{2+}$ plays the role of a photosensitizer, and $S_2O_8^{2-}$ is an acceptor of electrons. These compounds are typical precursors for the study of photocatalytic ability[42-44].

The experimental set up of such reaction is as follows: the cell with a standard Clark electrode on the bottom was continuously stirred using a small, Teflon-coated stirrer bar. Standard concentrations of components in catalytic system in a Clark cell were: 3 μM of Mn/Cu-containing complexes **1-4**, 100 μM of $[Ru(bipy)_3](ClO_4)_2$, 5 mM of $Na_2S_2O_8$ and the mixture of KH_2PO_4/K_2HPO_4 (50 mM) (pH = 7.0). The samples were transferred to the Clark cell and kept at 20 ^oC while the solution was made anaerobic by flushing the cell with argon gas. Air saturated water solutions ($[O_2]$ = 280 μM, T = 20 ^oC) were used for calibration of the electrode. Visible light of LEDs, λ = 470 ± 10 nm, was applied for the induction of photoreaction.

The investigation of catalytic activity for Mn/Cu cubane complexes **1-4** shows that all these compounds exhibit low activity, which is typical for Cu compounds. For comparison, photocatalytic water oxidation with 60 μM $Mn(NO_3)_2 \cdot 6H_2O$ and $Cu(NO_3)_2 \cdot 6H_2O$ was performed. No oxygen evolution was detected for the copper nitrate and for $Mn(NO_3)_2 \cdot 6H_2O$, the TON values being 2–3 times lower than for complexes **1-4**.

As can be seen from figure 2.31, after switching on the light (~ 30 s, λ = 470 nm), O_2 is forming.

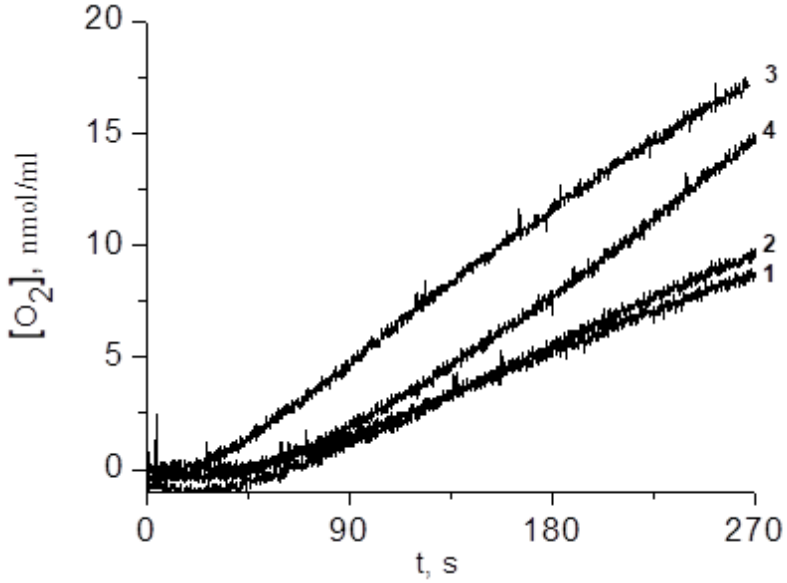

Figure 2.31. Oxygen evolution curves for complexes **1-4**.

The final concentrations of O_2 were 8.97, 10.14, 17.54, 17.35 nmol for complexes **1-4**, respectively. The total set of catalytic parameters are given in table 2.5. In the absence of at least one of the components of the catalytic system (light, catalyst, photosensitizer or electron acceptor), water oxidation was not observed.

Table 2.5. Catalityc activity of heterometallic complexes in water splitting reaction.

Complex		**TON**
$[Cu_3Mn(L^1)_4(CH_3OH)_3]I_3$	(**1**)	1,42
$[Cu_3Mn(L^1)_4(CH_3OH)_3]NCS{\cdot}2H_2O$	(**2**)	1,87
$[Cu_3Mn(L^1)_4(CH_3OH)(H_2O)_{2.55}]Br{\cdot}0.45H_2O$	(**3**)	2,65
$[Cu_3Mn(L^1)_4(H_2O)_{3,4}]BF_4{\cdot}0.6H_2O$	(**4**)	2,38

2.7. Photoconductivity of polymer composite films containing Mn/Cu complex.

Introducing of heterometallic complexes into polymer films promotes the appearance of an internal photoelectric effect[45-46]. In the visible region of the spectrum, the photoconductivity of polymer composite films (PCFs) is provided by photogeneration of charge carriers and their transport both within the particles of the complexes, separated by the polymer binder and between these particles. The latter allows us to suggest that such compounds are valuable nanosized structures for data media[47] and photoelectric transducers for solar energy[48].

Having this in mind, the photoelectric properties of PCF, based on polyvinil butyral (PVB) and the above-mentioned Mn/Cu cubane complexes **1-4** were investigated. Samples with polymer

composite films based on non-photoconducting PVB were prepared with a free PCF surface (glass substrate–polymer composite film) and as sandwich structures: glass substrate – SnO_2:In_2O_3 – polymer composite film – Ag. The content of complexes in the PVB was 33 wt.%, which is optimal for obtaining high electrical conductivity and photoconductivity of the polymer composite films with no deterioration in their compatibility and optical properties. For the prepared samples the absorption spectra of the polymer composite films in the 400–800 nm range, the conduction current density (j_d) and the photocurrent density (j_{PH}) during and after irradiation by light at λ_{irr} ~ 580 nm as a function of the voltage (U) applied to the electrical contacts were measured. Only PFCs containing complex **3** possess the photoconductivity.

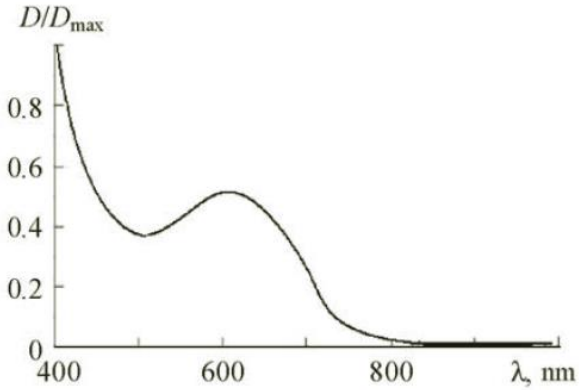

Figure 2.32. Absorption spectrum of the polymer composite film containing 33 wt.% complex **3**.

PVB films do not absorb in the visible region, but with additives of **3** particles, they have a green color which is determined by the intrinsic absorption of **3** (Figure 2.32). In samples of sandwich structures with PVB films but without compound **3**, there is no photocurrent in the visible range of light. In samples with polymer composite films containing **3**, upon irradiation by light, the conduction current increases up to a new, nearly steady state value, and once the light is turned off it recovers to the initial value (Figure 2.33). In this case, the value of j_{PH} is hundreds of times greater than for similar complexes[49]. The main parameters of photoconductivity measurements for compound **3** are given in Table 2.6. The parameters of heterometallic complex $[Cu(en)_2][Mn_2(C_2O_4)_3]\cdot 6H_2O$ are listed also for comparison reasons.

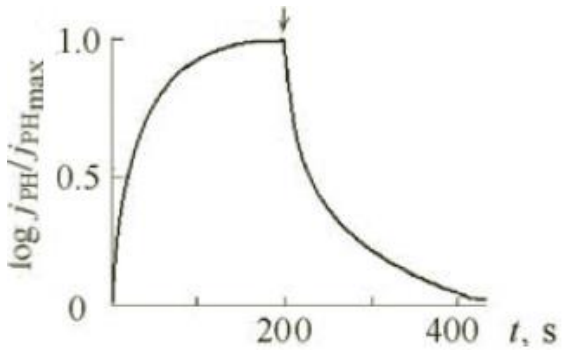

Figure 2.33. Photocurrent kinetics in PCF with complex **3**. The vertical arrow marks the time the light is turned off.

Table 2.6. The results of photoconductivity measurements for compound **3**

Complex	j_d, A/m^2	j_{PH}, A/m^2
$[Cu(en)_2][Mn_2(C_2O_4)_3]\cdot 6H_2O$[49]	0.2	0.008
$[Cu_3Mn(L^1)_4(CH_3OH)(H_2O)_{2.55}]Br\cdot 0.45H_2O$ (**3**)	2.5	4.5

The results obtained allow us to consider the studied compound as a promising component for the development and creation of new polymer composites with photoelectric properties. A

disadvantage of the studied polymer composite films for practical use is their slow response to photoexcitation.

2.8. Conclusion.

The successful utilization of the “direct synthesis” method allowed us to isolate a series of polynuclear heterometallic complexes with Schiff base ligands, formed *in situ*. The open-air reaction of Mn and Cu powders with condensation product of salicylaldehyde and ethanolamine resulted in four new $\{Cu_3^{II}Mn^{III}O_4\}$ cubane like complexes. On the other hand, increasing the basicity of Schiff base ligands, leads to the formation of series Mn/Co compounds, with tetranuclear $\{Co_2Mn_2(\mu\text{-}O)_6\}$ and hexanuclear mixed valence $\{Co^{III}_2Mn^{II}_2Mn^{III}_2(\mu_2\text{-}O)_8(\mu_3\text{-}OH)_2\}$ cores. The magnetochemical studies of the isolated metal complexes show the presence of dominating antiferromagnetic interaction between metal centers.

References

1. Scrutton, M. C., *FEBS Lett.* **1978,** *89*, 361-361.
2. Ardizzoia, G. A.; Brenna, S., *Coord. Chem. Rev.* **2016,** *311*, 53-74.
3. Umena, Y.; Kawakami, K.; Shen, J.-R.; Kamiya, N., *Nature* **2011,** *473*, 55.
4. Nguyen, A. I.; Ziegler, M. S.; Oña-Burgos, P.; Sturzbecher-Hohne, M.; Kim, W.; Bellone, D. E.; Tilley, T. D., *J. Am. Chem. Soc.* **2015,** *137*, 12865-12872.
5. Beattie, J. K.; Hambley, T. W.; Klepetko, J. A.; Masters, A. F.; Turner, P., *Polyhedron* **1998,** *17*, 1343-1354.
6. Jiang, X.; Li, J.; Yang, B.; Wei, X.-Z.; Dong, B.-W.; Kao, Y.; Huang, M.-Y.; Tung, C.-H.; Wu, L.-Z., *Angew. Chem. Int. Ed.* **2018,** *57*, 7850-7854.
7. Rutherford, A. W.; Boussac, A., *Science* **2004,** *303*, 1782.
8. Kokozay, V. N.; Vassilyeva, O. Y.; Makhankova, V. G., Direct Synthesis of Heterometallic Complexes. In *Direct Synthesis of Metal Complexes*, Kharisov, B., Ed. Elsevier: 2018; pp 183-237.
9. Nesterov, D. S.; Nesterova, O. V.; Kokozay, V. N.; Pombeiro, A. J. L., *Eur. J. Inorg. Chem.* **2014,** *2014*, 4496-4517.
10. Boyko, E. R.; Hall, D.; Kinloch, M. E.; Waters, T. N., *Acta Crystallogr.* **1966,** *21*, 614-617.
11. Dong, J.-F.; Li, L.-Z.; Xu, H.-Y.; Wang, D.-Q., *Acta Crystallogr., Sect. E* **2007,** *63* (9), m2300.
12. Zhang, L.-F.; Ni, Z.-H.; Zong, Z.-M.; Wei, X.-Y.; Ge, C.-H.; Kou, H.-Z., *Acta Crystallogr., Sect. C* **2005,** *61*, m542-m544.
13. Kessissoglou, D. P.; Butler, W. M.; Pecoraro, V. L., *J. Chem. Soc., Chem. Commun.* **1986,** *16*, 1253-1255.
14. Pryma, Oksana V.; Petrusenko, Svitlana R.; Kokozay, Volodymyr N.; Skelton, Brian W.; Shishkin, Oleg V.; Teplytska, Tetyana S., *Eur. J. Inorg. Chem.* **2003,** *2003*, 1426-1432.
15. Midões, A. C. D.; Aranha, P. E.; dos Santos, M. P.; Tozzo, É.; Romera, S.; Santos, R. H. d. A.; Dockal, E. R., *Polyhedron* **2008,** *27*, 59-64.
16. Li, Y.; Wu, Q.; Lecren, L.; Clérac, R., *J. Mol. Struct.* **2008,** *890*, 339-345.
17. Shit, S.; Rosair, G.; Mitra, S., *J. Mol. Struct.* **2011,** *991*, 79-83.
18. Brisdon, A., *Appl. Organomet. Chem.* **2010,** *24*, 489-489.
19. Li, C.-H.; Kui, S. C. F.; Sham, I. H. T.; Chui, S. S.-Y.; Che, C.-M., *Eur. J. Inorg. Chem.* **2008,** *2008*, 2421-2428.
20. Tatsumi, K.; Inoue, Y.; Kawaguchi, H.; Kohsaka, M.; Nakamura, A.; Cramer, R. E.; VanDoorne, W.; Taogoshi, G. J.; Richmann, P. N., *Organometallics* **1993,** *12*, 352-364.

21. Bernhardt, P. V.; Lawrance, G. A., 6.1 - Cobalt. In *Comprehensive Coordination Chemistry II*, McCleverty, J. A.; Meyer, T. J., Eds. Pergamon: Oxford, 2003; pp 1-145.

22. Gahan, L. R.; Henriksen, S. L., *Polyhedron* **2015,** *95*, 30-39.

23. Vafazadeh, R.; Willis, A. C., *J. Coord. Chem.* **2015,** *68*, 2240-2252.

24. Wang, P.; Shannigrahi, S.; Yakovlev, N. L.; Hor, T. S. A., *Inorg. Chem.* **2012,** *51*, 12059-12061.

25. Zhao, X.-Q.; Lan, Y.; Zhao, B.; Cheng, P.; Anson, C. E.; Powell, A. K., *Dalton Trans.* **2010,** *39*, 4911-4917.

26. Yang, L.; Li, J.; Pu, T.-C.; Kong, M.; Song, Y., *Dalton Trans.* **2017,** *46*, 6670-6676.

27. Kessler, V. G.; Gohil, S.; Kritikos, M.; Korsak, O. N.; Knyazeva, E. E.; Moskovskaya, I. F.; Romanovsky, B. V., *Polyhedron* **2001,** *20*, 915-922.

28. Bertrand, J. A.; Hightower, T. C., *Inorg. Chem.* **1973,** *12*, 206-210.

29. Dimitrou, K.; Brown, A. D.; Concolino, T. E.; Rheingold, A. L.; Christou, G., *Chem. Commun.* **2001,** *14*, 1284-1285.

30. Stetsiuk, O.; El-Ghayoury, A.; Kokozay, V. N.; Avarvari, N.; Petrusenko, S. R., *J. Coord. Chem.* **2018,** *71*, 68-77.

31. De, R. L.; Samanta, K.; Maiti, K.; Keller, E., *Inorg. Chim. Acta* **2001,** *316*, 113-116.

32. Nesterov, D. S.; Chygorin, E. N.; Kokozay, V. N.; Bon, V. V.; Boča, R.; Kozlov, Y. N.; Shul'pina, L. S.; Jezierska, J.; Ozarowski, A.; Pombeiro, A. J. L.; Shul'pin, G. B., *Inorg. Chem.* **2012,** *51*, 9110-9122.

33. Chygorin, E. N.; Nesterova, O. V.; Rusanova, J. A.; Kokozay, V. N.; Bon, V. V.; Boča, R.; Ozarowski, A., *Inorg. Chem.* **2012,** *51*, 386-396.

34. Chygorin, E. N.; Kokozay, V. N.; Omelchenko, I. V.; Shishkin, O. V.; Titiš, J.; Boča, R.; Nesterov, D. S., *Dalton Trans.* **2015,** *44*, 10918-10922.

35. Wörl, S.; Pritzkow, H.; Fritsky, I. O.; Krämer, R., *Dalton Trans.* **2005,** (1), 27-29.

36. Peng, Y.; Tian, C.-B.; Zhang, H.-B.; Li, Z.-H.; Lin, P.; Du, S.-W., *Dalton Trans.* **2012,** *41*, 4740-4743.

37. Peng, Y.; Tian, C.-B.; Lan, Y.-H.; Magnani, N.; Li, Q.-P.; Zhang, H.-B.; Powell, A. K.; Du, S.-W., *Eur. J. Inorg. Chem.* **2013,** *2013*, 5534-5540.

38. King, P.; Wernsdorfer, W.; Abboud, K. A.; Christou, G., *Inorg. Chem.* **2004,** *43*, 7315-7323.

39. King, P.; Wernsdorfer, W.; Abboud, K. A.; Christou, G., *Inorg. Chem.* **2005,** *44*, 8659-8669.

40. Murugesu, M.; Habrych, M.; Wernsdorfer, W.; Abboud, K. A.; Christou, G., *J. Am. Chem. Soc.* **2004,** *126*, 4766-4767.

41. Hull, J. F.; Balcells, D.; Blakemore, J. D.; Incarvito, C. D.; Eisenstein, O.; Brudvig, G. W.; Crabtree, R. H., *J. Am. Chem. Soc.* **2009,** *131*, 8730-8731.

42. Geletii, Y. V.; Huang, Z.; Hou, Y.; Musaev, D. G.; Lian, T.; Hill, C. L., *J. Am. Chem. Soc.* **2009,** *131*, 7522-7523.

43. Duan, L.; Xu, Y.; Zhang, P.; Wang, M.; Sun, L., *Inorg. Chem.* **2010,** *49*, 209-215.

44. Harriman, A.; Pickering, I. J.; Thomas, J. M.; Christensen, P. A., *Journal of the Chemical Society, Faraday Transactions 1: Physical Chemistry in Condensed Phases* **1988,** *84*, 2795-2806.

45. Ohkoshi, S.-i.; Tokoro, H.; Hozumi, T.; Zhang, Y.; Hashimoto, K.; Mathonière, C.; Bord, I.; Rombaut, G.; Verelst, M.; Cartier dit Moulin, C.; Villain, F., *J. Am. Chem. Soc.* **2006,** *128*, 270-277.

46. Davidenko, N. A.; Nikitina, V. N.; Dekhtyarenko, S. V.; Nesterova, O. V.; Kokozay, V. N., *Physics of the Solid State* **2009,** *51*, 421-426.

47. Vreshch, O. V.; Davidenko, N. A.; Dekhtyarenko, S. V.; Ishchenko, A. A.; Kokozay, V. N.; Kozinetz, A. V.; Skryshevsky, V. A.; Tretyak, O. V., *High Energ. Chem.* **2009,** *43*, 133-137.

48. Li, L.; Niu, S.-Y.; Jin, J.; Meng, Q.; Chi, Y.-X.; Xing, Y.-H.; Zhang, G.-N., *J. Solid State Chem.* **2011,** *184*, 1279-1285.

49. Davidenko, N. A.; Kokozay, V. N.; Ishchenko, A. A.; Beznishchenko, A. A.; Makhan'kova, V. G.; Spitsyna, N. G.; Lobach, A. S.; Davidenko, I. I.; Popenaka, A. N., *Semiconductors* **2007,** *41*, 634-640.

CHAPTER III

ELECTROACTIVE SCHIFF BASE LIGANDS AND THEIR COMPLEXES

3.1. Introduction

Combination of an electroactive fragment, such as tetrathiafulvalene (TTF)[1], with coordinating groups represents a fertile strategy to obtain functional metal complexes which can provide multifunctional molecular materials[2] where coexistence or synergy of different physical properties can occur. A large majority of reported TTF based ligands contain group V(B) heteroatoms with coordinating unit such as phosphines[3-7], pyridines[8-13], chelating dipyridylamines[14] and dipicolylamines[15-16], oxazolines[17-19], pyrazoles[20-22], triazoles[23-25], imino-pyridines[26], oxamates[27]. N, O-chelating moieties, as the Schiff base ligands, are promising candidates to obtain heterometallic polynuclear complexes that exhibit a synergetic effect caused by the presence of a few different spin carrier centers.

The first investigation in the TTF Schiff base ligands family was the work of S. Decurtins[28]. The synthesis of a planar π-extended TTF annulated N,N′-phenylenebis(salicylideneimine) (TTF-salphen, figure 3.1) ligand, **L**, and its corresponding transition metal (Fe(III), Co(II), Ni(II), Cu(II)) complexes, was described.

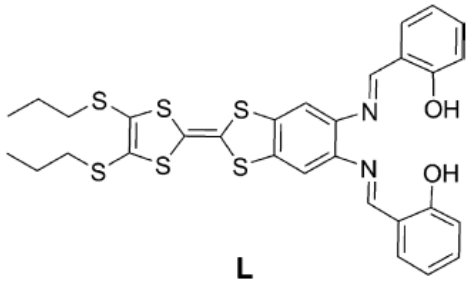

Figure 3.1. Molecular structure of the TTF-salphen ligand **L**

The Schiff base ligand **L** provides in its deprotonated form a tetradentate N_2O_2 coordination environment for metal centers. The corresponding transition metal complexes were obtained in good yields by mixing **L** with metal precursors (acetates for Co(II), Ni(II), Cu(II) and $FeCl_3 \cdot 6H_2O$ for Fe(III)). The crystal structure of the latter is shown in Figure 3.2, left.

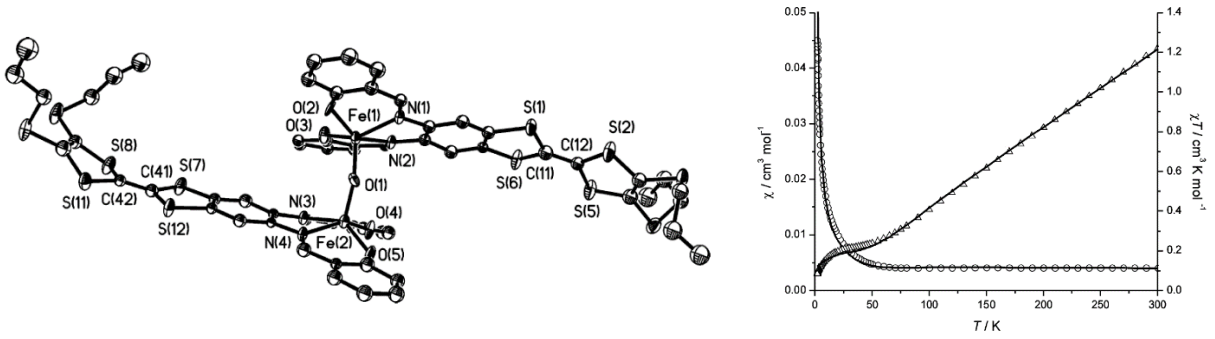

Figure 3.2. Crystal structure of 2 with thermal ellipsoids shown at the 50% probability level (left) and a plot of $\chi_M(T)$ (circles) and $\chi_M T(T)$ (triangles) (right).

Two [Fe(III)**L**] moieties are linked by a bridging oxygen atom which occupies the apical position of the square pyramidal coordination geometry around each Fe(III) center. Studies of the

magnetic susceptibilities (Figure 3.2, right) of the oxo-bridged Fe(III) complex reveal an intramolecular antiferromagnetic coupling similar to described in literature oxobridged Fe(III) compounds.

As a continuation of this research direction, the series of heterometallic 3*d*-4*f* complexes with the aforementioned macrocyclic ligand were reported later on by L. Ouahab and co-workers[29]. Both phenolate functions in **L** react as Lewis bases, whereas the $Ln(hfac)_3$ moieties can play the role of Lewis acids. Mixing the homometallic 3d complexes[28] with $Ln(hfac)_3 \cdot 2H_2O$ precursors in a non-coordinating solvent, such as chloroform, resulted in the series of heterometallic compounds with the general formula [(**L**)MLn(hfac)$_3$].

The crystalline structure of [(**L**)CuYb(hfac)$_3$] is shown in Figure 3.3 (left). Yb ion is in a slightly distorted bicapped square-faced trigonal-prismatic coordination environment made of eight oxygen atoms that arise from three bis-chelating $hfac^-$ anions and one bis-chelating [(**L**)Cu] metalloligand. Magnetochemical studies (Figure 3.3 right) reveal that $\chi_M T$ is slightly decreasing upon cooling from room temperature. This is related to the splitting of the ground-state multiplet of the lanthanide due to the local crystal field and indicates the presence of antiferromagnetic exchange between metal ions.

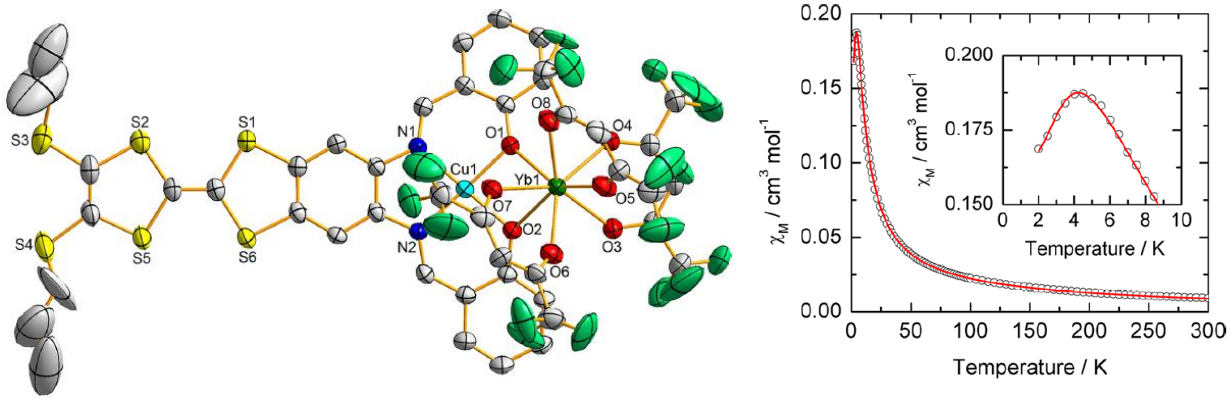

Figure 3.3. The crystalline structure of [(**L**)CuYb(hfac)$_3$] (left) and the temperature dependence of the molar magnetic susceptibility, χ_M of compound 3 with a zoom in the low-temperature range at the inset. The best-fitted curve is represented by the red line.

In 2012 J.-L. Zuo and co-workers have reported the synthesis of Tetrathiafulvalene-Fused π-Extended Schiff base ligands (Figure 3.4), derivative of pyridine and their corresponding transition metal complexes [M(hfac)$_2$(L)$_2$], where M = Cu(II), L = **L1**; M = Mn(II), L = **L1**; M = Cu(II), L = **L2**) and [Re(CO)$_4$(**L3**)][Re$_2$(CO)$_6$Cl$_3$], have been synthesized and structurally characterized[30].

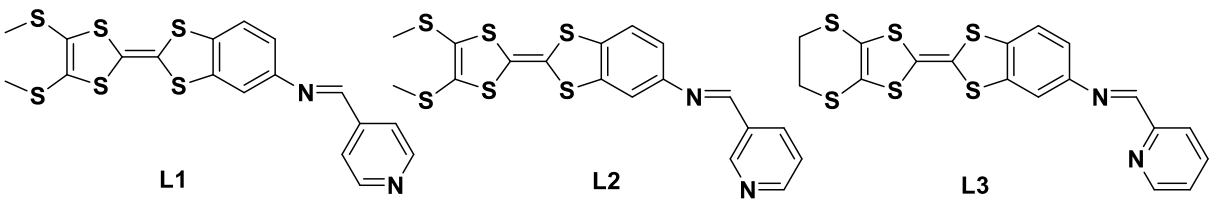

Figure 3.4. Structures of **L1**–**L3**.

The different coordination modes of the metal ions and relative orientation of the terminal N donors result in the different crystalline organization of the complexes in the solid state. Thus, both copper complexes [Cu(hfac)$_2$(**L1**)$_2$] and [Cu(hfac)$_2$(**L2**)$_2$] exhibit similar structural motifs (Figure 3.5), while the crystal packing of these compounds is completely different.

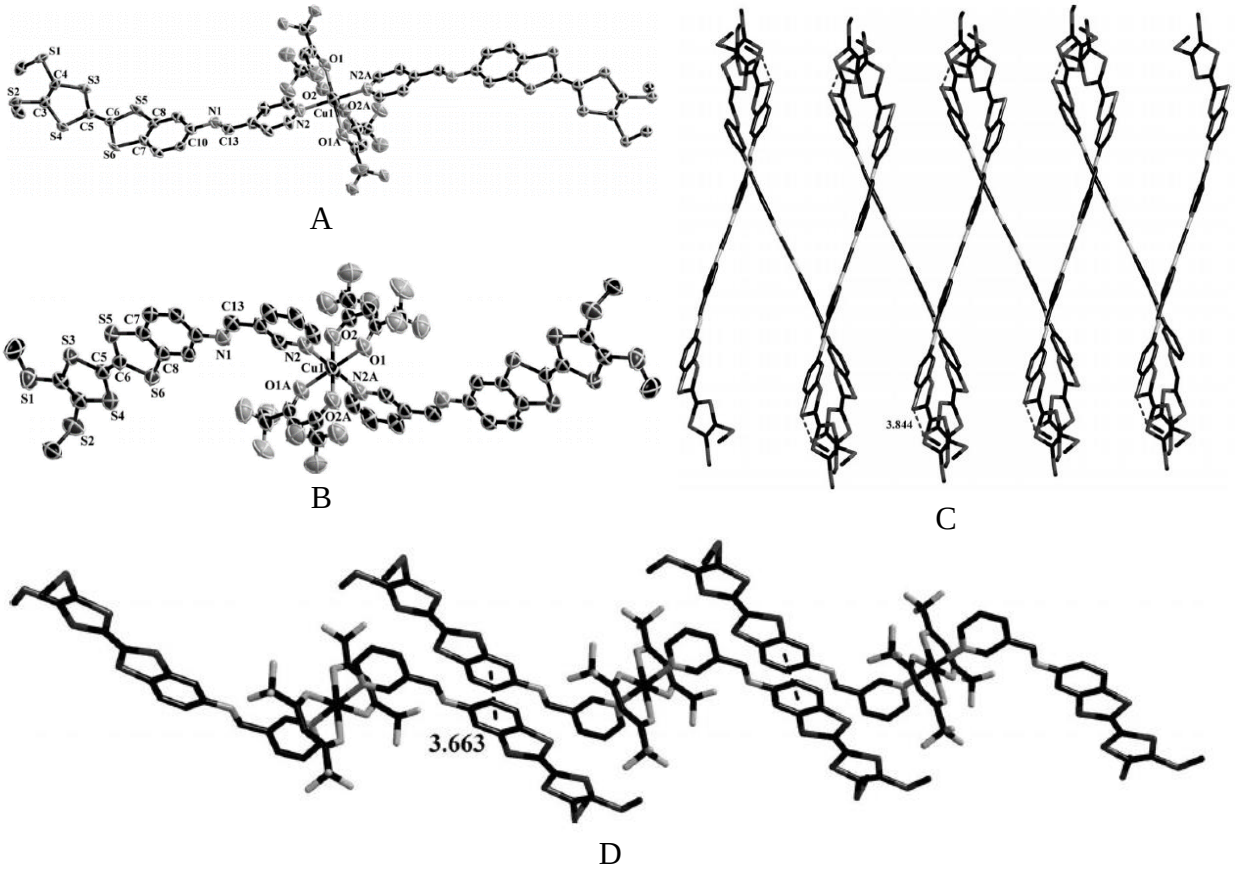

Figure. 3.5. Crystal structure (50% probability displacement ellipsoids, H atoms are omitted for clarity) of [Cu(hfac)$_2$(**L1**)$_2$] (A) with its crystal packing viewed along the *c* axis (C) and crystal structure of [Cu(hfac)$_2$(**L2**)$_2$] (B) and π–π stacking interactions observed along the *a* axis (D) .

In the unit cell of [Cu(hfac)$_2$(**L1**)$_2$] the neighboring molecules are stacked in an overlapping arrangement in a palisade fashion (Figure 3.5 C), while in the solid state of [Cu(hfac)$_2$(**L2**)$_2$] the molecules are face-to-face self-assembled to form a 1D chain-like structure along the *c* axis through short π–π stacking interactions (Figure 3.5 D). The results obtained demonstrate that these new imine-bridged TTF ligands that bear structural diversity are useful for the synthesis and design of new metal complexes.

Another example of electroactive TTF-Schiff base ligand **(TTF$_2$-BisIm-Py**) and its corresponding Zn-complex was reported by our group[26]. The ligand was obtained in a few-step reaction starting with a Stille coupling and followed by the reduction of the NO_2-derivative (Figure 3.6).

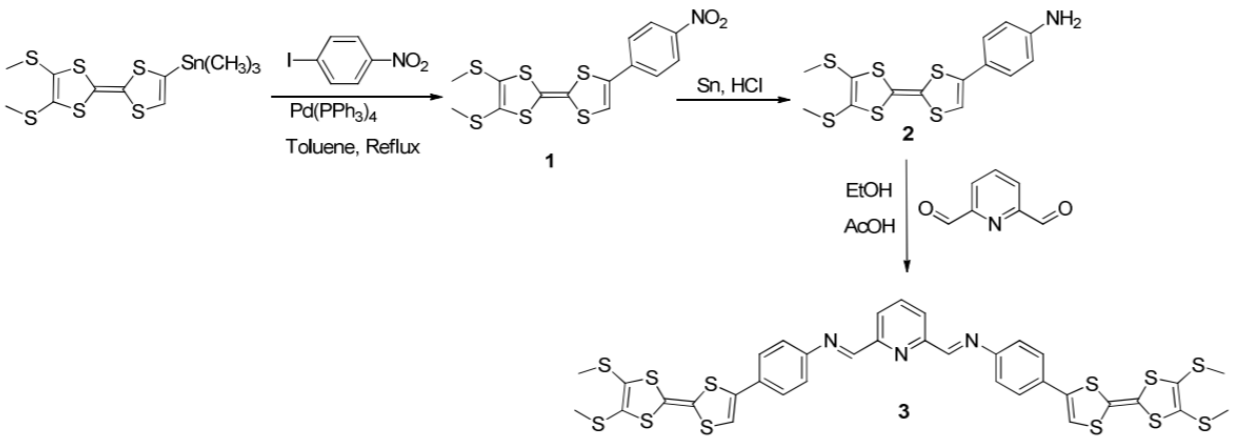

Figure 3.6. Synthesis of the TTF_2-BisIm-Py ligand.

The **TTF_2-BisIm-Py** was treated with zinc chloride ($ZnCl_2$) in a DCM/CH_3CN mixture to afford the [Zn(**TTF_2-BisImPy**)Cl_2] complex (Figure 3.7).

Cyclic voltammetry measurements performed for both the ligand and the Zn-complex show two reversible oxidations waves, which are slightly positively shifted (about 20 mV and 25 mV) for the Zn-complex (compared to the ligand), suggesting that the zinc metal cation is affecting the oxidation potential of the TTF moieties by decreasing the electron density on the TTF moieties. As a consequence of this electrochemical behavior, one can expect that radical cation salts of both compounds form readily upon electrochemical oxidation[8].

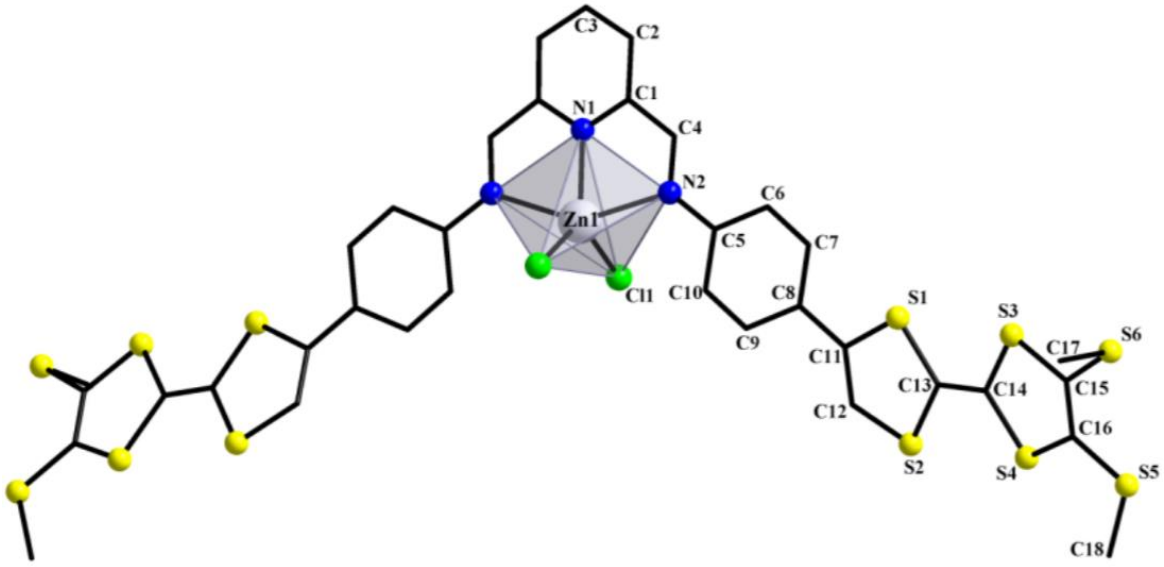

Figure 3.7. The crystalline structure of [Zn(**TTF_2-BisImPy**)Cl_2] with the atoms labeling scheme. Hydrogen atoms were omitted for clarity.

Based on the complex diversity described in the previous chapter by using aminoalcohol Schiff base ligands and also on the grounds of the results reported by combining TTF unit with different moieties we were interested in the introduction of the redox TTF unit with the complexing unit of non-symmetric Schiff base ligands (derivative of salicylaldehyde and aminoalcohols).

3.2. Synthesis and crystal structure of a redox active Schiff base ligand.

The synthesis of the TTF containing ligand **H_2L^{12}** is presented in Figure 3.8.

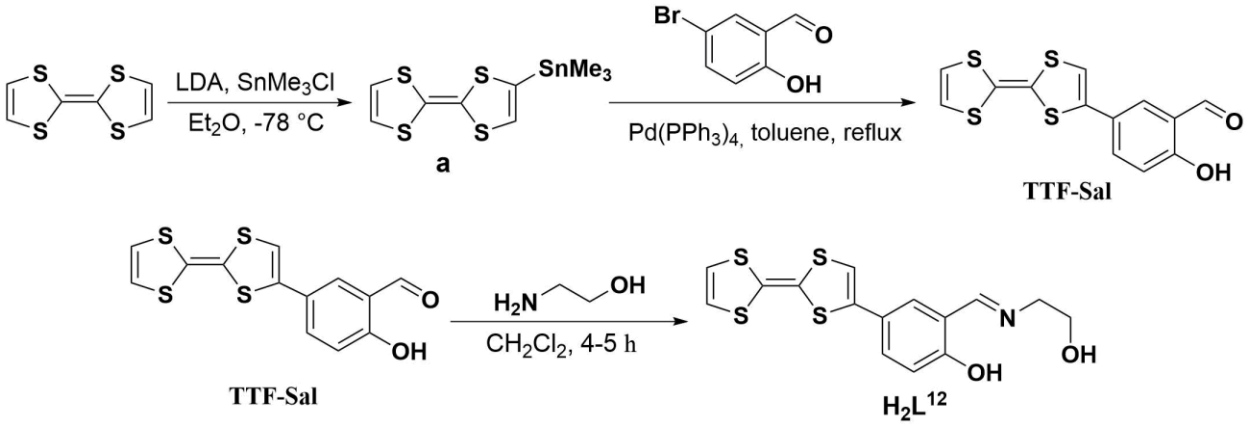

Figure 3.8. Synthesis of the **H_2L^{12}** ligand and **TTF-sal** precursor.

The **H_2L^{12}** ligand was synthesized in three steps by condensation of monoethanolamine with the **TTF-sal** precursor, which was previously isolated and prepared by the Stille coupling[31] between trimethylstannyl-TTF (TTF-$SnMe_3$, **a**)[32] and 5-bromosalicylaldehyde. Both compounds, **TTF-sal** and **H_2L^{12}**, were characterized by standard analysis techniques including single crystal X-ray diffraction analysis.

TTF-sal crystallizes in the centrosymmetric space *Pccn* group of the orthorhombic system, with one independent molecule in the asymmetric unit (Figure 3.9).

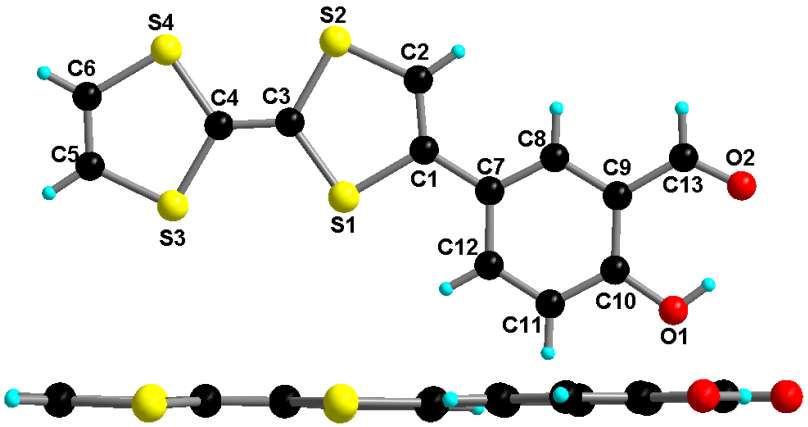

Figure 3.9. Crystalline structure of the **TTF-sal** along with the atom numbering scheme (top); side view emphasizing the planarity of the molecule (bottom).

TTF C=C central bond (C3=C4 1.347(3) Å) and C–S bonds (average of 1.754 Å for the internal C3–S and C4–S bonds) have typical values for neutral donors (Table 3.1).

Table 3.1. Selected distances (Å) of **TTF-sal**.

C1—C2	1.337(3)	C6—S4	1.740(3)
C1—C7	1.473(3)	C7—C12	1.408(3)
C1—S1	1.764(2)	C7—C8	1.387(3)
C2—S2	1.736(2)	C8—C9	1.397(3)
C3—C4	1.347(3)	C9—C10	1.406(3)

C3—S1	1.750(2)	C9—C13	1.455(3)
C3—S2	1.757(2)	C10—C11	1.388(3)
C4—S3	1.754(2)	C10—O1	1.354(3)
C4—S4	1.754(2)	C11—C12	1.375(3)
C5—C6	1.320(4)	C13—O2	1.223(3)
C5—S3	1.739(3)		

The molecule is perfectly planar due to the conjugation between the two units. The molecules pack by establishing intermolecular donor-acceptor interactions along direction *a* and S···S van der Waals interactions along *b* axis as short as 3.64 Å. The shortest intermolecular centroid-centroid distance of donor-acceptor type (Figure 3.10) amounts at 3.612 Å.

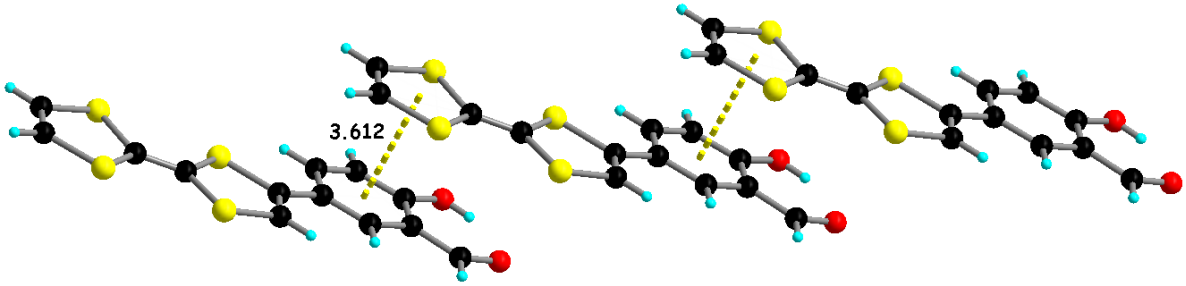

Figure 3.10. Donor-acceptor interactions in the structure of the **TTF-sal**.

The molecules can also associate into hydrogen-bonded centrosymmetric dimers through the formation of a $R^2_2(12)$ motif according to Etter's nomenclature[33], with a O(1)···O(2i) distance of 2.96 Å, besides the recurrent intramolecular hydrogen bonding of the ortho-hydroxy-aldehyde motif (Figure 3.11, Table 3.2). It is obvious, that when taking into account all these interactions that take place in the solid state, the **TTF-sal** donor appears to be a promising precursor for radical cation salts upon electrocrystallization, as the hydrogen bonding donor-acceptor character can be modulated with the oxidation state of TTF[34-35].

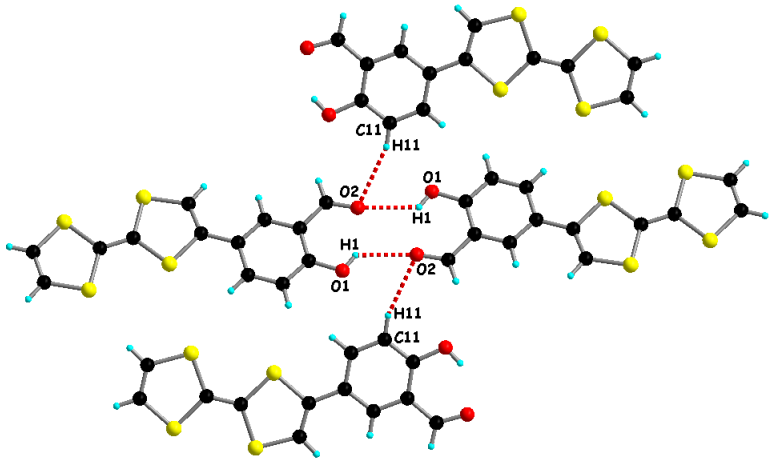

Figure 3.11. Hydrogen bonding interactions in the structure of **TTF-sal**

Table 3.2. Hydrogen bonds parameters for the **TTF-sal**.

d(O···H), Å	**d(A···D) , Å**	**∠ (A-H-D), °**
O(2)···H(1) = 2.36	O(1)···O(2) = 2.96	130
O(2)···H(11) = 2.66	O(2)···C(11) = 3.55	158

The **H_2L^{12}** ligand crystallizes in the monoclinic system, space group $P2_1$, with one independent molecule in the asymmetric unit (Figure 3.12). The molecule is not planar, as there is some deviation of the TTF-fragment from the plane of the aromatic ring. The value of the angle between TTF and the aromatic ring is 20°.

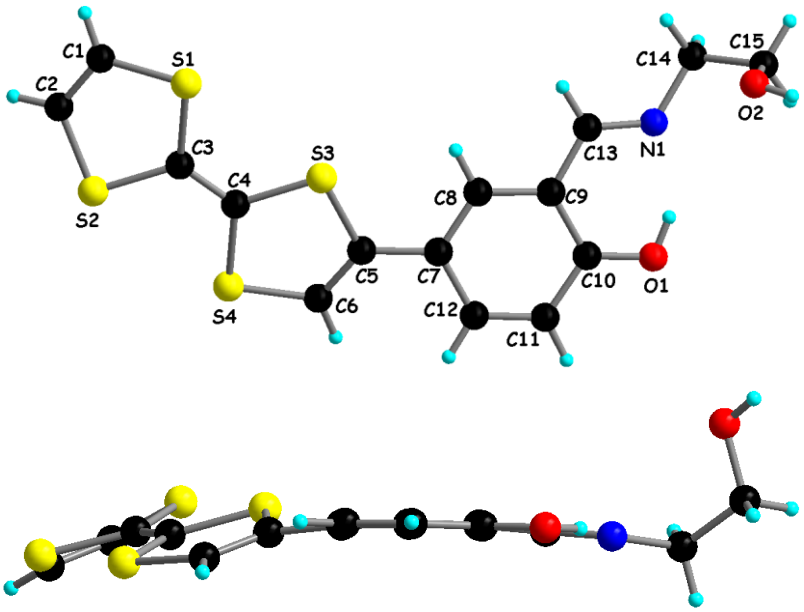

Figure 3.12. Crystalline structure of **H_2L^{12}** along with the atom numbering scheme (top); side view emphasizing the nonplanarity of the molecule (bottom).

The bond distances in the TTF fragment are similar to those in **TTF-sal**. Thus, C=C central bond (C3=C4 1.343(4) Å) and C–S bonds (average of 1.755 Å) are typical of the neutral donors (Table 3.3). Note that there are no particularly short intermolecular distances. The value of the closest S···S distance [3.8982(18) Å] is larger than the sum of the van der Waals radii of the respective atoms [3.6 Å]).

Table 3.3. Selected distances (Å) of **H_2L^{12}**.

C1—C2	1.326(5)	C7—C8	1.375(5)
C1—S1	1.757(3)	C7—C12	1.421(5)
C2—S2	1.745(4)	C8—C9	1.413(4)
C3—C4	1.343(4)	C9—C13	1.416(5)
C3—S1	1.757(4)	C9—C10	1.434(5)
C3—S2	1.757(3)	C10—O1	1.283(4)
C4—S4	1.755(4)	C10—C11	1.426(5)
C4—S3	1.760(3)	C11—C12	1.368(5)
C5—C6	1.339(5)	C13—N1	1.296(4)
C5—C7	1.469(4)	C14—N1	1.463(4)
C5—S3	1.767(4)	C14—C15	1.511(5)
C6—S4	1.740(3)	C15—O2	1.412(4)

The cyclic voltammetry of the ligand **H_2L^{12}** (Figure 3.13) shows the presence of two oxidation waves ($E^1_{1/2}$ = –0.032 V and $E^2_{1/2}$ = +0.379 V).

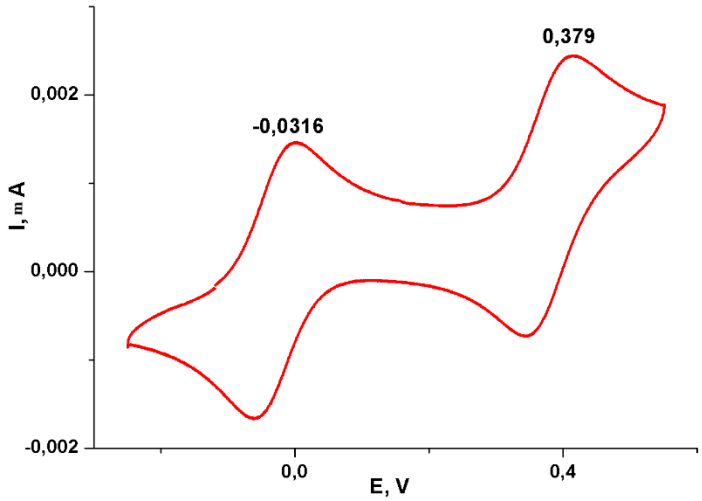

Figure 3.13. Cyclic voltammogram of the ligand $\mathbf{H_2L^{12}}$ (C = $1 \cdot 10^{-4}$ M in DCM) *vs* Fc/Fc^+.

The TTF-Schiff base ligand $\mathbf{H_2L^{12}}$ was reacted with Cu(II) acetate (2:1 stoichiometry) in methanol under moderate heating and a yellow precipitate was formed. Single crystals of the $\mathbf{[Cu(HL^{12})_2]_n}$ complex were grown by the slow diffusion technique starting from its solution in methanol, layered with diethyl ether.

X-ray diffraction analysis revealed that $\mathbf{[Cu(HL^{12})_2]_n}$ crystallizes in the monoclinic system, centrosymmetric space group $P2_1/c$, with half of the independent molecule in the asymmetric unit and the Cu atom on the inversion center (Figure 3.14). The primary coordination motif around the Cu(II) center is formed by two phenolic oxygen atoms O1 [Cu1–O1 = 1.941(1) Å] and two imine N1 atoms [Cu1–N1 = 1.996(1) Å] from two chelating imino-phenolato units within a square planar environment.

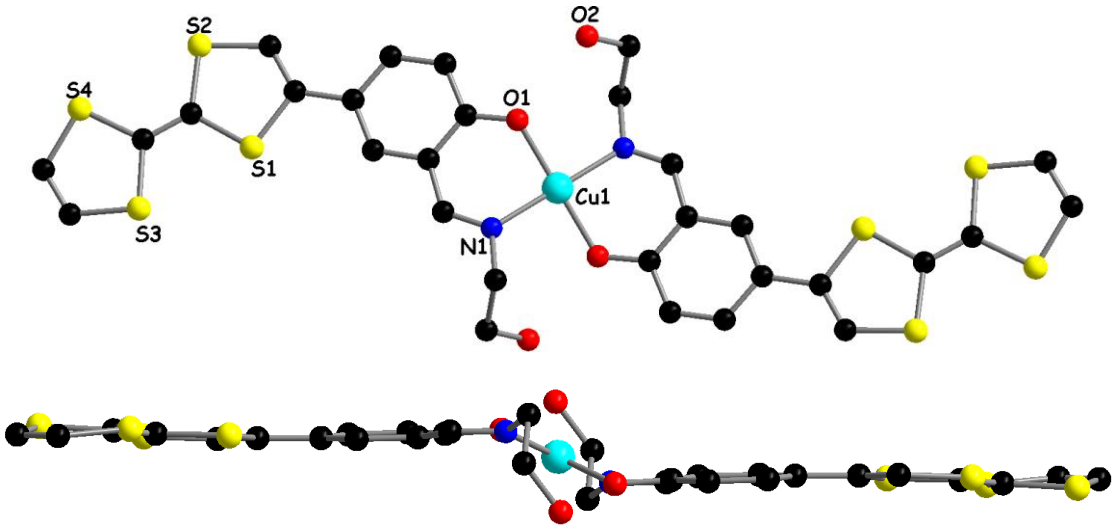

Figure 3.14. Fragment of the crystalline structure of $\mathbf{[Cu(HL^{12})_2]_n}$ with an emphasis on the equatorial coordination environment of the metal (top) and a side view emphasizing the planarity of the ligands and the square planar N_2O_2 motif around the Cu(II) center (bottom).

The planarity of the ligand is preserved in the complex due to the conjugation, while the values for the central C3=C4 bond [1.341 (3) Å] and C–S bonds are in favor of the neutral state of the donor. The two hydroxo oxygen atoms O2 further coordinate one top and one bottom

neighboring Cu atoms in the axial positions, thus leading to the formation of a one-dimensional coordination polymeric chain developing along the *a* direction (Figure 3.15).

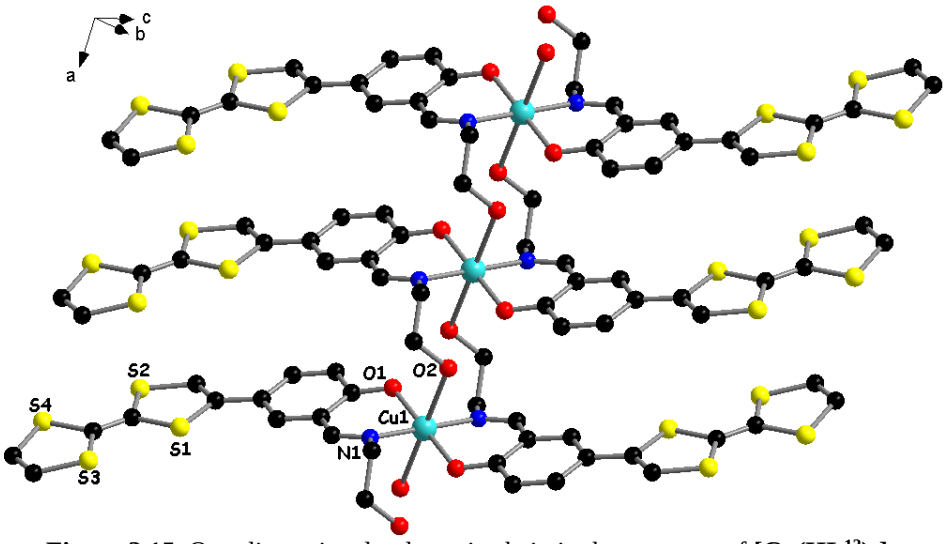

Figure 3.15. One-dimensional polymeric chain in the structure of **[Cu(HL^{12})$_2$]$_n$**.

The cyclic voltammetry of the **[Cu(HL^{12})$_2$]$_n$** complex shows a cathodic shift (compared to the pure **H$_2$L^{12}** ligand, Figure 3.13) of both oxidation waves, *i.e.* $E_1^{1/2}$ = –0.100 V and $E_2^{1/2}$ = +0.355 V, certainly as a consequence of the deprotonation of the phenolic oxygen atoms which induces a slight increase in the electron density on the TTF moieties in spite of the coordination to the Cu(II) ion (Figure 3.16). Very likely, the redox processes in solution characterize the presence of the mononuclear **[Cu(HL^{12})$_2$]** fragment. Such a behavior holds much promise in view of the use of this complex in electrocrystallization experiments towards radical cation salts in which the TTF units have the tendency to pre-organize within one-dimensional chains through OH coordination to Cu(II).

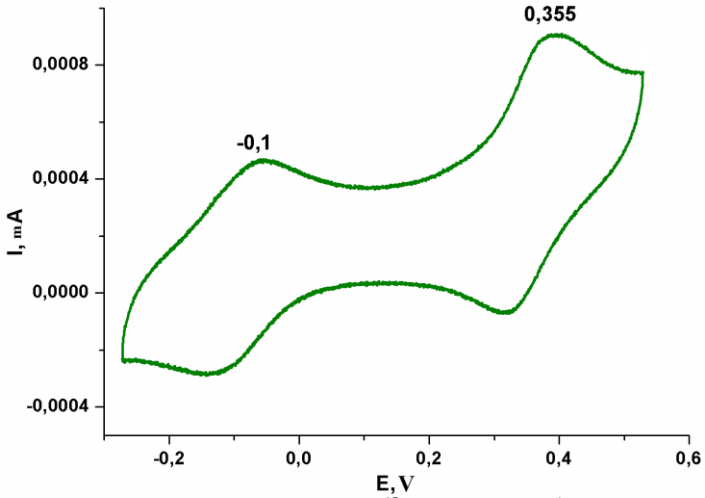

Figure 3.16. Cyclic voltammogram of **[Cu(HL^{12})$_2$]$_n$** (C = 1·10^{-4} M in CH_3CN) *vs* Fc/Fc^+.

It should be noted that the presence of mononuclear fragment **[Cu(HL^{12})$_2$]** in solution provides the additional opportunity to use these compounds as a precursor for the synthesis of heterometallic complexes.

3.3. Radical cation salts.

The synthesis of radical cation salts generally is based on the following redox processes resulting in charge transfer from a donor molecule to acceptor:

$$\text{Donor} - e^- \leftrightarrow \text{donor}^+$$

$$\text{Acceptor} + e^- \leftrightarrow \text{acceptor}^-$$

The main methods for the synthesis of cation-radical salts are chemical[36] and electrochemical[37] oxidation. The latter is widely used nowadays for obtaining highly pure radical cation salts. The redox process itself is based on the electrochemical oxidation of the donor molecules in different polar organic solvents. As a source of anion different electrolytes (*e.g.* $[TBA]PF_6$) can be used.

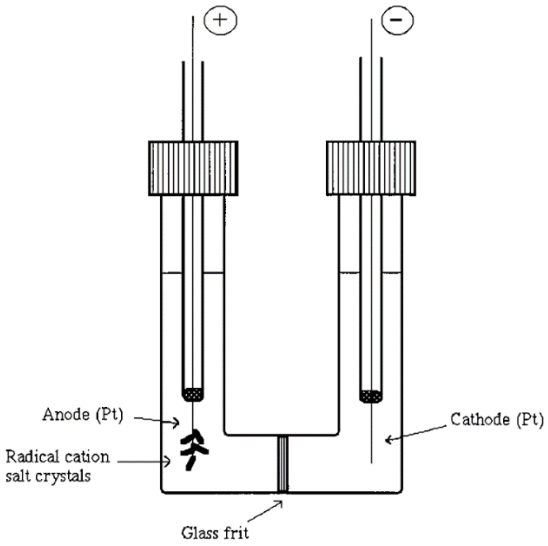

Figure 3.17. An electrocrystallization cell

A typical electrocrystallization cell is given in Figure 3.17. A platinum wire can be used as the working electrode. The choice of the solvent for the electrochemical oxidation process is limited by its ability to dissolve both the organic donor and the electrolyte. For this purpose, a mixture of two or more solvents may be required, but one must keep in mind that ultimately the product of the electro-oxidized species must not be soluble if it is to crystallize[37].

In our case, having the crystal structure of TTF-sal and motivated by its planar conformation and favorable electrochemical behavior, we performed electrocrystallization of this donor which afforded two radical cation salts with the PF_6^- and AsF_6^- anions.

Single crystal X-ray diffraction analysis revealed that the compounds **(TTF-Sal)$_2$PF$_6$** and **(TTF-Sal)$_2$AsF$_6$** are isostructural and crystallize in the monoclinic system with two independent **TTF-Sal** molecules and one corresponding anion in the asymmetric unit (Figure 3.18), indicating the formation of mixed valence species.

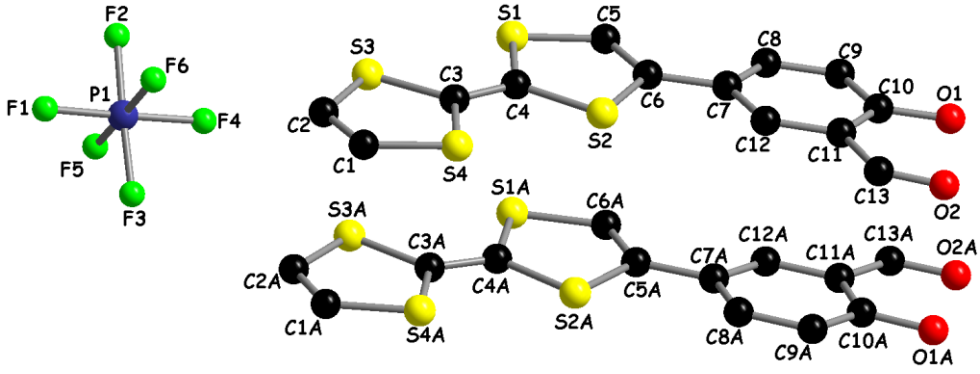

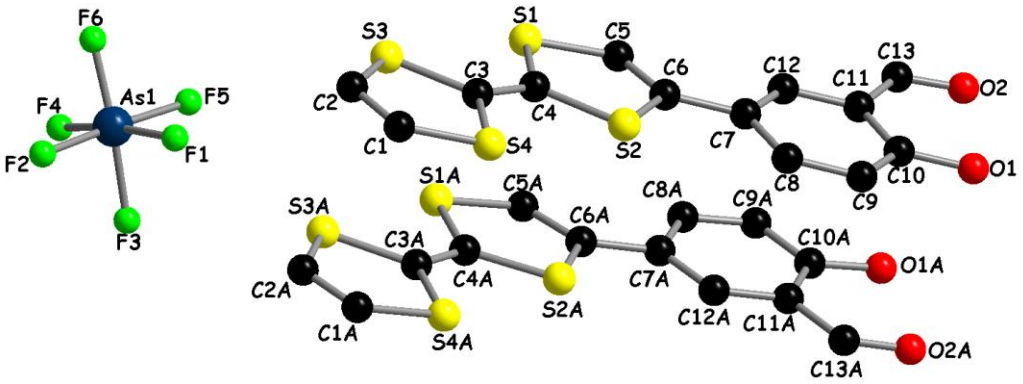

Figure 3.18. Crystalline structure of (**TTF-Sal)$_2$PF$_6$** (top) and (**TTF-Sal)$_2$AsF$_6$** (bottom). Hydrogen atoms were omitted for clarity.

The values of the central C=C bonds for both molecules of the aldehyde [(1.3616(102) and 1.3629(89) Å for (**TTF-Sal)$_2$PF$_6$**; 1.3505(59) and 1.3664(67) Å for (**TTF-Sal)$_2$AsF$_6$**)] and the average value of C–S bonds (1.74 Å) clearly indicate the partial oxidation state of the donors (formal charge is +0.5 for each molecule of the aldehyde) confirming the mixed valence nature of the salts.

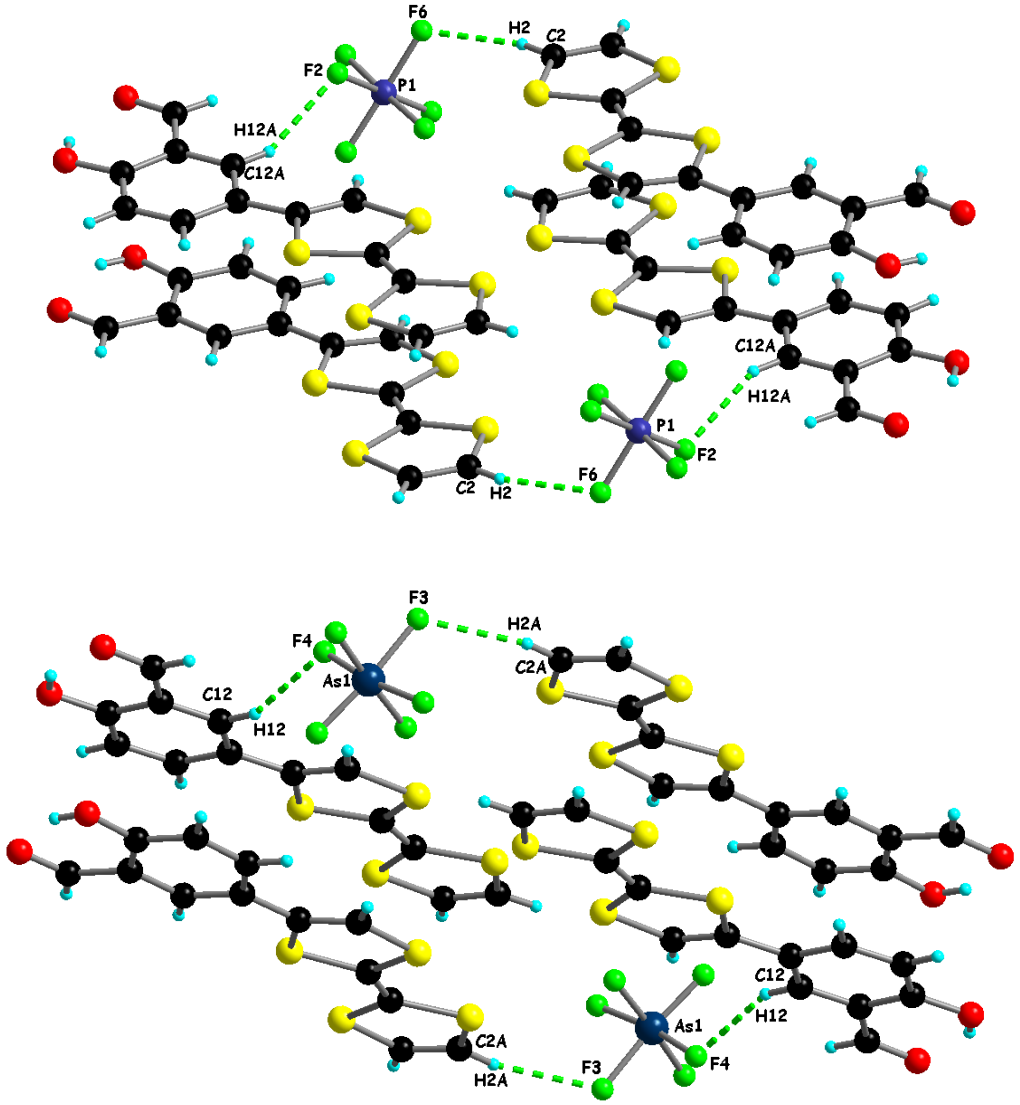

Figure 3.19. Intermolecular hydrogen bonds in crystalline structures of (**TTF-Sal)$_2$PF$_6$** (top) and (**TTF-Sal)$_2$AsF$_6$** (bottom).

The crystalline structures of both radical cation salts are stabilized by hydrogen bonds between the fluorine and hydrogen atoms of the aromatic rings and the TTF moiety (Figure 3.19). Each anion (PF_6^- or AsF_6^-) forms aforementioned contacts with two TTF-$Sal^{+1/2}$ radical cations. The main parameters of the hydrogen bonds are given in Table 3.4.

Table 3.4. Hydrogen bonds parameters for **(TTF-Sal)$_2$PF$_6$** and **(TTF-Sal)$_2$AsF$_6$**.

d(C···F), Å	**d(H···F), Å**	**∠(C–H–F), º**
	(TTF-Sal)$_2$PF$_6$	
C2···F6 = 3.2167(96)	H2···F6 = 2.3351(68)	157.99(45)
C12A···F2 = 3.2605(85)	H12A···F2 = 2.3968(60)	154.261(389)
	(TTF-Sal)$_2$AsF$_6$	
C12···F4 = 3.2230(96)	H12···F4 = 2.3533(86)	155.650(317)
C2A···F3 = 3.2101(114)	H2A···F3 = 2.3750(92)	152.803(473)

In the unit cell of the radical cation salts (Figure 3.20), the molecules of donors form layers where the TTF-sal moieties are packed one above the other, while the anions are located in the voids between the donor's layer.

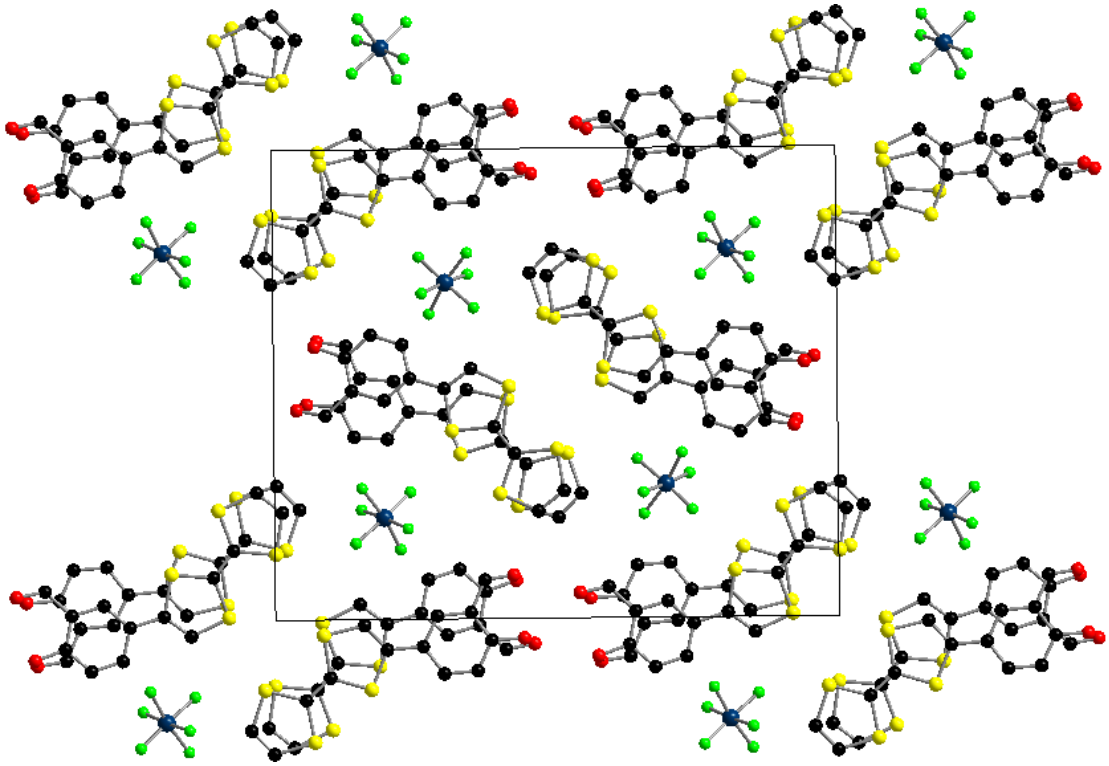

Figure 3.20. Unit cell of **(TTF-Sal)$_2$AsF$_6$**. Hydrogen atoms were omitted for clarity.

Short intermolecular S···S contacts between donor molecules are observed (Figure. 3.21). In the case of the smaller PF_6^- anion, stronger S···S interactions have been observed [<d(S···S)> ≈ 3,52 Å]. The presence of the bulky AsF_6^- anion leads to a higher distortion of the unit cell, consequently increasing the intermolecular S···S distances [<d(S···S)> ≈ 3,67 Å]. According to

the values of the intrastack S···S distances, one can consider that the donors are slightly dimerized along the stack.

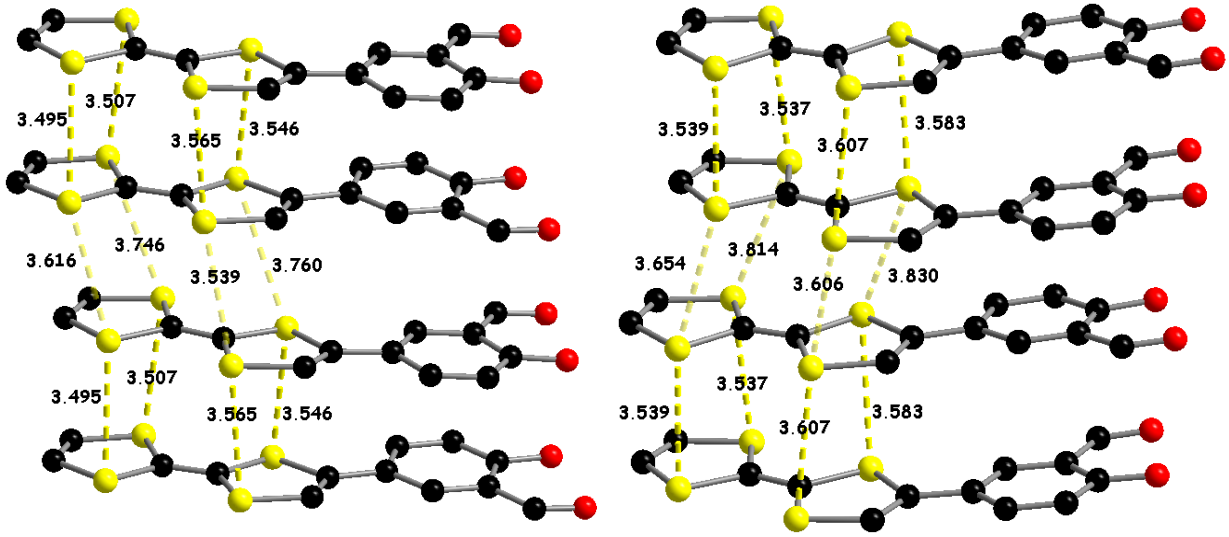

Figure. 3.21. Intermolecular S···S contacts in the crystalline structures of (**TTF-Sal)$_2$PF$_6$** (left) and (**TTF-Sal)$_2$AsF$_6$** (right). Hydrogen atoms together with anions were omitted for clarity.

The temperature dependence of the electrical resistivity ρ for single crystals of (**TTF-Sal)$_2$PF$_6$** and (**TTF-Sal)$_2$AsF$_6$** shows that both of them are semiconductors (Figure 3.22). The room temperature conductivity values are 10 Ohm^{-1}·cm^{-1}. During the experiment, a first order phase transition has been discovered at 160 K (for (**TTF-Sal)$_2$PF$_6$**) and 190 K (for (**TTF-Sal)$_2$AsF$_6$**). Due to this phenomenon, which induced the "explosion" of the crystals, it appeared impossible to obtain lower temperature dependence of the electrical resistivity. Nevertheless, up to 160 K both salts behave as semiconductors.

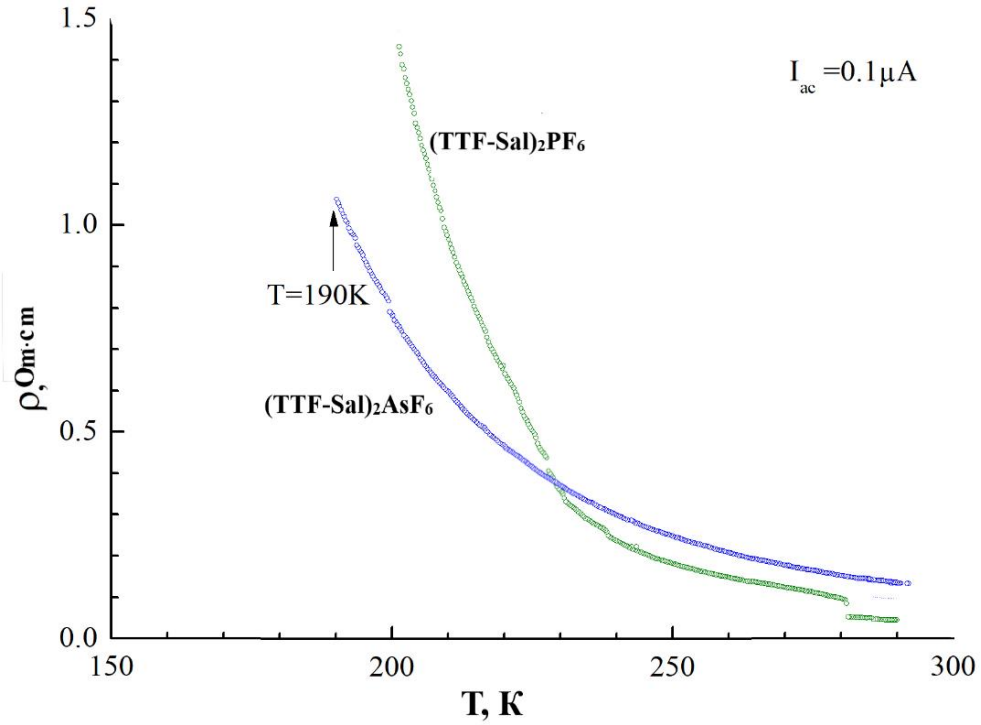

Figure 3.22. The temperature dependence of the electrical resistivity ρ for a single crystal of (**TTF-Sal)$_2$PF$_6$** (green line) and a single crystal of (**TTF-Sal)$_2$AsF$_6$** (blue line).

A comparison of these results can be can be made with the zwitterionic EDT-TTF-amidoglycine (Figure 3.23) (EDT-TTF – ethylenedithiotetrathiafulvalene) described by P. Batail and co-workers[38]. The room temperature conductivity value for this acid is 1 $Ohm^{-1} \cdot cm^{-1}$, which is lower than the one observed for the TTF-sal derivatives.

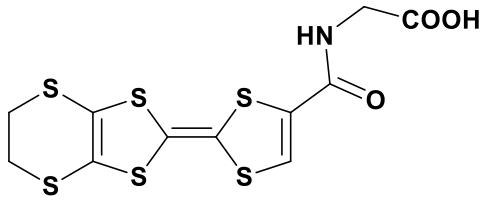

Figure 3.23. The structure of EDT-TTF-amidoglycine.

3.3. Conclusion.

A new TTF-modified Schiff base ligand has been obtained and fully characterized. Its reaction with copper(II) acetate leads to the formation of a homometallic complex, which possesses a polymeric structure. The cyclic voltammograms of the ligand and the complex indicate the excellent electron donating property of these compounds. The synthesis of TTF-salicylaldehyde, which was used as a precursor for the preparation of the TTF-Schiff base ligand, has been described. Electrocrystallization experiment allows us to isolate crystals of two radical cation salts. The temperature dependence of the electrical resistivity for these salts is indicative of a semiconducting behavior.

References

1. Canevet, D.; Sallé, M.; Zhang, G.; Zhang, D.; Zhu, D., *Chem. Commun.* **2009**, 2245-2269.

2. Lorcy, D.; Bellec, N.; Fourmigué, M.; Avarvari, N., *Coord. Chem. Rev.* **2009,** *253*, 1398-1438.

3. Avarvari, N.; Martin, D.; Fourmigué, M., *J. Organomet. Chem.* **2002,** *643-644*, 292-300.

4. Avarvari, N.; Fourmigué, M., *Chem. Commun.* **2004,** *11*, 1300-1301.

5. Devic, T.; Batail, P.; Fourmigué, M.; Avarvari, N., *Inorg. Chem.* **2004,** *43*, 3136-3141.

6. Gouverd, C.; Biaso, F.; Cataldo, L.; Berclaz, T.; Geoffroy, M.; Levillain, E.; Avarvari, N.; Fourmigué, M.; Sauvage, F. X.; Wartelle, C., *PCCP* **2005,** *7*, 85-93.

7. Avarvari, N.; Kiracki, K.; Llusar, R.; Polo, V.; Sorribes, I.; Vicent, C., *Inorg. Chem.* **2010,** *49*, 1894-1904.

8. Setifi, F.; Ouahab, L.; Golhen, S.; Yoshida, Y.; Saito, G., *Inorg. Chem.* **2003,** *42*, 1791-1793.

9. Liu, S.-X.; Dolder, S.; Franz, P.; Neels, A.; Stoeckli-Evans, H.; Decurtins, S., *Inorg. Chem.* **2003,** *42*, 4801-4803.

10. Devic, T.; Avarvari, N.; Batail, P., *Chem. Eur. J.* **2004,** *10*, 3697-3707.

11. Gavrilenko, K. S.; Gal, Y. L.; Cador, O.; Golhen, S.; Ouahab, L., *Chem. Commun.* **2007,** *3*, 280-282.

12. Geng, Y.; Wang, X.-J.; Chen, B.; Xue, H.; Zhao, Y.-P.; Lee, S.; Tung, C.-H.; Wu, L.-Z., *Chem. Eur. J.* **2009,** *15*, 5124-5129.

13. Liu, S.-X.; Ambrus, C.; Dolder, S.; Neels, A.; Decurtins, S., *Inorg. Chem.* **2006,** *45*, 9622-9624.

14. Branzea, D. G.; Fihey, A.; Cauchy, T.; El-Ghayoury, A.; Avarvari, N., *Inorg. Chem.* **2012,** *51*, 8545-8556.

15. Nazarenko, I.; Pop, F.; Sun, Q.; Hauser, A.; Lloret, F.; Julve, M.; El-Ghayoury, A.; Avarvari, N., *Dalton Trans.* **2015,** *44*, 8855-8866.

16. Pop, F.; Ding, J.; Daku, L. M. L.; Hauser, A.; Avarvari, N., *RSC Advances* **2013,** *3*, 3218-3221.

17. Réthoré, C.; Fourmigué, M.; Avarvari, N., *Chem. Commun.* **2004**, 1384-1385.

18. Madalan, A. M.; Réthoré, C.; Avarvari, N., *Inorg. Chim. Acta* **2007,** *360*, 233-240.

19. Riobé, F.; Avarvari, N., *Coord. Chem. Rev.* **2010,** *254*, 1523-1533.

20. Liu, W.; Xiong, J.; Wang, Y.; Zhou, X.-H.; Wang, R.; Zuo, J.-L.; You, X.-Z., *Organometallics* **2009,** *28*, 755-762.

21. Nihei, M.; Takahashi, N.; Nishikawa, H.; Oshio, H., *Dalton Trans.* **2011,** *40*, 2154-2156.

22. Li, G.-N.; Liao, Y.; Jin, T.; Li, Y.-Z., *Inorg. Chem. Commun.* **2013,** *35*, 27-30.

23. Biet, T.; Cauchy, T.; Avarvari, N., *Chem. Eur. J.* **2012,** *18*, 16097-16103.

24. Biet, T.; Avarvari, N., *Organic & Biomolecular Chemistry* **2014,** *12*, 3167-3174.

25. Biet, T.; Avarvari, N., *CrystEngComm* **2014,** *16*, 6612-6620.

26. Nita, G.; Branzea, D.; Pop, F.; El-Ghayoury, A.; Avarvari, N., *Crystals* **2012,** *2*, 338.

27. Cui, L.; Ge, J.-y.; Leong, C. F.; D'Alessandro, D. M.; Zuo, J.-L., *Dalton Trans.* **2017,** *46*, 3980-3988.

28. Wu, J.-C.; Liu, S.-X.; Keene, T. D.; Neels, A.; Mereacre, V.; Powell, A. K.; Decurtins, S., *Inorg. Chem.* **2008,** *47*, 3452-3459.

29. Cosquer, G.; Pointillart, F.; Le Guennic, B.; Le Gal, Y.; Golhen, S.; Cador, O.; Ouahab, L., *Inorg. Chem.* **2012,** *51*, 8488-8501.

30. Qin, J.; Qian, C.-X.; Zhou, N.; Zhu, R.-M.; Li, Y.-Z.; Zuo, J.-L.; You, X.-Z., *Eur. J. Inorg. Chem.* **2012,** *2012*, 234-245.

31. Cordovilla, C.; Bartolomé, C.; Martínez-Ilarduya, J. M.; Espinet, P., *ACS Catal.* **2015,** *5*, 3040-3053.

32. Riobé, F.; Avarvari, N.; Grosshans, P.; Sidorenkova, H.; Berclaz, T.; Geoffroy, M., *PCCP* **2010,** *12*, 9650-9660.

33. Etter, M. C., *Acc. Chem. Res.* **1990,** *23*, 120-126.

34. Baudron, S. A.; Avarvari, N.; Canadell, E.; Auban-Senzier, P.; Batail, P., *Chem. Eur. J.* **2004,** *10*, 4498-4511.

35. Murata, T.; Morita, Y.; Yakiyama, Y.; Fukui, K.; Yamochi, H.; Saito, G.; Nakasuji, K., *J. Am. Chem. Soc.* **2007,** *129*, 10837-10846.

36. Akamatu, H.; Inokuchi, H.; Matsunaga, Y., *Nature* **1954,** *173*, 168.

37. Batail, P.; Boubekeur, K.; Fourmigué, M.; Gabriel, J.-C. P., *Chem. Mater.* **1998,** *10*, 3005-3015.

38. El-Ghayoury, A.; Mézière, C.; Simonov, S.; Zorina, L.; Cobián, M.; Canadell, E.; Rovira, C.; Náfrádi, B.; Sipos, B.; Forró, L.; Batail, P., *Chem. Eur. J.* **2010,** *16*, 14051-14059.

CHAPTER IV

DITHIOLENE SCHIFF BASE COMPLEXES

4.1. Introduction

The wide interest of the metal dithiolene complexes is related to the ‘‘non-innocent” character of the dithiolene ligands[1], as there is a strong mixing of the ligand and metal contributions in the frontier orbitals in these systems, thus making the ligand an active partner in the reactivity and the redox processes. The vast majority of the work in this field has been focused upon simple monometallic systems. More recently, some effort has been directed at the synthesis of bimetallic dithiolene complexes with the idea that the properties that have attracted so much attention in monometallic systems may be enhanced, or perhaps to some degree tailored, in a metal dithiolene complex containing two or more metal atoms. Indeed, the works dedicated to the multimetallic dithiolene compounds are not numerous.

One of the first convergent approach (Figure 4.1) to the synthesis of multimetallic dithiolene complexes was proposed by J. P. Donahue[2].

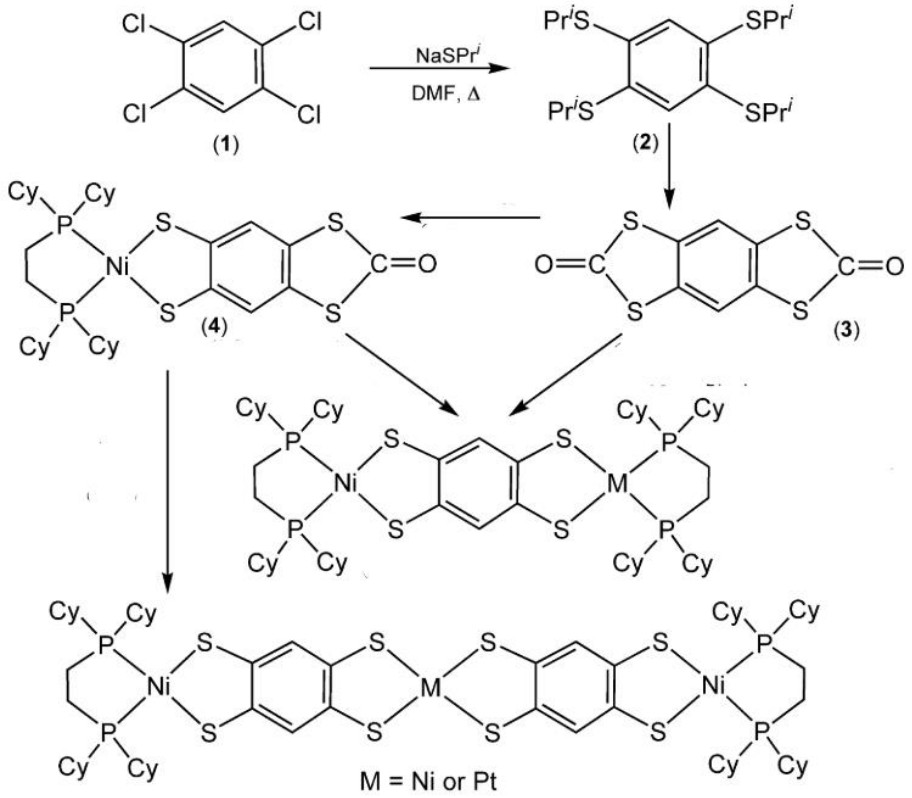

Figure 4.1. Synthesis of di- and trimetallic complexes with 1,2,4,5-benzenetetrathiolate (Cy – cyclohexyl; X – Halide)

Following the route, beginning with tetrachlorobenzene (**1**) and proceeding through **2**, large amounts of 1,3,5,7-tetrathia-*s*-indacene-2,6-dione (**3**) were obtained. The 1,3-dithiol moieties in molecule **3** are readily unmasked by base hydrolysis to liberate one or both of the arene-1,2-

dithiolate chelates resulting in the formation of the mononuclear Ni complex **4** (monodeprotection). The variation of the molar ratio creates the additional opportunity to isolate the bi- or trinuclear homo- and heterometallic dithiolene compounds. Later on, this work was continued by the same research team[3].

Another example of the peculiarity of dithiolene complexes was demonstrated by R. Kato[4]. The compound $[Mn(5\text{-}MeOsaltmen)(acetone)]_2[Ni(dmit)_2]_6$ (figure 4.2) was obtained using electrocrystallization and it can be considered as a hybrid material in which the magnetic properties are combined with the conductivity.

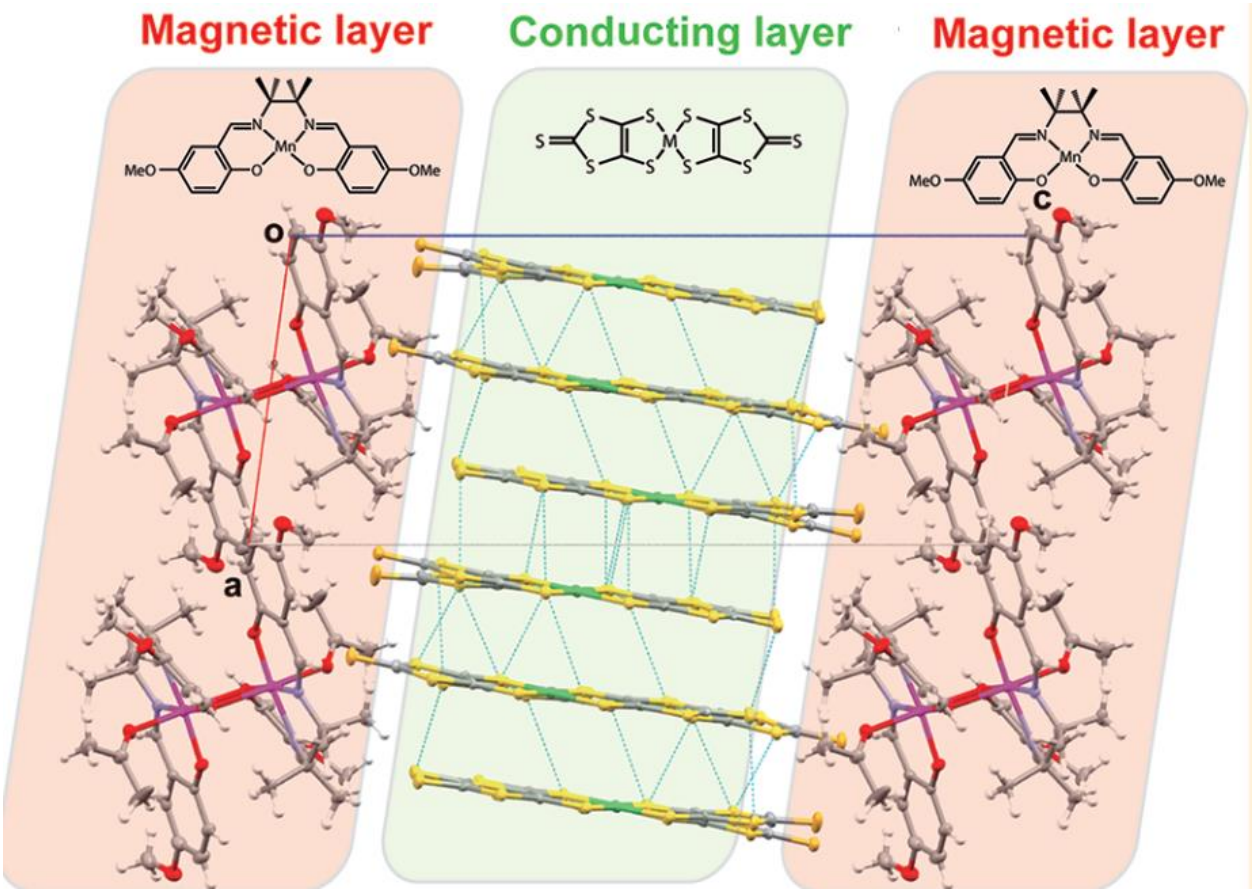

Figure 4.2. The crystal structure of $[Mn(5\text{-}MeOsaltmen)(acetone)]_2[Ni(dmit)_2]_6$, where 5-MeOsaltmen^{2-} = N,N′-(1,1,2,2-tetramethylethylene)*bis*(5-methoxysalicylideneiminate) and dmit^{2-} = 2-thioxo-1,3-dithiole-4,5-dithiolate)[4].

The slow relaxation of the magnetization was observed in Mn-containing moieties with the Schiff base ligand, while the $Ni(dmit)_2$ fragment was "responsible" for the conducting properties of this material.

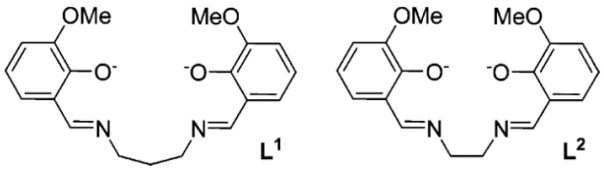

Figure 4.3. Schiff base ligands

One more direction in the coordination chemistry of dithiolene complexes was developed by M. Andruh and N. Avarvari[5]. The main idea was to synthesize 3*d*-4*f* heterospin systems, where, due to the presence

of Ln ions, the magnetic interaction can be strengthened, followed by combining these fragments with the dithiolene moiety. The series of heterotrimetallic Cu-Ln-Ni complexes were obtained using the electrocrystallization technique. The cyclic Schiff base ligands, *i.e.* derivatives of *o*-vaniline (Figure 4.3), were chosen to isolate the heterobimetallic Cu-Ln species which further crystallized together with $[Ni(mnt)_2]^{q-}$ (q = 1, 2; mnt – maleonitriledithiolate). The complexes thus obtained possess ferromagnetic interaction between Cu-Ln and slow relaxation of the magnetization, indicative of a SMM behavior. The crystal structure of the isolated compounds is similar to that of the hybrid material described by R. Kato (see above). As an example, the crystal packing of $[\{(CH_3OH)CuL^2\}\{CuL^2\}Gd(O_2NO)\{Ni(mnt)_2\}][Ni(mnt)_2]\cdot CH_2Cl_2$ (**C1**) is shown in Figure 4.4.

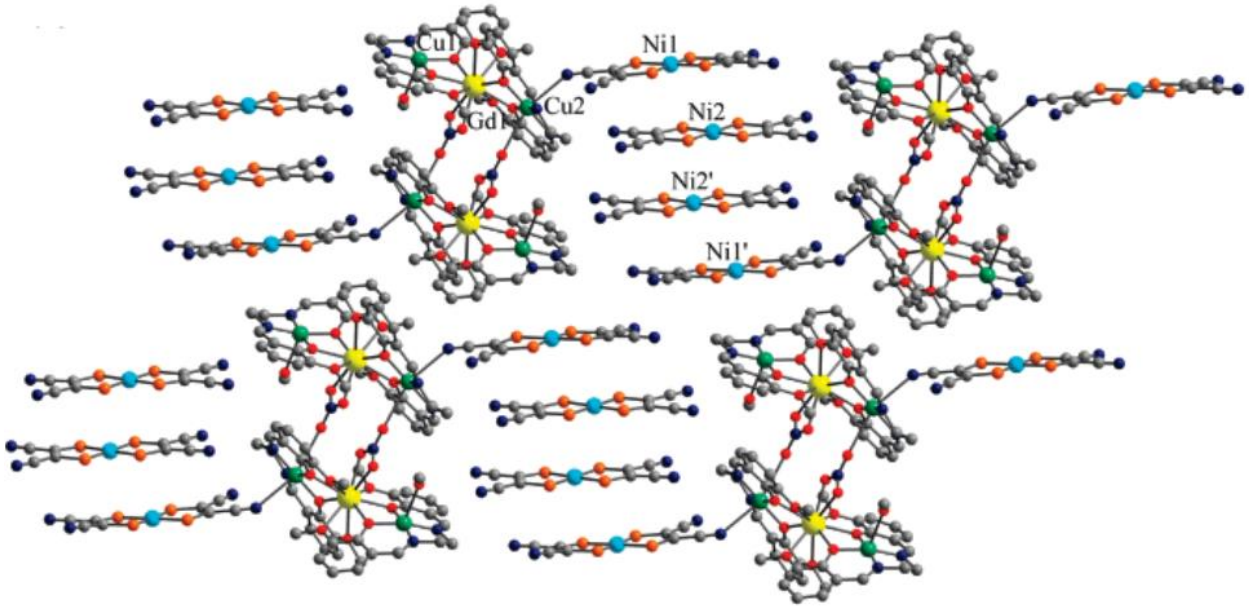

Figure 4.4. A packing diagram for compound **C1**, showing the association of the $[Ni(mnt)_2]^-$ ions into supramolecular tetramers.

The cationic species are constructed from two $[Cu_2Gd]$ moieties bridged by two nitro groups, while the $[Ni(mnt)_2]^-$ units are stacked in tetramers, with semi-coordinated anions embracing the uncoordinated ones.

Analyzing the literature, one may notice that the majority of the examples of multinuclear dithiolene complexes contain semi- or well-separated metal-ligand moieties, which are not linked through covalent bonds. The ligands and their corresponding complexes described by J. P. Donahue[2-3] are promising for the synthesis of heterometallic dithiolene complexes, yet the presence of only S- and P-donor atoms significantly limits the variety of metals that can be used for the complexation. Therefore, the synthesis of new multifunctional ligands and their complexes, where different properties such as magnetism and conductivity can be combined, is of particular interest.

In order to provide the opportunity to obtain multimetallic dithiolene complexes with a large variety of transition metals, a hybrid Schiff base dithiolene ligand, possessing a N_2O_2-chelating pocket, has been obtained.

4.2. Synthesis and crystal structures of the ligand and its corresponding homometallic complexes.

Synthesis of the new modified Schiff base ligand **H_2L^{13}** was done starting from the precursor 4,5-dibromobenzene-1,2-diamine (figure 4.5), which can be easily prepared at large scale according to the literature procedure[6].

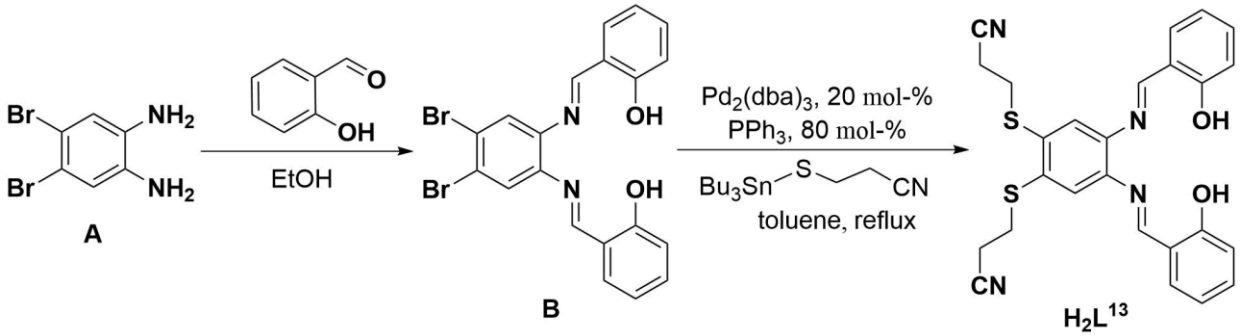

Figure 4.5. Synthetic route to the ligand **H_2L^{13}**.

The Schiff base precursor (**B**) was obtained by condensation reaction, in almost quantitive yield, between precursor **A** and salicylaldehyde. The stannyl-based reagent was prepared in two step reaction, according to the optimized synthetic procedure[7] shown in Figure 4.6.

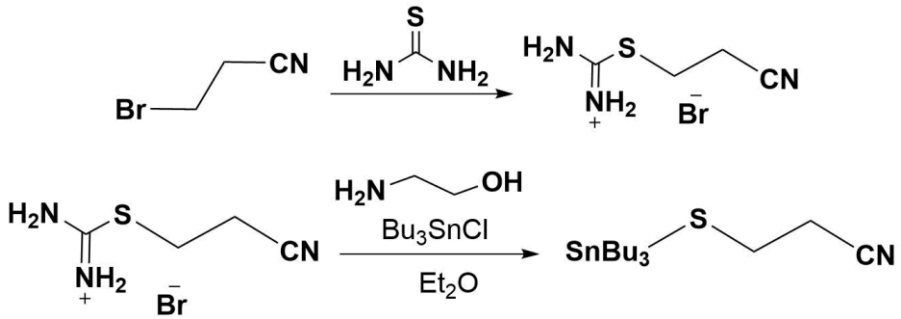

Figure 4.6. Synthesis of 3-((tributylstannyl)thio)propanenitrile.

Ligand **H_2L^{13}** was then prepared by the Stille coupling reaction[8] between **B** and the stannyl-derivative in toluene, in the presence of the Pd-catalyst. Single crystals, suitable for X-Ray analysis, were obtained by slow diffusion of diethyl ether into a solution of **H_2L^{13}** in chloroform. The compound crystallizes in the triclinic system with one independent molecule in the unit cell (Figure 4.7). The molecule itself is not planar. The central benzene fragment, one of the 3-thiopropanenitrile group are located in one plane together with the salicylaldehyde moiety, while the second thiopropanenitrile group together with the other Schiff base part are located in another plane. The value of the angle between these planes is 47°.

The main bond distances are given in table 4.1.

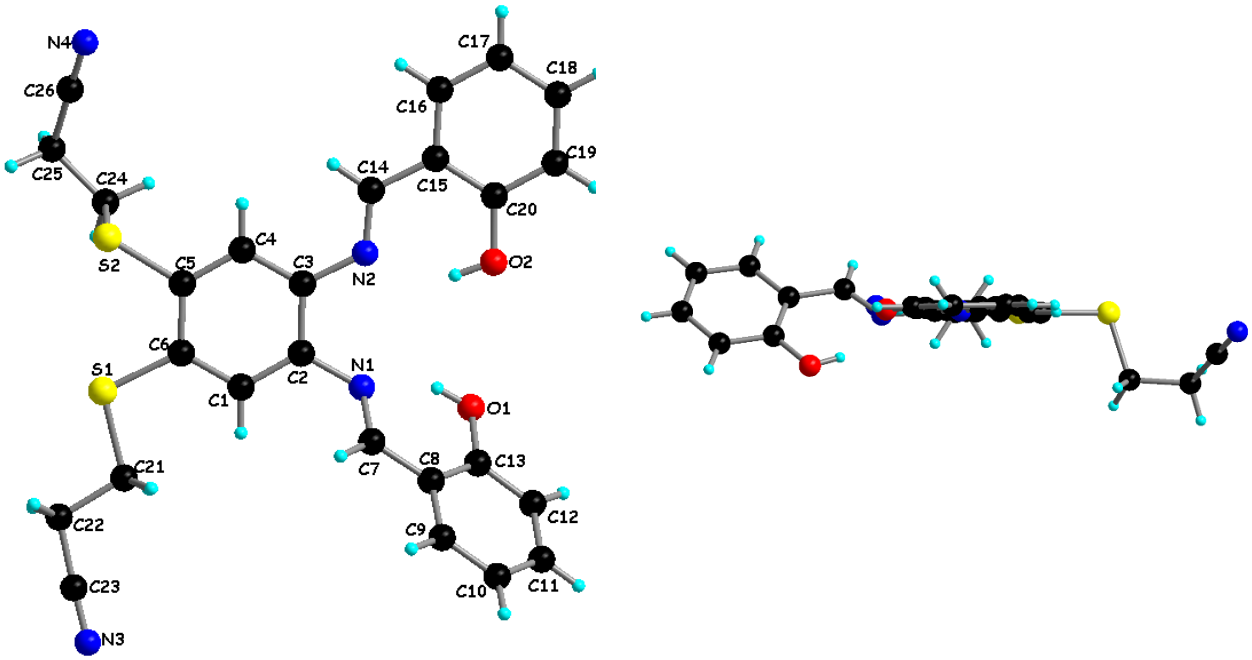

Figure 4.7. The crystal structure of the H_2L^{13} ligand (left) and its lateral view (right).

Table 4.1. Selected distances (Å) of H_2L^{13}.

C1—C6	1.3927(19)	C13—O1	1.349(2)
C1—C2	1.394(2)	C14—N2	1.282(2)
C2—C3	1.4055(19)	C14—C15	1.450(2)
C2—N1	1.4107(17)	C15—C16	1.398(2)
C3—C4	1.3981(19)	C15—C20	1.411(2)
C3—N2	1.4079(18)	C16—C17	1.375(2)
C4—C5	1.385(2)	C17—C18	1.391(2)
C5—C6	1.406(2)	C18—C19	1.382(2)
C5—S2	1.7773(14)	C19—C20	1.392(2)
C6—S1	1.7625(14)	C20—O2	1.3460(18)
C7—N1	1.2836(19)	C21—C22	1.531(2)
C7—C8	1.4539(19)	C21—S1	1.8105(15)
C8—C9	1.399(2)	C22—C23	1.463(2)
C8—C13	1.406(2)	C23—N3	1.142(2)
C9—C10	1.381(2)	C24—C25	1.530(2)
C10—C11	1.378(3)	C24—S2	1.8165(16)
C11—C12	1.384(3)	C25—C26	1.458(3)
C12—C13	1.397(2)	C26—N4	1.138(3)

In the unit cell of H_2L^{13} there are no additional intermolecular interactions, the molecules being well separated from each other (Figure 4.8).

The series of monometallic complexes with the corresponding ligand were isolated, using the known synthetic procedure[9-14].

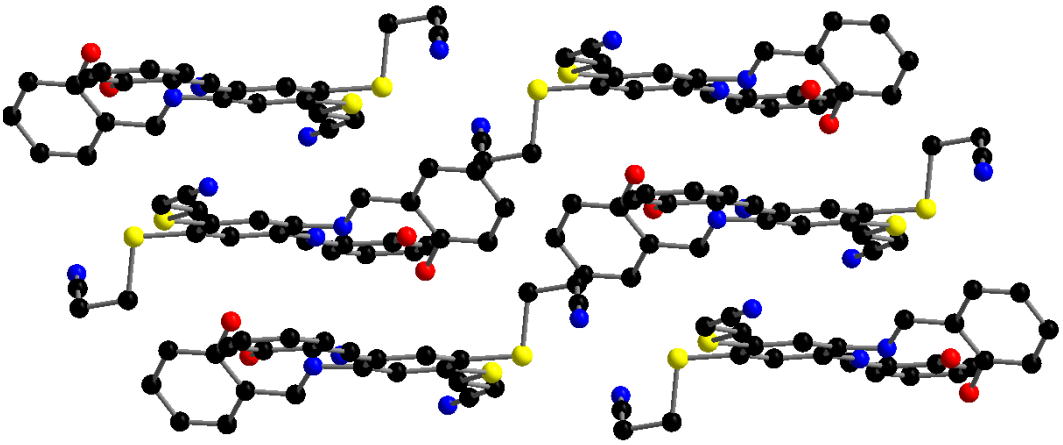

Figure 4.8. The unit cell of **H_2L^{13}**.

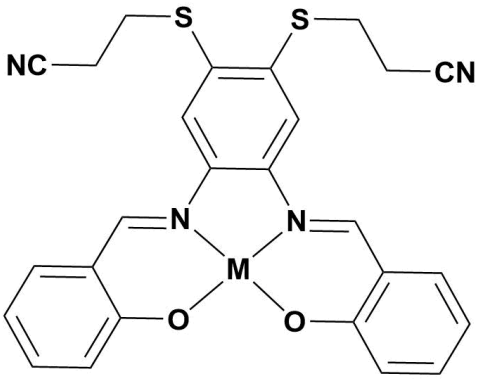

Figure. 4.9. Structure of homometallic complexes with **H_2L^{13}**.

The reaction of metal acetates (M = Cu^{+2}, Ni^{+2}, Zn^{+2}) with **H_2L^{13}** resulted in the formation of mononuclear metal complexes (Figure 4.9). The composition of these complexes was determined by elemental analysis and MALDI-TOF. In the case of Cu(II) complex single crystal X-Ray diffraction analysis has been performed.

The homometallic compound $[CuL^{13}]\cdot 0.5CH_3OH$ (**14**) crystallizes in the monoclinic system together with the molecule of solvent (Figure 4.10). It should be noted that the coordination of the metal ion can influence the geometry of the ligand – all the aromatic system is located in the same plane, while the two 3-thiopropanenitrile groups are outside of the plane.

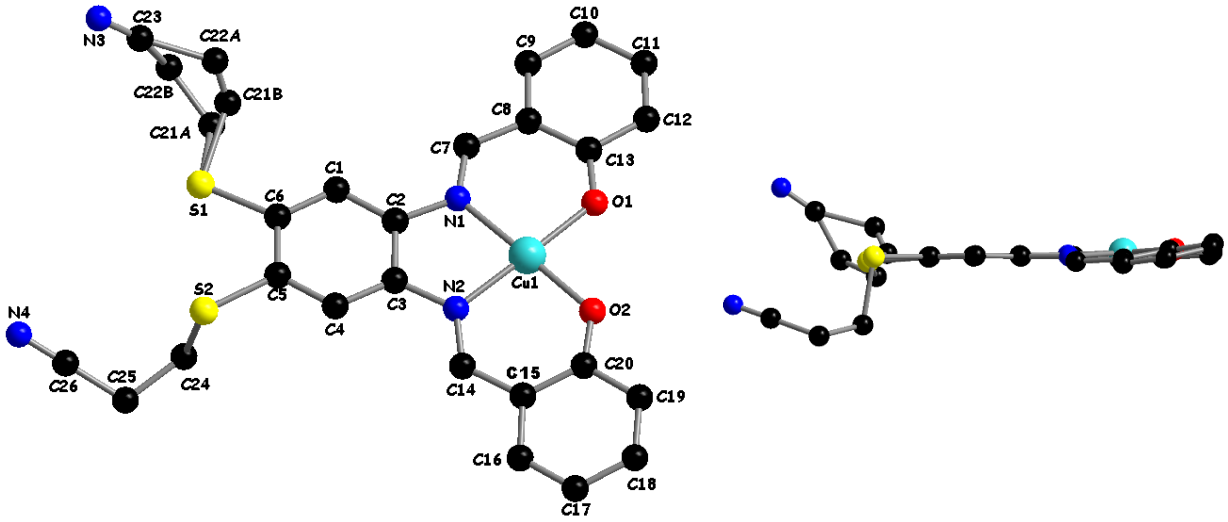

Figure. 4.10. The crystal structure of the $[CuL^{13}]\cdot 0.5CH_3OH$ **14** together with the atoms labeling (left) and its lateral view (right). Hydrogen atoms and solvent molecule were omitted for clarity.

Copper(II) ion possesses almost perfect square-planar coordination environment. The bond lengths Cu–O and Cu–N are 1.8932(25), 1.8909(22) Å; 1.9406(23), 1.9567(25) Å, respectively. The O–Cu–O(N)$_{cis}$ bond angles vary from 84.108(99)° to 94.046(98)°, while O–Cu–O(N)$_{trans}$ angles have almost identical values 177.612(99) and 177.868(95)°. The structural characteristics listed are similar to those of the complexes with the cyclic Schiff base ligands reported earlier in the literature[15-17].

4.3. Synthesis and crystal structure of the dithiolene complexes.

The mononuclear copper and nickel complexes were used as a metaloligand for the synthesis of homometallic trinuclear dithiolene complexes. Figure 4.11 illustrates the general steps for the preparation of these compounds.

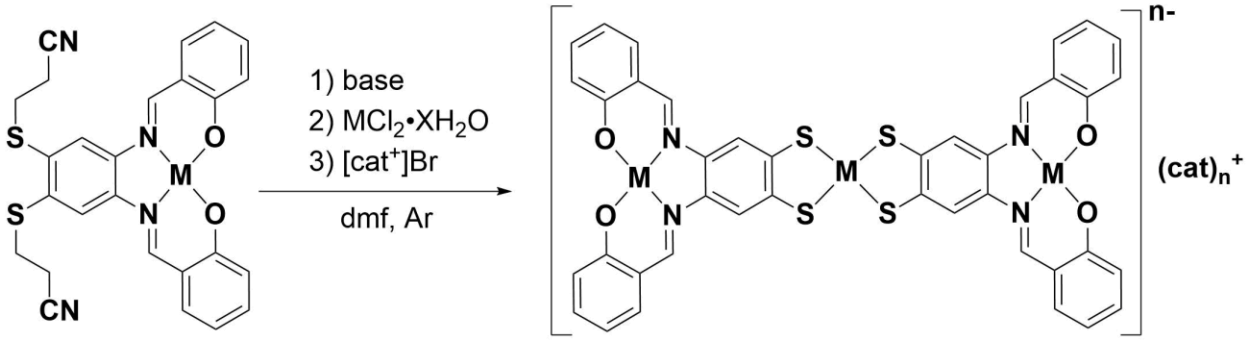

Figure 4.11. Synthesis of dithiolene complexes **15** (M – Ni, cat$^+$ – TBA) and **16** (M – Cu, cat$^+$ – TBA), **17** (M – Ni, cat$^+$ – PPh_4) and **18** (M – Cu, cat$^+$ – PPh_4).

The synthesis of these complexes is a three step reaction. The first step is the deprotection of thiopropanenitrile group in the presence of a base in dmf solution under argon atmosphere. Tetrabutylammonium hydroxide has been chosen as a base and a source of counter-ions in the final isolation of the metal complexes. The formation of dithiolate anion takes place directly after the addition of the base into the reaction mixture and a color change of the solution was observed. The addition of Nickel or Copper chloride in the second step resulted in the formation of the dithiolene complex. The last step is devoted to cation exchange reaction. As a source of cations, tetrabutylammonium ([TBA]Br) and tetraphenylphosphonium bromides ([PPh_4]Br) were chosen to increase the solubility of the final dithiolene metal complexes. At the end of the reaction the solvent was removed under reduced pressure and the crude product was dissolved in dichloromethane for further crystallization.

The series of homometallic Cu–Cu– Cu and Ni–Ni–Ni trinuclear dithiolene complexes were isolated using the aforementioned synthesis with two different cations. Single crystals of $[TBA]_2[\{Ni(L^{13})_2\}_2Ni]\cdot 6CH_2Cl_2$ (**15**), $[TBA]_2[\{Cu(L^{13})_2\}_2Cu]\cdot 5CH_2Cl_2$ (**16**), $[PPh_4][\{Ni(L^{13})_2\}_2Ni]\cdot 4CH_2Cl_2$ (**17**) and $[PPh_4][\{Cu(L^{13})_2\}_2Cu]\cdot 4CH_2Cl_2$ (**18**) were obtained by slow evaporation of the corresponding dichloromethane solutions .

Compounds **15** and **16** crystallize in the monoclinic and triclinic systems, respectively, with uncoordinated solvent molecules. The main structural unit of each complex is a trinuclear anionic complex with a planar structure (Figure 4.12). Crystal structure X-ray analysis revealed that the anions $[\{M(L^{13})_2\}_2M]^{2-}$ are doubly-charged since two TBA cations are present per anionic complex.

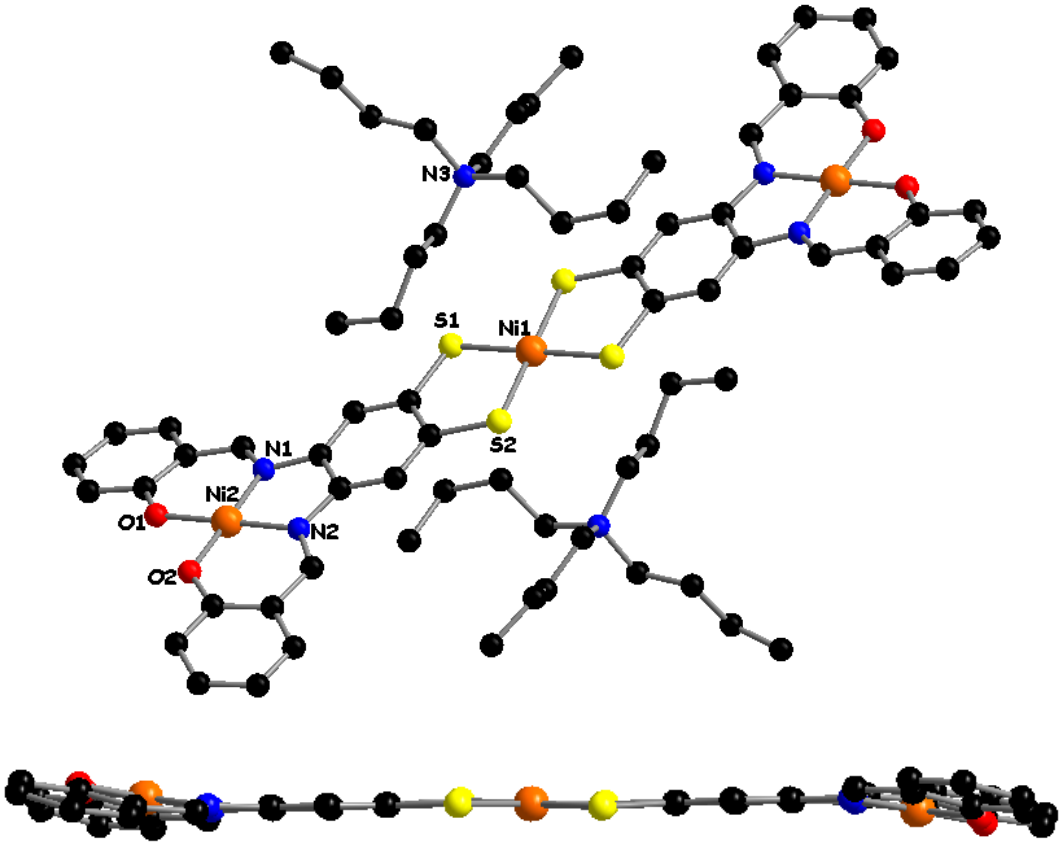

Figure 4.12. The crystal structure of **15** (top) and a side view emphasizing the planarity of the anion (bottom). Hydrogen atoms and solvent molecules were omitted for clarity.

All Ni(II) ions have a square planar coordination environment. The Ni1–S bond lengths are 2.1571(7) and 2.1771(7) Å. The values of S–Ni1–S_{cis} bond angles are 88.25(3) and 91.75(3)°, while S–Ni1–S_{trans} angles are straight. The other Ni2 ion exhibits N_2O_2 environment with Ni2–O and the Ni2–N close values of the distances are 1.841(2), 1.853(2) Å; 1.860(3), 1.869(3) Å, respectively.

Copper(II) complex **16** exhibits similar structural features, although it is not isostructural with the corresponding nickel(II) complex. The donor atoms from the ligand form a square planar coordination environment of all Cu(II) ions with the following bond distance values Cu1–S – 2.2585(17) and 2.2592(18) Å, whereas Cu2–O and Cu2–N have the following values 1.899(5)/1.902(4) Å; 1.958(5)/1.961(5) Å.

In the unit cells of **15** and **16**, the complex anions form layers, which are stabilized by $\pi\cdots\pi$ interactions. More careful inspection of these interaction reveals that in the case of complex **15**

only aromatic rings of the adjacent anions are involved, while for **16**, the $\pi\cdots\pi$ stacking was found mostly between the metalla cycles and the aromatic rings (Figure 4.13). The values of the corresponding interactions are 3.758 and 3.407 Å for compounds **15** and **16**, respectively.

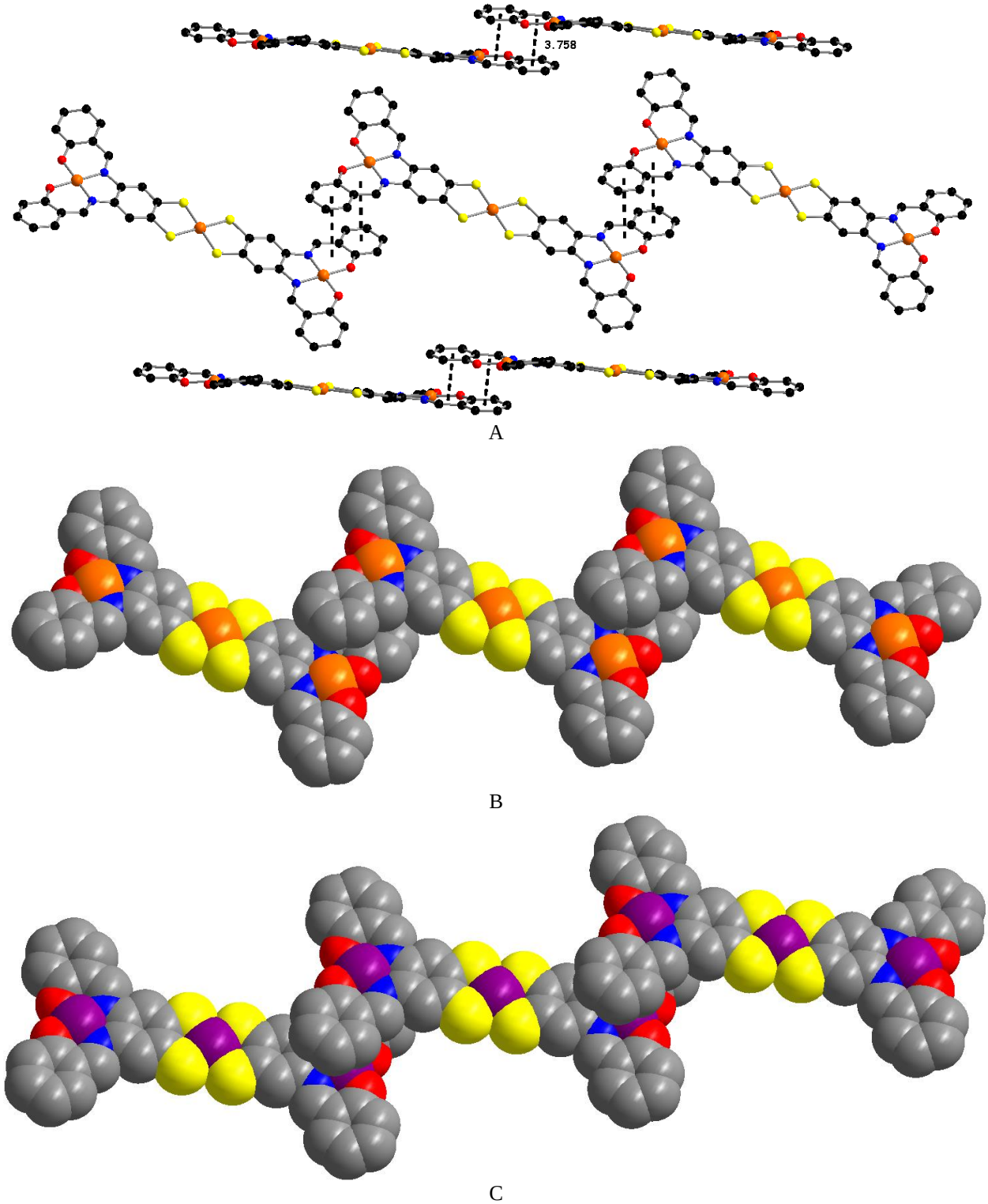

Figure 4.13. Ball-and-stick (A) and Space-filling (B) representation of the $\pi\cdots\pi$ interactions in **15** and overlapping of copper ions and the aromatic ring in **16** (C).

Utilization of PPh_4^+, as counter-cations, lead to the formation of a different series of homometallic dithiolene complexes **17** and **18**. These complexes crystallize in the orthorhombic

systems with uncoordinated molecules of dichloromethane and they are also isostructural. Crystal structure X-ray analysis shows that the trinuclear anions possess a similar square planar structure as for **15** and **16** (Figure 4.14), yet the anions $[\{M(L^{13})_2\}_2M]^-$ are mono-charged.

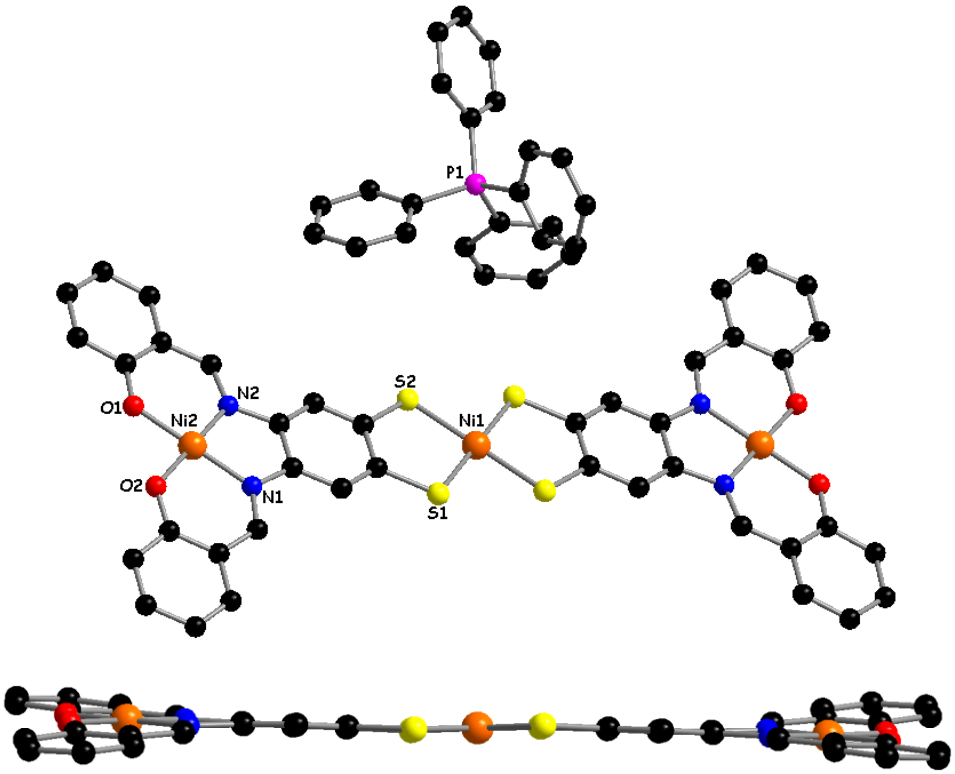

Figure 4.14. The crystal structure of **17** (top) and a side view emphasizing the planarity of the anion (bottom). Hydrogen atoms and solvent molecules were omitted for clarity.

Both complexes **17**, **18** possess similar structural features as the ones described above with TBA^+ cations. Thus, all Ni(II) or Cu(II) ions have square planar coordination environment. The bond distance values Ni1–S are 2.1431(8) and 2.1548(7) Å. The S–Ni1–S_{cis} bond angles are 87.619(27) and 92.381(20)°; S–Ni1–S_{trans} angles are straight. The Ni2 ion exhibits the same N_2O_2 coordination environment as in **15**, with the Ni2–O and Ni2–N close values of the distances [1.8458(24), 1.8506(24) Å; 1.8780(29), 1.8727(24) Å, respectively].

Copper complex **18** is isostructural to **17**, therefore, the values of the bond lengths are alike [Cu1–S – 2.1725(12) and 2.1762(10) Å; Cu2–O and Cu2–N have the following values 1.894(3)/1.915(4) Å; 1.945(4)/1.966(4) Å].

The difference in the Cu1–S bond lengths can be the additional proof of different oxidation states of the anions in the crystal structures **16** and **18**. Thus, Cu1–S – 2.2585(17) and 2.2592(18) Å distances in **16** are longer than those in **18**. The higher values of the central M–S distances are indicative of diaanionic complexes.

The unit cells of **17** and **18** exhibit similar features. The PPh_4^+ cations together with the uncoordinated solvent molecules are located in the voids, formed by the layers of the anions (Figure 4.15).

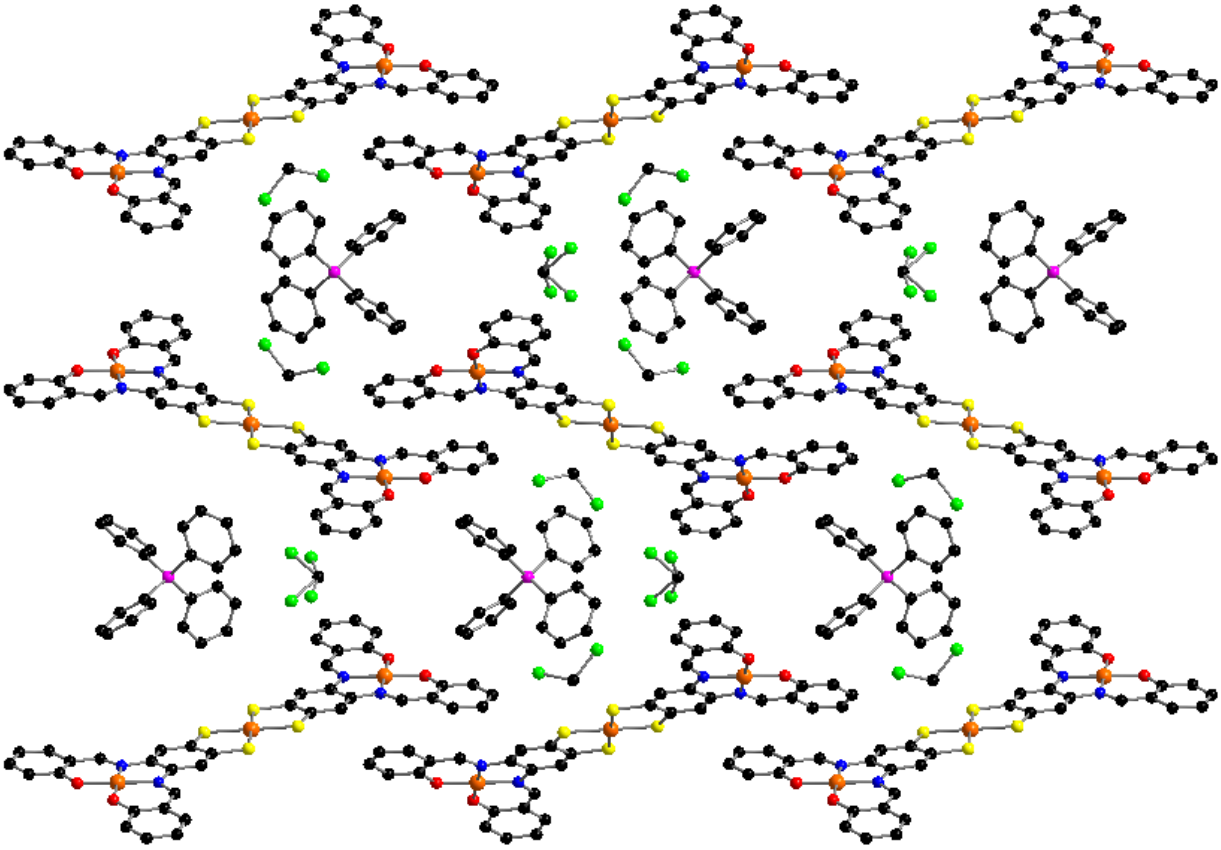

Figure 4.15. The unit cell of the $[PPh_4][\{Ni(L^{13})_2\}_2Ni]\cdot 4CH_2Cl_2$ (**17**) compound. Hydrogen atoms were omitted for clarity.

In the crystal packing of **17**, the anions lie parallel to each other, forming two types of layers (Figure 4.16). The unit cells of **17** and **18** are, in the same way as dithiolene complexes **15**, **16**, stabilized by the $\pi\cdots\pi$ interactions between the aromatic rings of the adjacent anions. The values of these contacts are very close (3.685 and 3.668 Å for compounds **17** and **18**, respectively.)

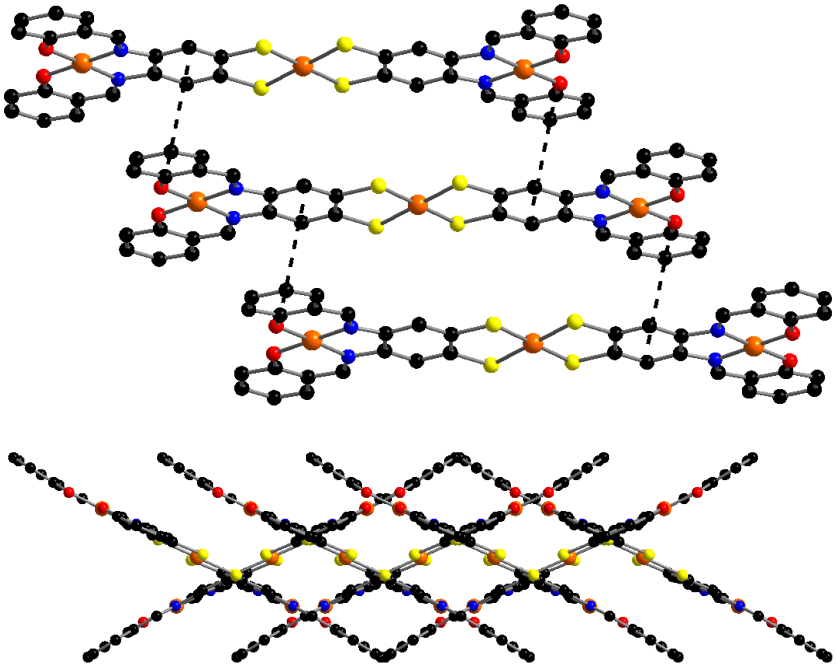

Figure 4.16. The $\pi\cdots\pi$ interactions in **17** (top) and the arrangement of the anion in the unit cell (bottom).

The homometallic copper complex **14** (Figure 4.10) was used to obtain the heterometallic Cu–Ni–Cu complex. The synthesis route is shown in Figure 4.17.

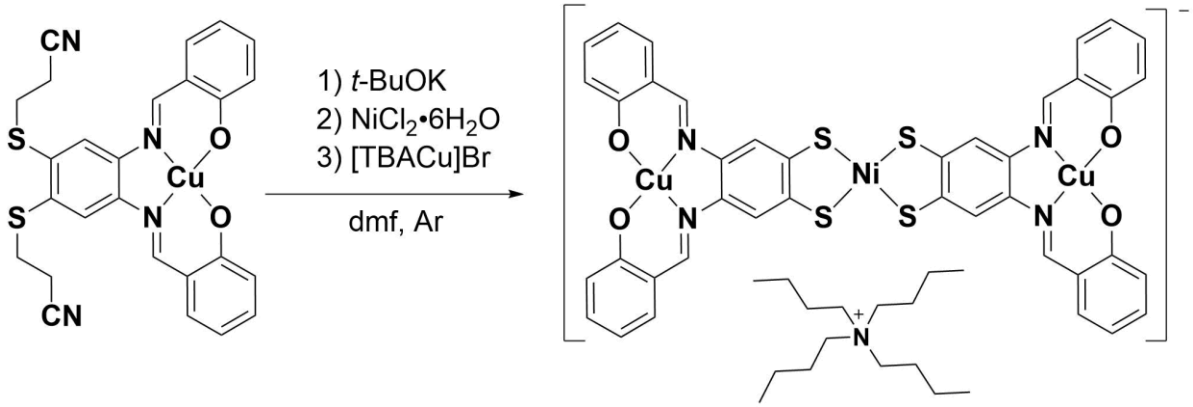

Figure 4.17. Synthesis of dithiolene complex $[TBA]_2[\{Cu(L^{13})_2\}_2Ni]_2 \cdot 2CH_2Cl_2$ (**19**).

The synthesis procedure is similar to compounds **15-18**, described above. Crystals suitable for the X-ray analysis were obtained by vapor diffusion of pentane into the solution of **19** in dichloromethane.

The complex crystallizes in the triclinic system with one entire anion and one cation as independent parts (Figure 4.18). The geometry of the anion is planar as in the case of compounds **15-18**. However, more careful analysis showed that one of the fragments $\{Cu(L^{13})_2\}$ (CuN_2O_2 unit) is slightly distorted and goes beyond the plane of the anion due to the interaction with the deprotonated phenolic oxygen atom from the adjacent anion. Thus, the anion is dimeric due to the additional bonding of the Cu2 ion with the neighboring fragment and the heterometallic complex **19** itself can be considered as hexanuclear.

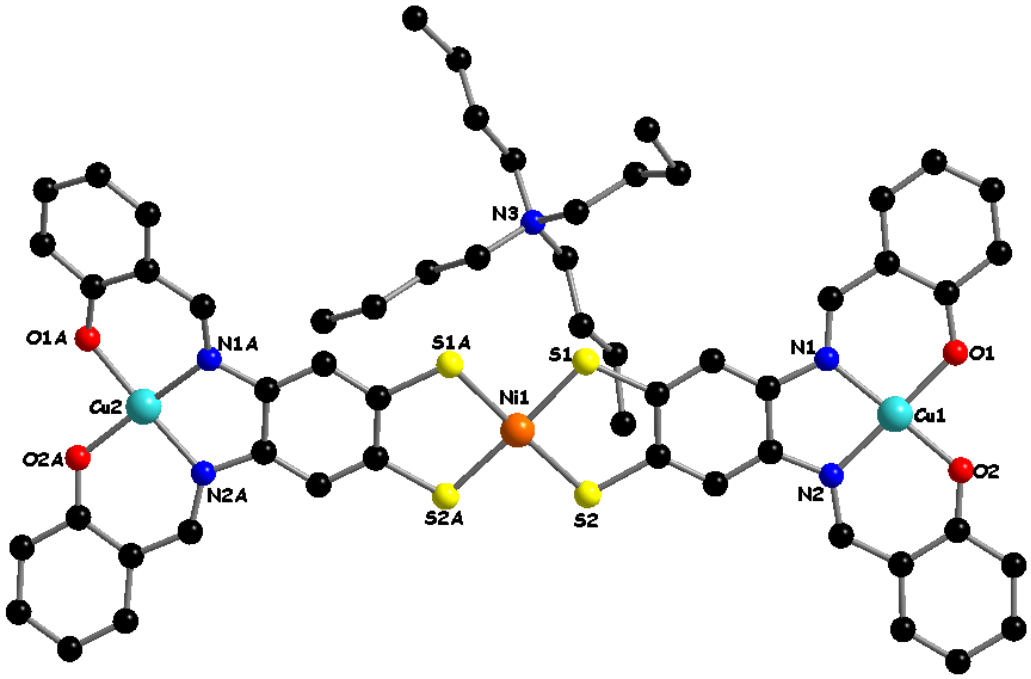

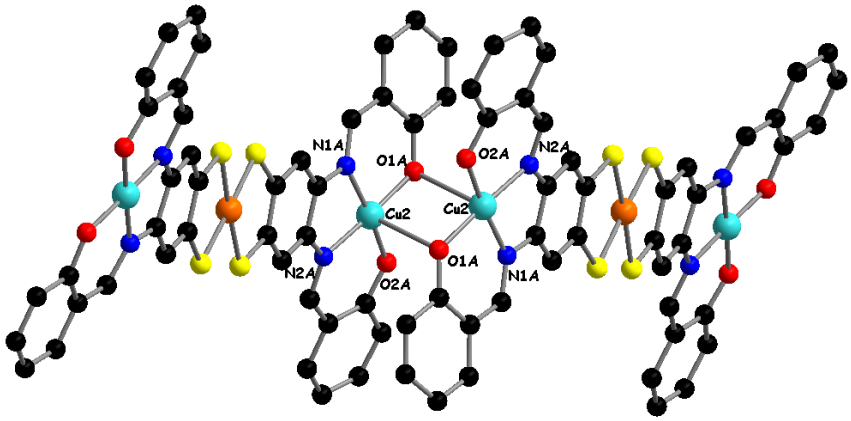

Figure 4.18. The crystal structure of **19** (top) and the representation of the dimeric anion (bottom). Hydrogen atoms and solvent molecules were omitted for clarity.

Metal ions Ni1 and Cu1 have a square planar coordination environment, formed by the donor sulfur atoms (for nickel) and nitrogen/oxygen atoms from the Schiff base moiety (for copper). The bond lengths Ni1–S vary from 2.1422(18) to 2.1664 (19) Å. The values of S–Ni1–S_{cis} bond angles span from 85.810(66) to 92.295(69)°, while S–Ni1–S_{trans} angles have almost equal values 177,975(77) and 177,130(79)°.

The values of the Cu1–O and Cu1–N bond lengths [1.8657(39)/1.8745(43) Å; 1.8998(43)/1.9200(47) Å] are similar to those found in Cu-containing complexes **16**, **18**.

The coordination polyhedra of the second copper ion Cu(2) is a square pyramid (figure 4.19). The equatorial Cu–O(N) bond lengths range from 1.8906(51) to 1.9284(50) Å, while the apical Cu2–O1A distance is 2.6303(59) Å. It should be noted that only one example of such Cu-dimer with phenolic bridge oxygen atom has been described to date[18]. The apical Cu–O was much longer 2.783(11) and was therefore considered as a covalent bond.

The distances Cu···Ni within anion are 8.0743(15) and 8.1239(14) Å, while the interanionic Cu2···Cu2 contact is much shorter [3.1884(17) Å]. In the dimer complex, described in literature, this value is 3.436 Å.

In the unit cell of **19** (Figure 4.20) the anions form voids with TBA^+ and dichloromethane molecules inside.

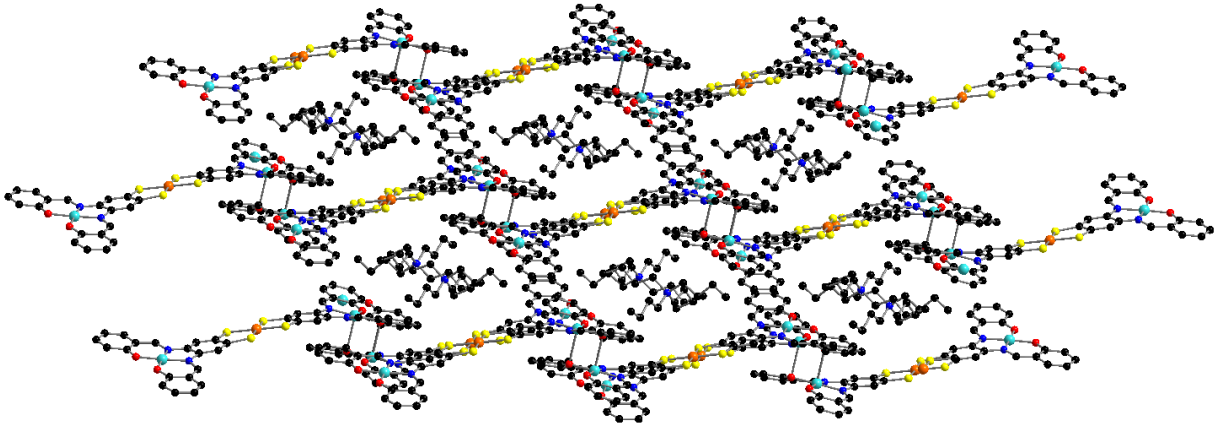

Figure 4.20. The unit cell of **19**. Hydrogen atoms and solvent molecules were omitted for clarity.

4.3. Conductivity measurements.

The physical characterization of homometallic Ni-containing compounds **15**, **17** shows that these complexes present similar trends. The electrical resistivity measurements for both complexes **15**, **17** show that they are semiconductors (Figure 4.21) having the conductivity values of 10^{-6} S·cm^{-1} at room temperature (Table 4.2).

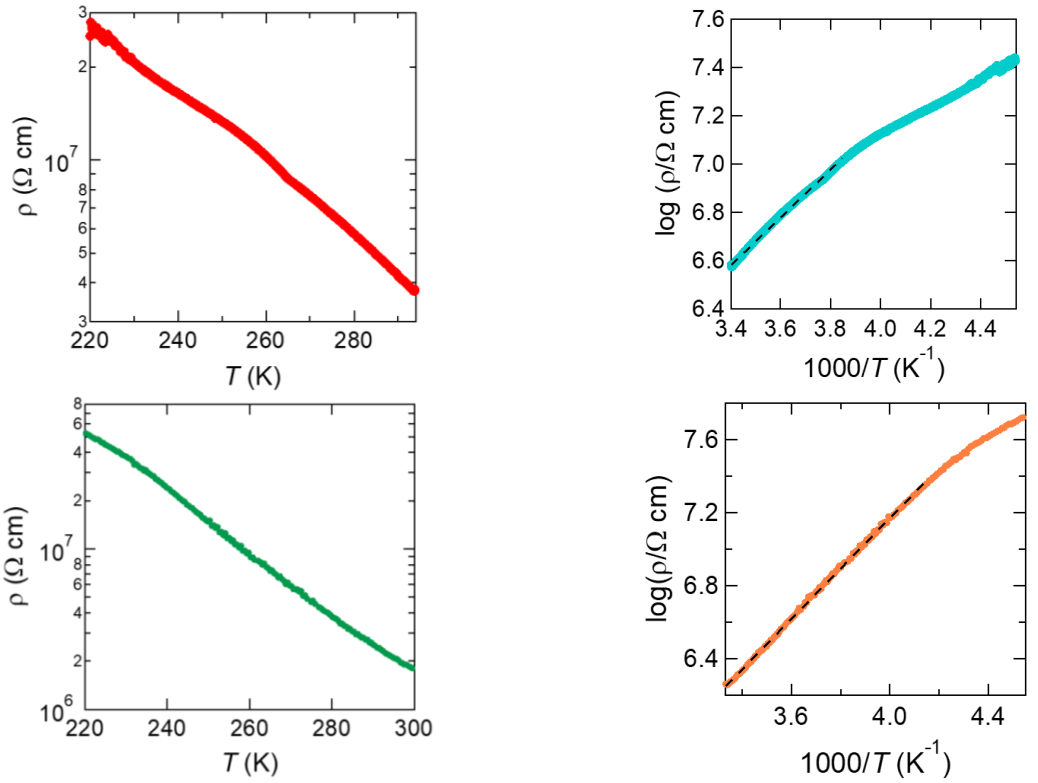

Figure 4.21. Temperature dependences of the electrical resistivity ρ for a single crystal of **15** (top, left) and **17** (bottom, left); ρ (in logarithm scale) versus the inverse temperature (right) for **15** (top, right) and **17** (bottom, right);.

The presence of several short $\pi\cdots\pi$ interactions connecting dithiolene units of the neighboring complexes or along the plane in compounds **15** and **17** provides a feasible path for electron delocalization.

On the other hand, the twice less value of the electrical resistivities of diaanionic dithiolene complexes **15**, compared to the monoanionic **17** can be explained due to the closed-shell character of the first one. Nevertheless, this small value of the conductivities in **15** may be attributed to a counterion PPh_4^+ which is not very suitable for a good electron transport as it's extremely bulky and therefore hinders the close packing between complexes.

Table 4.2. Electrical conductivities and activation energies of compounds **15–18**.

Compound	σ_{294}, **S·cm^{-1}**	**E_a,eV**
$[TBA]_2[\{Ni(L^{13})_2\}_2Ni]\cdot 6CH_2Cl_2$ (**15**)	1.8×10^{-6}	0.27 (260 K < *T* < 294 K)
$[PPh_4][\{Ni(L^{13})_2\}_2Ni]\cdot 4CH_2Cl_2$ (**17**)	3.8×10^{-6}	0.20 (260 K < *T* < 294 K)

The single crystals of both copper complexes **16**, **18** and heterometallic Cu-Ni-Cu compound **19** were too small and fragile and could not be measured successfully.

4.4. Conclusion.

An unprecedented Schiff base ligand containing thiopropionitrile groups has been synthesized. This ligand possesses a chelating N,O-donor pocket together with S-donor atoms from thiopropannitrile moieties. The ability to form stable mononuclear complexes, which can be used as precursors for the synthesis of polynuclear dithiolene complexes, has been demonstrated. A series of homo- and heterometallic complexes with various nuclearity has been obtained. The formation of mono- and diaanionic homometallic Ni-Ni-Ni and Cu-Cu-Cu complexes with tetraphenylphosphonium (PPh_4^+) and tetrabutylammonium (TBA^+), respectively, has been observed. Crystal structure X-ray analysis revealed that the heterometallic Cu-Ni-Cu complex was based on the hexanuclear monoanion due to the interaction of the copper ion with the deprotonated phenolic oxygen atom from the adjacent anion.

The electrical resistivity measurements show that the mono- and diaanionic Ni-containing compounds are semiconductors.

References

1. Eisenberg, R.; Gray, H. B., *Inorg. Chem.* **2011,** *50*, 9741-9751.

2. Arumugam, K.; Yu, R.; Villagrán, D.; Gray, T. G.; Mague, J. T.; Donahue, J. P., *Inorg. Chem.* **2008,** *47*, 5570-5572.

3. Arumugam, K.; Shaw, M. C.; Chandrasekaran, P.; Villagrán, D.; Gray, T. G.; Mague, J. T.; Donahue, J. P., *Inorg. Chem.* **2009,** *48*, 10591-10607.

4. Kubo, K.; Shiga, T.; Yamamoto, T.; Tajima, A.; Moriwaki, T.; Ikemoto, Y.; Yamashita, M.; Sessini, E.; Mercuri, M. L.; Deplano, P.; Nakazawa, Y.; Kato, R., *Inorg. Chem.* **2011,** *50*, 9337-9344.

5. Madalan, A. M.; Avarvari, N.; Fourmigué, M.; Clérac, R.; Chibotaru, L. F.; Clima, S.; Andruh, M., *Inorg. Chem.* **2008,** *47*, 940-950.

6. Burmester, C.; Faust, R., *Synthesis* **2008,** *2008*, 1179-1181.

7. Murata, M.; Kaji, S.; Nishimura, H.; Wakamiya, A.; Murata, Y., *Eur. J. Inorg. Chem.* **2016,** *2016*, 3228-3232.

8. Cordovilla, C.; Bartolomé, C.; Martínez-Ilarduya, J. M.; Espinet, P., *ACS Catal.* **2015,** *5*, 3040-3053.

9. Eltayeb, N. E.; Teoh, S. G.; Chantrapromma, S.; Fun, H.-K.; Adnan, R., *Acta Crystallogr., Sect. E* **2008,** *64*, m626-m627.

10. Tamaki, Y.; Tomono, K.; Hata, Y.; Saita, N.; Yamamoto, T.; Miyamura, K., *Bull. Chem. Soc. Jpn.* **2012,** *85*, 592-598.

11. Lin, H.; Wang, J.-G.; Shi, H.-T.; Chen, Q.; Zhang, Q.-F., *Acta Crystallogr., Sect. E* **2013,** *69*, m404.

12. Zhang, X.; Wei, P.; Li, B.; Wu, C.; Hu, B., *Acta Crystallogr., Sect. E* **2009,** *65*, m707.

13. Anselmo, D.; Escudero-Adán, E. C.; Martínez Belmonte, M.; Kleij, A. W., *Eur. J. Inorg. Chem.* **2012,** *2012*, 4694-4700.

14. Wickramasinghe, L. D.; Mazumder, S.; Kpogo, K. K.; Staples, R. J.; Schlegel, H. B.; Verani, C. N., *Chem. Eur. J.* **2016,** *22*, 10786-10790.

15. Ferrari, M. B.; Fava, G. G.; Pelizzi, C., *Acta Crystallogr., Sect. B* **1976,** *32*, 901-908.

16. Baggio, R.; Garland, M. T.; Atria, A. M.; Hidalgo, O.; Solezi, S., *Acta Crystallogr., Sect. E* **2001,** *57*, m19-m20.

17. Suresh, E.; Bhadbhade, M. M.; Srinivas, D., *Polyhedron* **1996,** *15*, 4133-4144.

18. Yu, G.; Ding, Y.; Wang, L.; Fu, Z.; Hu, X., *Acta Crystallogr., Sect. E* **2008,** *64*, m504.

CHAPTER V

TETRAZINE BASED LIGANDS AND THEIR COMPLEXES

5.1. Introduction.

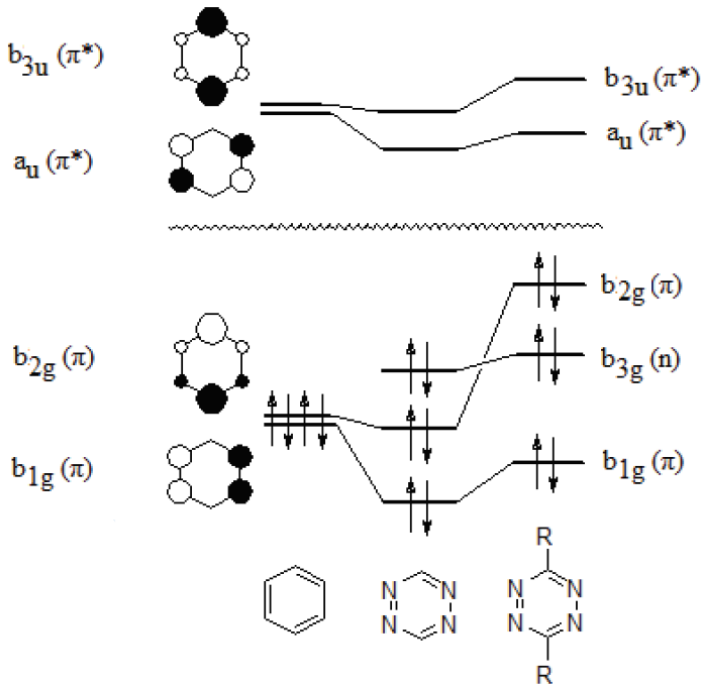

Figure 5.1. Diagram illustrating the energy shifts of the frontier orbitals of the aromatic and tetrazine rings.

Homo- and heterometallic complexes with classical (chapter II) and modified (chapters III, IV) Schiff base ligands were the platform of choice for multifunctional materials, particularly for the combination of magnetic and conducting properties in the same compound. The electron-withdrawing character of an aromatic ring can, in principle, allow the access to stable radical anion species in order to strengthen or to modulate the magnetic exchange between metal ions. On the other hand, the π acidity of the aromatic ring may support the establishment of anion–π interactions in the solid state, which possibly interplay with other weak intermolecular forces to provide original supramolecular architectures. However, the high-lying π*-orbitals of benzene, together with the large energy gap between bonding and anti-bonding molecular orbitals (Figure 5.1), do not allow the opportunity for the structural features mentioned above. This problem can be solved by the introduction of heteroatoms into the aromatic ring, which are capable to form the non-bonding molecular orbitals (NBMOs), resulting in the decrease of the energy gap between the NBMOs and anti-bonding MOs.

From this point of view, the 1,2,4,5-tetrazine or s-tetrazine unit, containing four nitrogen atoms, is a good candidate due to its low-lying π* orbitals (Figure 5.1), resulting in a forbidden *n*-π* transition in the visible range. The π* orbitals of tetrazine possess lower energy compared to benzene and, therefore, one can expect stable radical anion species[1-5].

The majority of the complexes containing tetrazine radical anion were reported by the research team of K. Dunbar. The Co(II)[6] and Ni(II)[7] complexes, $[\{Co(TPMA)\}_2(bmtz)](CF_3SO_3)_3 \cdot CH_3CN$ and $[\{Ni(TPMA)\}_2(bmtz)](BF_4)_3 \cdot 3CH_3CN$ (bmtz = 3,6-bis(2′-pyrimidyl)-1,2,4,5-tetrazine, TPMA = tris(2pyridylmethyl)amine), exhibit slow

magnetic relaxation in the applied DC field with a barrier to spin reversal of 39 K (Figure 5.2) and a strong ferromagnetic exchange between the S =1 Ni(II) centers and the bridging S = ½ bmtz radical with $J = 96 \pm 5$ cm^{-1}, respectively.

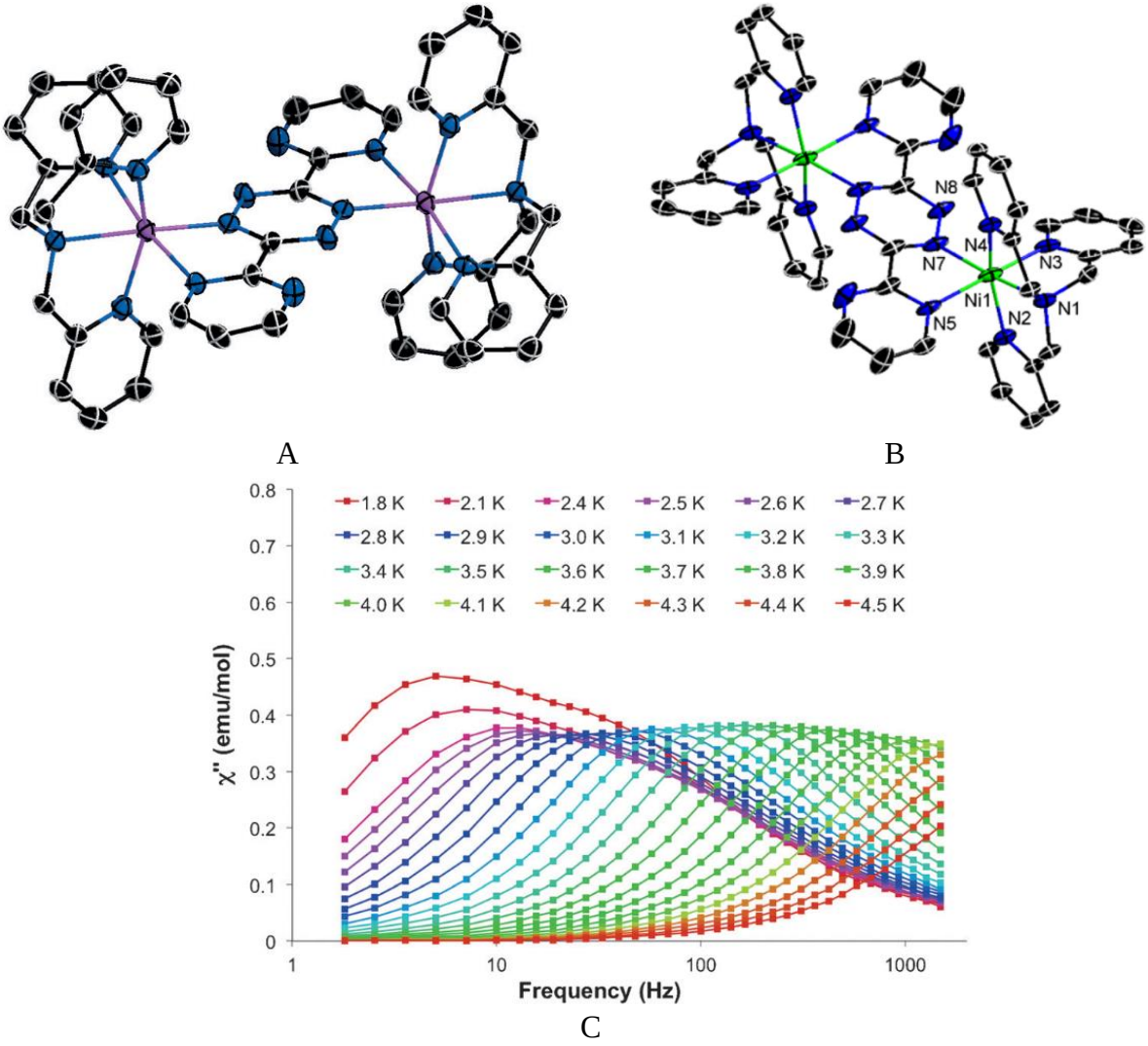

Figure 5.2. The crystal structures of Co(II) (A) and Ni(II) (B) complexes and the frequency dependences for Co(II) compound in an 800 Oe applied DC field (C).

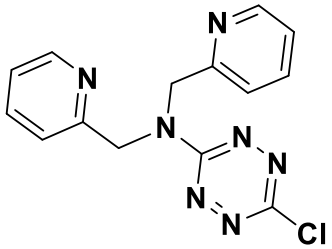

Figure 5.3. Molecular structure of the Cl-TTZ-dipica ligand [8].

The extensive investigation of a such s-tetrazine based ligands, which may be considered as symmetric ditopic ligands, prompted the scientists to obtain non-symmetric molecules, which contain two different substituents in the 3 and 6 positions of the tetrazine ring. One of the first nonsymmetric ligand, containing tetrazine and di(2-picolyl)-amine fragments (Figure 5.3) within a series of four neutral transition metal complexes formulated as [Cl-TTZ-dipica-MCl_2]$_2$, with M = Zn(II), Cd(II), Mn(II) and Co(II) were reported by our group in 2015[8]. All the complexes are isostructural, showing a dinuclear structure in the solid state through the formation of the μ-Cl bridged [M_2Cl_2] cores (Figure 5.4), with variable M–Cl distances. A switch-on of the tetrazine based fluorescence has been observed

in the Zn(II) and Cd(II) complexes compared to the free ligand. The Mn(II) and Co(II) complexes show some differences in their magnetic behavior, as an antiferromagnetic coupling occurs in the former (J = −1.25 cm^{-1}) while a ferromagnetic coupling takes place in the latter (J = +0.55 cm^{-1}).

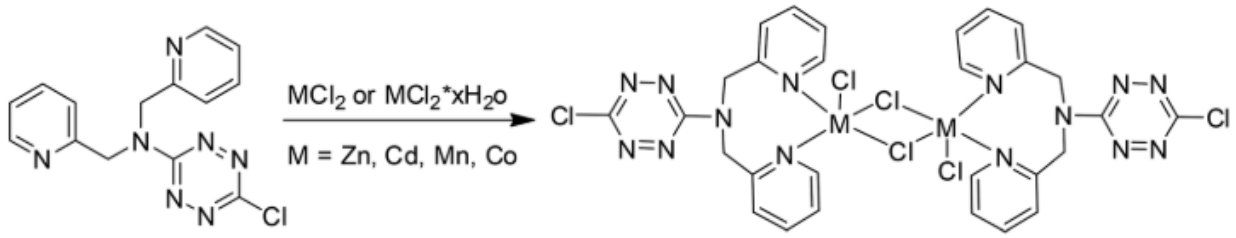

Figure 5.4. The synthesis scheme of the complexes.

The presence of two different substituents in the tetrazine rings promotes the luminescence properties of halogen- and oxygen-substituted derivatives, arising from a symmetry forbidden n–π* excitation (Figure 5.1). As a continuation of this research work, our first attempt was the substitution of one chlorine atom in the 3,6-dichlorotetrazine derivative by a picolylamine (**HL^{14}**). The synthesis and properties of the ditopic chelating **H_2L^{15}** ligand (Figure 5.5), which is the product of the substitution of the two chlorine atoms on the tetrazine ring, complete this work.

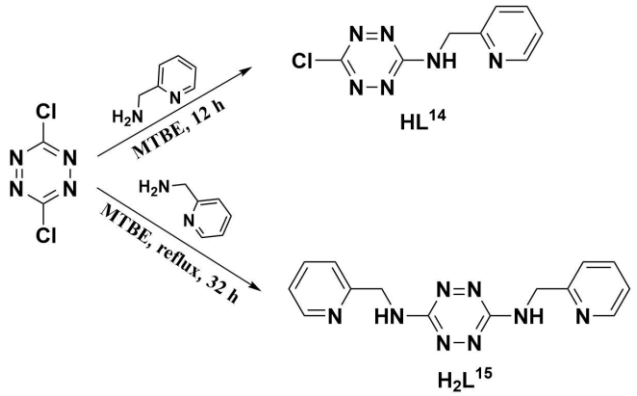

Figure 5.5. Synthesis of the tetrazine based **HL^{14}** and **H_2L^{15}** ligands.

For the synthesis of the two ligands, 3,6-dichlorotetrazine, previously reported in the literature,[9] was chosen.

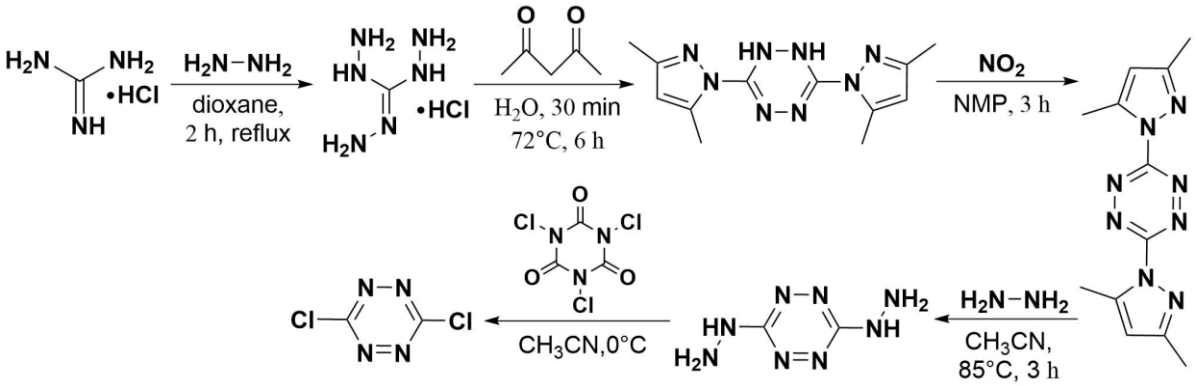

Figure 5.6. Synthesis of 3,6-dichlorotetrazine[9].

5.2. Crystal structure of the HL[14] ligand and its complexes.

The Cl-TTZ-monopica (**HL[14]**) ligand was prepared by the nucleophilic substitution of one of the chlorine substituents of 3,6-dichlorotetrazine with 2-picolyl-amine (monopica) in methyl-*t*-butylether (MTBE) (Figure 5.5) according to the procedure previously described for the Cl-TTZ-(dipica) ligand [8].

Single crystals of **HL[14]** suitable for X-ray crystal structure analysis were grown by slow evaporation of ethylacetate/dichloromethane (3/1, v/v) solution. The compound crystallizes in the monoclinic system, space group $P2_1/c$, with one independent molecule in the unit cell (Figure 5.1). The geometry of the molecule is not planar, with a dihedral angle between the tetrazine and pyridine rings of 66.8°. The N–N and C–N central bonds of the tetrazine ring (Table 5.7) show typical values which are in good agreement with other reported tetrazine-based ligands [10].

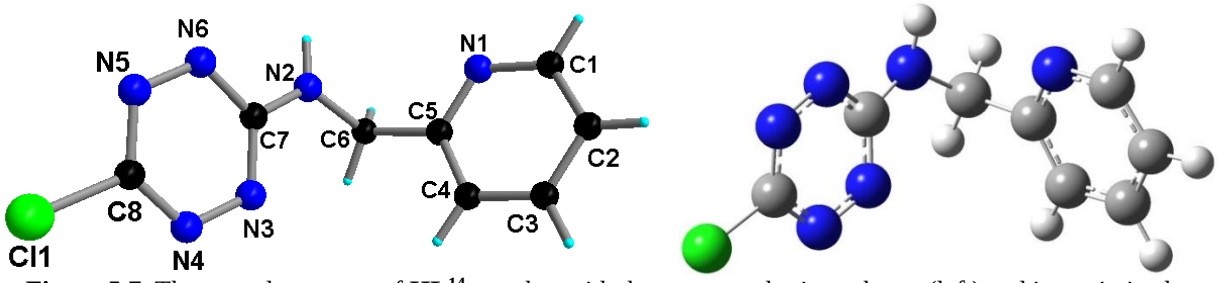

Figure 5.7. The crystal structure of **HL[14]** together with the atom numbering scheme (left) and its optimized geometry at the DFT/M11L/6-311G(d,p) level (right).

Table 5.1. Selected distances (Å) of the **HL[14]** ligand.

C1—C2	1.374(5)	C7—N2	1.338(4)
C1—N1	1.333(4)	C7—N3	1.342(4)
C2—C3	1.378(6)	C7—N6	1.359(4)
C3—C4	1.373(5)	C8—Cl1	1.722(3)
C4—C5	1.378(4)	C8—N4	1.308(5)
C5—C6	1.511(5)	C8—N5	1.330(5)
C5—N1	1.328(4)	N3—N4	1.328(4)
C6—N2	1.462(4)	N5—N6	1.308(4)

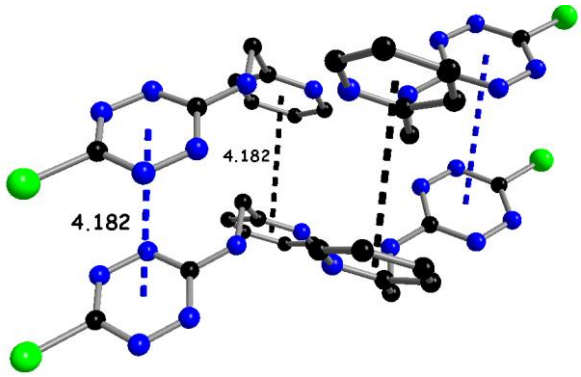

Figure 5.8. Interaction between the tetrazine (blue line) and pyridine (black line) rings in **HL[14]**. The hydrogen atoms were omitted.

The molecules of the ligand pack along the *a* direction through TTZ···TTZ and Pyr···Pyr π-π interactions with centroid···centroid distances of 4.18 Å as shown in figure 5.8, forming a 2D network in the *bc* plane due to the N1···H2 intermolecular hydrogen bonds giving rise to $R^2_2(10)$ motifs[11] interconnected through Cl1···H4 contacts (Figure 5.9).

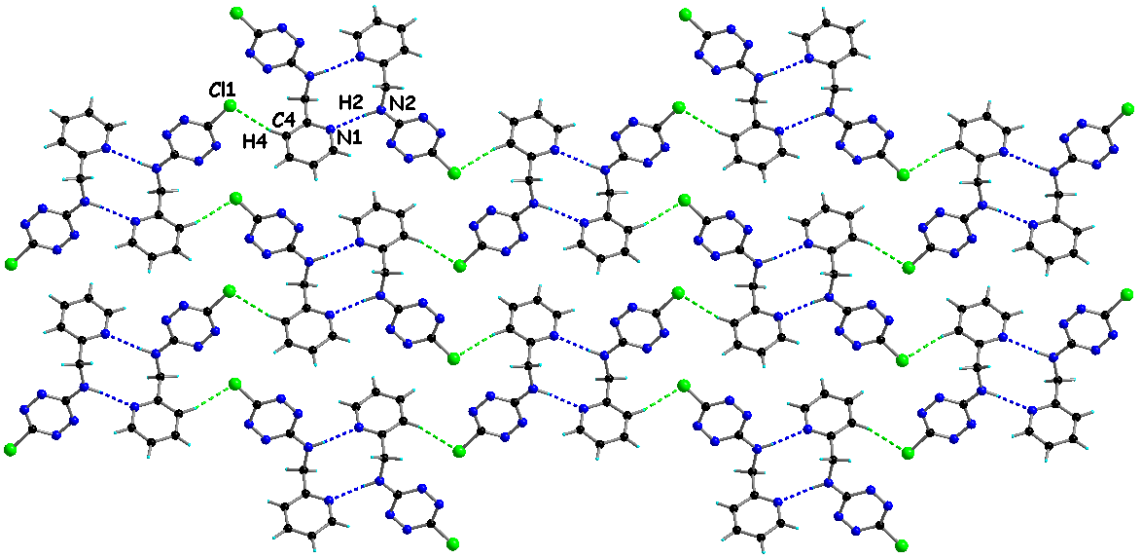

Figure 5.9. Intermolecular hydrogen bonds [d(N(1)···N(2)) = 2,90 Å, ∠(N(1)–H(2)–N(2)) = 162˚; d(Cl(1)···C(4)) = 3,82 Å, ∠(Cl(1)–H(4)–C(4)) = 159˚] in **HL**[14].

The optimized geometry of **HL**[14] is in good agreement with the experimental X-ray structure (Figure 5.7) concerning the bond lengths, while a dihedral angle of 80.52° between TTZ and Py rings has been calculated (66.8° is the experimental value).

Interestingly, the molecular orbitals diagram shows a π* type LUMO with equal contributions from the four N tetrazine atoms and a n-type HOMO also based on the tetrazine N atoms in spite of the presence of the amino substituent[9], which however raises the energy of the π type HOMO-1 orbital compared to dichloro-tetrazine[9]. The pyridine nitrogen lone pair is the HOMO-2 orbital (Figure 5.10).

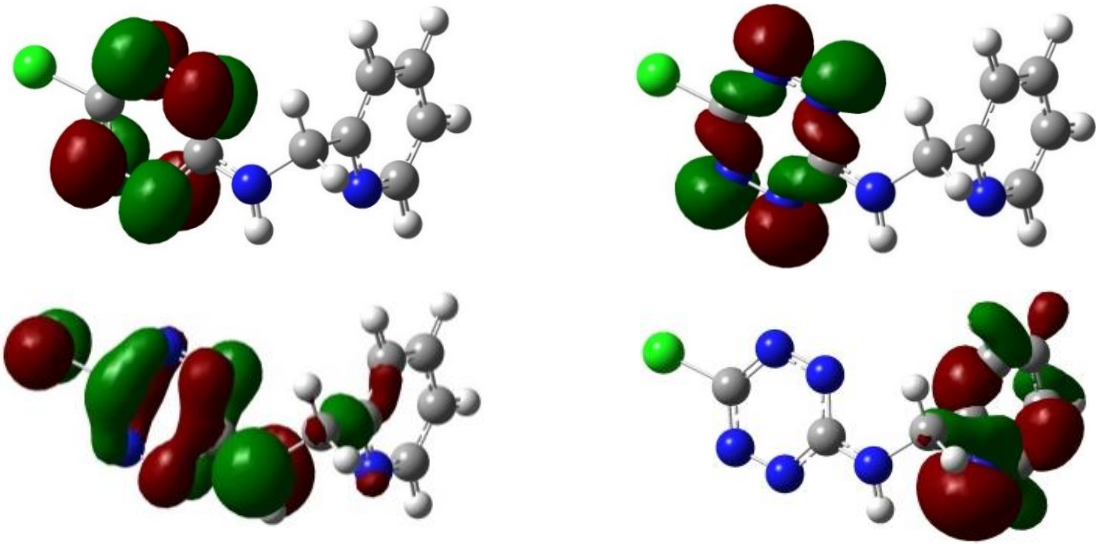

Figure 5.10. Molecular orbitals of **HL**[1]: LUMO (E = -3.7406 eV, top left), HOMO (E = -6.0707 eV, top right), HOMO-1 (E = -6.4733 eV, bottom left) and HOMO-2 (E = -7.0297 eV, bottom right); DFT/M11L/6-311G(d,p) level, isovalue 0.04.

The **HL**[14] ligand may, in principle, either coordinate a metal center in its amino form or, due to the electron withdrawing of the tetrazine unit, lose the proton to generate the equivalent of the

formamidinate/guanidinate ligands[12-18], which would here have a pyridine as an additional coordinating moiety. To emphasize the latter, we have chosen **HL^{14}** to react with copper(II) hexafluoroacetylacetonate Cu(Hfac)$_2$ precursor in a DCM/MeOH solvent mixture, hypothesizing that the anionic Hfac$^-$ ligand could act *in situ* as a base towards **HL^{14}**. Quite surprisingly, not only **HL^{14}** was deprotonated and replaced Hfac in the coordination sphere of copper, but also the compound which crystallized out of the reaction mixture appeared to be the mixed valence dinuclear complex [Cu$_2$(μ_2-Cl)(L^{14})$_2$] (**21**) (Figure 5.11), with the amido-tetrazine fragments bridging the dimeric Cu$_2$-unit, further capped by a μ-chloride, very likely generated *in situ* from the partial replacement of the Cl substituent of TTZ by a methoxy group from methanol. The formation of complex **21** is a rare example of the *in situ* partial reduction of Cu(II) to Cu(I) using a classical "wet chemistry" approach, whereas usually this reduction occurs under the solvothermal conditions and in the presence of the SCN$^-$, CN$^-$ anions, which may serve as reducing agents[19]. Careful inspection of literature shows that in very few cases the Hal$^-$ anion can partially reduce Cu(II) to Cu(I). This fact has been reported only for Br$^-$,[20] rather than for other halogenides. We suppose that in our case the deprotonated **HL^{14}** acts as a reducing agent, since the closest analogies of the above-mentioned reduction were described for the N-donor ligand[21], in particular, the Schiff base molecule[22]. As the bimetallic complex **21** is neutral, the charge balance requires that the copper centers should be in a mixed valence state Cu^{I}Cu^{II}.

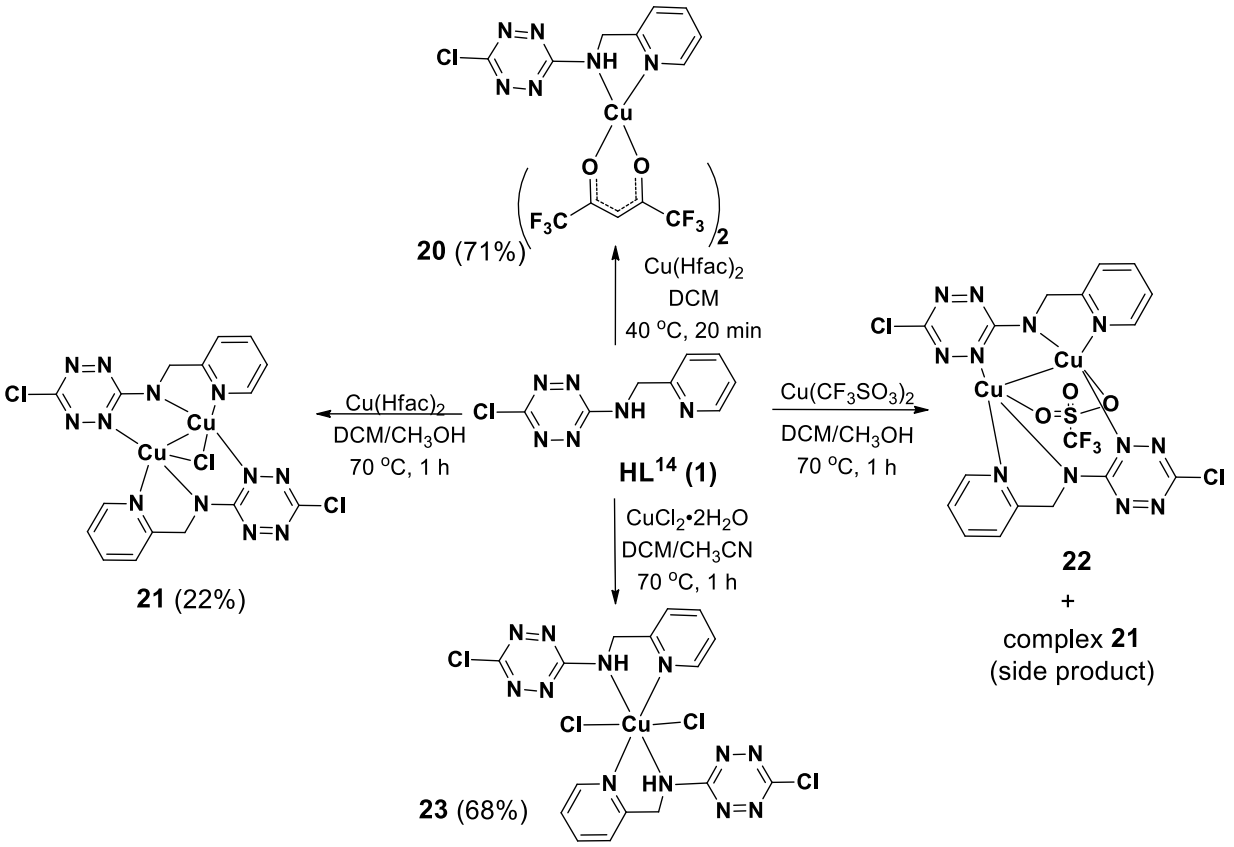

Figure 5.11. Reactivity of the **HL^{14}** ligand towards Cu^{II} precursors

To study the influence of the reaction conditions on the deprotonation of the **HL^{14}** and formation of the dinuclear mixed-valence copper complex **21**, the **HL^{14}** ligand was reacted with copper(II) chloride dihydrate in a DCM/MeCN mixture (Figure 5.11). Now, the "expected" octahedral mononuclear Cu(II) complex **23** formulated as $[CuCl_2(HL^{14})_2]\cdot 2CH_3CN$ crystallized from the reaction mixture in spite of the 1:1 stoichiometry used, indicating the importance of the basicity of the ligand in the Cu(II) precursor, i.e. hexafluoro-acetylacetonate *versus* chloride, for the deprotonation of **HL^{14}**. It turns out, however, that the polarity and protic character of the solvent are also of paramount importance for the reaction product formation, since when $Cu(Hfac)_2$ was used as a precursor in methylene chloride as a solvent, the "normal" octahedral mononuclear complex $[Cu(Hfac)_2(HL^{14})]$ **20** was once again isolated without any trace of the mixed valence complex **21**.

Finally, upon the reaction of the ligand with copper(II) triflate $Cu(CF_3SO_3)_2$ under the same conditions as those for the mixed valence complex **21**, i.e. DCM/MeOH mixture, the mixed valence Cu^I/Cu^{II} complex **22** was obtained (Figure 5.11) together with a minor crystalline phase which proved to be complex **21**.

5.2.1. The crystal structure and properties of the copper complexes.

X-ray crystal structure analysis revealed that both binuclear Cu complexes crystallize in the monoclinic system, space group $P2_1/c$, with one independent bimetallic molecule in the unit cell (Figure 5.12).

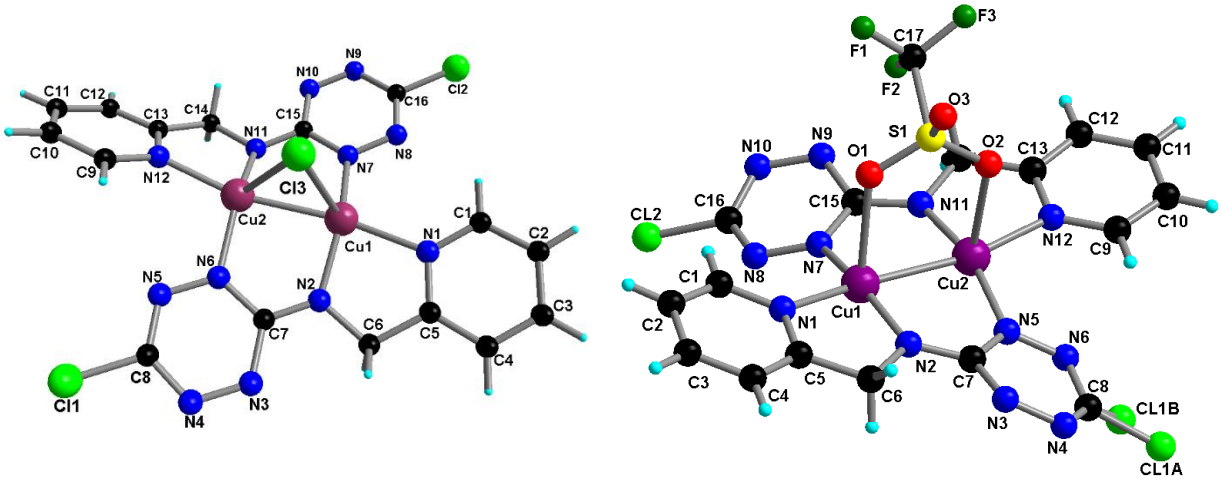

Figure 5.12. The crystal structures of complexes **21, 22** together with the atom numbering scheme.

The coordination geometry of each copper atoms Cu1 and Cu2 in both compounds is a distorted butterfly if the Cu–Cu bond is not considered, with three Cu–N bonds of each Cu center showing close bond length values between 1,8922(38) and 2.0614(18) Å. Surprisingly, the Cu–N_{TTZ} and Cu–N_{amido} distances are substantially shorter than the Cu–N_{Pyr} ones (Tables 5.2 and 5.3). It is very likely that due to the negative charge on the amido-TTZ fragments the metal-ligand

interaction is enhanced. The apical Cu1–Cl3 and Cu2–Cl3 distances in the crystal structure of **21** with the bridging chloride ligand are 2.4854(5) and 2.4576(6) Å, respectively. The apical sites in **22** are occupied by O1 and O2, from the triflate anion, with Cu1-O1 and Cu2–O2 distances of 2.3722(50) and 2.4205(70) Å, respectively. The most important feature is the presence of rather short Cu–Cu distances amounting 2.4314(4) Å (for **21**) and 2.5198(10) Å (for **22**).

At the supramolecular level, the intermolecular hydrogen bonds between chlorine atoms Cl2 (TTZ) and bridging Cl3 and hydrogen atoms of the pyridine ring as well as the anion-π interactions, characterized by Cl···$TTZ_{centroid}$ short distances of 3.76 Å (Cl1···TTZ) and 3.45 Å (Cl3···TTZ), are observed (figure 5.13, top). In the case of **22** short Cl···TTZ contacts of 3.488 Å can be observed (Figure 5.13, bottom) in the crystal packing.

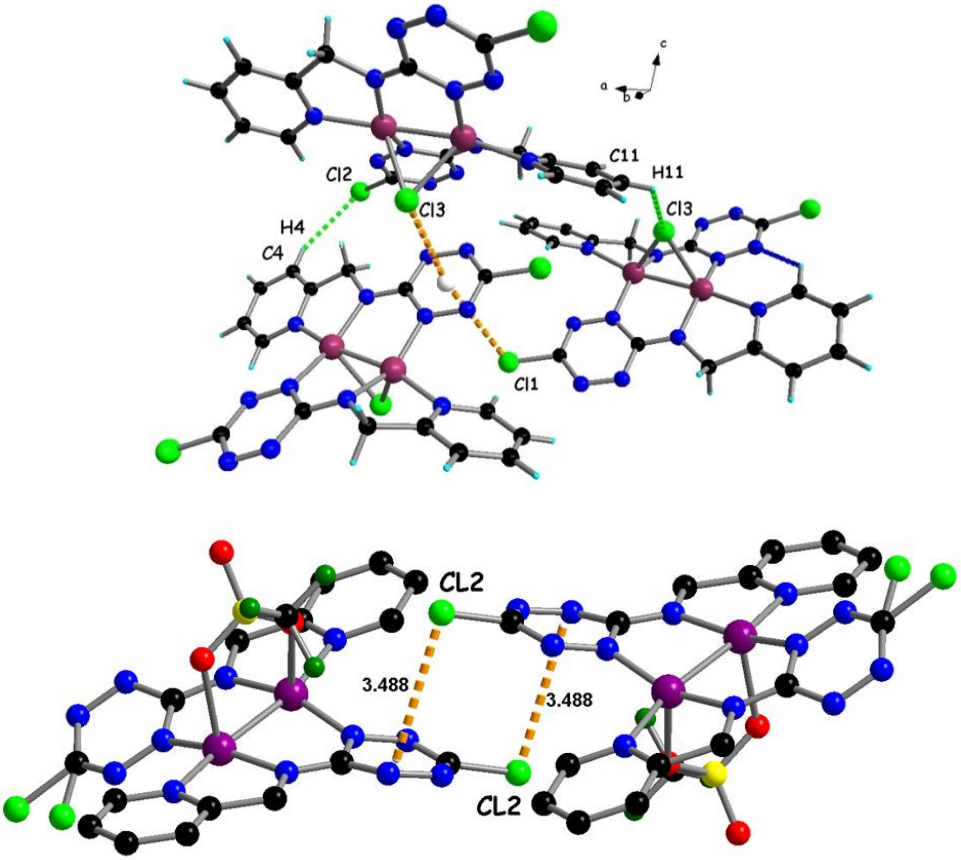

Figure 5.13. Intermolecular hydrogen bonds and anion-π interactions in structure **21**. A dummy atom has been generated in the center of the TTZ ring to highlight the anion-π interactions (top) and Cl···TTZ interactions in structure **22** (bottom).

As was mentioned above, the bimetallic complexes **21** and **22** are neutral and the charge balance requires that the copper centers should be in a mixed valence state $Cu^{I}Cu^{II}$. According to literature, mixed valence copper complexes belong to the three types I-III in the Robin and Day classification[23]. Most examples are type I systems[23], where the unpaired electron is localized on one metal center. There are far fewer examples of the type II and type III $Cu^{I}Cu^{II}$ complexes. Synthetic type II systems have only been reported for the complexes with Robson's-type macrocyclic binuclear ligands[24-25], while type III $Cu^{I}Cu^{II}$ complexes, in which the unpaired

electron is delocalized between the two copper ions at all temperatures, were described by R. P. Houser[26] and A. S. Borovik.[27] In addition to the synthetic species, the CuA site in cytochrome *c* oxidase[28] and the active site in nitrous oxide reductase[29] contain fully delocalized mixed-valent $Cu^{I}Cu^{II}$ centers.

The peculiarity of complex **21** prompted us to undertake DFT calculations (collaboration with A. Lupan, University of Cluj, Romania) in order to evaluate its intrinsic stability and characterize its mixed valence nature. In particular, the DFT optimized geometry (Figure 5.14) obtained starting from the X-ray structure is in agreement with the experimental one, as shown by the values of the Cu–L and Cu1–Cu2 distances (Table 5.2).

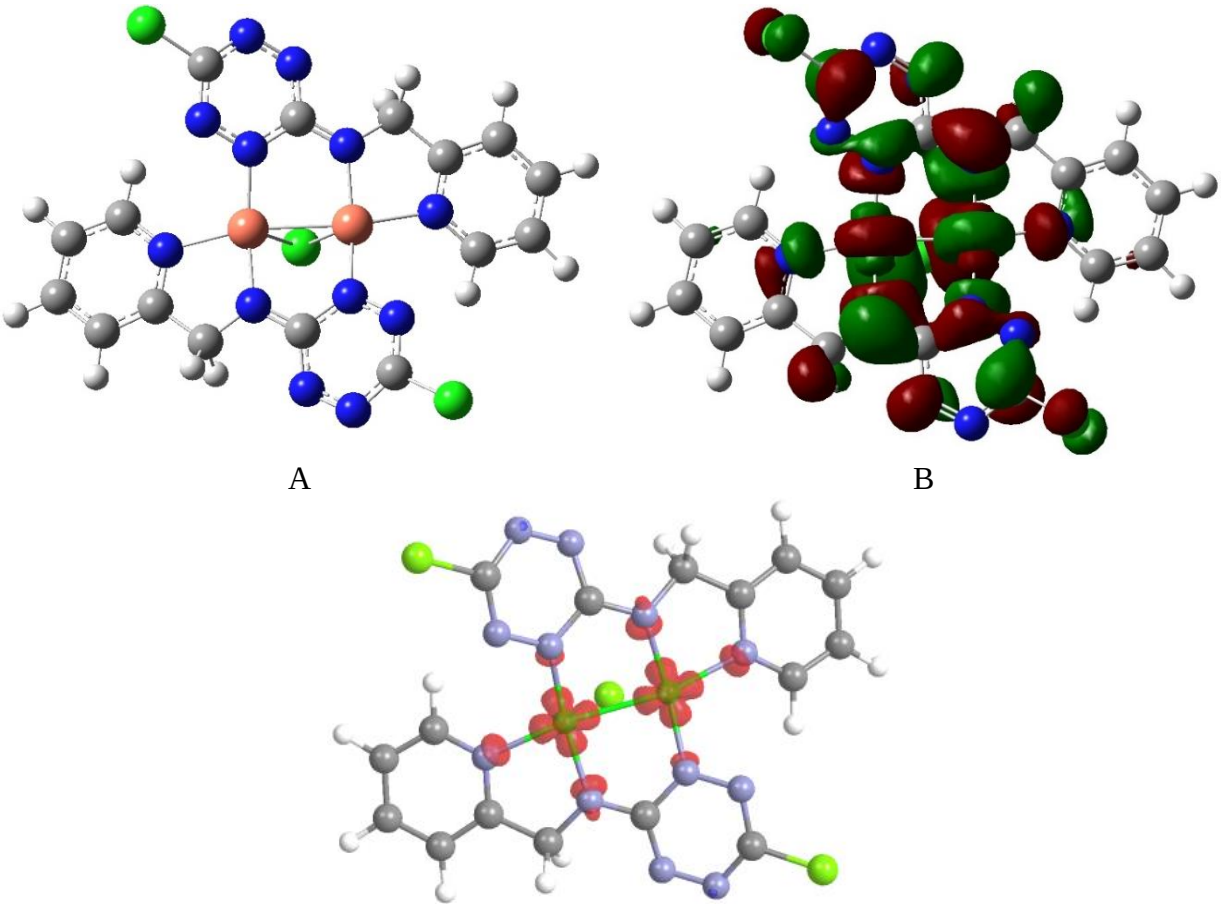

Figure 5.14. The optimized geometry (A) and the graphical representation of the singly occupied molecular orbital (SOMO, orbital 151α) (B) at the M11L/6-311G(d,p) level of theory; spin density map in complex **21** (C) (isovalue 0.006). The spin density value on each Cu equals 0.3846.

Table 5.2. Experimental (X-ray) and calculated (DFT) selected bond lengths (Å) for complex **21**

Bond	Experimental	Calculated	Bond	Experimental	Calculated
Cu1–N1	2.0614(18)	2.007	Cu2–N12	2.0139(18)	2.007
Cu1–N2	1.9329(17)	1.855	Cu2–N11	1.9163(17)	1.855
Cu1–N7	1.9618(17)	1.850	Cu2–N6	1.9404(17)	1.850
Cu1–Cl3	2.4853(6)	2.532	Cu2–Cl3	2.4575(6)	2.532
Cu1–Cu2	2.4313(4)	2.419			

DFT calculations done for complex **22** yield similar results, with the SOMO orbital containing an antibonding combination of the metal d orbitals and the spin density map showing that the unpaired electron is shared between the $d_{x^2-y^2}$ orbitals of the Cu centers (Figure 5.15).

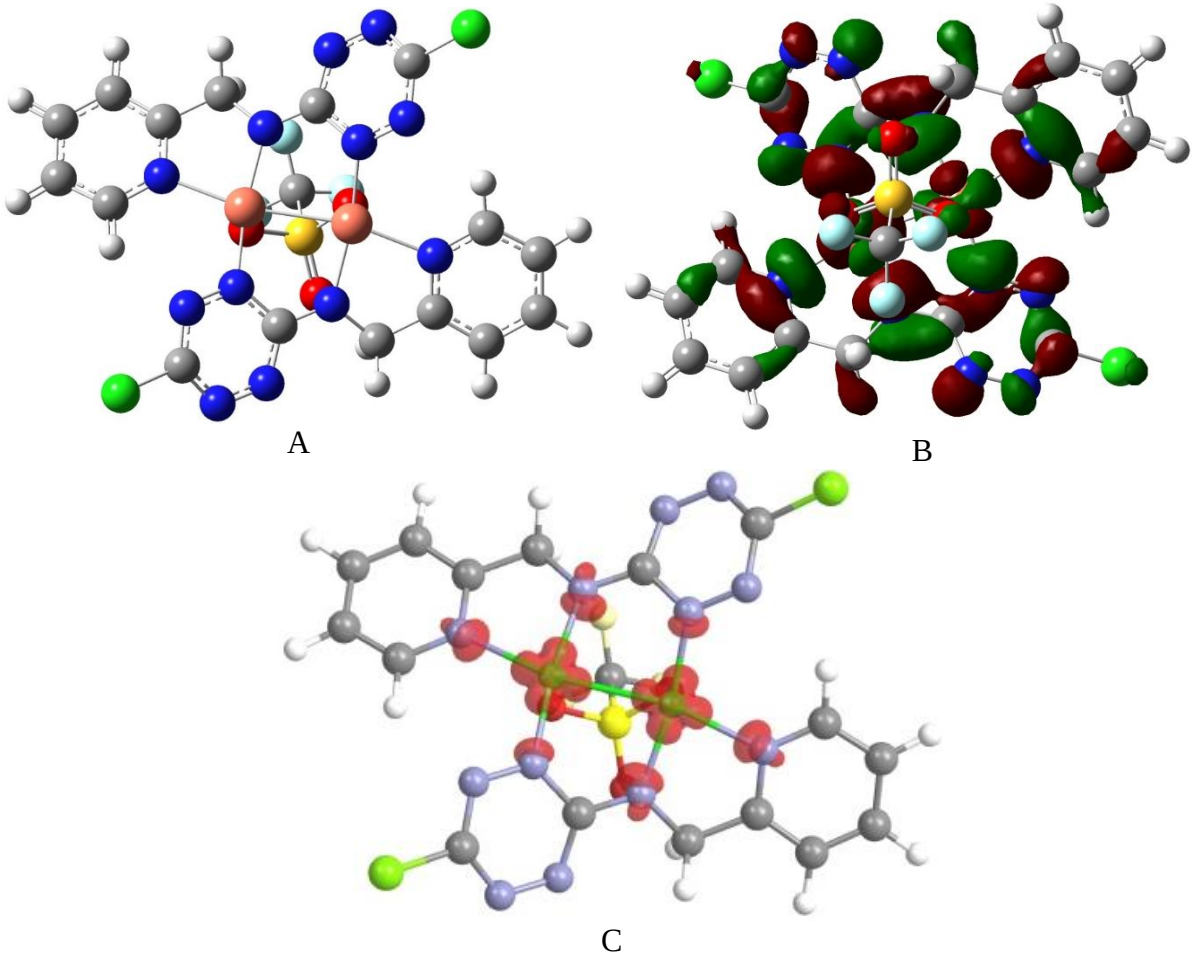

Figure 5.15. The optimized geometry (A) and the graphical representation of the singly occupied molecular orbital (SOMO, orbital 179α) (B) at the M11L/6-311G(d,p) level of theory; Spin density map in complex **22** (isovalue 0.005). The spin density value on each Cu equals 0.3749 (Cu1) and 0.3659 (Cu2).

Table 5.3. Experimental (X-ray) and calculated (DFT) selected bond lengths (Å) for complex **22**

Bond	Experimental	Calculated	Bond	Experimental	Calculated
Cu1–N1	2.028(4)	2.060	Cu2–N12	2.051(4)	2.072
Cu1–N2	1.892(4)	1.909	Cu2–N11	1.903(5)	1.903
Cu1–N7	1.930(5)	1.905	Cu2–N5	1.923(5)	1.902
Cu1–O1	2.372(4)	2.273	Cu2–O2	2.422(5)	2.279
Cu1–Cu2	2.5199(11)	2.490			

The temperature dependent X-band (υ ~ 9.39 GHz) EPR spectra of **2**, recorded in frozen solutions of DMSO/CH_3OH (Figure 5.16), show the typical features of the class III mixed valent Cu^{I}/Cu^{II} complexes. Indeed, the spectra show the distinctive seven-line hyperfine coupling pattern due to the single unpaired electron interacting with two equivalent $I = {}^3/_2$ copper centers, which is particularly evident for the parallel-type transitions, occurring from the lowest (269 mT) to the highest (354 mT) resonant field. Furthermore, the spectral features are temperature independent,

indicating that the delocalization does not depend on temperature, as expected for the class III system. Simulations[30] of the 60 K spectrum (Figure 5.16) provided as best simulation parameters g_x = 2.050 ± 0.005, g_y =2.120 ± 0.005, g_z = 2.158 ± 0.002, with corresponding hyperfine coupling constants of A_x = 30 ± 5 MHz, A_y = 222 ± 3 MHz, A_z = 420 ± 5 MHz. These values point to a considerable rhombicity of the paramagnetic species, in agreement with the structural features obtained by X-ray crystallography. The best simulation parameters are further in the range with those reported for other fully delocalized mixed-valent copper complexes[21, 26-27, 31].

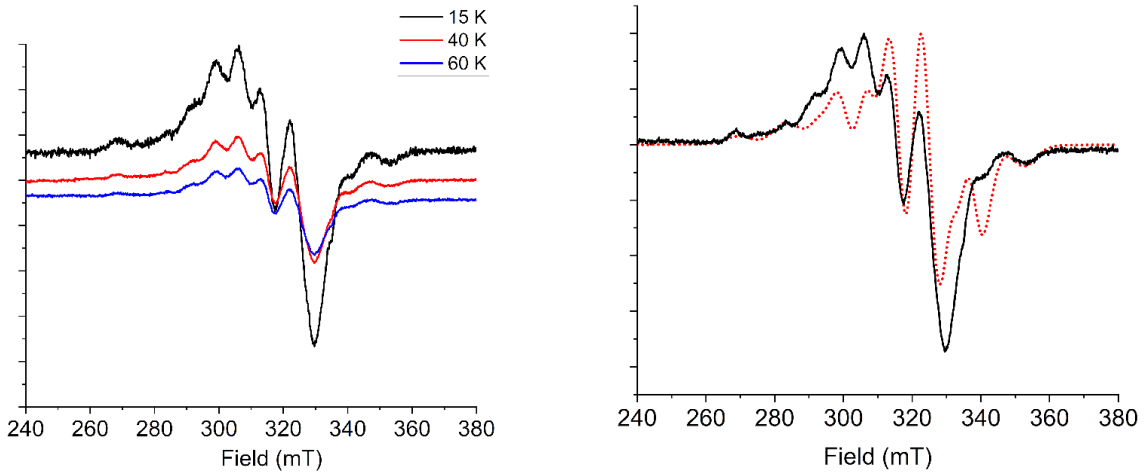

Figure 5.16. Temperature dependence of the X-band EPR spectrum of **21** (left), and comparison between the experimental (continuous black line) and simulated (dotted red line) spectrum at 60 K (right).

The mononuclear complex **20** crystallizes in the monoclinic system, space group $P2_1/n$, with one independent molecule in the unit cell (Figure 5.17, left). The Cu(II) center has a distorted elongated (4+2) octahedral environment, which is very likely a consequence of the Jahn-Teller effect, with the O_4N_2 donor set formed by nitrogen atoms from the amino-pyridine unit and oxygen atoms from two hexafluoro-acetylacetonate ligands. Indeed, the equatorial Cu–O(N) bond lengths range from 1.9476(17) to 1.9826(19) Å, while the apical Cu1–N2 and Cu1-O2 distances measure 2.5906(21) and 2.2694(19) Å, respectively.

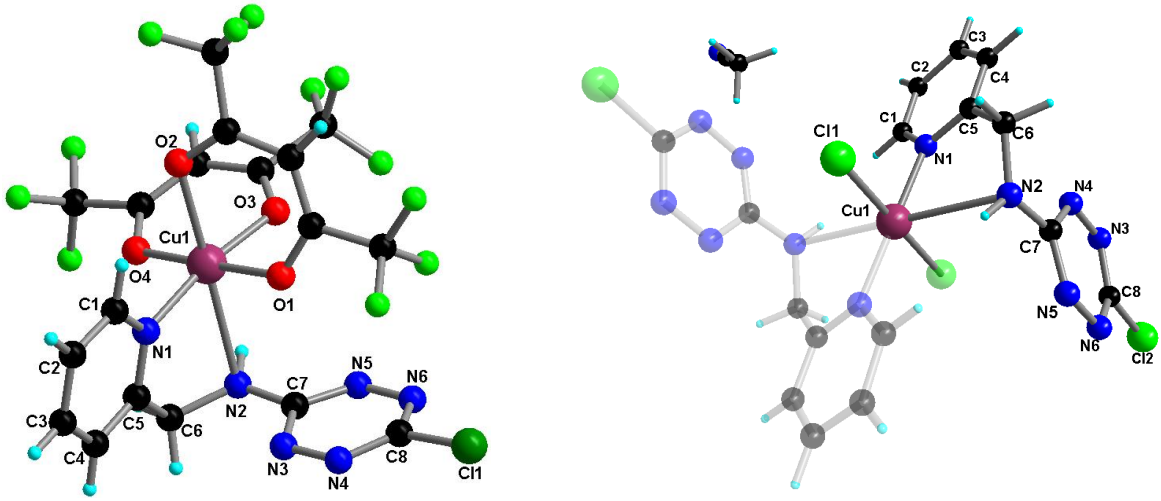

Figure 5.17. The crystal structure of complex **20** together with a partial atom numbering scheme (left) and complex **23** with the independent motif highlighted, together with the atom numbering scheme (right).

Complex **23** crystallizes in the triclinic system, space group *P*-1, with one half independent molecule in general position and the metal ion on an inversion center in the asymmetric unit (Figure 5.17, right). To accommodate the chelation of the metal ion by the amino-pyridine unit, the dihedral angle between the pyridine and tetrazine rings passes from 66.8° in the free ligand to 82.0° in **23**. The metal center shows a distorted elongated octahedral environment (4+2) with a N_4Cl_2 donor sets. The equatorial Cu1–N1 and Cu1-Cl1 bond lengths amount 1.998(2) and 2.3080(6) Å, respectively, while the apical Cu1–N2 distance is 2.675(2) Å. In the crystal packing intermolecular TTZ···TTZ $\pi\ldots\pi$ interactions (3.607 Å) and intramolecular Cl···TTZ anion-π contacts (3.343 Å) are disclosed (figure 5.18).

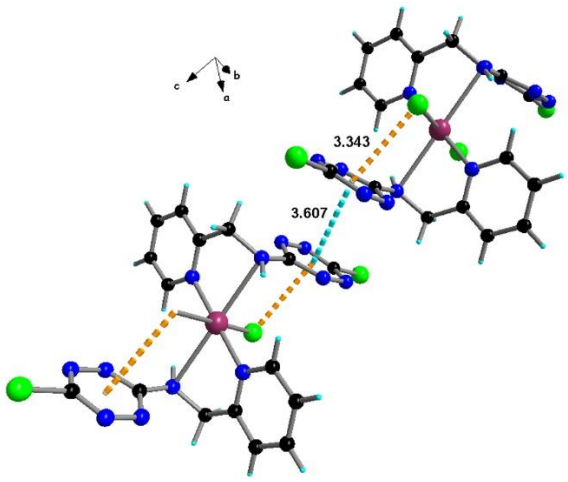

Figure 5.18. Crystal packing in the structure of **23** with an emphasis on the intramolecular Cl···TTZ and intermolecular TTZ···TTZ interactions highlighted in dotted orange and blue lines, respectively.

EPR spectra of **20** and **23** are also substantially different from the one of the binuclear **21**, recorded both in frozen solution and solid state (Figure 5.19), showing typical features of a single Cu(II) center in tetragonally elongated octahedral coordination ($g_{//} >> g_{\perp} > g_e$), with the loss of hyperfine structure because of the intermolecular interaction. The observation of partially resolved superhyperfine structure in frozen solution spectra further indicates partial delocalization of the unpaired electron on the coordinating nitrogen (^{14}N, $I = 1$) atoms.

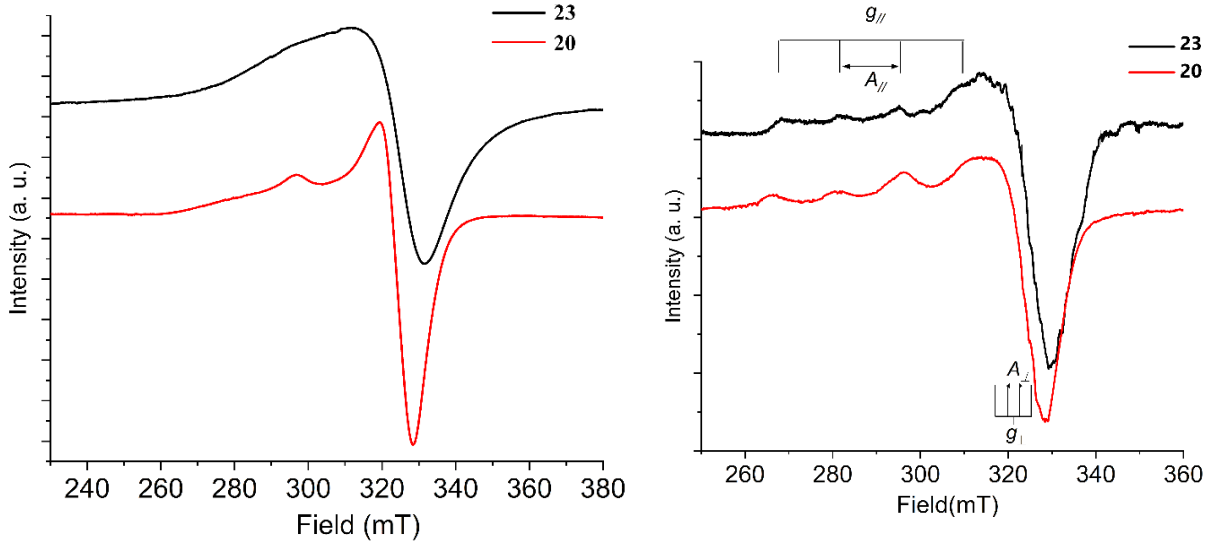

Figure 5.19. X-Band (ν ca. 9.4 GHz) EPR spectra of **23** and **20** recorded at 50 K on microcrystalline powder (left) and frozen solution (right).

5.3. Crystal structure of the H_2L^{15} ligand and its complexes.

Single crystals of the **H_2L^{15}** ligand were grown by slow evaporation of ethyl acetate/dichloromethane (3:1, v/v) solution. The compound crystallizes in the triclinic system, space group *P*–1, with one independent molecule in the unit cell (Figure 5.20). The geometry of the molecule is not linear, and the dihedral angles between the tetrazine and pyridine planes are 77.6 and 70.7° (Figure 5.20, right), respectively. The N–N bonds in the tetrazine ring (1.32 A) show their typical values that are in good agreement with those reported for other tetrazine-based ligands[8, 10] (Table 5.4).

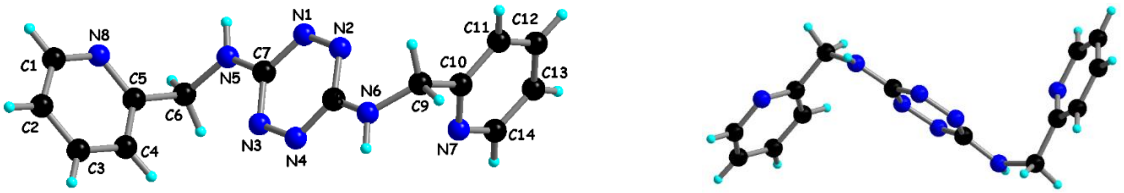

Figure 5.20. Crystal structure of **H_2L^{15}** together with the atom-numbering scheme (left); lateral view of **H_2L^{15}** (right).

Table 5.4. Selected distances (Å) of the **H_2L^{14}** ligand.

C1—N8	**1.3364(16)**	**C8—N2**	**1.3488(15)**
C1—C2	**1.3828(18)**	**C8—N6**	**1.3567(15)**
C2—C3	**1.3738(18)**	**C9—N6**	**1.4487(15)**
C3—C4	**1.3834(17)**	**C9—C10**	**1.5176(16)**
C4—C5	**1.3849(17)**	**C10—N7**	**1.3352(15)**
C5—N8	**1.3404(15)**	**C10—C11**	**1.3884(16)**
C5—C6	**1.5095(16)**	**C11—C12**	**1.3768(18)**
C6—N5	**1.4493(17)**	**C12—C13**	**1.374(2)**
C7—N1	**1.3451(16)**	**C13—C14**	**1.378(2)**
C7—N3	**1.3469(16)**	**C14—N7**	**1.3440(16)**
C7—N5	**1.3538(16)**	**N1—N2**	**1.3263(14)**
C8—N4	**1.3446(16)**	**N3—N4**	**1.3259(14)**

The consideration of the crystal packing of **H_2L^{15}** shows the presence of hydrogen bonds between the amino groups and nitrogen atoms of the pyridine rings to form the $R_2^2(10)$ motif in the Etter's nomenclature[11] (Figure 5.21).

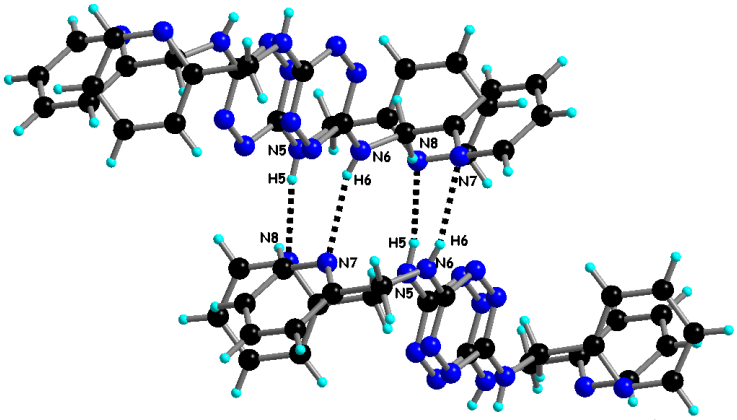

Figure 5.21. Intermolecular hydrogen bonds (broken lines) [d(N(5)···N(8)) = 2,94 Å, ∠(N(5)–H(5)–N(8)) = 167°; d(N(6)···N(7)) = 3,01 Å, ∠(N(6)–H(6)–N(7)) = 157°] in the **H_2L^{15}** structure.

As **H_2L^{15}** is a ditopic ligand containing two chelating units, its reaction with metal centers could, in principle, lead to discrete mono- and dinuclear metal complexes or coordination polymers, depending on the number of available coordination sites on the metal center. Accordingly, this new tetrazine based ligand was used as a chelating unit towards the paramagnetic Co(II), Ni(II) and Cu(II) ions with two coordinative positions in the [M(Hfac)$_2$] precursor. In the beginning, the reaction of **H_2L^{15}** in dichloromethane with one equivalent of [M(Hfac)$_2$] in CH_3CN afforded the series of mononuclear complexes [Cu(Hfac)$_2$(H_2L^{15})] (**24**), [Ni(Hfac)$_2$(H_2L^{15})] (**25**), [Co(Hfac)$_2$(H_2L^{15})]·CH_3CN (**26**) (Figure 5.22). It should be noted that the amine groups of the **H_2L^{15}** ligand remain protonated during the coordination process.

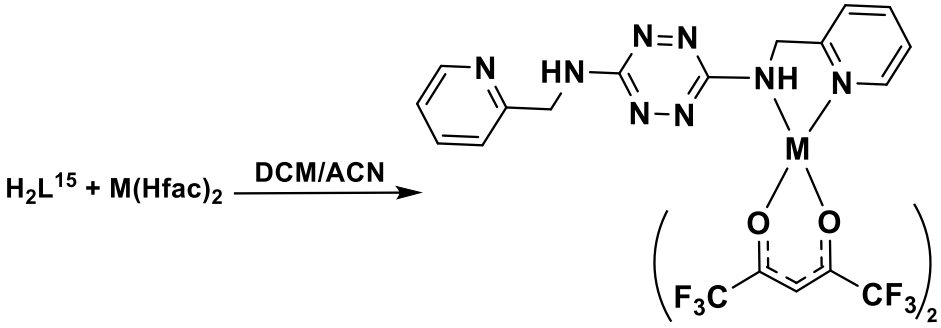

Figure 5.22. Synthesis of the mononuclear **24-26** complexes.

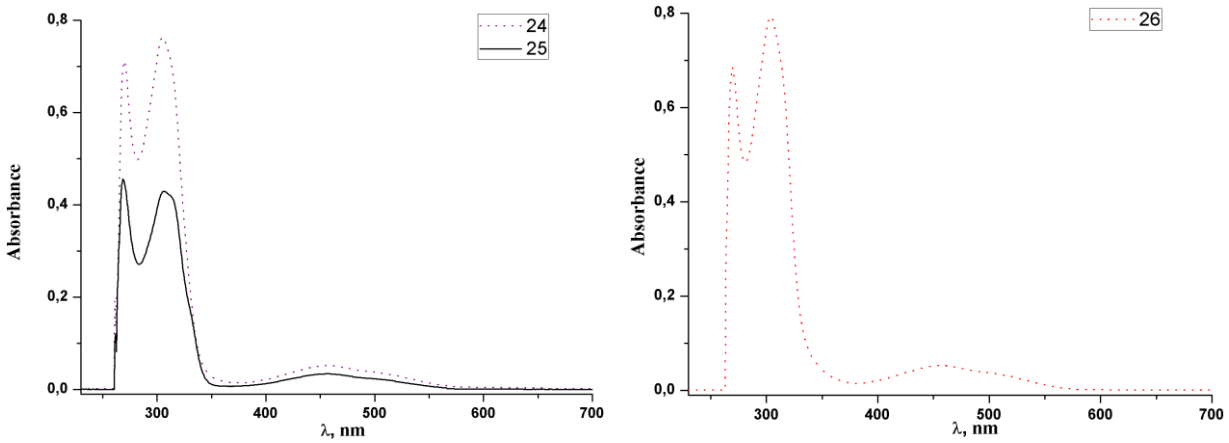

Figure 5.23. UV/Vis spectra of **24** (C_M = 3,89·10^{-5} M), **25** (C_M = 1,83·10^{-5} M) and **26** (C_M = 3,59·10^{-5} M) in methanol.

The UV/Vis absorption spectra of **24-26** in methanol solutions at room temperature are shown in Figure 5.23. The three compounds studied exhibit common absorption bands at λ ≈ 270 nm, which corresponds to π–π* transitions, and a broad band between λ = 400 and 500 nm for overlapping π–π* and n–π* transitions that are essentially centered on the tetrazine unit[8, 32]. In addition, the two metal complexes display a third absorption band at λ ≈ 305 nm, which corresponds to the *π–π** intraligand transitions of the diketonato groups[32].

Single crystal X-ray diffraction analysis revealed that complexes **24**, **25** are isostructural and crystallize in the monoclinic system. The **H_2L^{15}** ligand coordinates to the metal ions through the nitrogen atoms of the picolylamine fragment, thus providing the octahedral environment (MO_4N_2 chromophore) of each metal center (Figure 5.24).

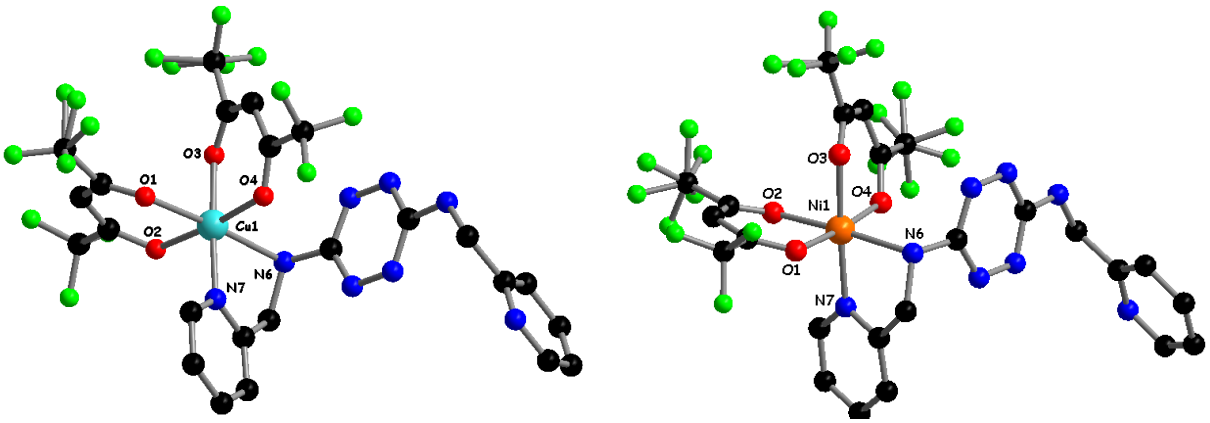

Figure 5.24. The crystal structure of the **24** complex (left) and **25** (right) together with the atom numbering scheme. Hydrogen atoms were omitted.

The higher distortion of the octahedron of Cu(II) ion compared to Ni(II) observed in the structures **24** and **25**, is very likely due to the Jan-Teller effect. The Cu–O(N) bond distances vary from 1.940(2) to 2.318(3) Å, while for Ni–O(N) in **25** this range is much narrower [2,016(2)–2,170(2) Å]. The *cis* and *trans* O–Cu–O(N) bond angles span from 85.64(10) to 95.63(12)° and from 173.26(10) to 174.72(12)°, respectively. The corresponding angles for nickel complex **25** are similar to those in complex **24**: 85,53(8)–95,00(9) ° and from 174,78(8) to 175,57(9)°.

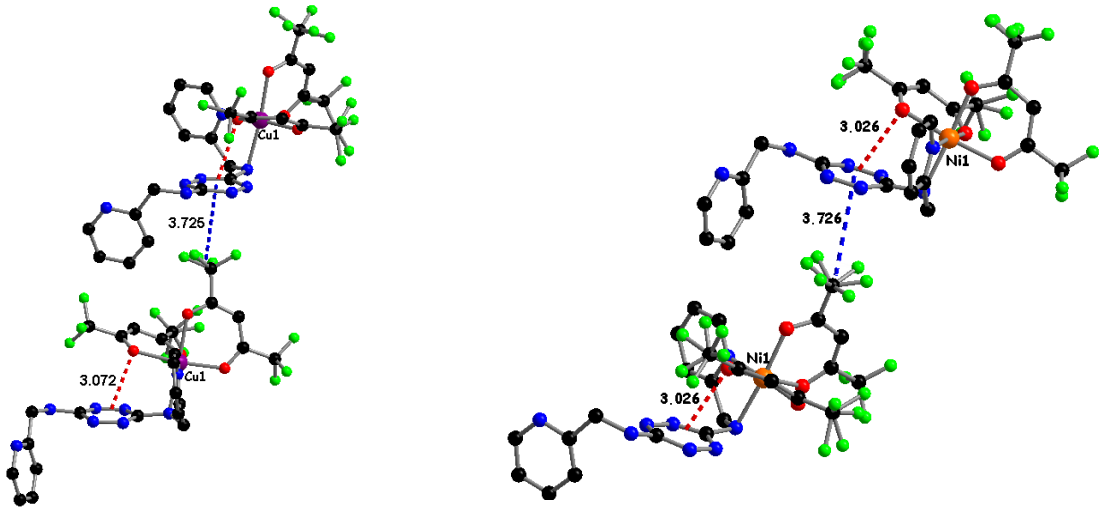

Figure 5.25. Anion–π interactions between tetrazine units and fluorine atoms (blue lines), tetrazine units and oxygen atoms (red line) in **24** (left) and **25** (right). Hydrogen atoms were omitted for clarity.

The crystal packing of **24** and **25** is stabilized by the intermolecular anion–π interactions between tetrazine units and fluorine/oxygen atoms (Figure 5.25).

Mononuclear Co-complex **26** is not isostructural to **24** and **25**, and crystallizes in the triclinic system, space group *P*–1, with one independent complex molecule and one acetonitrile solvent

molecule in the unit cell (Figure 5.26). It should be noted that the coordination of the metal ion influences the geometry of the ligand, as the angles between the tetrazine and the pyridine planes in **26** are nearly 90°.

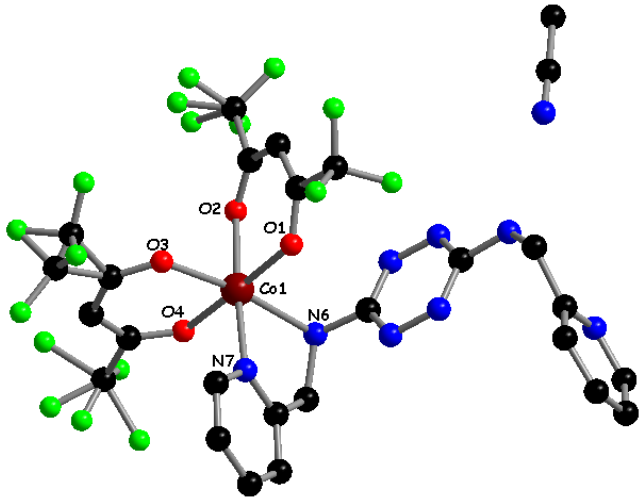

Figure 5.26. The crystal structure of complex **26** together with an atom numbering scheme. Hydrogen atoms were omitted.

Cobalt(II) ion shows a distorted octahedral environment (5+1) with an O_4N_2 donor set formed by nitrogen atoms from the amine group (N6) and pyridine ring (N7) and the oxygen atoms from the two *hfac* ligands. The equatorial Co–O(N) bond lengths range from 2.043(4) to 2.083(4) Å, whereas the apical Co–N6 distance is 2.255(4) Å. The O–Co–O(N)$_{cis}$ bond angles vary from 87.01(17) to 97.80(15)°, whereas the O–Co–O(N)$_{trans}$ angles span from 171.37(16) to 177.72(17)°.

The packing is stabilized by intermolecular interactions as well as $\pi\cdots\pi$ stacking between the pyridine and TTZ rings (3.962 and 3.456 Å, respectively; Figure 5.27). The shortest intermolecular cobalt–cobalt separation is 8.4075(57) Å.

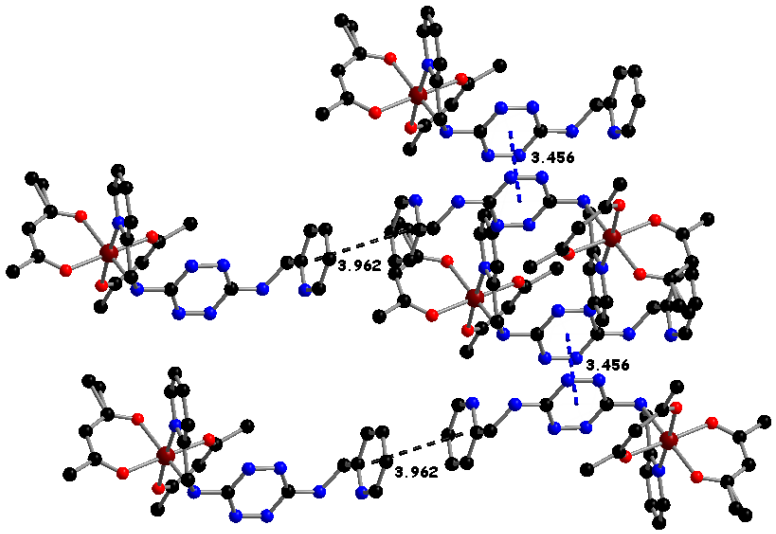

Figure 5.27. Interaction between tetrazine (blue line) and pyridine rings (black line) in **26**.

As mentioned above, the **H_2L^{15}** ligand contains two chelating units and its reaction with metal centers could, in principle, lead to discrete mono- and dinuclear metal complexes. The reaction of **H_2L^{15}** in dichloromethane in excess of [M(Hfac)$_2$] leads to the series of binuclear complexes [{Cu(Hfac)$_2$}$_2$(H_2L^{15})]·2CH_3OH (**27**), [{Ni(Hfac)$_2$}$_2$(H_2L^{15})]·2CH_3CN (**28**), {[Co(Hfac)$_2$(H_2L^{15})]·[Co(Hfac)$_2$(CH_3OH)$_2$]}$_n$ (**29**) (Figure 5.28).

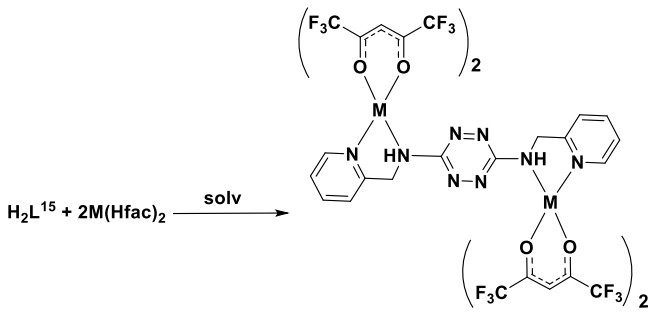

Figure 5.28. Synthesis of the mononuclear complexes **27**, **28**.

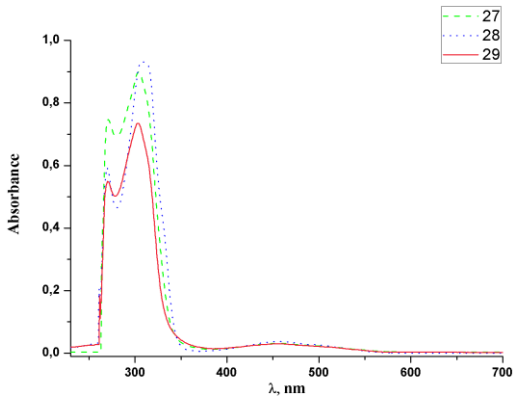

Figure 5.29. UV/Vis spectra of **27** (C_M = 1,14·10^{-5} M), **28** (C_M = 1,21·10^{-5} M) and **29** (C_M = 1,30·10^{-5} M) in methanol.

The normalized UV/Vis absorption spectra of **27-29** in methanol solutions at room temperature are shown in Figure 5.29 The three compounds studied exhibit common absorption bands at $\lambda \approx 270$ nm, which correspond to the π–π* transitions, and a broad band between λ = 400 and 550 nm for overlapping π–π* and n–π* transitions that are essentially centered on the tetrazine unit.

All the compounds crystallize in the triclinic system, possessing similar structures, however, they are not isostructural. X-Ray analysis revealed that complexes **27** and **28** are discrete binuclear molecular compounds, while **29** possesses a polymeric structure.

The crystal structures of complexes **27** and **28** is are shown in Figure 5.30.

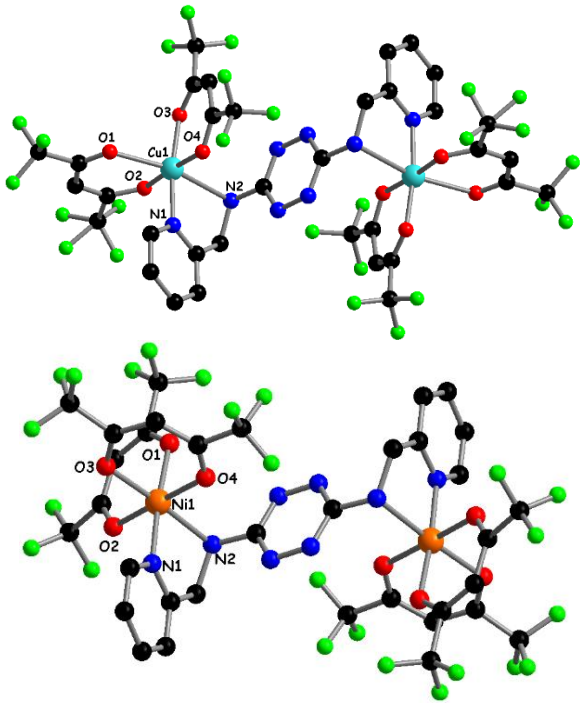

Figure 5.30. The crystal structures of **27** (top) and **28** (bottom). Hydrogen atoms and solvent molecules were omitted.

The coordination environment of Cu(II) ions in **27** is elongated octahedron, due to the Jan-Teller effect. The equatorial Cu–O(N) bond lengths vary from 1.960(3) to 1.995(4) Å, while the apical Cu–O1, Cu–N2 distances are 2.270(4) and 2.498(5) Å, respectively. The O–Cu–O(N)$_{cis}$ bond angles vary from 86.95(14) to 92.29(14)°, while O–Cu–O(N)$_{trans}$ angles span from 165.82(14) to 176.42(14)°.

Ni(II) ion in **28** exhibits distorted octahedral geometry (5+1) with a much narrower range of equatorial Ni–O(N) bond lengths [2.0230(17)–2.0399(19) Å].

The apical Ni–N2 distance is 2.1810(18) Å. The tight range of angle's value [*cis*- and *trans*-angles are in the range 86,40(7)–97,17(7)° and 175,10(7)–176,76(6)°, respectively] indicate the lower distortion of coordination polyhedra compared to Cu complex **27**.

Additional anion···π interactions between tetrazine ring and oxygen atom (3.325 Å) and π···π interactions between pyridine rings (3.863 Å) were found for complex **27** (Figure 5.31).

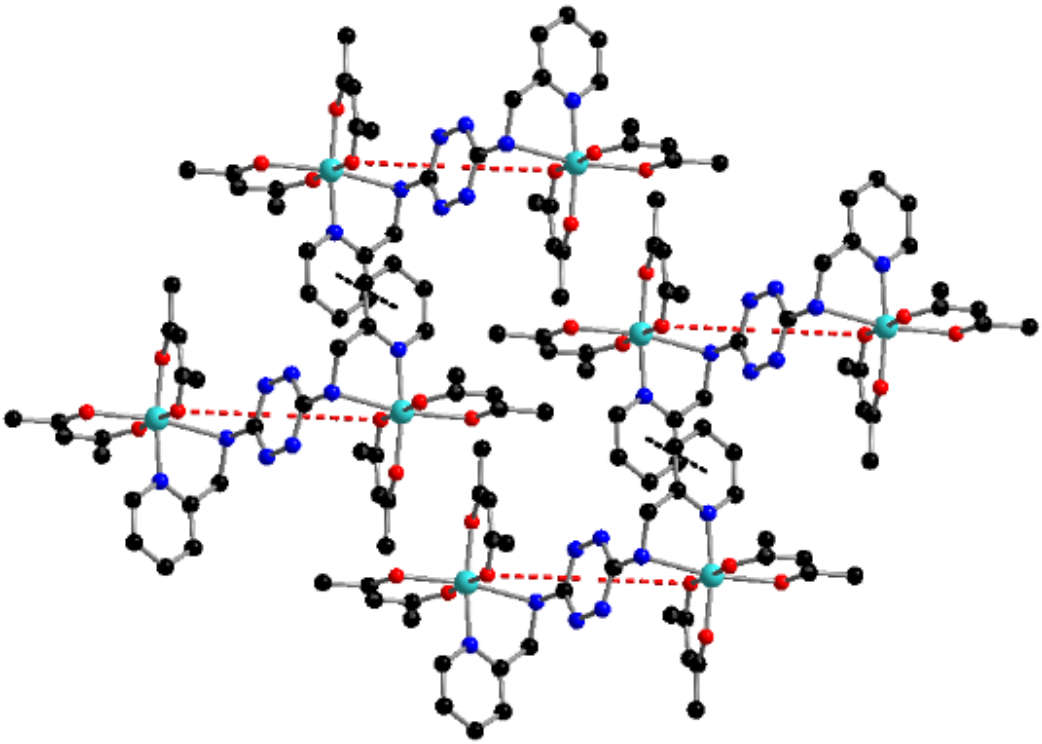

Figure 5.31. Anion···π interactions (red dotted line) and π···π interactions (black dotted line) in **27**. Hydrogen and fluorine atoms were omitted.

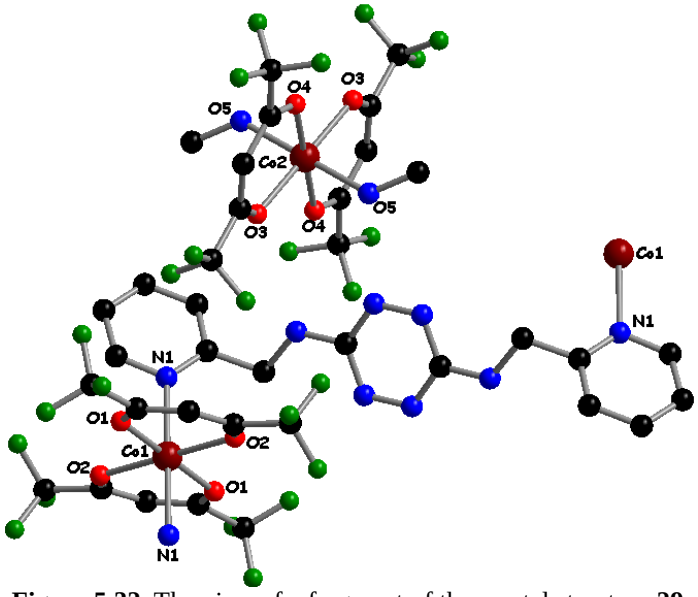

Figure 5.32. The view of a fragment of the crystal structure **29**. Hydrogen atoms were omitted.

Complex **29** crystallizes in the triclinic system, space group *P*–1, with half of a ligand and $Co(Hfac)_2$ as the independent motifs in the unit cell (Figure 5.32); thus, both metal ions have a site occupancy factor of 0.5. X-Ray analysis indicated the formation of cocrystals composed of the $[Co(Hfac)_2(\mu\text{-}H_2L^{15})]_n$ chain, in which the H_2L^{15} ligand adopts a bismonodentate bridging mode through the two pyridyl nitrogen atoms, and the mononuclear $[Co(Hfac)_2(CH_3OH)_2]$ complex.

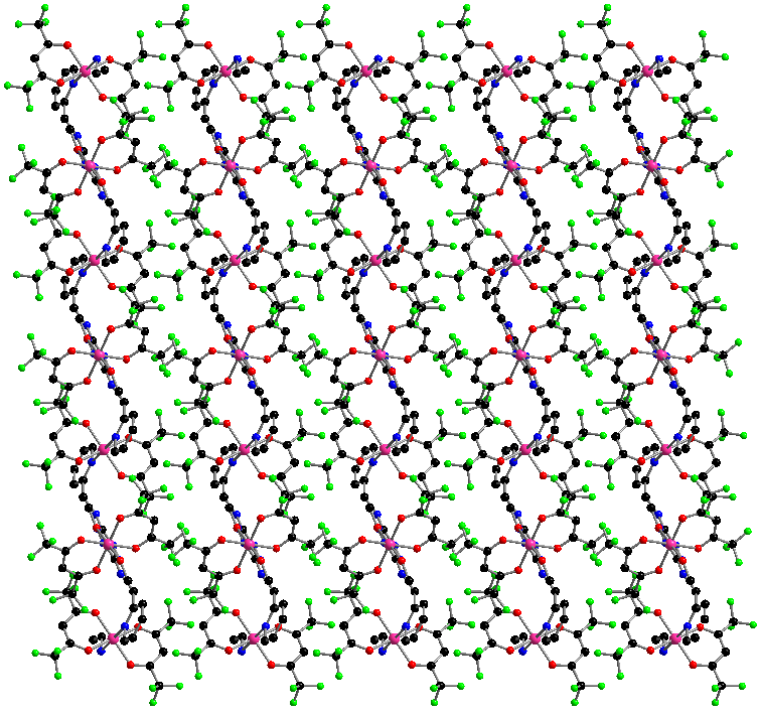

Figure 5.33. Packing diagram for **29** showing the zigzag chain along the crystallographic *b* axis. The hydrogen atoms were omitted for clarity

The Co1 ion has a distorted octahedral environment (4+2, CoO_4N_2 chromophore). The equatorial Co–O bond lengths are 2.0337(16) and 2.0616(16) Å, whereas the apical Co–N bond length is 2.215(2) Å. The coordination of the nitrogen atoms to the Co1 atom in **29** in the axial positions leads to the formation of a zigzag chain along the *b* direction (Figure 5.33). The O–Co–O(N)$_{cis}$ bond angles vary from 85.83(7) to 92.16(7)°, whereas the O(N)–Co–O(N)$_{trans}$ angles are 180°. It should be noted that the utilization of the same reaction conditions to obtain the binuclear Co complex, similar to the Cu and Ni compounds, did not allow any convincing results. Thus, the crystalline mixture of [Co(Hfac)$_2$(H$_2$L^{15})]·CH$_3$CN (**26**) and Co(Hfac)$_2$ was isolated.

5.4. Magnetic properties

5.4.1. Binuclear mixed valence [*Cu$_2$(μ$_2$-Cl)(L^{14})$_2$] (**21**) complex*

The magnetic properties of the mixed valence complex **21** have been investigated in collaboration with L. Sorace, University of Florence, Italy.

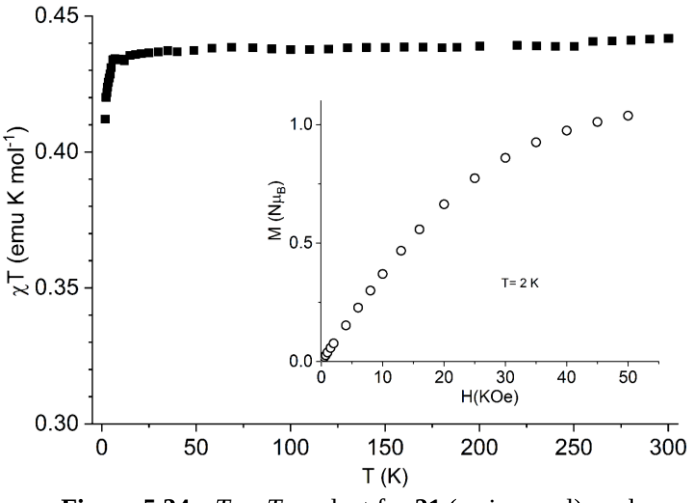

Figure 5.34. χT vs T product for **21** (main panel), and isothermal field dependent magnetization measured at 2 K.

The temperature dependence of the χT product, reported in Figure 5.34, confirms the presence of a single unpaired electron per molecule. The value is essentially constant throughout all temperature range investigated at 0.43 emu·K·mol^{-1}, which is consistent with the Curie value expected for the average g = 2.15 and S = ½ (0.375 emu·K·mol^{-1}). The decrease observed at low temperature

can be attributed to either saturation effects or weak intermolecular interactions. The persistence of the S = ½ state at low temperature is evidenced by the value of the isothermal magnetization measured at 2 K, pointing to a saturation value slightly higher than 1 μ_B per molecule.

*5.4.2. Mononuclear [Co(Hfac)$_2$(H$_2$L^{15})]·CH$_3$CN (**26**) complex*

The magnetic properties of complexes **26** and **29** have been investigated in collaboration with M. Julve and F. Lloret, University of Valencia, Spain.

The direct-current (dc) magnetic properties of complex **26** in the form of a plot of $\chi_M T$ *vs* T are shown in Figure 5.35. At room temperature, $\chi_M T$ is 2.90 cm^3·mol^{-1}·K, which is higher than the spin-only value (1.874 cm^3·mol^{-1}·K for S_{Co} = 3/2 and g = 2.0) and it indicates a significant orbital contribution to the magnetic moment[33]. Upon cooling, $\chi_M T$ continuously decreases to the value of 1.67 cm^3·mol^{-1}·K at 1.9 K. No maximum was observed in the χ_M *vs* T plot. The possible reason for the decrease of $\chi_M T$ in complex **26** might be due to the intermolecular antiferromagnetic interactions between the Co(II) ions or the depopulation of the higher energy Kramers doublets of the six coordinate Co(II) centers, or both. Owing to the mononuclear nature of **26** and the large value for the shortest intermolecular Co···Co distance (8.41 Å), the magnetic interaction between the metals center is expected to be negligible. The magnetic data of **26** were analyzed with the Hamiltonian:

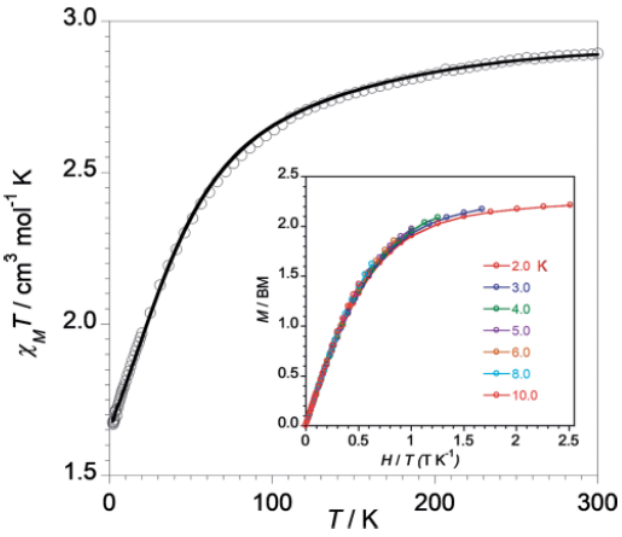

Figure 5.35. Temperature dependence of the $\chi_M T$ for **26**: (o) experimental, (—) best-fit curves. The inset shows the M versus H/T plots in the temperature range 2.0–10.0 K.

$$\boldsymbol{H} = -\alpha\lambda \boldsymbol{L}\cdot\boldsymbol{S} + \Delta[\boldsymbol{L}^2_z - 1/3L(L+1)] + \beta H(-\alpha\boldsymbol{L} + g_e\boldsymbol{S})$$

The first term in this equation accounts for the spin-orbit coupling with $\alpha = A\kappa$; A is a parameter with a value that depends on the strength of the crystal field (A = 1.5 and 1 for the weak and strong crystal-field limits, respectively), κ is the orbital reduction factor, and λ is the spin-orbit coupling constant. The second term is responsible for the axial distortion on the six-coordinate cobalt(II) ion, and the last term corresponds to the Zeeman interaction. The best-fit parameters for compound **26** are: α = 1,31(1), Δ = 534(25) cm^{-1} i λ = –130(2) cm^{-1}. One can see in figure 5.35 that the theoretical curve matches well the experimental data over the whole temperature range explored. All of these values are similar to those found for other octahedral Co(II) complexes.

To check the possible single-ion magnet (SIM) characteristics of **26**, the frequency-dependent alternating-current (ac) magnetic susceptibility was measured in the temperature range from 8.0 to 2.0 K. No out-of-phase signals (χ''_M) were observed in the absence of any external static field. The application of the external dc fields of 1000 and 2500 G (Figure 5.36, left) clearly resulted in the signals for both components as a function of frequency in the above temperature range. The high-temperature data can be fitted to the exponential Arrhenius expression, as expected for the thermally activated Orbach process (Figure 5.36, right).

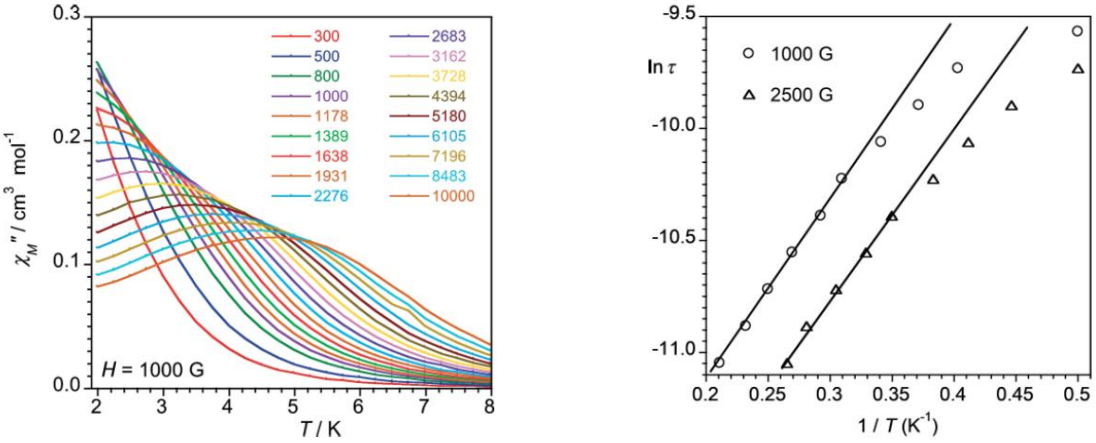

Figure 5.36. Frequency dependence of the ac out-of-phase molar magnetic susceptibility of **26** under the applied static field of H_{dc} = 1000 G in the temperature range 2.0–8.0 K (left) and the Arrhenius plots for **26** under the applied static fields of 1000 (o) and 2500 G (Δ) (right).

The best-fit parameters for the effective energy barriers for the reversal of the magnetization are (E_a) of 5.8(2) (H_{dc} = 1000 G) and 5.3(2) cm^{-1} (H_{dc} = 2500 G) with pre-exponential factors (τ_0) of 2.8·10^{-6} (H_{dc} = 1000 G) and 2.2·10^{-}6 (H_{dc} = 2500 G). From the equation $E_a = D(S^2 - ¼)$, a rough estimate for $|D|$ of ca. 2.7 cm^{-1} results for compound **26**.

The attempt to fit the relaxation times of **26** to the combination of two processes, videlicet, the one-phonon direct and the two-phonon Raman processes has been made through the following equation: .

$$\tau^{-1} = A_{direct}T + B_{Raman}T^n$$

The best-fit parameters are: A = 4500 s^{-1}·K–1, B = 500 s^{-n} (where n = 2.9 at H_{dc} = 1000 G); A = 5900 s^{-1}·K^{-1}, B = 490 s^{-n} (where n = 3.3 at H_{dc} = 2500 G). The Cole–Cole plots for **26** in the temperature range 2.0–4.75 K (Figure 5.37) exhibit semicircular shapes, as expected for the Orbach processes.

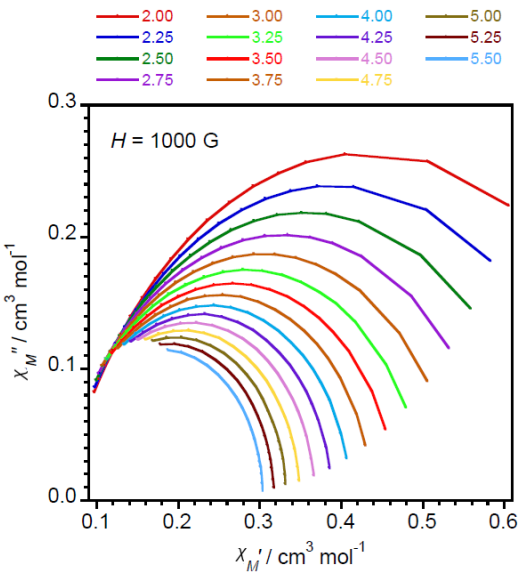

Figure 5.37. The Cole-Cole plot for **26** at H_{dc} = 1000 G.

*5.4.3. Polymeric {[Co(Hfac)$_2$(H$_2$L^{15})]·[Co(Hfac)$_2$(CH$_3$OH)$_2$]}$_n$ (**29**) complex*

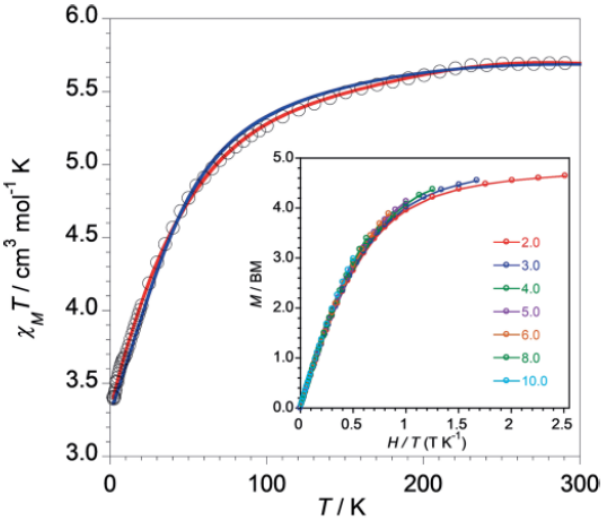

Figure 5.38. Temperature dependence of the $\chi_M T$ product (o) for 3: blue line: best-fit curve for the equivalent Co(1) and Co(2); red line: best-fit curves for the nonequivalent Co(1) and Co(2). The inset shows the M versus H/T plots in the temperature range of 2.0–10.0 K

The direct-current magnetic properties of **29** are shown in the plot of $\chi_M T$ *vs* T (Figure 5.38). The value of $\chi_M T$ is 5.69 cm^3·mol^{-1}·K at room temperature, is higher than the spin-only (3.758 cm^3·mol^{-1}·K for the two isolated spin quartets with g = 2.0) due to the unquenched angular momentum of the six-coordinate high-spin Co(II) ions. The $\chi_M T$ value for **29** decreases continuously with the temperature and reaches the value of 3.37 cm^3·mol^{-1}·K at 1.9 K. The reason for this decrease could be the thermal depopulation of the higher energy Kramers doublets of the Co(II) centers, the antiferromagnetic interactions between the high-spin cobalt(II) ions, or both. Separation between the Co centers across the extended the **H$_2$L^{15}** ligand bridge in the chain motif and also between the chain and the mononuclear units (ca. 12.18 and 8.13 A, respectively) allow us to discard the possibility of the magnetic exchange between the local spin quartets in **29**. The magnetic data of **29** were analyzed with the Hamiltonian:

$$\boldsymbol{H} = -\alpha_1\lambda_1\boldsymbol{L}_1\cdot\boldsymbol{S}_1 - \alpha_2\lambda_2\boldsymbol{L}_2\cdot\boldsymbol{S}_2 + \Delta_1[\boldsymbol{L}^2_{z,1} - 1/3L(L+1)] + \Delta_2[\boldsymbol{L}^2_{z,2} - 1/3L(L+1)] + \beta H[-\alpha_1\boldsymbol{L}_1 - \alpha_2\boldsymbol{L}_2 + g_e(\boldsymbol{S}_1 + \boldsymbol{S}_2)]$$

Two approaches for the reconstruction of magnetic behavior were applied. First-one considered that the two cobalt(II) ions in **29** (Co1 and Co2) are equivalent. The best-fit parameters for the experimental data in this case are α = 1.29(1), Δ = 477(20) cm^{-1}, and λ = –118(1) cm^{-1}. Although the calculated curve (blue line in figure 5.38) reproduces the experimental data well. But, the fact that the coordination environment of the two Co^{II} ions in complex **29** are different (Co1O$_4$N$_2$ and Co2O$_6$ chromophores) prompted us to try the fit for the two nonequivalent paramagnetic centers. This appeared to be quite difficult due to a large number of the parameters involved. To overcome these difficulties, a value of zero was fixed for Δ_2 in the fit because of the quasi-ideal O_h symmetry at Co2, whereas a positive value was assigned to Δ_1 because of the elongated octahedral geometry at Co1. The new conditions led to the following values: α_1 = 1.32(1), Δ_1 = 736(12) cm^{-1}, λ_1 = –110(2) cm^{-1}, α_2 = 1.39(1), Δ_2 = 0 cm^{-1} (fixed), and λ_2 = –130(2) cm^{-1}. Red solid line in Figure 5.38 represents the calculated curve and matches very well the magnetic data recorded.

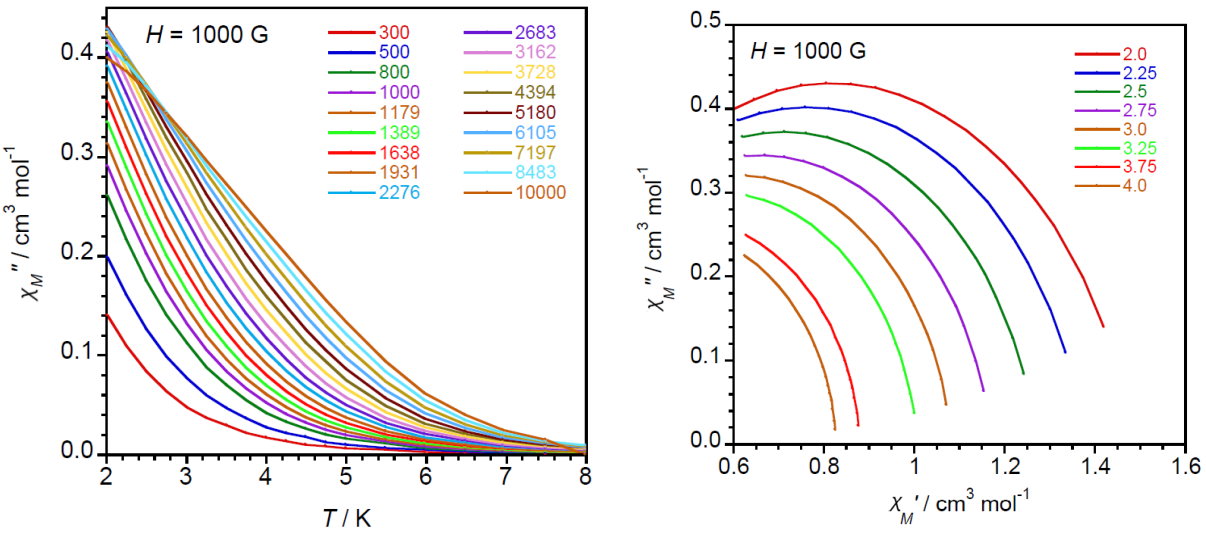

Figure 5.39. Frequency dependence of the ac out-of-phase molar magnetic susceptibility of **29** under the applied static field of H_{dc} = 1000 G in the temperature range of 2.0–8.0 K (left) and the Cole-Cole plot for **29** at H_{dc} = 1000 G (right).

The frequency-dependent ac magnetic susceptibility for complex **29** was measured in the temperature range of 2.0–8.0 K. Similarly, with mononuclear Co-complex **26**, no out-of-phase signals were observed in the absence of the external magnetic field. However, under a 1000 G external static field, the incipient out-of-phase frequency-dependent signals were observed (Figure 5.39, left), which are indicative of SIM behavior. The Cole-Cole plots showing the inceptive semicircles are shown in Figure 5.39 (right).

5.5. Conclusion.

1,2,4,5-tetrazine based picolylamine ligands (**HL**[14], **H$_2$L**[15]) were obtained by the nucleophilic mono- or di-substitution reaction using 3,6-dichloro-1,2,4,5-tetrazine. X-ray diffraction analysis showed that in the case of **HL**[14] and **H$_2$L**[15] a 2*D* lattice that involve a $R_2^2(10)$ motif were formed due to intermolecular hydrogen bonds.

The reaction of **HL**[14] with copper(II) precursors afforded mixed valence Cu(II)/Cu(I) complexes. EPR spectroscopy indicated a temperature-independent delocalization of the unpaired electron between the two copper atoms.

A series of mono- and binuclear cobalt(II), copper(II) and nickel(II) complexes with the ditopic **H$_2$L**[15] ligand has been prepared.

The investigation of magnetic properties has been done for the complexes $[Co(Hfac)_2(H_2L^{15})]\cdot CH_3CN$ (**26**) and $\{[Co(Hfac)_2(H_2L^{15})]\cdot[Co(Hfac)_2(CH_3OH)_2]\}_n$ (**29**). Slow relaxation of the magnetization at low temperatures (2 – 8 K) has been observed, indicating a single molecule magnet behaviour.

References

1. Jordan, B. J.; Pollier, M. A.; Miller, L. A.; Tiernan, C.; Clavier, G.; Audebert, P.; Rotello, V. M., *Org. Lett.* **2007,** *9*, 2835-2838.

2. Qing, Z.; Audebert, P.; Clavier, G.; Miomandre, F.; Tang, J.; Vu, T. T.; Méallet-Renault, R., *J. Electroanal. Chem.* **2009,** *632*, 39-44.

3. Zhou, Q.; Audebert, P.; Clavier, G.; Méallet-Renault, R.; Miomandre, F.; Shaukat, Z.; Vu, T.-T.; Tang, J., *The Journal of Physical Chemistry C* **2011,** *115*, 21899-21906.

4. Parimal, K.; Vyas, S.; Chen, C.-H.; Hadad, C. M.; Flood, A. H., *Inorg. Chim. Acta* **2011,** *374*, 620-626.

5. Kurach, E.; Djurado, D.; Rimarčik, J.; Kornet, A.; Wlostowski, M.; Lukeš, V.; Pécaut, J.; Zagorska, M.; Pron, A., *PCCP* **2011,** *13*, 2690-2700.

6. Woods, T. J.; Ballesteros-Rivas, M. F.; Ostrovsky, S. M.; Palii, A. V.; Reu, O. S.; Klokishner, S. I.; Dunbar, K. R., *Chem. Eur. J.* **2015,** *21*, 10302-10305.

7. Woods, T. J.; Stout, H. D.; Dolinar, B. S.; Vignesh, K. R.; Ballesteros-Rivas, M. F.; Achim, C.; Dunbar, K. R., *Inorg. Chem.* **2017,** *56*, 12094-12097.

8. Nazarenko, I.; Pop, F.; Sun, Q.; Hauser, A.; Lloret, F.; Julve, M.; El-Ghayoury, A.; Avarvari, N., *Dalton Trans.* **2015,** *44*, 8855-8866.

9. Clavier, G.; Audebert, P., *Chem. Rev.* **2010,** *110*, 3299-3314.

10. Kaim, W., *Coord. Chem. Rev.* **2002,** *230*, 127-139.

11. Etter, M. C., *Acc. Chem. Res.* **1990,** *23*, 120-126.

12. Ren, T., *Coord. Chem. Rev.* **1998,** *175*, 43-58.

13. Baldamus, J.; Berghof, C.; Cole, Marcus L.; Hey-Hawkins, E.; Junk, Peter C.; Louis, Lance M., *Eur. J. Inorg. Chem.* **2002,** *2002*, 2878-2884.

14. Junk, P. C.; Cole, M. L., *Chem. Commun.* **2007,** *16*, 1579-1590.

15. Jones, C.; Schulten, C.; Fohlmeister, L.; Stasch, A.; Murray, K. S.; Moubaraki, B.; Kohl, S.; Ertem, M. Z.; Gagliardi, L.; Cramer, C. J., *Chem. Eur. J.* **2011,** *17*, 1294-1303.

16. Tanaka, S.; Mashima, K., *Dalton Trans.* **2013,** *42*, 2831-2840.

17. Chiarella, G. M.; Feng, C.; Murillo, C. A.; Zhao, Q., *Inorg. Chem.* **2016,** *55*, 9471-9481.

18. Gámez-Rivera, S. A.; Francos, J.; Borge, J.; Cadierno, V., *Eur. J. Inorg. Chem.* **2017,** *2017*, 4138-4146.

19. Sadhukhan, D.; Rizzoli, C.; Garribba, E.; Gómez-García, C. J.; Yahia-Ammar, A.; Charbonnière, L. J.; Mitra, S., *Dalton Trans.* **2012,** *41*, 11565-11568.

20. Vinogradova, K. A.; Krivopalov, V. P.; Nikolaenkova, E. B.; Pervukhina, N. V.; Naumov, D. Y.; Rakhmanova, M. I.; Boguslavsky, E. G.; Sheludyakova, L. A.; Bushuev, M. B., *Polyhedron* **2013,** *57*, 1-13.

21. Tong, M.-L.; Li, L.-J.; Mochizuki, K.; Chang, H.-C.; Chen, X.-M.; Li, Y.; Kitagawa, S., *Chem. Commun.* **2003,** *3*, 428-429.

22. Jana, S.; Bhowmik, P.; Chattopadhyay, S., *Dalton Trans.* **2012,** *41*, 10145-10149.

23. Robin, M. B.; Day, P., Mixed Valence Chemistry-A Survey and Classification. In *Advances in Inorganic Chemistry and Radiochemistry*, Emeléus, H. J.; Sharpe, A. G., Eds. Academic Press: 1968; Vol. 10, pp 247-422.

24. Long, R. C.; Hendrickson, D. N., *J. Am. Chem. Soc.* **1983,** *105*, 1513-1521.

25. Gagne, R. R.; Koval, C. A.; Smith, T. J.; Cimolino, M. C., *J. Am. Chem. Soc.* **1979,** *101*, 4571-4580.

26. Yang, L.; Powell, D. R.; Klein, E. L.; Grohmann, A.; Houser, R. P., *Inorg. Chem.* **2007,** *46*, 6831-6833.

27. Gupta, R.; Zhang, Z. H.; Powell, D.; Hendrich, M. P.; Borovik, A. S., *Inorg. Chem.* **2002,** *41*, 5100-5106.

28. Tsukihara, T.; Aoyama, H.; Yamashita, E.; Tomizaki, T.; Yamaguchi, H.; Shinzawa-Itoh, K.; Nakashima, R.; Yaono, R.; Yoshikawa, S., *Science* **1995,** *269*, 1069-1074.

29. Brown, K.; Tegoni, M.; Prudêncio, M.; Pereira, A. S.; Besson, S.; Moura, J. J.; Moura, I.; Cambillau, C., *Nature Structural Biology* **2000,** *7*, 191.

30. Stoll, S.; Schweiger, A., *Journal of Magnetic Resonance* **2006,** *178*, 42-55.

31. A. Farrar, J.; Grinter, R.; Neese, F.; Nelson, J.; J. Thomson, A., *J. Chem. Soc., Dalton Trans.* **1997,** *21*, 4083-4088.

32. Yuan, S.; Jaramillo, R.; Rosenbaum, T. F.; Yu, L., *Macromolecules* **2006,** *39*, 8652-8658.

33. Carlin, R. L., Paramagnetism and Crystalline Fields: The Iron Series Ions. In *Magnetochemistry*, Springer Berlin Heidelberg: Berlin, Heidelberg, 1986; pp 52-69.

GENERAL CONCLUSIONS AND PERSPECTIVES

This thesis was devoted to the synthesis of metal complexes with Schiff base ligands and electroactive ligands such as tetrazine, dithiolene and tetrathiafulvalene. During this work, using elaborated procedures four new ligands, 16 homo- and 14 heterometallic complexes were obtained and fully characterized.

The literature search was performed in the first chapter and it was shown that the polynuclear homo- and heterometallic complexes are worth of investigation due to their wide range of properties, starting from the magnetic to catalytic ones. In addition, these properties can be associated with the properties derived from the electroactive TTF, TTZ and dithiolene moieties such as conductivitiy, thus leading to multifunctional materials.

The successful utilization of "serendipitous assembly", particularly the "direct synthesis" approach, led to the series of heterometallic Mn/Cu, Mn/Co complexes, described in chapter two. X-ray crystal structures analysis revealed that the Mn/Co complexes based on tetra- and hexanuclear cores (*{$Co_2Mn_2(\mu$-O)$_6$}* and *{$Co^{III}{}_2Mn^{II}{}_2Mn^{III}{}_2(\mu_2$-O)$_8(\mu_3$-OH)$_2$}*, respectively) were crystallographically characterized for the first time. These metal complexes possess notable catalytic and photophysical properties, making them interesting multifunctional materials.

A TTF-functionalized Schiff base ligand and its corresponding Cu(II) complex were described in chapter three. Generally, the TTF-containing compounds are well known to be used as active components (upon chemical or electro oxidation) for the preparation of crystalline molecular conductors. Thus, electrocrystallization experiments performed for TTF-salicylaldehyde ligand resulted in the obtaining of two radical cation salts, possessing a semiconducting behavior. Moreover, the crystal structure of the copper(II) complex opens up the opportunity of its additional use as metalloligand towards heterometallic compounds.

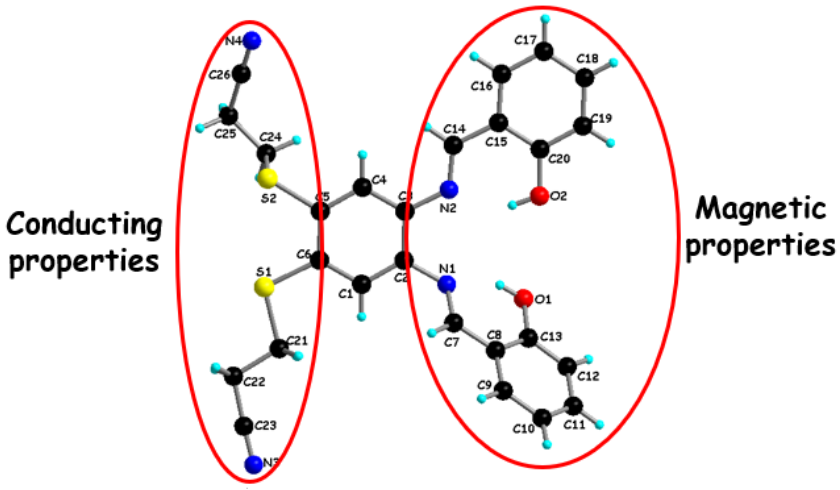

Figure C1. The view of two coordination pockets of the **H_2L^{13}** ligand.

Chapter four was devoted to the combination of Schiff base fragments with dithiolate entities, leading to the formation of new heteroleptic ligands. Thus, an unprecendented ligand containing a chelating N,O-donor pocket from one side and

S-donor atoms from the other, allows the access to dithiolene homo- and heterometallic complexes with most of the transition metals.

The switching and modulation of the magnetic, electronic and conducting properties can be reached by changing the metal centers (Figure C1). The peculiarity of dithiolene complexes obtained and described in this work prompted us to explore the possibility of preparing similar compounds with higher nuclearity. This can be reached by the introduction of additional chelation moieties. Having this in mind, we have chosen the *o*-vanilin derivative and synthesized the new ligand (Figure C2).

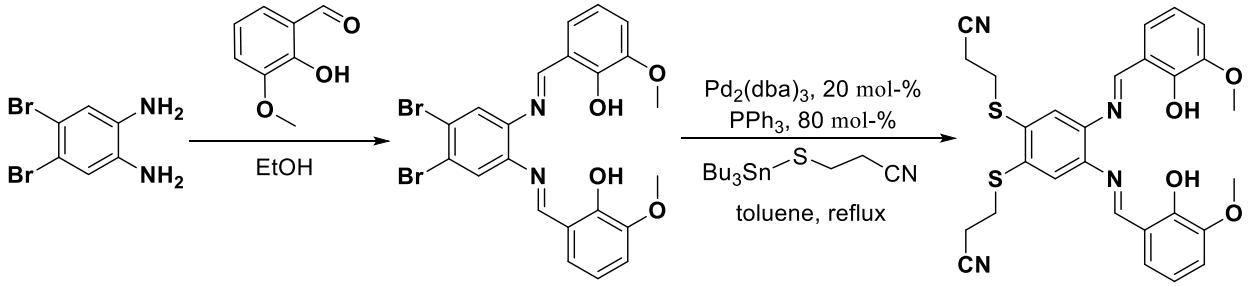

Figure C2. The synthetic pathway to the *o*-vanilin derivative.

X-ray crystal structure analysis performed for the new ligand revealed that the compound crystallizes in the triclinic system (Figure C3).

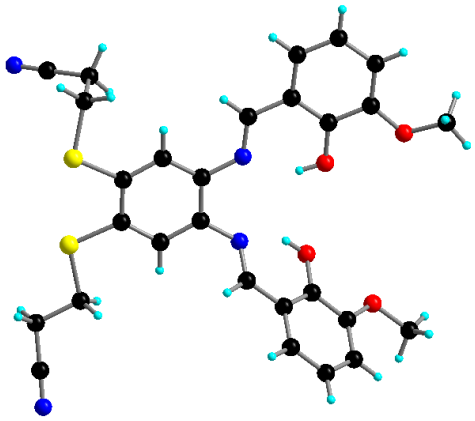

Figure C3. The crystal structure of the ligand, derivative of *o*-vanilin.

The presence of the additional O,O-chelating pocket drives the possibility to coordinate lanthanides, thus giving pentanuclear 3*d*-4*f* complexes. The synthetic route can be similar as for the trinuclear 3d-metal complexes, described in chapter four of this manuscript (Figure C4).

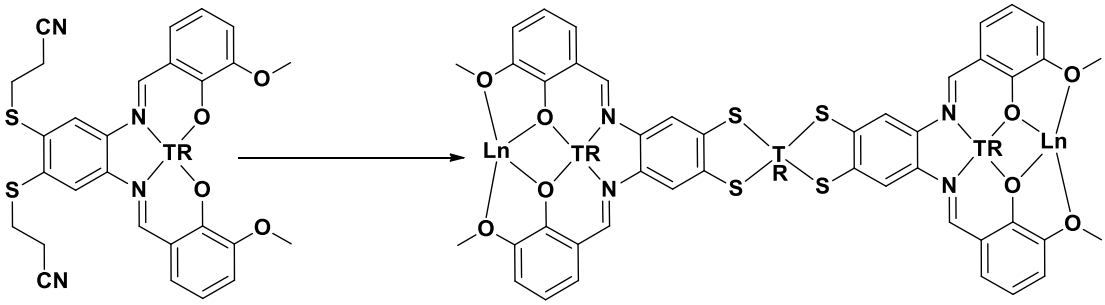

Figure C4. The possible synthetic pathway to the pentabuclear 3*d*-4*f* complexes.

The last part of the thesis work was focused on the use of the electron withdrawing tetrazine unit with a chelating unit. Thus two new ligands, mono- and disubstituted derivatives of picolylamine and 3,6-dichloro-1,2,4,5-tetrazine, were described in chapter five. The possibility of deprotonation of the monosubstituted derivative, forming quanidinate like ligands was discovered together with the formation of mixed-valence $Cu^{I}Cu^{II}$ complexes with a temperature-independent delocalization of the unpaired electron between the two copper ions (class III). This feature can be further used in the synthesis of lanthanide complexes with the deprotonated form of the ligand. On the other hand, the disubstituted ligand containing two chelating units can be further reduced *in situ* to form stable radical anions. The presence of the latter in the complexes may strengthen the magnetic exchange between metal ions.

Appendix 1

Crystallographic data, details of data collection, and structure refinement parameters

Compound	**1**	**2**	**3**	**4**
Formula	$C_{39}H_{48}N_4O_{11}I_3MnCu_3$	$C_{40}H_{52}N_5O_{13}SMnCu_3$	$C_{37}H_{46}N_5O_{12}BrMnCu_3$	$C_{36}H_{44}N_4O_{14}BF_4MnCu_3$
M [g·mol^{-1}]	1375.07	1088.49	1064.25	1057.12
Crystal system	monoclinic	monoclinic	monoclinic	monoclinic
Space group	$P2_1/n$	$P2_1/n$	$P2_1/n$	$P2_1/n$
a [Å]	13.3737(11)	18.5500(12)	17.9628(14)	16.8093(9)
b [Å]	15.6103(8)	12.9260(8)	13.0651(9)	13.6009(7)
c [Å]	23.0857(18)	19.8784(14)	19.7336(14)	19.1235(10)
α [°]	90	90	90	90
β [°]	92.535(9)	98.170(10)	96.001(7)	93.479(5)
γ [°]	90	90	90	90
V [Å^3]	4814.8(6)	4718.0(5)	4605.8(6)	4364.0(4)
Z	4	4	4	4
$P_{calcd.}$ [g/cm^3]	1.897	1.532	1.535	1.613
μ [mm^{-1}]	3.544	1.705	2.560	1.804
$F(000)$	2676	2236	2156	2148
T [K]	213	213	103	298
$2\Theta_{max}$	50	50	52	55
R_{int}	0.0368	0.0456	0.1225	0.0746
T_{min}/T_{max}	0.5460/0.6600	0.6340/0.7600	0.37845/1.00000	0.24317/1.00000
R_1 [$I > 2\sigma(I)$]	0.0309	0.0466	0.1023	0.0778
wR_2 (all data)	0.0718	0.1394	0.3183	0.2870
G.O.F.	0.859	0.928	0.978	0.993
Largest difference peak/hole (e·Å^{-3})	1.456/-0.957	1.343/-0.942	1.366/-1.063	1.469/-0.766
CCDC	1516021	1516022	1453203	1453204

Compound	**5**	**6**	**7**	**8**
Formula	$C_{84}H_{104}N_{12}O_{24}S_4Mn_3Cu_6$	$C_{31}H_{35}N_6O_8S_2Co_2Cu_2$	$C_{50}H_{74}N_6O_{24}Co_2Mn_2$	$C_{53}H_{67}N_7O_{20}Br_4Co_2Mn_2$
M [g·mol^{-1}]	2340.09	928.71	1370.90	1669.51
Crystal system	triclinic	monoclinic	trigonal	triclinic
Space group	*P*-1	$P2_1/n$	*R* -3	*P*-1
a [Å]	13.5453(4)	18.7222(9)	26.8686(8)	9.2493(7)
b [Å]	15.1781(4)	9.6195(3)	26.8686(8)	14.0229(10)
c [Å]	26.9837(9)	21.5100(12)	24.3501(11)	14.0684(10)
α [°]	90.892(2)	90	90	64.080(3)
β [°]	103.293(2)	105.374(5)	90	79.759(3)
γ [°]	114.678(2)	90	120	89.454(3)
V [Å^3]	4866.7(3)	3735.3(3)	15223.7(11)	1610.2(2)
Z	2	4	9	1
$P_{calcd.}$ [g/cm^3]	1.597	1.651	1.352	1.816
μ [mm^{-1}]	1.821	9.634	7.403	3.454
F(000)	2394	1884	6383	888
T [K]	173	150	150	150
$2\Theta_{max}$	50	140	134	50
R_{int}	0.1120	0.0416	0.0190	0.0424
T_{min}/T_{max}	0.690/0.7065	0.44147/1.00000	0.71690/1.00000	0.6360/0.7454
R_1 [$I > 2\sigma(I)$]	0.0573	0.0576	0.0877	0.0589
wR_2 (all data)	0.1118	0.1582	0.2930	0.0877
G.O.F.	0.904	1.056	1.316	1.036
Largest difference peak/hole (e·Å^{-3})	0.557/-0.577	1.493/-0.92	2.480/-0.911	1.409/-0.929
CCDC	1516023	1573198	1540212	1540215

Compound	**9**	**10**	**11**	**12**
Formula	$C_{53}H_{71}N_{11}O_{30}Co_2Mn_2$	$C_{69}H_{83}N_7O_{22}Co_2Mn_2$	$C_{62}H_{86}N_{10}O_{18}Br_4Co_2Mn_2$	$C_{56}H_{86}N_{12}O_{31}Co_2Mn_2$
M [g·mol^{-1}]	1569.94	1629.50	1806.78	1651.10
Crystal system	triclinic	triclinic	monoclinic	trigonal
Space group	*P*-1	*P*-1	$P2_1/c$	*R* -3
a [Å]	9.0145(5)	10.8390(8)	9.2094(6)	38.756(4)
b [Å]	13.5054(17)	17.9875(11)	23.3824(12)	38.756(4)
c [Å]	16.4881(9)	21.335(2)	16.9763(10)	14.5712(10)
α [°]	93.333(7)	101.877(6)	90	90
β [°]	100.569(5)	103.183(7)	99.967(6)	90
γ [°]	91.182(7)	96.712(5)	90	120
V [Å^3]	1968.9(3)	3904.3(5)	3600.5(4)	18954(4)
Z	1	2	2	9
$P_{calcd.}$ [g/cm^3]	1.381	1.386	1.667	1.132
μ [mm^{-1}]	6.530	6.512	9.556	5.982
F(000)	844	1686	1832	6638
T [K]	150	130	164	150
$2\Theta_{max}$	134	134	134	130
R_{int}	0.0418	0.1159	0.0750	0.0494
T_{min}/T_{max}	0.42783/1.00000	0.88355/1.00000	0.47657/1.00000	0.96951/1.00000
R_1 [I > 2σ(I)]	0.1192	0.1099	0.0738	0.0767
wR_2 (all data)	0.3704	0.3673	0.2287	0.2519
G.O.F.	1.287	0.958	1.062	0.984
Largest difference peak/hole (e·Å^{-3})	1.611/-0.466	1.231/-0.510	1.605/-0.985	0.906/-0.506
CCDC	1540213	1540216	1540214	1583232

Compound	**13**	**14**	**15**	**16**
Formula	$C_{58}H_{84}N_{10}O_{20}Cl_2Co_2Mn_4$	$C_{27}H_{19}N_4O_3S_2Cu$	$C_{78}H_{108}N_6O_4S_4Cl_{12}Ni_3$	$C_{77}H_{106}N_6O_4S_4Cl_{10}Cu_3$
M [g·mol^{-1}]	1649.86	575.12	1923.41	1853.17
Crystal system	monoclinic	monoclinic	monoclinic	triclinic
Space group	$P2_1/c$	$P2_1/n$	$P2_1/c$	P-1
a [Å]	8.5730(2)	8.2974(2)	12.2581(5)	11.7669(18)
b [Å]	21.4804(4)	17.3118(3)	25.5520(10)	13.304(2)
c [Å]	18.9257(4)	17.7096(3)	14.8340(5)	16.5960(17)
α [°]	90	90	90	68.334(13)
β [°]	91.632(2)	101.523(2)	96.305(4)	75.572(11)
γ [°]	90	90	90	68.546(15)
V [Å^3]	3483.78(13)	2492.59(9)	4618.2(3)	2227.6(6)
Z	2	4	2	1
$P_{calcd.}$ [g/cm^3]	1.571	1.533	1.383	1.381
μ [mm^{-1}]	10.722	3.122	5.127	4.845
F(000)	1696	1176	2004	963
T [K]	150	150	130.0(3)	140
$2\Theta_{max}$	140	140	138	136
R_{int}	0.0214	0.0443	0.0609	0.0785
T_{min}/T_{max}	0.62828/1.00000	0.62894/1.00000	0.57910/1.00000	0.48448/1.00000
R_1 [$I > 2\sigma(I)$]	0.0282	0.0629	0.0640	0.1177
wR_2 (all data)	0.0749	0.1820	0.1891	0.3685
G.O.F.	1.026	1.066	1.019	1.140
Largest difference peak/hole (e·Å^{-3})	0.608/-0.399	2.151/-0.857	1.064/-0.968	1.230/-1.556
CCDC	1819913	-	-	-

Compound	**17**	**18**	**19**	**20**
Formula	$C_{68}H_{52}N_4O_4PS_4Cl_8Ni_3$	$C_{68}H_{52}N_4O_4PS_4Cl_8Cu_3$	$C_{57}H_{62}O_4N_5S_4Cl_4Cu_4Ni_2$	$C_{18}H_9F_{12}N_6O_4ClCu$
M [g·mol^{-1}]	1608.07	1622.56	1266.04	700.30
Crystal system	orthorhombic	orthorhombic	triclinic	monoclinic
Space group	*Pccn*	*Pccn*	*P*-1	$P2_1/n$
a [Å]	7.4302(2)	7.4228(3)	12.9902(6)	15.9292(3)
b [Å]	27.7347(5)	27.6319(11)	13.6128(7)	9.21150(10)
c [Å]	32.7220(5)	32.8417(12)	17.0367(8)	17.4056(3)
α [°]	90	90	92.247(4)	90
β [°]	90	90	109.249(4)	101.765(2)
γ [°]	90	90	107.038(4)	90
V [Å^3]	6743.2(2)	6736.0(5)	2688.6(2)	2500.30(7)
Z	4	4	2	4
$P_{calcd.}$ [g/cm^3]	1.584	1.600	1.564	1.860
μ [mm^{-1}]	5.696	5.828	4.114	3.450
F(000)	3276	3288	1310	1380
T [K]	170	130	150	150
$2\Theta_{max}$	140	134	136	140
R_{int}	0.0541	0.0410	0.0649	0.0184
T_{min}/T_{max}	0.38894/1.00000	0.63765/1.00000	0.56917/1.00000	0.77540/1.00000
R_1 [$I > 2\sigma(I)$]	0.0540	0.0625	0.0791	0.0407
wR_2 (all data)	0.1527	0.1764	0.2273	0.1100
G.O.F.	1.039	1.035	0.987	1.032
Largest difference peak/hole (e·Å^{-3})	0.505/-0.633	1.410/-1.528	1.344/-1.034	1.074/-0.755
CCDC	-	-	-	1850387

Compound	**21**	**22**	**23**	**24**
Formula	$C_{16}H_{12}N_{12}Cl_3Cu_2$	$C_{17}H_{12}Cl_2F_3N_{12}O_3SCu_2$	$C_{20}H_{20}N_{14}Cl_4Cu$	$C_{24}H_{16}F_{12}N_8O_4Cu$
M [g·mol^{-1}]	605.81	719.43	661.85	771.99
Crystal system	monoclinic	monoclinic	triclinic	monoclinic
Space group	$P2_1/c$	$P2_1/c$	P-1	$P2_1/n$
a [Å]	13.5525(3)	15.3612(4)	8.1726(7)	9.479(3)
b [Å]	11.4392(2)	10.9054(3)	8.7426(7)	14.191(5)
c [Å]	13.7445(3)	15.4148(5)	10.3892(8)	22.002(6)
α [°]	90	90	82.662(7)	90
β [°]	104.474(2)	111.358(4)	67.773(8)	98.581(2)
γ [°]	90	90	79.566(7)	90
V [Å^3]	2063.18(8)	2404.94(13)	674.35(10)	2926.5(16)
Z	4	4	1	4
$P_{calcd.}$ [g/cm^3]	1.950	1.987	1.630	1.752
μ [mm^{-1}]	6.433	5.723	5.140	2.216
F(000)	1204	1428	335	1540
T [K]	150	150	150	89.9(3)
$2\Theta_{max}$	140	140	140	142
R_{int}	0.0226	0.0293	0.0254	0.0315
T_{min}/T_{max}	0.56872/1.00000	0.77540/1.00000	0.47116/1.00000	0.80747/1.00000
R_1 [I > 2σ(I)]	0.0281	0.0716	0.0466	0.0632
wR_2 (all data)	0.0799	0.2003	0.1236	0.1635
G.O.F.	1.039	1.085	1.122	1.027
Largest difference peak/hole (e·Å^{-3})	0.571/-0.550	2.162/-0.798	0.725/-1.185	1.530/-0.677
CCDC	1850585	1850388	1850386	-

Compound	**25**	**26**	**27**	**28**
Formula	$C_{24}H_{16}N_8O_4F_{12}Ni$	$C_{26}H_{19}N_9O_4F_{12}Co$	$C_{36}H_{26}N_8O_{10}F_{24}Cu_2$	$C_{38}H_{24}N_{10}O_8F_{24}Ni_2$
M [g·mol^{-1}]	767.16	808.43	1313.75	1322.05
Crystal system	monoclinic	triclinic	triclinic	triclinic
Space group	$P2_1/n$	P-1	P-1	P-1
a [Å]	9.4370(10)	9.977(9)	9.901(7)	9.2160(2)
b [Å]	14.299(2)	12.534(10)	11.416(7)	10.5636(3)
c [Å]	22.162(4)	13.712(12)	11.823(3)	13.4199(3)
α [°]	90	94.319(7)	91.277(4)	89.369(2)
β [°]	99.569(15)	100.510(7)	96.619(5)	77.005(2)
γ [°]	90	103.039(7)	100.342(5)	73.279(2)
V [Å^3]	2948.9(7)	1630(2)	1304.6(13)	1217.30(5)
Z	4	2	1	1
$P_{calcd.}$ [g/cm^3]	1.728	1.647	1.672	1.803
μ [mm^{-1}]	2.103	5.214	2.343	2.388
F(000)	1536	810	652	658
T [K]	150	200	150	150
$2\Theta_{max}$	142	140	140	140
R_{int}	0.0290	0.0535	0.0294	0.0576
T_{min}/T_{max}	0.56872/1.0000	0.91253/1.00000	0.49085/1.00000	0.79202/1.00000
R_1 [$I > 2\sigma(I)$]	0.0555	0.0714	0.0881	0.0573
wR_2 (all data)	0.1498	0.2164	0.2525	0.1589
G.O.F.	1.041	1.029	1.080	1.055
Largest difference peak/hole (e·Å^{-3})	0.705/-0.612	0.610/-0.492	1.988/-0.820	0.826/-0.726
CCDC	-	1580449	-	-

Compound	**29**	**$[Cu(HL^{12})_2]_n$**	**$(TTF\text{-}Sal)_2PF_6$**	**$(TTF\text{-}Sal)_2AsF_6$**
Formula	$C_{36}H_{26}F_{24}N_8O_{10}Co_2$	$C_{30}H_{24}N_2O_4S_8Cu$	$C_{26}H_{16}O_4S_8PF_6$	$C_{26}H_{16}O_4S_4AsF_6$
M [g·mol^{-1}]	1304.51	796.54	793.84	837.79
Crystal system	triclinic	monoclinic	monoclinic	monoclinic
Space group	*P*-1	$P2_1/c$	$P2_1/n$	$P2_1/n$
a [Å]	9.2966(4)	5.09570(10)	7.0423(3)	7.1391(2)
b [Å]	10.7857(4)	23.0889(7)	22.5463(10)	22.7368(5)
c [Å]	12.1766(6)	13.2310(4)	18.7112(8)	18.9508(4)
α [°]	89.952(4)	90	90	90
β [°]	87.243(4)	94.990(3)	90.716(5)	90.870(2)
γ [°]	76.567(4)	90	90	90
V [Å^3]	1186.11(9)	1550.78(7)	2970.7(2)	3075.74(13)
Z	1	2	4	4
$P_{calcd.}$ [g/cm^3]	1.826	1.706	1.775	1.809
μ [mm^{-1}]	6.950	6.384	6.758	7.231
F(000)	648	814	1604	1676
T [K]	150	150	150	295
$2\Theta_{max}$	140	140	133	135
R_{int}	0.0222	0.0284	0.0478	0.0221
T_{min}/T_{max}	0.84123/1.00000	0.79480/1.00000	0.90830/1.00000	0.44530/1.00000
R_1 [$I > 2\sigma(I)$]	0.0410	0.0284	0.0651	0.0550
wR_2 (all data)	0.1095	0.0736	0.1545	0.1651
G.O.F.	1.037	1.042	1.100	1.042
Largest difference peak/hole (e·Å^{-3})	0.623/-0.497	0.611/-0.509	0.741/-0.380	0.659/-0.542
CCDC	1580450	1565897	-	-

Compound	**H_2L^{12}**	**H_2L^{13}**	**HL^{14}**	**H_2L^{15}**	**TTF-Sal**
Formula	$C_{15}H_{13}NO_2S_4$	$C_{26}H_{22}N_4O_2S_2$	$C_8H_7N_6Cl$	$C_{14}H_{14}N_8$	$C_{13}H_8O_2S_4$
M [g·mol^{-1}]	367.50	486.59	222.65	294.33	324.43
Crystal system	monoclinic	triclinic	monoclinic	triclinic	orthorhombic
Space group	$P2_1$	P-1	$P2_1/c$	P-1	$Pccn$
a [Å]	5.022(5)	8.9570(5)	4.1825(5)	7.9604(7)	26.0816(8)
b [Å]	10.615(5)	11.6803(8)	23.824(2)	9.4610(7)	11.8579(3)
c [Å]	14.810(5)	11.9606(3)	9.9296(9)	10.2450(5)	8.4318(2)
α [°]	90	91.880(4)	90	85.512(5)	90
β [°]	96.476(5)	96.491(4)	97.827(10)	74.820(6)	90
γ [°]	90	109.944(5)	90	69.549(7)	90
V [Å^3]	784.5(9)	1165.32(11)	980.22(17)	697.65(9)	2607.73(12)
Z	2	2	4	2	8
$P_{calcd.}$ [g/cm^3]	1.556	1.387	1.509	1.401	1.653
μ [mm^{-1}]	5.614	2.333	3.265	0.760	6.645
F(000)	380	508	456	308	1328
T [K]	150	150	152	200	150
$2\Theta_{max}$	136	140	136	140	144
R_{int}	0.0257	0.0214	0.0484	0.0166	0.0434
T_{min}/T_{max}	0.69616/1.00000	0.83749/1.00000	0.20518/1.00000	0.94254/1.00000	0.29320/1.00000
R_1 [$I > 2\sigma(I)$]	0.0287	0.0331	0.0774	0.0376	0.0436
wR_2 (all data)	0.0755	0.0897	0.2537	0.1022	0.1298
G.O.F.	1.040	1.032	1.070	1.054	1.051
Largest difference peak/hole (e·Å^{-3})	0.389/-0.294	0.292/-0.253	0.380/-0.713	0.162/-0.249	0.447/-0.458
CCDC	-	-	1850384	1580448	1565896

Appendix 2

Experimental section.

General methods

Nuclear magnetic resonance (NMR). The NMR spectroscopy was performed with a Bruker Avance DRX 300 spectrometer operating at 300 MHz for ^{1}H and 76 MHz for ^{13}C. The chemical shifts are expressed in ppm downfield from external tetramethylsilane (TMS). The following abbreviations are used:

s, singlet;

d, doublet;

dd, doublet of doublets;

td, triplet of doublets,

m, multiplet.

Mass-spectrometry. MALDI-TOF MS was performed with a Bruker Biflex-IIITM apparatus equipped with a N_2 laser (λ = 337 nm). The ESI-MS spectra were recorded with a Bruker MicrO-Tof-Q 2 spectrometer.

Infrared spectroscopy. FT-IR spectra were recorded with a Bruker Vertex 70 attenuated total reflectance (ATR) spectrophotometer in the ν = 4000–400 cm^{-1} range.

Absorption spectroscopy. The UV-visible spectra were recorded with a Perkin Elmer Lambda 19 or Lambda 950. The positions of the absorption bands are expressed in nm.

Cyclic voltammetry (CV). CV experiments were carried out on a BioLogic SP-150 potentiostat, calibrated using internal ferrocene, in the following conditions: 0.1 mol/L solution of (n-Bu_4N)PF_6 in HPLC grade acetonitrile and dichloromethane (1/1), Ag wire pseudo-reference electrode, Pt working electrode, and Pt counter electrode. All experiments were performed at room temperature at 100 mV/s. Ferrocene was used as an internal reference and then the Fc/Fc^{+} couple values have been adjusted to zero.

Magnetochemistry. Magnetic data for complexes **1-5**, **7-9**, **11**, **12** were recorded on a SQUID magnetometer (MPMS-XL7, Quantum Design). The susceptibility taken at B = 0.1 T between T = 2–300 K has been corrected for the underlying diamagnetism and converted to the effective magnetic moment. The magnetization has been measured at two temperatures: T = 2.0 and T = 4.6 K.

For complexes **26**, **29** variable-temperature (1.9–295 K) dc magnetic susceptibility measurements were performed under applied magnetic fields of 5000 (T > 50 K) and 250 G (1.9 ≤ T ≤ 50 K), and variable-field (0–5 T) magnetization measurements of polycrystalline with a Quantum Design superconducting quantum interference device (SQUID) magnetometer. Variable-temperature

(2.0–8.0 K) ac magnetic susceptibility measurements were performed in 0, 1000, and 2500 G static fields under a ±4.0 G oscillating field and in the frequency range 300–10000 Hz. Corrections for the diamagnetic contribution of the constituent atoms and for the sample holder were also applied.

EPR spectroscopy. EPR spectra were recorded using an Elexsys E500 Bruker spectrometer, equipped with a SHQ cavity and a continuous flow ESR900 cryostat to work at variable temperatures. Samples were dissolved in a mixture of DMSO/methanol to obtain a frozen glass.

DFT calculations. Geometry optimizations at the DFT level were performed using the Gaussian 09 software package. The meta GGA DFT functional M06-L was employed for geometry optimization calculations coupled with the triple zeta 6–311G(d,p) basis set. The M06-L functional has been designed to include medium-range electron correlation effects and has been specifically recommended for transition-metal containing systems; several benchmark studies have confirmed its excellent accuracy in this respect. Vibrational analyses were performed for each structure to ensure the stationary points are genuine minima.

Oxygen evolution experiments. A standard Clark electrode (Hansatech Instruments) was used for oxygen detection. The electrode was separated from the sample solution by a teflon membrane and the signal was recorded at 0.1 s intervals by using the Oxygraph v1.02 software package. Air-saturated aqueous solutions ($[O_2]_{20^oC}$ = 276 μM) were used for calibration of the electrode. The cell was purged with argon gas before each experiment. Fresh solutions of the complexes were prepared in deionized H_2O/DMSO before each experiment. Visible-light LEDs (λ=470nm) were used as illumination sources in the photoinduced reactions. Standard concentrations of the components in the catalytic systems in the Clark cell were as follows: 2.5 μM of Mn/Cu compound, 100 μM of $[Ru(bpy)_3](ClO_4)_2$, 5 mM of $Na_2S_2O_8$, and the phosphate buffer (KH_2PO_4/K_2HPO_4, 50 mM, pH = 7.0).

Electrical Conductivity Measurements. Electrical resistivity was measured on needle-shaped single crystals of the radical cation salts [(**TTF-Sal)$_2$PF$_6$**, (**TTF-Sal)$_2$AsF$_6$**] and complexes **[TBA]$_2$[{Ni(L^{13})$_2$}$_2$Ni]·6CH$_2$Cl$_2$** (**15**) and **[PPh$_4$][{Ni(L^{13})$_2$}$_2$Ni]·4CH$_2$Cl$_2$** (**17**) by using a four-point method. Four gold contacts were evaporated on both faces of the crystals and gold wires (17 μm diameter) were glued with silver paste onto those contacts. A low-frequency (<100 Hz) lock-in technique was used with a measuring current I_{ac} =1 μA. Low temperature (in the range of 15–300 K) was provided by cryocooler equipment.

Synthetic procedures for the ligands

Synthesis of 5-(tetrathiafulvalenyl)-2-hydroxybenzaldehyde (TTF-Sal)

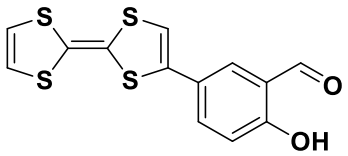

In a Schlenk tube under Ar atmosphere in 50 mL of anhydrous toluene, TTF-$SnMe_3$ (1.62 g , 4.41 mmol), 5-bromosalicylaldehyde (0.88 g, 4.41 mmol) and $Pd(PPh_3)_4$ (0.51 g, 0.4 mmol) were dissolved. The mixture was refluxed for 12 h. After the reaction, the solvent was removed under vacuum to afford a black precipitate, which was subjected to chromatography column (silica gel, CH_2Cl_2/Petroleum ether (1/1, v/v)) to give **TTF-Sal** as an orange precipitate (0.52 g, 37%). Single crystals suitable for X-ray diffraction analysis were obtained by slow evaporation of solution after column chromatography. ^{1}H NMR (300 MHz, $CDCl_3$): δ 6.35 (s, 2H), 6.44 (s, 1H), 7.00 (d, *J* = 8.7 Hz, 1H), 7.65-7.51 (m, 2H); 9.91 (s, 1H), 11.08 (s, 1H), ^{13}C NMR (75 MHz, $CDCl_3$) δ 196.3, 161.6, 134.1, 131.33, 128.5, 120.4, 119.1, 119.0, 118.5, 113.2, 112.7, 108.2. MALDI-TOF MS: *m/z* = 324.0; IR (ATR, cm^{-1}): 3057 (w), 2922 (w), 1662 (s), 1614 (w), 1540 (s), 774 (s), 713 (s), 636 (s). Anal. calc. for $C_{13}H_8O_2S_4$: C 48.13, H 2.49, S 39.53 %; Found: C 48.11, H 2.33, S 33.26 %. The compound is soluble in most common solvents and insoluble in water.

Synthesis of 4-(tetrathiafulvalenyl)-2-((2-hydroxyethyl)iminomethyl)-phenol (H_2L^{12})

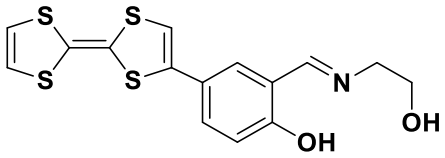

The **TTF-Sal** aldehyde (0.3 g, 0.93 mmol) was dissolved in 75 mL of CH_2Cl_2. Then 2-aminoethanol (0.056 g, 0.93 mmol) was added slowly. The mixture was stirred at room temperature during 4-5 h. The solvent was removed under vacuum to afford **H_2L^{12}** as red precipitate, which was used without further purification (0.24 g, 71 %). Crystals suitable for X-ray diffraction analysis were obtained by slow evaporation of solution after the reaction. ^{1}H NMR (300 MHz, $CDCl_3$): δ 3.78 (m, 1H), 3.94 (m, 1H), 6.34 (d, *J* = 3.6 Hz, 1H), 6.95 (d, *J* = 8.7 Hz, 1H), 7.28 (d, *J* = 2.4 Hz, 1H), 7.40 (dd, *J* = 8.7, 2.4 Hz, 1H), 8.40 (s, 1H), ^{13}C NMR (75 MHz, $CDCl_3$) δ 166.5, 161.8, 135.5, 130.3, 129.5, 119.1. 119.0, 118.4, 117.9, 111.7, 111.5, 109.1, 62.1; 61.5. MALDI-TOF MS: *m/z* = 367.0; IR (ATR, cm^{-1}): 3241 (br), 3054 (w), 2908 (w), 1636 (s), 1540 (w), 1495 (m), 636 (w), 613 (s). Anal. calc. for $C_{15}H_{13}NO_2S_4$: C 49.02, H 3.57, N 3.81, S 34.89 %;

Found: C 48.80, H 3.35, N 3.48, S 34.80 %. The compound is soluble in dmso, dmf, sparingly soluble in CH_3OH and CH_3CN, insoluble in water.

Synthesis of 4,5-dibromo-1,2-phenylene-*bis*-azaneylylidene-*bis*-methaneylylidene-diphenol

(Schiff base **B**)

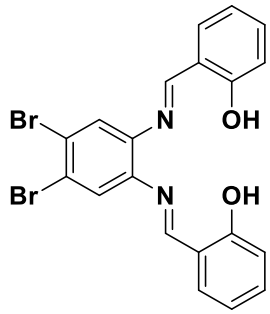

4,5-Dibromo-1,2-phenylenediamine (2 g, 7.51 mmol) was dissolved in 100 mL of EtOH. Then salicylaldehyde (2.0 mL, 18.78 mmol) was added slowly. The mixture was stirred at room temperature during 1-2 h. The yellow precipitate was formed during the reaction, filtered off and washed with ethanol (3.1 g, 87 %). ^{1}H NMR (300 MHz, $CDCl_3$): δ 8.60 (s, 1H), 7.49 (s, 1H), 7.43 – 7.36 (m, 2H), 7.05 (d, J = 8.2 Hz, 1H), 6.94 (t, J = 8.0 Hz, 1H). ^{13}C NMR (75 MHz, $CDCl_3$) δ 164.5, 161.4, 142.7, 134.1, 132.7, 124.2, 122.8, 119.3, 118.9, 117.7. Anal. calc. for $C_{20}H_{14}N_2O_2Br_2$: C 50.66, H 2.98, N 5.91 %, ; Found: C 50.05, H 2.89, N 5.62 %,. The compound is soluble in dmso, dmf, sparingly soluble in CH_3OH and CH_3CN, insoluble in water.

Synthesis of 3,3'-((4,5-*bis*(((E)-2-hydroxybenzylidene)amino)-1,2-phenylene)*bis*(sulfanediyl))dipropanenitrile (H_2L^{13})

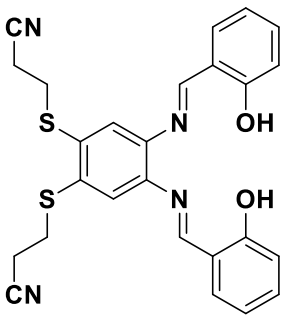

In a Schlenk tube under Ar in 50 mL of anhydrous toluene the Schiff base **B** (1.9 g, 4 mmol), the stannyl derivative (4.5 g, 12 mmol), $Pd_2(dba)_3$ (0.37 g, 20 mol-%) and triphenylphosphine (0.42 g, 80 mol-%) were dissolved. The mixture was refluxed for 14-16 h. After the reaction, the solution was slightly cooled and filtered off and the filtrate was cooled to RT. The orange precipitate of **H_2L^{13}** was obtained and washed with hexane (1.3 g, 67%). ^{1}H NMR (300 MHz, $CDCl_3$): δ 8.64 (s, 2H); 7.40 (t, *J* = 7.5 Hz, 4H); 7,29 (s, 2H); 7,04 (d, *J* = 8.0 Hz, 2H), 6.95 (td, *J* = 7.6, 1.1 Hz,

2H), 3.25 (t, *J* = 7.0 Hz, 4H), 2.73 (t, J = 7.0 Hz, 4H). ^{13}C NMR (75 MHz, $CDCl_3$) δ 165.23, 161.90, 142.94, 135.25, 134.60, 133.31, 123.71, 119.85, 119.49, 118.26, 30.13, 18.80. MALDI-TOF MS: *m/z* = 486.0; IR (ATR, cm^{-1}): 3055 (w), 2920 (w), 2100 (s), 1660 (s), 1615 (w), 1545 (s), 775 (s), 715 (s), 640 (s). Anal. calc. for $C_{26}H_{22}N_4O_2S_2$: C 64.1, H 4.56, N 11.51, S 13.18 %; Found: C 63.56, H 4.48, N 11.28, S 12.98 %. The compound is soluble in dmso, dmf, CH_3CN, CH_2Cl_2, sparingly soluble in alcohols, insoluble in water.

Synthesis of 6-chloro-3-amino-(pyridin-2'-ylmethyl)-1,2,4,5-tetrazine (HL^{14}).

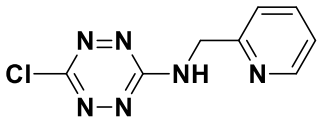

To a solution of 3,6-dichloro-*s*-tetrazine (0.250 g, 1.656 mmol) in 50 mL of methyl-*t*-butylether (MTBE), a solution of picolylamine (0.34 mL, 3.312 mmol) in 10 mL of MTBE was added. The mixture was stirred at room temperature for 12 hours, and then a black precipitate was filtered off and the red filtrate was evaporated under reduced pressure. The product was purified by column chromatography (ethyl acetate / dichloromethane (3/1)) to give **HL^{14}** as a red solid (0.336 g, 91%). Red prismatic crystals, suitable for X-ray analysis, were obtained by slow evaporation of solution after column chromatography. ^{1}H NMR (300 MHz, $CDCl_3$): δ 8.61 (d, J = 4.9 Hz, 1H), 7.72 (td, J = 7.7, 1.7 Hz, 1H), 7.57 (s, 1H), 7.35 (d, J = 7.8 Hz, 1H), 7.27 (dd, J = 7.9, 4.5 Hz, 1H), 4.85 (d, J = 5.0 Hz, 2H). ^{13}C NMR (75 MHz, $CDCl_3$) δ 161.24, 160.82, 154.27, 148.65, 137.68, 123.13, 122.58, 45.52. IR (ATR, cm^{-1}): 2901 (br), 1578 (s), 1498 (m), 1481 (m), 1192 (m), 1041 (m), 1006 (m), 939 (s), 768 (m), 612 (m), 538 (s). Anal. calc. for $C_8H_7N_6Cl$: C 43.16, H 3.17, N 37.75 %; Found: C 43.29, H 3.18, N 37.60 %. The compound is soluble in most common solvents and insoluble in water.

Synthesis of N^3,N^6-bis(pyridin-2-ylmethyl)-1,2,4,5-tetrazine-3,6-diamine (H$_2$L^{15}).

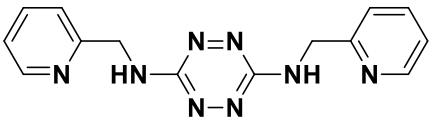

To a solution of 3,6-dichloro-s-tetrazine (0.125 g, 0.83 mmol) in 30 mL of methyl-*t*-butylether (MTBE), was added a solution of picolylamine (0.34 mL, 3.31 mmol) in 10 mL of MTBE. The mixture was refluxed for 32 hours. After the reaction, the black precipitate was filtered off and the red filtrate was evaporated under reduced pressure. The product was purified by column chromatography (ethyl acetate / dichloromethane (3/1)) to give **H$_2$L^{15}** as red precipitate (0.085 g, 35%). Single crystals suitable for X-ray diffraction analysis were obtained by slow evaporation of solution after column chromatography. ^{1}H NMR (300 MHz, $CDCl_3$) δ 8.58 (d, *J* = 4.8 Hz, 2H),

7.66 (td, *J* = 7.7, 1.7 Hz, 2H), 7.34 (d, *J* = 7.8 Hz, 2H), 7.20 (dd, *J* = 7.4, 5.4 Hz, 2H), 6.45 (t, *J* = 5.1 Hz, 2H), 4.78 (d, *J* = 5.4 Hz, 4H). ^{13}C NMR (75 MHz, $CDCl_3$) δ 160.63, 156.66, 149.25, 136.69, 122.41, 122.00, 46.50. IR (ATR, cm^{-1}): 3197 (br), 3009 (w), 1706 (w), 1534 (s), 1477 (w), 1455 (m), 1032 (s), 923 (s), 753 (s), 615 (m). Anal. calc. for $C_{14}H_{14}N_8$: C 57.13, H 4.79, N 38.07 %; Found: C 57.21, H 4.89, N 38.12 %. The compound is soluble in most common solvents and insoluble in water.

Synthetic procedures for the complexes

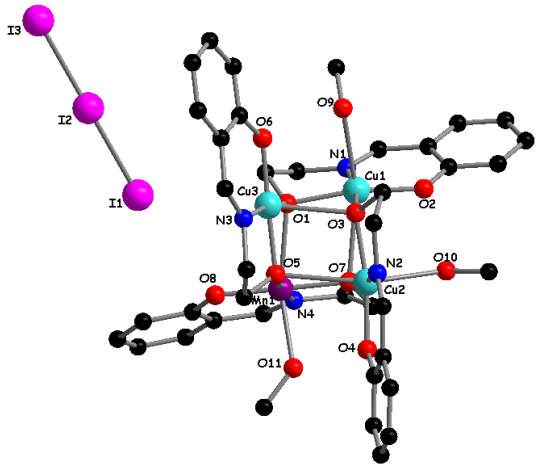

Synthesis of $[Cu_3Mn(L^1)_4(CH_3OH)_3]I_3$ (1)

Salicylaldehyde (0.31 mL, 3.0 mmol) and ethanolamine (0.18 mL, 3.0 mmol) were dissolved in methanol (20 mL), forming a yellow solution of $\mathbf{H_2L^1}$ which was stirred at 50–60 °C (10 min). Then, manganese powder (0.05 g, 1.0 mmol), copper powder (0.06 g, 1.0 mmol), calcium oxide (0.05 g, 1.0 mmol) and NH_4I (0.29 g 2.0 mmol) were added to the hot yellow solution of the ligand and stirred until the total dissolution of the metal powders was observed (4 h). Dark-green crystals of complex **1** suitable for X-ray analysis were isolated after one day from the resulting dark-brown solution. Yield: 0.25 g, 61 % (per Cu). Anal. calc. for $C_{39}H_{48}N_4O_{11}I_3Cu_3Mn$: C, 34.06; H, 3.52; N, 4.07; Mn, 4.00; Cu, 13.86 %. Found: C, 33.70; H, 3.25; N, 3.89; Mn, 3.60; Cu, 13.60 %. IR (KBr, cm^{-1}): 3290 (br), 2915 (w), 2868 (w), 1633 (s), 1538 (s), 1447 (s), 1392 (m), 1297 (s), 1192 (m), 1148 (s), 1041 (s), 936 (m), 896 (m), 757 (s), 650 (s), 579 (m), 526 (w), 467 (m), 435 (m). The compound is soluble in dmso, dmf and CH_3CN and insoluble in water.

Synthesis of $[Cu_3Mn(L^1)_4(CH_3OH)_3(H_2O)]NCS\cdot H_2O$ (2)

This complex was prepared in a similar way to that of **1**, but using barium oxide (0.15 g, 1.0 mmol) and NH_4NCS (0.15 g, 2.0 mmol) instead of calcium oxide and NH_4I. Dark-green crystals suitable for X-ray analysis were obtained after one day from the resulting dark-brown solution. Yield: 0.13 g, 40 % (per Cu). Anal. calc. for $C_{40}H_{52}N_5O_{13}SCu_3Mn$: C, 44.14; H, 4.82; N, 6.43; S, 2.95; Mn, 5.05; Cu, 17.51 %. Found: C, 43.90; H, 4.55; N, 6.15; S, 2.88; Mn, 5.3; Cu, 17.2 %. IR (KBr, cm^{-1}): 3372 (br), 2915 (w), 2868 (w), 2056 (s), 1631 (s), 1532 (s), 1443 (s), 1390 (m), 1296 (s), 1191 (m), 1034 (s), 971 (w), 756 (s), 646 (s), 579 (m), 525 (w), 462 (m), 437 (m). The compound is soluble in dmso, dmf and CH_3CN and insoluble in water.

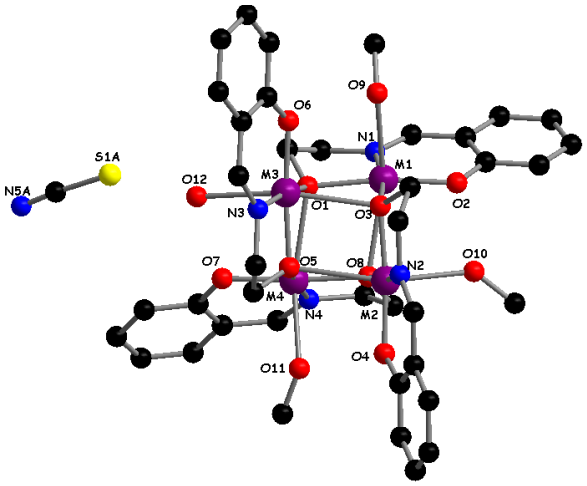

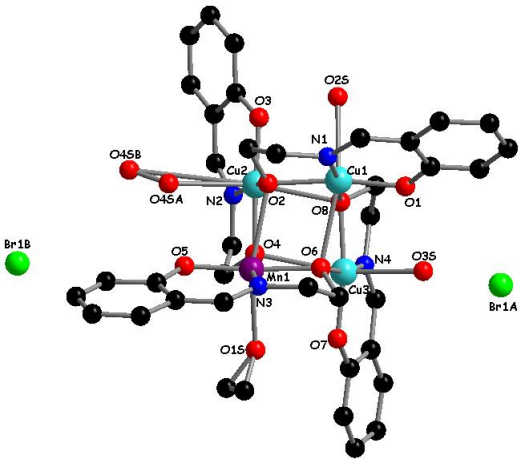

Synthesis of

$[Cu_3Mn(L^1)_4(CH_3OH)(H_2O)_{2.55}]Br\cdot 0.45H_2O$ (3)

This complex was prepared in a similar way to that of **1**, but using barium oxide (0.15 g, 1.0 mmol) and NH_4Br (0.19 g, 2.0 mmol) instead of calcium oxide and NH_4I. Dark-green crystals suitable for X-ray analysis were formed after one day from the resulting dark-brown solution. Yield: 0.19 g, 59 % (per Cu). Anal. calc. for $C_{37}H_{46}N_4O_{12}BrCu_3Mn$: C, 41.76; H, 4.36; N, 5.26; Mn, 5.16; Cu, 17.91 %. Found: C, 41.23; H, 3.95; N, 4.90; Mn, 5.1; Cu, 16.8 %. IR (KBr, cm^{-1}): 3350 (br), 2896 (w), 1638 (s), 1541 (s), 1444 (s), 1388 (m), 1300 (s), 1198 (m), 1035 (s), 978 (w), 759 (s), 657 (s), 580 (m), 533 (w), 467 (m), 436 (m). The compound is soluble in dmso, dmf and CH_3CN and insoluble in water.

Synthesis of $[Cu_3Mn(L^1)_4(H_2O)_{3.4}]BF_4\cdot 0.6H_2O$ (4)

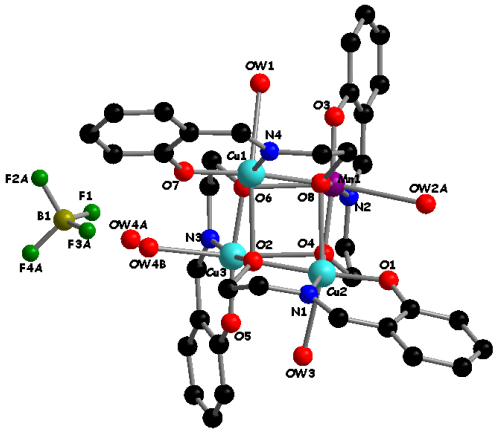

This complex was prepared in a similar way to that of 1, but using barium oxide (0.15 g, 1.0 mmol) and NH_4BF_4 (0.21 g, 2.0 mmol) instead of calcium oxide and NH_4I. Dark-green crystals suitable for X-ray analysis were isolated after one day from the resulting dark-brown solution. Yield: 0.16 g, 51 % (per Cu). Anal. calc. for $C_{36}H_{44}N_4O_{12}BF_4Cu_3Mn$: C, 40.90; H, 4.20; N, 5.30; Mn, 5.05; Cu, 18.03 %. Found: C, 40.25; H, 3.89; N, 4.90; Mn, 5.6; Cu, 18.1 %. IR (KBr, cm^{-1}): 3338 (br), 2933 (w), 2870 (w), 1638 (s), 1541 (s), 1444 (s), 1395 (m), 1297 (s), 1190 (m), 1035 (s), 981 (w), 759 (s), 649 (s), 581 (m), 533 (w), 464 (m), 435 (m). The compound is sparingly soluble in dmso, dmf and CH_3CN and insoluble in water.

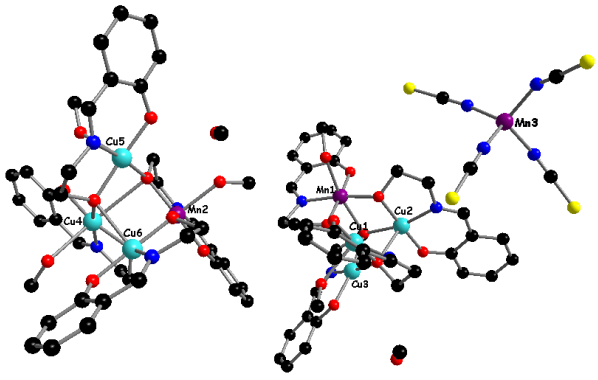

Synthesis of

$[Cu_3Mn(L^1)_4(CH_3OH)_3]_2[Mn(NCS)_4]\cdot 2CH_3OH$ (5)

Manganese(II) acetate tetrahydrate (0.12 g, 0.5 mmol), $[Cu(HL^1)_2]$ (0.18 g, 0.5 mmol), and NH_4NCS (0.08 g, 1.0 mmol) were dissolved in methanol (20 mL) and magnetically stirred at

50–60 °C (60 min). Dark-green crystals suitable for X-ray analysis were isolated after one day from the resulting dark-brown solution. Yield: 0.06 g, 31 % (per Cu). Anal. calc. for $C_{84}H_{104}N_{12}O_{24}S_4Cu_6Mn_3$: C, 43.11; H, 4.48; N, 7.18; S, 5.48; Mn, 7.04; Cu, 16.29 %. Found: C, 42.80; H, 4.00; N, 6.95; S, 5.10; Mn, 6.9; Cu, 16.8 %. IR (KBr, cm^{-1}): 3500 (br), 3050 (w), 2900 (w), 2080 (m), 1620 (s), 1510 (s), 1480 (s), 1250 (s), 1050 (s), 680 (m), 470 (m). The compound is sparingly soluble in dmso, dmf and CH_3CN and insoluble in water.

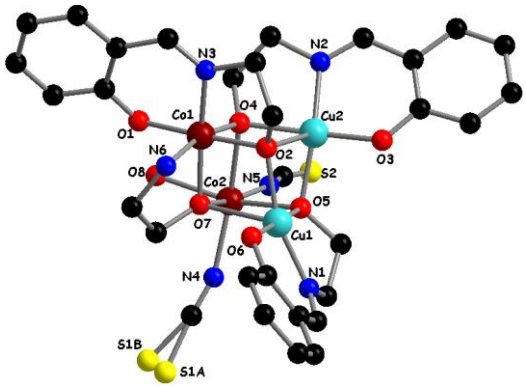

Synthesis of $[Co_2Cu_2(L^1)_3(ea)(H_2O)(NCS)_2]$ (6)

Cobalt(II) acetate tetrahydrate (0.13 g, 0.5 mmol), $[Cu(HL^1)_2]$ (0.18 g, 0.5 mmol) and NH_4NCS (0.08 g, 1.0 mmol) were dissolved in methanol (30 mL) and magnetically stirred at 55–60 °C during 2 h. A mixture of purple and brown crystals was obtained after one day from the resulting dark brown solution. Single crystal X-ray analysis carried out for both types of crystals revealed formation of the new heterometallic complex **6** (brown crystals) and known Co(III) mononuclear complex $[Co(HL^1)(L^1)]\cdot CH_3OH\cdot H_2O$ (purple crystals).

Synthesis of

$[Co_2Mn_2(HL^3)_4(dmf)_2]\cdot 6H_2O$ (7)

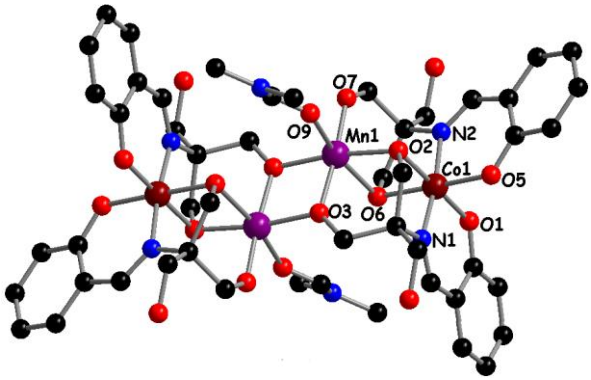

Salicylaldehyde (0.31 ml, 3.0 mmol) and *tris*-(hydroxymethyl)-aminomethane (0.36 g, 3.0 mmol) were dissolved in dmf (20 mL), forming a yellow solution of H_4L^3 which was magnetically stirred at 100–120 °C (10 min). Then, cobalt powder (0.06 g, 1.0 mmol), manganese acetate tetrahydrate (0.24 g, 1.0 mmol), were added to the hot yellow solution of the ligand and magnetically stirred until the total dissolution of metal powders was observed (2 h). Dark brown crystals of **7** suitable for X-ray analysis were obtained from the reaction mixture after addition of Et_2O after 7 days. Yield: 0.12 g, 18 % (per Co). Anal. calc. for $C_{50}H_{74}N_6O_{24}Co_2Mn_2$: C, 48.80; H, 5.36; N, 6.21; Mn, 8.02; Co, 8.60 %. Found: C, 43.74; H, 5.44; N, 6.13; Mn, 6.65; Co, 7.56 %. IR (KBr, cm^{-1}): 3285 (br), 2925 (w), 2875 (w), 1630 (s), 1535 (s), 1440 (s), 1396 (m), 1294 (s), 1192 (m), 1145 (s), 1042 (s), 934 (m), 900 (m), 755 (s), 650 (s), 579 (m), 526 (w), 467 (m), 435 (m). The compound is soluble in dmso and dmf, sparingly soluble in CH_3OH and CH_3CN and insoluble in water.

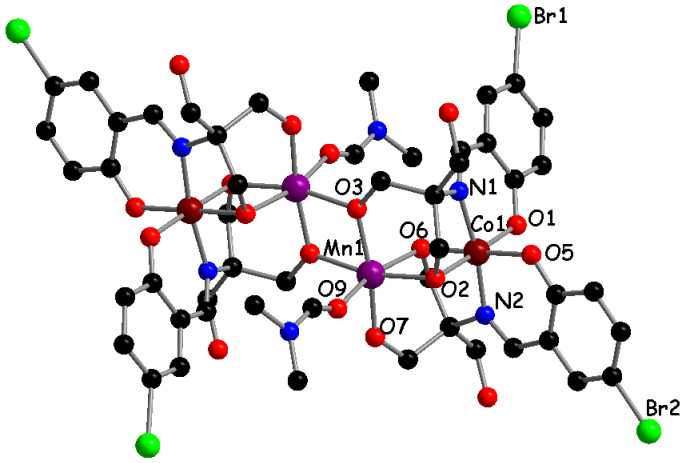

Synthesis of $[Co_2Mn_2(HL^7)_4(dmf)_2]\cdot dmf\cdot H_2O$ (8)

This complex was prepared in a similar way to that of **7**, but using 5-bromo-salicylaldehyde (0.6 g, 3.0 mmol) and *tris*-(hydroxymethyl)-aminomethane (0.36 g, 3.0 mmol) to form the H_4L^7 ligand. Dark brown crystals of **8** suitable for X-ray analysis were obtained from the reaction mixture after addition of Et_2O after 7 days. Yield: 0.15 g, 18 % (per Co). Anal. calc. for $C_{53}H_{67}N_7O_{20}Br_4Co_2Mn_2$: C, 38.13; H, 4.05; N, 5.87; Mn, 6.58; Co, 7.06 %. Found: C, 38.05; H, 3.85; N, 5.80; Mn, 6.28; Co, 6.93 %. IR (KBr, cm^{-1}): 3290 (br), 2930 (w), 2885 (w), 1624 (s), 1535 (s), 1444 (s), 1397 (m), 1287 (s), 1199 (m), 1155 (s), 1042 (s), 934 (m), 910 (m), 744 (s), 654 (s), 582 (m), 526 (w), 467 (m), 435 (m). The compound is soluble in dmso and dmf, sparingly soluble in CH_3OH and CH_3CN and insoluble in water.

Synthesis of $[Co_2Mn_2(HL^{11})_4(dmf)_2]\cdot dmf\cdot 3H_2O$ (9)

This complex was prepared in a similar way to that of **7**, but using 5-nitro-salicylaldehyde (0.5 g, 3.0 mmol) and *tris*-(hydroxymethyl)-aminomethane (0.36 g, 3.0 mmol) to form the H_4L^{11} ligand. Dark brown crystals of **9** suitable

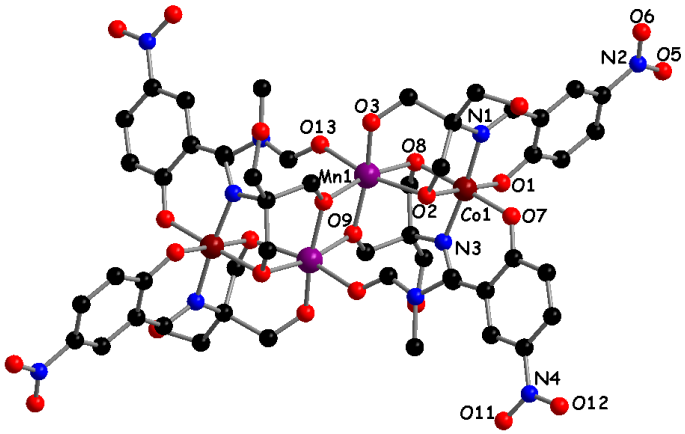

for X-ray analysis were obtained from the reaction mixture after addition of Et_2O after 7 days. Yield: 0.17 g, 22 % (per Co). Anal. calc. for $C_{53}H_{71}N_{11}O_{30}Co_2Mn_2$: C, 40.40; H, 4.76; N, 9.78; Mn, 6.98; Co, 7.49 %. Found: C, 40.61; H, 4.06; N, 9.42; Mn, 6.29; Co, 7.38 %. IR (KBr, cm^{-1}): 3295 (br), 2934(w), 2886 (w), 1623 (s), 1534 (s), 1443 (s), 1400 (m), 1286 (s), 1210 (m), 1150 (s), 1045 (s), 938 (m), 925 (m), 744 (s), 644 (s), 582 (m), 526 (w), 467 (m), 443 (m). The compound is soluble in dmso and dmf, sparingly soluble in CH_3OH and CH_3CN and insoluble in water.

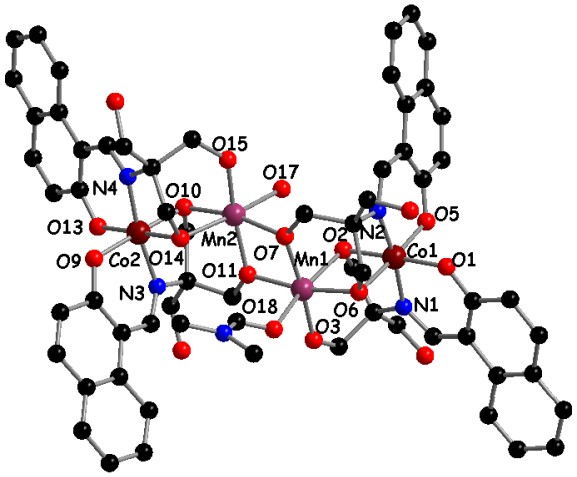

Synthesis of

$[Co_2Mn_2(HL^{10})_4(dmf)(H_2O)]\cdot 2dmf \cdot 2H_2O$

(10)

This complex was prepared in a similar way to that of **7**, but using 2-hydroxy-1-naphthaldehyde (0.25 g, 1.5 mmol) and *tris*-(hydroxymethyl)-aminomethane (0.18 g, 1.5 mmol) to form the H_4L^{10} ligand. Dark brown crystals of **10** suitable for X-ray analysis were obtained from the reaction mixture after addition of Et_2O after 7 days. Yield: 0.18 g, 23 % (per Co). Anal. calc. for $C_{69}H_{83}N_7O_{22}Co_2Mn_2$: C, 53.43; H, 3.71; N, 6.93; Mn, 7.3; Co, 6.8 %. Found: C, 54.00; H, 4.01; N, 6.03; Mn, 8.0; Co, 6.1 %. IR (KBr, cm^{-1}): 3293 (br), 2936 (w), 2888 (w), 1625 (s), 1540 (s), 1444 (s), 1402 (m), 1288 (s), 1215 (m), 1155 (s), 1044 (s), 937 (m), 925 (m), 743 (s), 648 (s), 582 (m), 525 (w), 467 (m), 442 (m). The compound is soluble in dmso and dmf, sparingly soluble in CH_3OH and CH_3CN and insoluble in water.

Synthesis of

$[Co_2Mn_2(L^6)_4(dmf)_2]\cdot 2dmf$ (11)

This complex was prepared in a similar way to that of **7**, but using 5-bromo-salicylaldehyde (0.6 g, 3.0 mmol) and 2-amino-2-methyl-1,3-propanediol (0.16 g, 1.5 mmol) to form the H_3L^6 ligand. Dark brown crystals of **11** suitable for X-ray analysis were obtained from the reaction mixture after addition of Et_2O after 7 days.

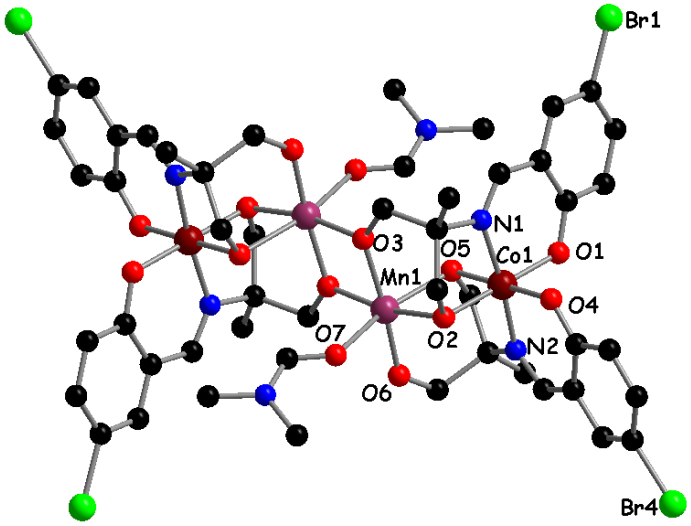

Yield: 0.24 g, 29 % (per Co). Anal. calc. for $C_{56}H_{72}N_8O_{16}Br_4Co_2Mn_2$: C, 40.50; H, 4.37; N, 6.75; Mn, 6.62; Co, 7.10 %. Found: C, 40.45; H, 4.50; N, 6.71; Mn, 6.5; Co, 6.93 %. IR (KBr, cm^{-1}): 3299 (br), 2937 (w), 2888 (w), 1624 (s), 1545 (s), 1448 (s), 1402 (m), 1278 (s), 1225 (m), 1155(s), 1044 (s), 937 (m), 925 (m), 743 (s), 645 (s), 582 (m), 527 (w), 467 (m), 442 (m). The compound is soluble in dmso and dmf, sparingly soluble in CH_3OH and CH_3CN and insoluble in water.

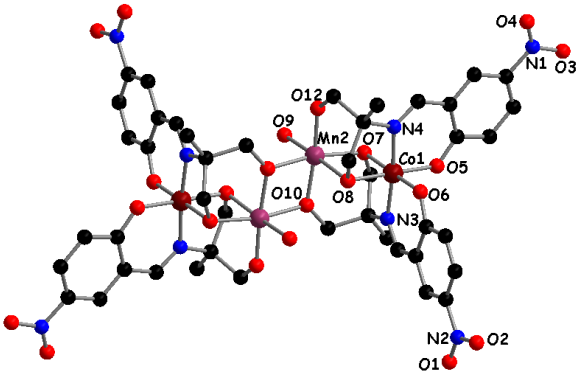

Synthesis of

$[Co_2Mn_2(L^9)_4(dmf)_2]\cdot 2dmf \cdot 7H_2O$ (12)

This complex was prepared in a similar way to that of **7**, but using 5-nitro-salicylaldehyde (0.25 g, 1.5 mmol) and 2-amino-2-methyl-1,3-propanediol (0.16 g, 1.5 mmol) to form the H_3L^9 ligand. Dark brown crystals of **12** suitable for X-ray analysis were obtained from the reaction mixture after addition of Et_2O after 7 days. Yield: 0.2 g, 24 % (per Co). Anal. calc. for $C_{56}H_{86}N_{12}O_{31}Co_2Mn_2$: C, 40.74; H, 5.25; N, 10.18; Mn, 6.65; Co, 7.14 %. Found: C, 40.25; H, 4.44; N, 9.95; Mn, 6.74; Co, 6.85 %. IR (KBr, cm^{-1}): 3299 (br), 2932 (w), 2884 (w), 1623 (s), 1545 (s), 1446 (s), 1410 (m), 1280 (s), 1225 (m), 1155 (s), 1044 (s), 938 (m), 925 (m), 745 (s), 645 (s), 582 (m), 527 (w), 467 (m), 442 (m). The compound is soluble in dmso and dmf, sparingly soluble in CH_3OH and CH_3CN and insoluble in water.

Synthesis of

$[Co_2Mn^{II}_2Mn^{III}_2(L^4)_4Cl_2(\mu_3\text{-}OH)_2(dmf)_4]\cdot 2dmf$ (13)

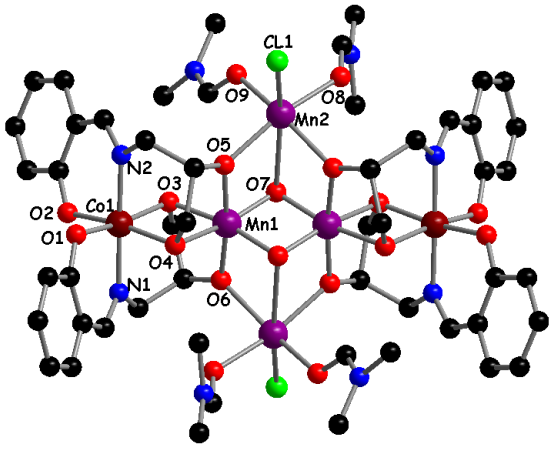

Salicylaldehyde (0.1 mL, 1.0 mmol), 2-hydroxy-aminopropanol (0.08 g, 1.0 mmol) and triethylamine (0.28 ml, 2.0 mmol) were dissolved in dmf (20 mL), forming a yellow solution of H_3L^4 which was stirred at 100–120 °C (10 min). Then, cobalt powder (0.06 g, 1.0 mmol), manganese acetate tetrahydrate (0.24 g, 1.0 mmol), were added to the hot yellow solution of the ligand and stirred until the total dissolution of metal powders was observed (4 h). Dark brown crystals of **13** suitable for X-ray analysis were obtained from the reaction mixture upon diffusion of Et_2O after 7 days. Yield: 0.12 g, 29 % (per Mn). Anal. calc. for $C_{58}H_{84}N_{10}O_{20}Cl_2Co_2Mn_4$: C, 40.75; H, 4.69; N, 8.80; Mn, 13.81; Co, 7.40 %. Found: C, 40.78; H, 4.88; N, 8.75; Mn, 13.65; Co, 7.66 %. IR (KBr, cm^{-1}): 3283 (br), 2930 (w), 2870 (w), 1635 (s), 1533 (s), 1445 (s), 1399 (m), 1290 (s), 1190 (m), 1140 (s), 1040 (s), 935 (m), 900 (m), 755 (s), 656 (s), 590 (m), 530 (w), 467 (m), 435 (m). The compound is soluble in dmso and dmf, sparingly soluble in CH_3OH and CH_3CN and insoluble in water.

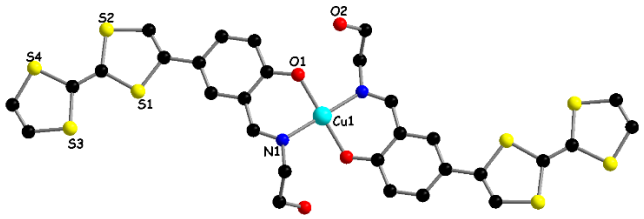

Synthesis of $[Cu(HL^{12})_2]_n$

The H_2L^{12} ligand (0.025 g, $6.8 \cdot 10^{-5}$ mol) was dissolved in 15 mL of methanol and $Cu(OAc)_2 \cdot H_2O$ (0.0068 g, $3.4 \cdot 10^{-5}$ mol) was added. The solution was stirred at 65°C for 1 h. After the reaction the resulting yellow precipitate was collected (0.015 g, 56 %). X-ray quality single crystals were obtained by slow diffusion of diethyl ether into methanol solution. IR (ATR, cm^{-1}): 3320 (br), 3056 (w), 2903 (w), 1621 (s), 1531 (s), 1478 (s), 1389 (m), 1322 (m), 1064 (m), 632 (m), 616 (w). Anal. calc. for $C_{30}H_{24}N_2O_4S_8Cu$: C 45.24, H 3.04, N 3.52, S 32.20 %; Found: C 45.10, H 2.87, N 3.30, S 32.00 %.

Synthesis of (TTF-Sal)$_2$PF$_6$

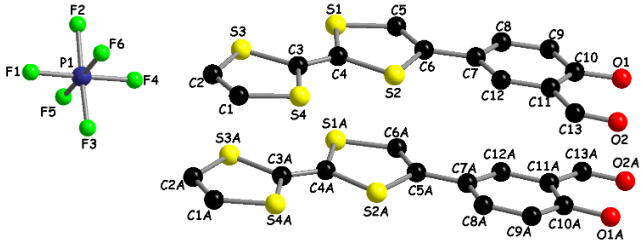

TBA[PF_6] (0.06 g, 0.16 mmol) was dissolved in dichloromethane (6 mL) and the solution was poured into the cathodic compartment of the electrocrystallization cell. The anodic chamber was filled with **TTF-Sal** (0.005 g, 0.016 mmol) dissolved in dichloromethane (6 mL). Black-green needle-like single crystals of the salt were grown at 25 °C over a period of 7 days on a platinum wire electrode by applying a constant current of 0.5 µA.

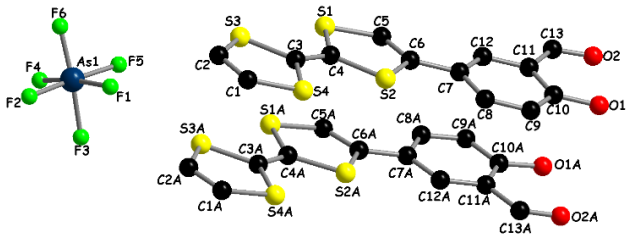

Synthesis of (TTF-Sal)$_2$AsF$_6$

This compound was prepared following the same method used for **(TTF-Sal)$_2$PF$_6$** from TBA[AsF_6] (0.067 g, 0.16 mmol) instead of TBA[PF_6].

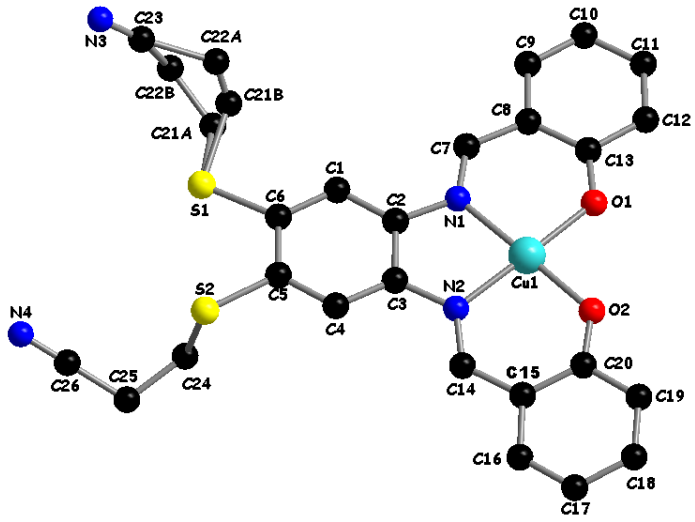

Synthesis of [CuL^{13}]·0.5CH$_3$OH (14)

Ligand H_2L^{13} (0.4 g, 0.82 mmol) was dissolved in DCM (30 mL), forming an orange solution. Then, a solution of copper(II) acetate monohydrate (0.16 g, 0.82 mmol) in methanol (30 mL) was added. The resulted mixture was heated for one hour. The formation of a brown precipitate was observed. The powder was filtered off and washed with DCM. Yield: 0.45 g, (96 %). Brown crystals of **14** suitable for X-ray analysis were obtained by the slow evaporation of the filtrate. Anal. calc. for $C_{27}H_{19}N_4O_3S_2Cu_2$: C, 56.38; H, 3.33; N, 9.74; S, 11.15 %. Found: C, 56.34; H, 3.15; N, 9.33; S, 10.87 %. IR (ATR, cm^{-1}): 3283 (br), 2930(w), 2870 (w), 2120 (s), 1634 (s), 1535 (s), 1437 (s), 1400 (m), 1290 (s), 1190 (m), 1140 (s), 1040 (s), 935 (m), 900 (m), 755 (s), 656 (s), 590 (m), 530 (w), 435 (m). The compound is soluble in dmso and dmf, sparingly soluble in CH$_3$OH and CH$_3$CN and insoluble in water.

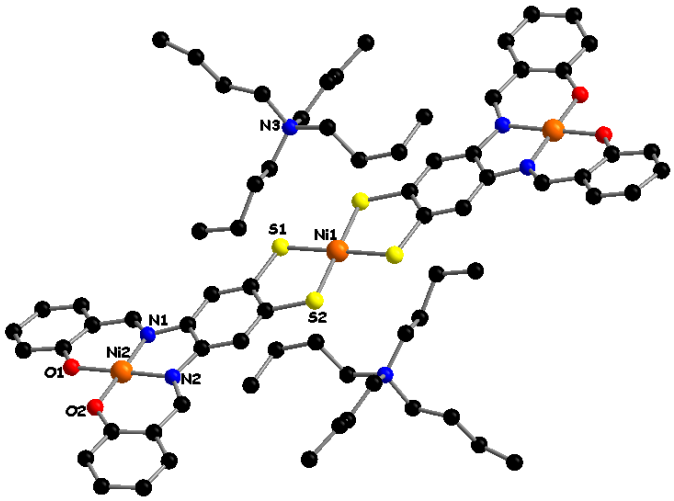

Synthesis of [TBA]$_2$[{Ni(L^{13})$_2$}$_2$Ni]·6CH$_2$Cl$_2$ (15)

Nickel complex [NiL^{13}] (0.1 g, 0.18 mmol) was dissolved in degassed dmf (12 mL) and to the solution obtained [TBA]OH (0.5 mL, 0.1 M) was added. The resulting mixture was stirred at RT 30 min. The color of the solution was changed from brown to saturated reddish brown. Nickel(II) chloride hexahydrate $NiCl_2·6H_2O$ (0.021 g, 0.087 mmol) was added to the resulted solution and stirred at RT 15 min. The black-purple solution was evaporated under reduced pressure and the crude product was dissolved in DCM and filtered off. Black crystals, suitable for X-ray analysis were obtained by the slow evaporation of the filtrate under vacuum. Yield: 0.035 g, (20 %). Anal. calc. for $C_{78}H_{108}N_6O_4S_4Cl_{12}Ni_3$: C, 48.71; H, 5.66; N, 4.37; S, 6.67 %. Found: C, 47.66; H, 5.25; N, 4.25; S, 6.55 %. The compound is soluble in most common organic solvents and insoluble in water.

Synthesis of

$[TBA]_2[\{Cu(L^{13})_2\}_2Cu]\cdot 5CH_2Cl_2$

(16)

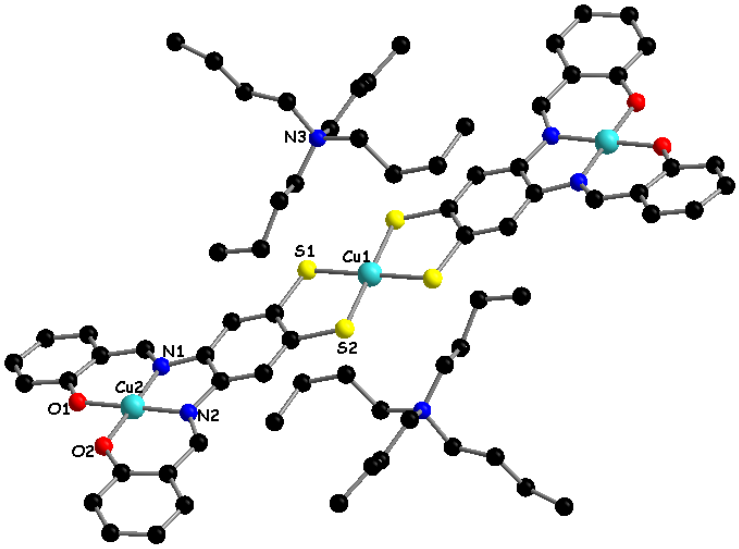

This complex was prepared in a similar way to that of **15**, but using complex **14** (0.1 g, 0.17mmol) and copper chloride dihydrate (0.016 g, 0.084 mmol) instead of $[NiL^{13}]$ and $NiCl_2\cdot 6H_2O$, respectively. Black crystals, suitable for X-ray analysis were obtained by slow evaporation of the filtrate under vacuum. Yield: 0.028 g, (18 %). Anal. calc. for $C_{77}H_{106}N_6O_4S_4Cl_{10}Cu_3$: C, 49.91; H, 5.77; N, 4.54; S, 6.92 %. Found: C, 49.56; H, 5.37; N, 4.35; S, 6.85 %. The compound is soluble in most common organic solvents and insoluble in water.

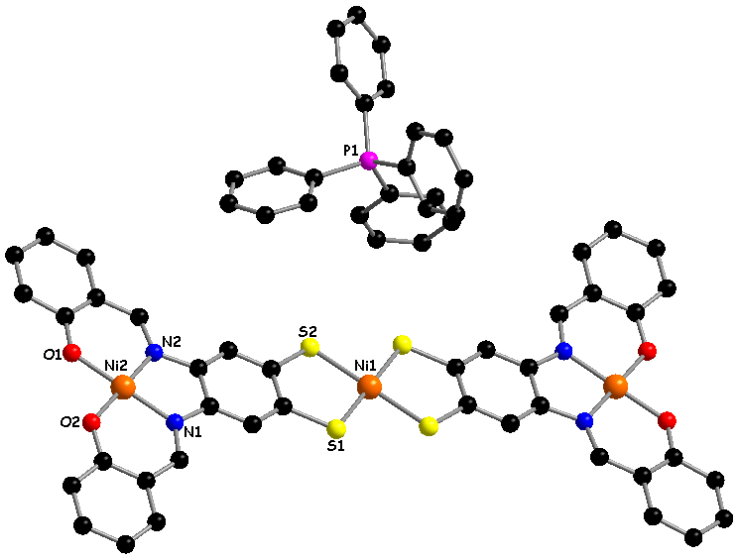

Synthesis of

$[PPh_4][\{Ni(L^{13})_2\}_2Ni]\cdot 4CH_2Cl_2$

(17)

To a solution of nickel complex $[NiL^{13}]$ (0.1 g, 0.18 mmol) in degassed dmf (12 mL), *tert*-BuOK (0.052 g, 0.46 mmol) was added. The resulting mixture was stirred at RT for 30 min. The color of the solution was changed from brown to saturated black-purple. Nickel(II) chloride hexahydrate $NiCl_2\cdot 6H_2O$ (0.021 g, 0.087 mmol) and $[PPh_4]Br$ (0.039 g, 0.092 mmol) were added to the resulted solution and stirred at RT for 15 min. The black-purple solution was evaporated under reduced pressure and the crude was dissolved in DCM and filtered of. The black crystals, suitable for X-ray analysis were obtained by the slow evaporation of the filtrate in vacuum. Yield: 0.012 g, (8 %). Anal. calc. for $C_{68}H_{52}N_4O_4PS_4Cl_8Ni_3$: C, 50.79; H, 3.26; N, 3.48; S, 7.98 %. Found: C, 50.17; H, 2.87; N, 3.00; S, 7.66 %. The compound is soluble in most common organic solvents and insoluble in water.

Synthesis of

$[PPh_4][\{Cu(L^{13})_2\}_2Cu]\cdot 4CH_2Cl_2$ (18)

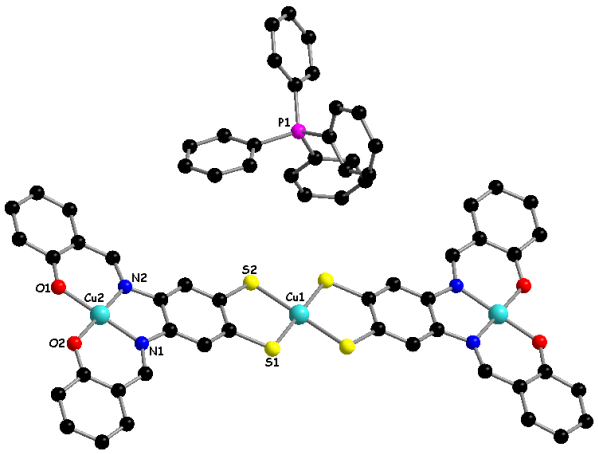

This complex was prepared in a similar way to that of **17**, but using complex **14** (0.1 g, 0.17mmol) and copper chloride dihydrate (0.016 g, 0.084 mmol) instead of [NiL^{13}] and $NiCl_2\cdot 6H_2O$, respectively. The black crystals, suitable for X-ray analysis were obtained by the slow evaporation of the filtrate in vacuum. Yield: 0.01 g, (7 %). Anal. calc. for $C_{68}H_{52}N_4O_4PS_4Cl_8Cu_3$: C, 50.33; H, 3.23; N, 3.45; S, 7.90 %. Found: C, 50.11; H, 3.11; N, 3.27; S, 7.85 %. The compound is soluble in most common solvents and insoluble in water.

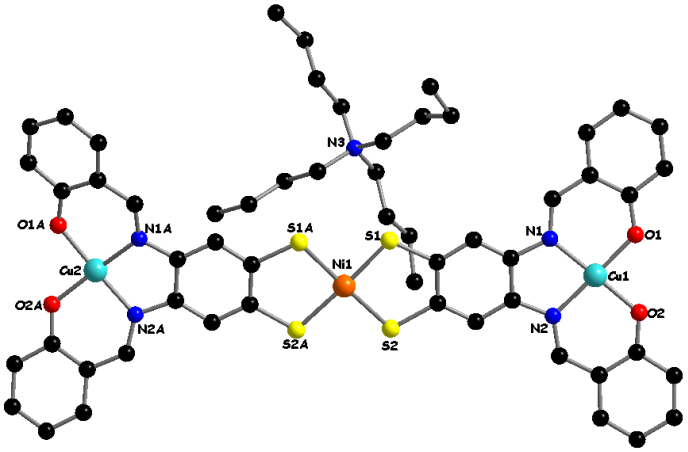

Synthesis of

$[TBA]_2[\{Cu(L^{13})_2\}_2Ni]_2\cdot 2CH_2Cl_2$ (19)

This complex was prepared in a way similar to that of **17**, but using complex **14** (0.1 g, 0.17mmol) instead of [NiL^{13}] and nickel chloride hexahydrate (0.021 g, 0.087 mmol). The black crystals, suitable for X-ray analysis were obtained by the slow evaporation of the filtrate in vacuum. Yield: 0.01 g, (7 %). Anal. calc. for $C_{114}H_{124}N_{10}O_8S_8Cl_4Cu_4Ni_2$: C, 54.07; H, 4.94; N, 5.53; S, 10.13%. Found: C, 54.37; H, 4.65; N, 5.24; S, 10.07%. The compound is soluble in most common organic solvents and insoluble in water.

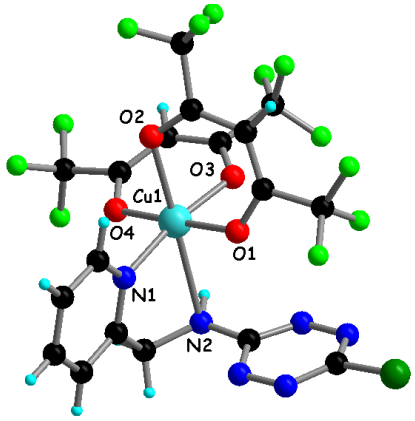

Synthesis of $[Cu(Hfac)_2(HL^{14})]$ (20)

To a solution of HL^{14} (0.020 g, 0.090 mmol) in 10 mL of dichloromethane, a solution of $Cu(Hfac)_2$ (0.043 g, 0.090 mmol) in 20 mL of dichloromethane was added. The mixture was stirred at 40 ˚C for 20 minutes. During the reaction the colour changed from red to brown. The resulting solution was left undisturbed for 1 day at room temperature. Yellow crystals (0.045 g, 71%), suitable for

X-ray analysis, were obtained. MALDI-TOF MS: *m/z* = 705.1 $[Cu(Hfac)_2(HL^{14})]^+$. IR (ATR, cm^{-1}): 1652 (s), 1549 (m), 1537 (m), 1268 (s), 1195 (s), 1158 (s), 1017 (s), 763 (w), 555 (s), 457 (w), 424 (w). Anal. calc. for $C_{18}H_9ClF_{12}N_6O_4Cu$: C 30.87, H 1.30, N 12.00 %; Found: C 30.65, H, 1.00, N 11.70 %. The compound is soluble in dmso, dmf, CH_3OH and CH_3CN, insoluble in water.

Synthesis of $[Cu_2(\mu_2\text{-}Cl)(L^{14})_2]$ (21)

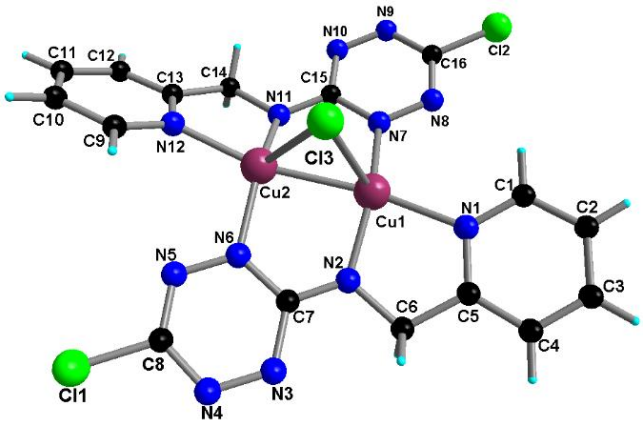

To a solution of **HL^{14}** (0.025 g, 0.112 mmol) in 10 mL of dichloromethane, was added a solution of copper(II) hexafluoro-acetylacetonate hydrate $Cu(Hfac)_2$ (0.054 g, 0.112 mmol) in 20 mL of methanol. The mixture was stirred at 70 ˚C for 1 hour. During the reaction the colour changed from red to red-brown. The resulting solution was left undisturbed for 4 days at room temperature. Plate-like dark-red crystals (0.015 g, 22 % yield), suitable for X-ray analysis, were obtained. MALDI-TOF MS: *m/z* = 567.7 $[Cu_2(L^{14})_2]^+$. ESI-MS: *m/z* = 567.7 $[Cu_2(L^{14})_2]^+$, 1176.66 $[Cu_4Cl(L^{14})_4]^+$. IR (ATR, cm^{-1}): 1641 (s), 1556 (m), 1536 (m), 1254 (s), 1194 (s), 1143 (s), 1005 (s), 750 (m), 547 (s), 460 (m), 410 (m). Anal. calc. alcd. for $C_{16}H_{12}Cl_3N_{12}Cu_2$: C 31.72, H 2.00, N 27.75 %; found: C 32.10, H 2.17, N 28.00 %.

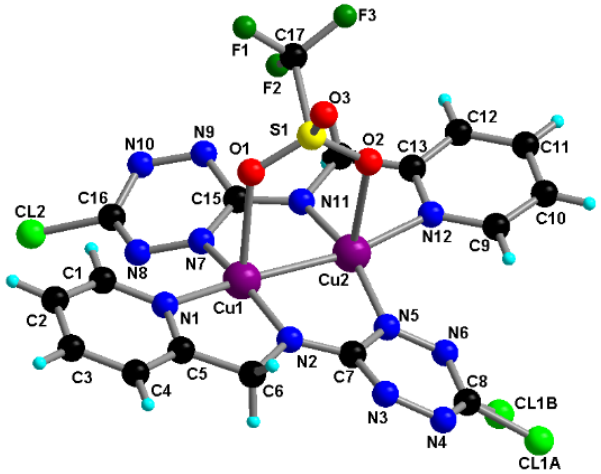

Synthesis of $[Cu_2(OTf)(L^{14})_2]$ (22)

To a solution of **HL^{14}** (0.025 g, 0.112 mmol) in 10 mL of dichloromethane, a solution of copper(II) triflate $Cu(OTf)_2$ (0.040 g, 0.112 mmol) in 20 mL of methanol was added. The mixture was stirred at 70 ˚C for 1 hour. During the reaction the colour changed from red to red-brown. The resulting solution was left undisturbed for 4 days at room temperature. Plate-like dark-red crystals (0.015 g), suitable for X-ray analysis, consisting in a mixture of **22** (main compound) and **21** (minor compound) were obtained. MALDI-TOF MS: m/z = 568.4 $[Cu_2(L^{14})_2]^+$. IR (ATR, cm^{-1}): 1639 (s), 1550 (m), 1526 (m), 1247 (s), 1195 (s), 1138 (s), 1011 (s), 759 (m), 565 (s), 470 (m), 420 (m).

Synthesis of $[CuCl_2(HL^{14})_2]\cdot 2CH_3CN$ (23)

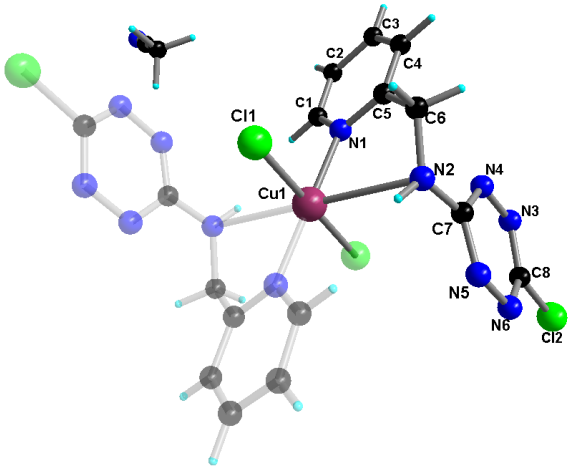

To a solution of **HL^{14}** (0.025 g, 0.112 mmol) in 10 mL of dichloromethane, a solution of $CuCl_2\cdot 2H_2O$ (0.019 g, 0.112 mmol) in 20 mL of acetonitrile was added. The mixture was stirred at 70 ˚C for 1 hour. During the reaction the colour changed from red to dark-brown. The resulting solution was left undisturbed for 2 days at room temperature. Prismatic dark-yellow crystals (0.05 g, 68% yield), suitable for X-ray analysis, were obtained. MALDI-TOF MS: *m/z* = 542.3 $[CuCl(HL^{14})_2]^+$. ESI-MS: *m/z* = 567.7 $[CuCl(HL^{14})_2]^+$. IR (ATR, cm^{-1}): 1648 (s), 1553 (m), 1540 (m), 1261 (s), 1189 (s), 1149 (s), 1010 (s), 757 (w), 549 (s), 462 (w), 418 (w). Anal. calc. for $C_{20}H_{20}Cl_4N_{14}Cu$: C 36.30, H 3.05, N 29.63 %; Found: C 35.90, H 2.75, N 29.30 %. The compound is soluble in dmso, dmf, CH_3OH and CH_3CN, insoluble in water.

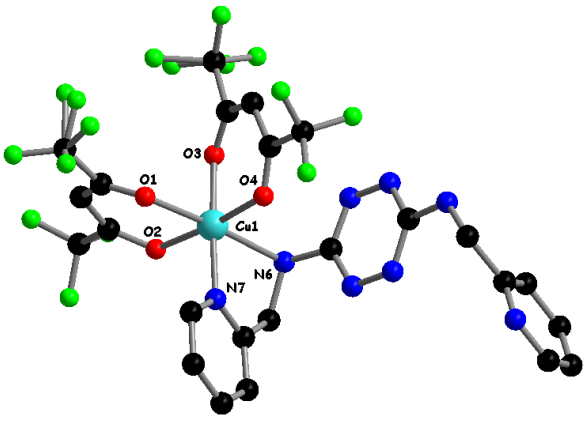

Synthesis of $[Cu(Hfac)_2(H_2L^{15})]$ (24)

To a solution of **H_2L^{15}** (0.02 g, $6.8\cdot 10^{-5}$ mol) in 10 mL of dichloromethane, was added a solution of copper(II) hexafluoro-acetylacetonate hydrate $Cu(Hfac)_2$ 32.5 mg ($6.8\cdot 10^{-5}$ mol) in 10 mL of methanol. The mixture was stirred at room temperature for 1 hour. During the reaction colour was changed from red to brown. The resulting solution was left undisturbed for 2 days at room temperature. The yellow-brown crystals (0.025 g, 47%) suitable for X-ray were obtained. MALDI-TOF MS: *m/z* = 563.9 $[Cu(Hfac)(H_2L^{15})]^+$, 712.3. ESI-MS: *m/z* = 563.9 $[Cu(Hfac)(H_2L^{15})]^+$, 651.1 $[Cu(H_2L^{15})_2]^+$. IR (ATR, cm^{-1}): 3415 (w), 1643 (s), 1551 (m), 1252 (s), 1199 (s), 1135 (s), 928 (w), 793 (s), 669 (s), 583 (s), 516 (m). Anal. calc. for $C_{24}H_{16}F_{12}N_8O_4Cu$: C 37.34, H 2.09, N 14.54 %; Found: C 34.55, H 2.36, N 14.78 %. The compound is soluble in dmso, dmf, CH_3OH and CH_3CN, insoluble in water.

Synthesis of [Ni(Hfac)$_2$(H$_2$L^{15})] (25)

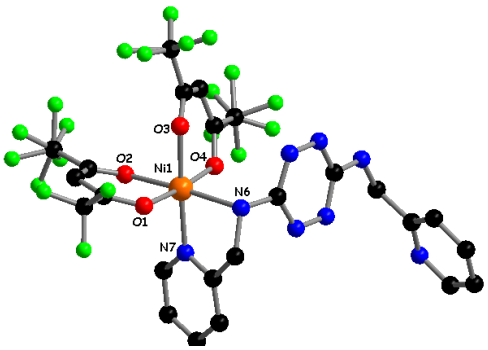

To a solution of **H$_2$L^{15}** (0.02 g, 6.8·10^{-5} mol) in 10 mL of dichloromethane, was added a solution of nickel (II) hexafluoro-acetylacetonate hydrate Ni(Hfac)$_2$ 32.1 mg (6.8·10^{-5} mol) in 10 mL of acetonitrile. The mixture was stirred at room temperature for 1 hour. During the reaction colour was changed from red to brown. The resulting solution was left undisturbed for 1 days at room temperature. The brown crystals (0.037 g, 70%) suitable for X-ray were obtained. ESI-MS: *m/z* = 766 [Ni(Hfac)$_2$(H$_2$L^{15})]$^+$. IR (ATR, cm^{-1}): 3219 (w), 1642 (s), 1482 (s), 1253 (s), 1189 (s), 1139 (s), 945 (w), 792 (s), 671 (s), 585 (s), 529 (m). Anal. calc. for $C_{24}H_{16}F_{12}N_8O_4Ni$: C 37.57, H 2.10, N 14.60 %; Found: C 37.65, H 2.44, N 14.85 %. The compound is soluble in dmso, dmf, CH_3OH and CH_3CN, insoluble in water.

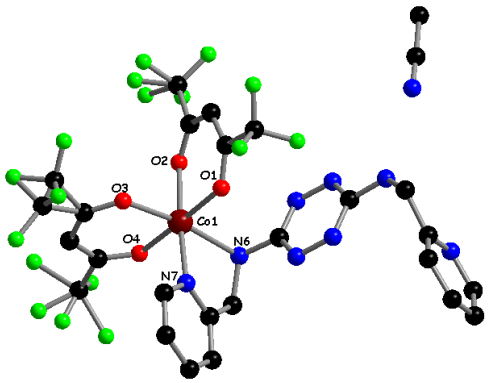

Synthesis of

[Co(Hfac)$_2$(H$_2$L^{15})]·CH$_3$CN (26)

To a solution of **H$_2$L^{15}** (0.02 g, 6.8·10^{-5} mol) in 10 mL of dichloromethane, was added a solution of cobalt (II) hexafluoro-acetylacetonate hydrate Co(Hfac)$_2$ 32.1 mg (6.8·10^{-5} mol) in 10 ml of acetonitrile. The mixture was stirring at room temperature for 1 hour. During the reaction colour was changed from red to dark red. The resulting solution was left undisturbed for 2 days at room temperature. Red crystals (0.027 g, 49 %) suitable for X-ray were obtained. ESI-MS: *m/z* = 560.1 [Co(Hfac)(H$_2$L^{15})]$^+$, 767 [Co(Hfac)$_2$(H$_2$L^{15})]$^+$. IR (ATR, cm^{-1}): 3311 (w), 1639 (s), 1482 (s), 1256 (s), 1189 (s), 1137 (s), 953 (w), 796 (s), 667 (s), 584 (s), 529 (m). Anal. calc. for $C_{26}H_{19}F_{12}N_9O_4Co$: C 38.63, H 2.36, N 15.59 %; Found: C 38.87, H 2.74, N 15.64 %. The compound is soluble in dmso, dmf, CH_3OH and CH_3CN, insoluble in water.

Synthesis of

[{Cu(Hfac)$_2$}$_2$(H$_2$L^{15})]·2CH$_3$OH (27)

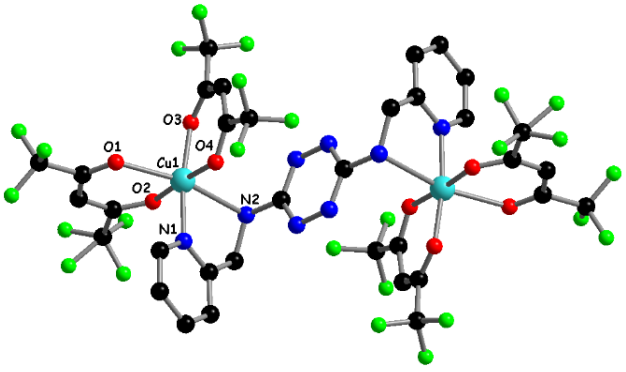

To a solution of **H$_2$L^{15}** (0.02 g, 6.8·10^{-5} mol) in 10 mL of dichloromethane, was added a solution of copper(II) hexafluoro-acetylacetonate hydrate Cu(Hfac)$_2$ 130 mg (27.2·10^{-5} mol) in 20 mL of methanol. The

mixture was stirring at 70 °C for 1 hour. During the reaction, colour was changed from red to brown. The resulting solution was left undisturbed for 1 day at room temperature. Yellow-brown crystals (0.051 g, 57%) suitable for X-ray were obtained. MALDI-TOF MS: *m/z* = 1312, 1246, 626. IR (ATR, cm^{-1}): 3415 (w), 1642 (s), 1552 (m), 1253 (s), 1199 (s), 1201 (s), 928 (w), 794 (s), 670 (s), 584 (s), 517 (m). Anal. calc. for $C_{36}H_{26}F_{24}N_8O_{10}Cu_2$: C 32.91, H 1.99, N 8.52 %; Found: C 33.35, H 2.12, N 8.67 %. The compound is soluble in dmso, dmf, CH_3OH and CH_3CN, insoluble in water.

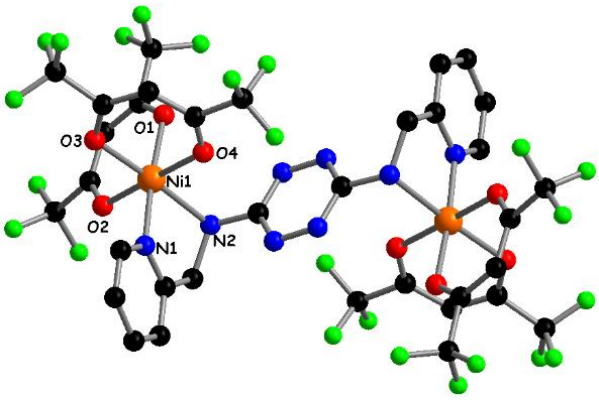

Synthesis of

[{Ni(Hfac)$_2$}$_2$(H$_2$L^{15})]·2CH$_3$CN (28)

To a solution of **H$_2$L^{15}** (0.02 g, $6.8\cdot10^{-5}$ mol) in 10 ml of dichloromethane, was added a solution of nickel(II) hexafluoro-acetylacetonate hydrate Ni(Hfac)$_2$ 96.5 mg ($20.4\cdot10^{-5}$ mol) in 20 mL of acetonitrile. The mixture was stirring at 70 °C for 1 hour. During the reaction colour was changed from red to red-brown. The resulting solution was left undisturbed for 1 days at room temperature. The yellow-brown crystals (0.06 g, 67%) suitable for X-ray were obtained. MALDI-TOF MS: *m/z* = 1320, 1238, 621. IR (ATR, cm^{-1}): 3418 (w), 1646 (s), 1548 (m), 1249 (s), 1203 (s), 1195 (s), 932 (w), 798 (s), 667 (s), 579 (s), 509 (m). Anal. calc. for $C_{38}H_{24}F_{24}N_{10}O_8Ni_2$: C 34.52, H 1.83, N 8.88 %; Found: C 34.89, H 1.95, N 9.32 %. The compound is soluble in dmso, dmf, CH_3OH and CH_3CN, insoluble in water.

Synthesis of

{[Co(Hfac)$_2$(H$_2$L^{15})]·[Co(Hfac)$_2$(CH$_3$OH)$_2$]}$_n$

(29)

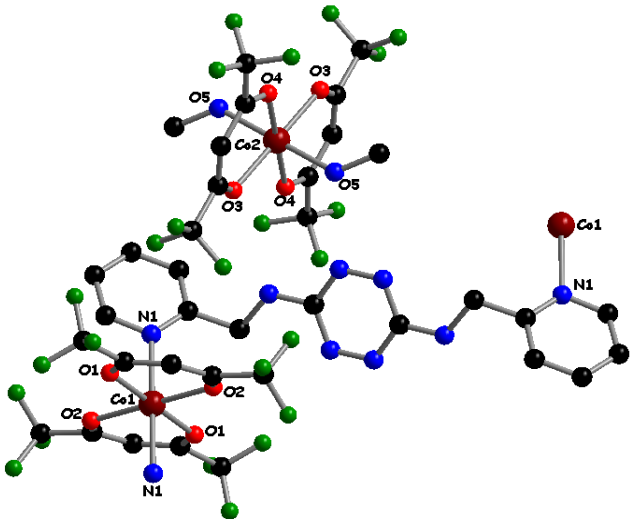

To a solution of **H$_2$L** 0.02 g ($6.8\cdot10^{-5}$ mol) in 10 mL of dichloromethane, was added a solution of cobaltl(II) hexafluoro-acetylacetonate hydrate Co(Hfac)$_2$ 96.5 mg ($20.4\cdot10^{-5}$ mol) in 20 ml of methanol. The mixture was stirring at 70 °C for 1 hour. During the reaction colour was changed from red to dark red. The resulting solution was left undisturbed for 1 day at room temperature. The small red crystals (0.048 g, 55 %) suitable for X-ray were obtained. It should be noted that in case of using acetonitrile instead of methanol led to the formation of complex **3**. MALDI-TOF MS: *m/z*

= 1304, 767. IR (ATR, cm^{-1}): 3380 (w), 1637 (s), 1536 (m), 1490 (m), 1449 (m), 1256 (s), 1197 (s), 1135 (s), 957 (w), 795 (s), 670 (s), 587 (s), 526 (m). Anal. calc. for $C_{36}H_{26}F_{24}N_8O_{10}Co_2$: C 33.15, H 2.01, N 8.59 %; Found: C 33.25, H 2.12, N 8.75 %. The compound is soluble in dmso, dmf, CH_3OH and CH_3CN, insoluble in water.

Appendix 3.

Selected geometrical parameters (distances/Å and angles/°) for **1**

$[Cu_3Mn(L^1)_4(CH_3OH)_3]I_3$

Cu1–O1	1.992(2)	Cu3–O1	1.963(2)
Cu1–O2	1.909(2)	Cu3–O3	2.474(2)
Cu1–O3	1.958(2)	Cu3–O5	1.968(2)
Cu1–O7	2.580(2)	Cu3–O6	1.901(2)
Cu1–O9	2.501(3)	Cu3–N3	1.929(3)
Cu1–N1	1.942(3)	Mn1–O1	2.411(2)
Cu2–O3	1.972(2)	Mn1–O5	1.942(2)
Cu2–O4	1.904(2)	Mn1–O7	1.944(2)
Cu2–O5	2.576(2)	Mn1–O8	1.865(2)
Cu2–O7	1.968(2)	Mn1–O11	2.320(3)
Cu2–O10	2.379(3)	Mn1–N4	1.958(3)
Cu2–N2	1.938(3)		
O1–Cu1–O2	169.24(10)	O1–Cu3–O3	75.07(8)
O1–Cu1–O3	87.58(9)	O1–Cu3–O5	86.11(9)
O1–Cu1–O7	74.83(8)	O1–Cu3–O6	95.60(10)
O1–Cu1–O9	91.88(9)	O1–Cu3–N3	168.50(11)
O1–Cu1–N1	83.86(10)	O3–Cu3–O5	78.82(8)
O2–Cu1–O3	94.68(9)	O3–Cu3–O6	99.70(9)
O2–Cu1–O7	95.76(9)	O3–Cu3–N3	109.52(9)
O2–Cu1–O9	98.69(10)	O5–Cu3–O6	177.40(11)
O2–Cu1–N1	94.14(11)	O5–Cu3–N3	84.53(10)
O3–Cu1–O7	72.81(8)	O6–Cu3–N3	93.99(11)
O3–Cu1–O9	88.41(8)	O1–Mn1–O5	75.26(8)
O3–Cu1–N1	171.17(10)	O1–Mn1–O7	79.84(8)
O7–Cu1–O9	157.15(8)	O1–Mn1–O8	100.06(10)
O7–Cu1–N1	106.83(9)	O1–Mn1–O11	159.06(9)
O9–Cu1–N1	89.72(10)	O1–Mn1–N4	101.81(9)
O3–Cu2–O4	170.35(10)	O5–Mn1–O7	89.50(9)
O3–Cu2–O5	76.22(8)	O5–Mn1–O8	93.66(11)
O3–Cu2–O7	88.11(9)	O5–Mn1–O11	89.31(11)
O3–Cu2–O10	91.16(8)	O5–Mn1–N4	172.86(10)
O3–Cu2–N2	83.52(9)	O7–Mn1–O8	176.71(11)
O4–Cu2–O5	95.08(9)	O7–Mn1–O11	86.06(10)
O4–Cu2–O7	93.32(9)	O7–Mn1–N4	83.55(10)
O4–Cu2–O10	98.45(10)	O8–Mn1–O11	94.89(12)
O4–Cu2–N2	94.21(10)	O8–Mn1–N4	93.27(11)
O5–Cu2–O7	72.63(8)	O11–Mn1–N4	91.81(11)
O5–Cu2–O10	155.88(8)		
O5–Cu2–N2	100.93(9)		
O7–Cu2–O10	86.69(9)		
O7–Cu2–N2	170.52(10)		
O10–Cu2–N2	97.88(10)		

Selected geometrical parameters (distances/Å and angles/^{o}) for **2**

$[Cu_3Mn(L^1)_4(CH_3OH)_3(H_2O)]NCS\cdot H_2O$

M1–O1	1.986(3)	M3–O1	1.956(3)
M1–O2	1.916(3)	M3–O3	2.489(3)
M1–O3	1.957(2)	M3–O5	1.964(3)
M1–O8	2.564(2)	M3–O6	1.904(3)
M1–O9	2.466(4)	M3–O12	2.476(4)
M1–N1	1.934(3)	M3–N3	1.929(4)
M2–O3	1.957(3)	M4–O1	2.480(3)
M2–O4	1.898(3)	M4–O5	1.949(3)
M2–O5	2.544(3)	M4–O7	1.895(3)
M2–O8	1.964(3)	M4–O8	1.949(3)
M2–O10	2.373(3)	M4–O11	2.383(5)
M2–N2	1.943(3)	M4–N4	1.943(4)
O1–M1–O2	170.58(13)	O1–M3–O3	74.59(9)
O1–M1–O3	87.47(11)	O1–M3–O5	87.59(11)
O1–M1–O8	75.85(10)	O1–M3–O6	94.49(13)
O1–M1–O9	91.70(13)	O1–M3–O12	86.73(14)
O1–M1–N1	83.80(13)	O1–M3–N3	169.98(13)
O2–M1–O3	94.64(11)	O3–M3–O5	79.36(10)
O2–M1–O8	95.96(10)	O3–M3–O6	95.64(11)
O2–M1–O9	97.58(13)	O3–M3–O12	157.66(13)
O2–M1–N1	94.33(13)	O3–M3–N3	109.25(12)
O3–M1–O8	72.93(9)	O5–M3–O6	173.89(13)
O3–M1–O9	86.73(12)	O5–M3–O12	87.86(13)
O3–M1–N1	171.00(13)	O5–M3–N3	84.13(13)
O8–M1–O9	156.38(11)	O6–M3–O12	97.98(14)
O8–M1–N1	106.89(12)	O6–M3–N3	94.32(15)
O9–M1–N1	91.30(15)	O12–M3–N3	87.31(15)
O3–M2–O4	173.58(13)	O1–M4–O5	74.46(10)
O3–M2–O5	78.09(9)	O1–M4–O7	97.81(11)
O3–M2–O8	88.30(11)	O1–M4–O8	78.55(11)
O3–M2–O10	88.84(12)	O1–M4–O11	156.06(13)
O3–M2–N2	83.52(12)	O1–M4–N4	109.33(14)
O4–M2–O5	96.81(11)	O5–M4–O7	95.30(12)
O4–M2–O8	93.92(13)	O5–M4–O8	88.01(11)
O4–M2–O10	97.20(13)	O5–M4–O11	85.46(15)
O4–M2–N2	94.02(14)	O5–M4–N4	170.42(14)
O5–M2–O8	72.54(10)	O7–M4–O8	174.27(14)
O5–M2–O10	157.89(11)	O7–M4–O11	96.89(15)
O5–M2–N2	103.91(11)	O7–M4–N4	92.90(14)
O8–M2–O10	89.49(12)	O8–M4–O11	88.02(14)
O8–M2–N2	171.64(13)	O8–M4–N4	84.24(13)
O10–M2–N2	92.09(14)	O11–M4–N4	88.65(18)

Selected geometrical parameters (distances/Å and angles/°) for **3**

$[Cu_3Mn(L^1)_4(CH_3OH)(H_2O)_{2.55}]Br\cdot 0.45H_2O$

Cu1–O1	1.894(7)	Cu3–O4	2.553(7)
Cu1–O2	1.985(7)	Cu3–O6	1.961(6)
Cu1–O6	2.508(7)	Cu3–O7	1.883(7)
Cu1–O8	1.983(7)	Cu3–O8	1.970(6)
Cu1–O2S	2.472(7)	Cu3–O3S	2.382(10)
Cu1–N1	1.901(9)	Cu3–N4	1.927(8)
Cu2–O2	1.953(7)	Mn1–O2	2.451(7)
Cu2–O3	1.892(6)	Mn1–O4	1.948(6)
Cu2–O4	1.951(7)	Mn1–O5	1.883(7)
Cu2–O8	2.438(7)	Mn1–O6	1.940(6)
Cu2–O4SA	2.536(18)	Mn1–O1S	2.355(9)
Cu2–N2	1.932(8)	Mn1–N3	1.960(8)
O1–Cu1–O2	170.9(3)	O4–Cu3–O6	72.4(2)
O1–Cu1–O6	95.9(3)	O4–Cu3–O7	95.8(3)
O1–Cu1–O8	94.3(3)	O4–Cu3–O8	75.6(3)
O1–Cu1–O2S	98.2(3)	O4–Cu3–O3S	157.4(3)
O1–Cu1–N1	93.9(3)	O4–Cu3–N4	103.9(3)
O2–Cu1–O6	75.9(2)	O6–Cu3–O7	94.3(3)
O2–Cu1–O8	87.2(3)	O6–Cu3–O8	88.0(3)
O2–Cu1–O2S	90.8(3)	O6–Cu3–O3S	88.1(3)
O2–Cu1–N1	84.9(3)	O6–Cu3–N4	170.7(3)
O6–Cu1–O8	73.8(2)	O7–Cu3–O8	170.0(3)
O6–Cu1–O2S	158.3(2)	O7–Cu3–O3S	96.9(3)
O6–Cu1–N1	106.9(3)	O7–Cu3–N4	94.6(3)
O8–Cu1–O2S	88.7(3)	O8–Cu3–O3S	93.0(3)
O8–Cu1–N1	171.6(3)	O8–Cu3–N4	82.8(3)
O2S–Cu1–N1	88.5(3)	O3S–Cu3–N4	93.6(3)
O2–Cu2–O3	94.9(3)	O2–Mn1–O4	73.9(3)
O2–Cu2–O4	86.4(3)	O2–Mn1–O5	98.1(3)
O2–Cu2–O8	76.2(3)	O2–Mn1–O6	78.1(3)
O2–Cu2–O4SA	83.9(5)	O2–Mn1–O1S	156.7(3)
O2–Cu2–N2	168.1(3)	O2–Mn1–N3	105.6(3)
O3–Cu2–O4	176.9(3)	O4–Mn1–O5	94.3(3)
O3–Cu2–O8	98.8(3)	O4–Mn1–O6	88.3(3)
O3–Cu2–O4SA	94.1(5)	O4–Mn1–O1S	86.7(3)
O3–Cu2–N2	94.0(3)	O4–Mn1–N3	171.8(3)
O4–Cu2–O8	78.8(3)	O5–Mn1–O6	174.6(3)
O4–Cu2–O4SA	88.9(5)	O5–Mn1–O1S	96.1(3)
O4–Cu2–N2	85.1(3)	O5–Mn1–N3	93.9(3)
O8–Cu2–O4SA	157.1(5)	O6–Mn1–O1S	88.8(3)
O8–Cu2–N2	110.2(3)	O6–Mn1–N3	83.6(3)
O4SA–Cu2–N2	87.6(5)	O1S–Mn1–N3	91.8(3)

Selected geometrical parameters (distances/Å and angles/°) for **4**

$[Cu_3Mn(L^1)_4(H_2O)_{3.4}]BF_4 \cdot 0.6H_2O$

Cu1–O2	2.451(4)	Cu3–O2	1.965(3)
Cu1–O6	1.967(4)	Cu3–O4	2.534(5)
Cu1–O7	1.894(4)	Cu3–O5	1.880(4)
Cu1–O8	1.965(4)	Cu3–O6	1.949(4)
Cu1–OW1	2.606(6)	Cu3–OW4B	2.45(2)
Cu1–N4	1.940(4)	Cu3–N3	1.926(5)
Cu2–O1	1.862(5)	Mn1–O3	1.882(4)
Cu2–O2	1.942(4)	Mn1–O4	1.955(4)
Cu2–O4	1.977(4)	Mn1–O6	2.475(4)
Cu2–O8	2.501(4)	Mn1–O8	1.947(4)
Cu2–OW3	2.465(7)	Mn1–OW2A	2.741(11)
Cu2–N1	1.948(5)	Mn1–N2	1.940(5)
O2–Cu1–O6	73.80(13)	O2–Cu3–O4	72.80(14)
O2–Cu1–O7	93.81(16)	O2–Cu3–O5	95.45(16)
O2–Cu1–O8	79.99(15)	O2–Cu3–O6	171.46(19)
O2–Cu1–OW1	157.86(13)	O2–Cu3–OW4B	89.7(5)
O2–Cu1–N4	112.96(16)	O2–Cu3–N3	169.37(19)
O6–Cu1–O7	94.97(17)	O4–Cu3–O5	92.87(15)
O6–Cu1–O8	87.74(16)	O4–Cu3–O6	79.71(15)
O6–Cu1–OW1	85.99(16)	O4–Cu3–OW4B	160.7(4)
O6–Cu1–N4	167.78(19)	O4–Cu3–N3	109.25(19)
O7–Cu1–O8	172.28(17)	O5–Cu3–O6	171.46(19)
O7–Cu1–OW1	96.91(17)	O5–Cu3–OW4B	97.0(4)
O7–Cu1–N4	94.70(18)	O5–Cu3–N3	94.87(18)
O8–Cu1–OW1	90.47(17)	O6–Cu3–OW4B	91.4(4)
O8–Cu1–N4	83.63(17)	O6–Cu3–N3	83.73(18)
OW1–Cu1–N4	85.44(18)	OW4B–Cu3–N3	86.5(5)
O1–Cu2–O2	174.55(19)	O3–Mn1–O4	173.7(2)
O1–Cu2–O4	95.0(2)	O3–Mn1–O6	94.06(16)
O1–Cu2–O8	96.93(17)	O3–Mn1–O8	95.57(17)
O1–Cu2–N1	94.3(2)	O3–Mn1–N2	93.9(2)
O2–Cu2–O4	87.44(17)	O4–Mn1–O6	81.16(16)
O2–Cu2–O8	79.10(15)	O4–Mn1–O8	87.26(16)
O2–Cu2–OW3	86.66(17)	O4–Mn1–OW2A	84.43(18)
O2–Cu2–N1	83.47(18)	O4–Mn1–N2	83.7(2)
O4–Cu2–O8	72.84(14)	O6–Mn1–O8	75.02(14)
O4–Cu2–OW3	88.5(2)	O6–Mn1–OW2A	155.29(15)
O4–Cu2–N1	170.4(2)	O6–Mn1–N2	108.5(2)
O8–Cu2–OW3	156.87(15)	O8–Mn1–OW2A	84.37(18)
O8–Cu2–N1	108.37(18)	O8–Mn1–N2	169.6(2)
OW3–Cu2–N1	87.8(2)	OW2A–Mn1–N2	89.6(2)

Selected geometrical parameters (distances/Å and angles/°) for **5**

$[Cu_3Mn(L^1)_4(CH_3OH)_3]_2[Mn(NCS)_4]\cdot 2CH_3OH$

Cu3–N3	1.926(4)	Mn2–O14	1.937(4)
Cu4–O9	1.904(4)	Mn2–O15	1.857(4)
Cu4–O10	1.975(4)	Mn2–O16	1.917(4)
Cu4–O12	1.958(4)	Mn2–O23	2.215(4)
Cu4–O21	2.435(4)	Mn2–N8	1.977(5)
Cu4–N5	1.938(5)	Mn3–N9	2.060(7)
Cu5–O11	1.916(4)	Mn3–N10	2.060(7)
Cu5–O12	1.964(4)	Mn3–N11	2.020(6)
Cu5–O16	1.953(4)	Mn3–N12	2.040(7)
O1–Cu1–O2	174.81(15)	O16–Cu5–N6	172.12(19)
O1–Cu1–O8	94.88(15)	O22–Cu5–N6	89.00(18)
O1–Cu1–O17	91.25(15)	O10–Cu6–O12	73.39(15)
O1–Cu1–N1	91.42(18)	O10–Cu6–O13	95.77(16)
O2–Cu1–O8	89.62(14)	O10–Cu6–O14	84.97(15)
O2–Cu1–O17	91.39(14)	O10–Cu6–N7	158.44(19)
O2–Cu1–N1	83.76(17)	O12–Cu6–O13	92.95(17)
O8–Cu1–O17	89.46(14)	O12–Cu6–O14	87.69(16)
O8–Cu1–N1	169.72(17)	O12–Cu6–N7	124.94(17)
O17–Cu1–N1	98.54(16)	O13–Cu6–O14	179.13(16)
O2–Cu2–O3	96.26(13)	O13–Cu6–N7	94.51(18)
O2–Cu2–O4	85.27(13)	O14–Cu6–N7	84.64(18)
O2–Cu2–O6	74.81(12)	O4–Mn1–O6	76.76(13)
O2–Cu2–N2	113.99(15)	O4–Mn1–O7	97.04(15)
O3–Cu2–O4	178.43(15)	O4–Mn1–O8	88.32(15)
O3–Cu2–O6	95.91(15)	O4–Mn1–O18	91.67(15)
O3–Cu2–N2	94.68(17)	O4–Mn1–N4	171.17(16)
O4–Cu2–O6	84.83(14)	O6–Mn1–O7	90.69(14)
O4–Cu2–N2	84.36(17)	O6–Mn1–O8	87.39(14)
O6–Cu2–N2	165.38(16)	O6–Mn1–O18	168.39(13)
O2–Cu3–O5	95.69(14)	O6–Mn1–N4	100.75(15)
O2–Cu3–O6	85.76(13)	O7–Mn1–O8	173.74(16)
O2–Cu3–O19	92.70(14)	O7–Mn1–O18	89.77(15)
O2–Cu3–N3	169.72(16)	O7–Mn1–N4	91.42(16)
O5–Cu3–O6	169.95(16)	O8–Mn1–O18	93.31(15)
O5–Cu3–O19	94.59(16)	O8–Mn1–N4	83.09(16)
O5–Cu3–N3	94.49(16)	O18–Mn1–N4	90.84(17)
O6–Cu3–O19	95.28(14)	O10–Mn2–O14	76.57(14)
O6–Cu3–N3	83.96(16)	O10–Mn2–O15	89.84(15)
O19–Cu3–N3	87.90(16)	O10–Mn2–O16	88.41(14)
O9–Cu4–O10	167.09(16)	O10–Mn2–O23	165.20(15)
O9–Cu4–O12	96.81(16)	O10–Mn2–N8	102.76(17)
O9–Cu4–O21	97.73(15)	O14–Mn2–O15	95.35(16)
O9–Cu4–N5	94.36(18)	O14–Mn2–O16	90.60(15)
O10–Cu4–O12	85.84(15)	O14–Mn2–O23	88.63(16)
O10–Cu4–O21	94.89(14)	O14–Mn2–N8	173.56(19)
O10–Cu4–N5	83.23(17)	O15–Mn2–O16	173.24(17)

O12–Cu4–O21	90.09(15)	O15–Mn2–O23	92.14(17)
O12–Cu4–N5	168.84(18)	O15–Mn2–N8	91.05(19)
O21–Cu4–N5	88.58(16)	O16–Mn2–O23	91.22(16)
O11–Cu5–O12	173.89(17)	O16–Mn2–N8	82.98(18)
O11–Cu5–O16	94.31(16)	O23–Mn2–N8	91.88(18)
O11–Cu5–O22	94.65(16)	N9–Mn3–N10	102.8(3)
O11–Cu5–N6	92.15(19)	N9–Mn3–N11	105.9(3)
O12–Cu5–O16	88.19(15)	N9–Mn3–N12	109.8(3)
O12–Cu5–O22	90.68(14)	N10–Mn3–N11	118.4(3)
O12–Cu5–N6	84.94(18)	N10–Mn3–N12	106.6(3)
O16–Cu5–O22	94.95(15)	N11–Mn3–N12	112.8(3)

Selected geometrical parameters (distances/Å and angles/^{o}) for **6**

$[Co^{II}Co^{III}Cu_2(L^1)_3(ea)(NCS)_2(H_2O)]$

Co1—O1	1.877(4)	Cu1—O2	1.984(3)
Co1—O2	1.901(3)	Cu1—O5	1.990(3)
Co1—O4	1.967(4)	Cu1—O6	1.872(4)
Co1—O7	1.895(3)	Cu1—O7	2.369(3)
Co1—N3	1.882(4)	Cu1—N1	1.911(4)
Co1—N6	1.938(5)	Cu2—O2	2.398(3)
Co2—O4	2.202(3)	Cu2—O3	1.883(3)
Co2—O5	2.185(3)	Cu2—O4	1.991(3)
Co2—O7	2.036(4)	Cu2—O5	1.979(3)
Co2—O8	2.156(5)	Cu2—N2	1.913(4)
Co2—N4	2.050(5)		
Co2—N5	2.031(6)		
O1—Co1—O2	174.97(17)	O2—Cu1—O5	88.21(13)
O1—Co1—O4	90.67(16)	O2—Cu1—O7	74.81(11)
O1—Co1—O7	91.42(15)	O5—Cu1—O7	76.82(13)
O1—Co1—N3	94.79(16)	O6—Cu1—O2	92.14(14)
O1—Co1—N6	92.87(18)	O6—Cu1—O5	176.35(15)
O2—Co1—O4	84.41(13)	O6—Cu1—O7	99.76(14)
O2—Co1—N6	92.16(16)	O6—Cu1—N1	95.69(17)
O7—Co1—O2	89.05(13)	N1—Cu1—O2	162.82(15)
O7—Co1—O4	83.51(15)	N1—Cu1—O5	84.95(16)
O7—Co1—N6	81.80(17)	N1—Cu1—O7	118.62(14)
N3—Co1—O2	85.13(14)	O3—Cu2—O2	101.83(13)
N3—Co1—O4	100.62(16)	O3—Cu2—O4	173.07(15)
N3—Co1—O7	172.48(16)	O3—Cu2—O5	94.44(14)
N3—Co1—N6	93.64(18)	O3—Cu2—N2	95.37(18)
N6—Co1—O4	164.97(16)	O4—Cu2—O2	71.93(12)
O5—Co2—O4	77.25(12)	O5—Cu2—O2	77.71(12)
O7—Co2—O4	74.61(13)	O5—Cu2—O4	87.22(13)
O7—Co2—O5	80.30(13)	N2—Cu2—O2	114.06(14)

O7—Co2—O8	89.3(2)	N2—Cu2—O4	84.75(17)
O7—Co2—N4	91.43(17)	N2—Cu2—O5	162.64(16)
O8—Co2—O4	87.07(15)		
O8—Co2—O5	162.99(17)		
N4—Co2—O4	166.03(17)		
N4—Co2—O5	100.13(15)		
N4—Co2—O8	93.50(18)		
N5—Co2—O4	94.49(17)		
N5—Co2—O5	92.12(19)		
N5—Co2—O7	167.81(18)		
N5—Co2—O8	95.7(3)		
N5—Co2—N4	99.3(2)		

Selected geometrical parameters (distances/Å and angles/°) for **7**

$[Co_2Mn_2(HL^3)_4(dmf)_2]\cdot 6H_2O$

Mn1—O7	1.851(3)	Co1—O1	1.876(3)
Mn1—O3^{i}	1.937(3)	Co1—O5	1.896(3)
Mn1—O3	1.963(3)	Co1—O6	1.900(3)
Mn1—O2	1.968(3)	Co1—N1	1.905(4)
Mn1—O6	2.146(3)	Co1—N2	1.907(4)
Mn1—O9	2.208(4)	Co1—O2	1.910(3)
O7—Mn1—O3^{i}	175.66(13)	O1—Co1—O5	91.01(17)
O7—Mn1—O3	96.49(14)	O1—Co1—O6	91.15(15)
O3^{i}—Mn1—O3	79.34(14)	O5—Co1—O6	177.82(16)
O7—Mn1—O2	91.05(14)	O1—Co1—N1	95.81(17)
O3^{i}—Mn1—O2	93.17(13)	O5—Co1—N1	88.90(16)
O3—Mn1—O2	172.01(15)	O6—Co1—N1	90.59(16)
O7—Mn1—O6	94.56(14)	O1—Co1—N2	88.40(16)
O3^{i}—Mn1—O6	87.24(14)	O5—Co1—N2	95.63(15)
O3—Mn1—O6	97.84(14)	O6—Co1—N2	84.73(15)
O2—Mn1—O6	78.88(13)	N1—Co1—N2	173.77(16)
O7—Mn1—O9	89.25(16)	O1—Co1—O2	177.83(15)
O3^{i}—Mn1—O9	90.07(17)	O5—Co1—O2	91.08(15)
O3—Mn1—O9	97.08(16)	O6—Co1—O2	86.77(14)
O2—Mn1—O9	85.60(15)	N1—Co1—O2	84.83(17)
O6—Mn1—O9	164.07(15)	N2—Co1—O2	90.80(15)

Symmetry code: ^{i} 1–*x*, 1–*y*, 1–*z*

Selected geometrical parameters (distances/Å and angles/°) for **8**

$[Co_2Mn_2(HL^7)_4(dmf)_2]\cdot dmf\cdot H_2O$

Mn1—O7	1.856(5)	Co1—O5	1.887(3)
Mn1—O3	1.955(4)	Co1—N2	1.887(4)
Mn1—O2	2.045(4)	Co1—O6	1.891(3)
Mn1—O3^{i}	2.047(4)	Co1—O1	1.893(4)

Mn1—O6	2.102(4)	Co1—O2	1.897(4)
Mn1—O9	2.133(6)	Co1—N1	1.901(4)
O7—Mn1—O3	171.96(18)	O5—Co1—N2	95.76(16)
O7—Mn1—O2	94.94(17)	O5—Co1—O6	178.76(16)
O3—Mn1—O2	92.82(15)	N2—Co1—O6	85.08(16)
O7—Mn1—O3^{i}	97.09(18)	O5—Co1—O1	89.52(17)
O3—Mn1—O3^{i}	75.43(16)	N2—Co1—O1	90.67(17)
O2—Mn1—O3^{i}	166.58(15)	O6—Co1—O1	91.39(16)
O7—Mn1—O6	91.14(17)	O5—Co1—O2	92.36(17)
O3—Mn1—O6	92.59(15)	N2—Co1—O2	89.68(17)
O2—Mn1—O6	77.66(14)	O6—Co1—O2	86.72(16)
O3^{i}—Mn1—O6	96.14(15)	O1—Co1—O2	178.05(16)
O7—Mn1—O9	85.0(3)	O5—Co1—N1	89.87(16)
O3—Mn1—O9	93.2(3)	N2—Co1—N1	171.69(17)
O2—Mn1—O9	87.5(2)	O6—Co1—N1	89.20(16)
O3^{i}—Mn1—O9	99.5(2)	O1—Co1—N1	95.49(16)
O6—Mn1—O9	164.3(2)	O2—Co1—N1	83.97(16)

Symmetry code: ^{i} 1–*x*, –*y*, 2–*z*.

Selected geometrical parameters (distances/Å and angles/^{o}) for **9**

[Co$_2$Mn$_2$(HL^{11})$_4$(dmf)$_2$]·dmf·3H$_2$O

Mn1—O3	1.824(5)	Co1—O1	1.893(6)
Mn1—O9^{i}	1.949(5)	Co1—O7	1.895(5)
Mn1—O9	2.039(6)	Co1—N3	1.898(5)
Mn1—O8	2.071(6)	Co1—N1	1.899(6)
Mn1—O2	2.133(5)	Co1—O2	1.907(6)
Mn1—O13	2.151(7)	Co1—O8	1.920(5)
O3—Mn1—O9^{i}	169.0(3)	O1—Co1—O7	90.7(3)
O3—Mn1—O9	94.2(3)	O1—Co1—N3	87.2(3)
O9^{i}—Mn1—O9	75.0(2)	O7—Co1—N3	95.3(2)
O3—Mn1—O8	96.2(3)	O1—Co1—N1	95.3(3)
O9^{i}—Mn1—O8	94.8(2)	O7—Co1—N1	89.3(2)
O9—Mn1—O8	168.11(19)	N3—Co1—N1	174.7(2)
O3—Mn1—O2	88.7(2)	O1—Co1—O2	178.2(2)
O9^{i}—Mn1—O2	94.70(19)	O7—Co1—O2	90.5(2)
O9—Mn1—O2	97.6(2)	N3—Co1—O2	91.4(2)
O8—Mn1—O2	76.9(2)	N1—Co1—O2	86.0(3)
O3—Mn1—O13	87.6(3)	O1—Co1—O8	92.6(3)
O9^{i}—Mn1—O13	91.8(2)	O7—Co1—O8	176.6(3)
O9—Mn1—O13	98.3(3)	N3—Co1—O8	84.2(2)
O8—Mn1—O13	87.9(3)	N1—Co1—O8	91.1(2)
O2—Mn1—O13	163.9(3	O2—Co1—O8	86.2(2)

Symmetry code: ^{i} 1–*x*, –*y*, 1–*z*.

Selected geometrical parameters (distances/Å and angles/^{o}) for **10**

$[Co_2Mn_2(HL^{10})_4(dmf)(H_2O)]\cdot 2fmf\cdot 2H_2O$

Mn1—O3	1.845(6)	N1—Co1	1.900(9)
Mn1—O7	1.920(6)	Co1—O5	1.881(8)
Mn1—O6	1.970(8)	Co1—N2	1.886(9)
Mn1—O11	1.982(7)	Co1—O1	1.889(9)
Mn1—O2	2.173(7)	Co1—O2	1.914(8)
Mn1—O18	2.189(7)	Co1—O6	1.918(8)
Mn2—O15	1.850(7)	Co2—O9	1.886(7)
Mn2—O11	1.985(6)	Co2—N4	1.887(7)
Mn2—O10	2.028(7)	Co2—O13	1.887(7)
Mn2—O7	2.060(7)	Co2—O10	1.892(7)
Mn2—O14	2.104(7)	Co2—N3	1.896(7)
Mn2—O17	2.171(7)	Co2—O14	1.914(7)
O3—Mn1—O7	173.8(3)	O5—Co1—N2	94.9(4)
O3—Mn1—O6	92.7(3)	O5—Co1—O1	88.8(4)
O7—Mn1—O6	93.5(3)	N2—Co1—O1	92.1(4)
O3—Mn1—O11	95.8(3)	O5—Co1—N1	90.9(4)
O7—Mn1—O11	78.1(3)	N2—Co1—N1	172.4(5)
O6—Mn1—O11	169.2(3)	O1—Co1—N1	93.0(4)
O3—Mn1—O2	92.8(3)	O5—Co1—O2	89.9(4)
O7—Mn1—O2	88.6(3)	N2—Co1—O2	91.7(4)
O6—Mn1—O2	79.0(3)	O1—Co1—O2	176.1(3)
O11—Mn1—O2	93.9(3)	N1—Co1—O2	83.3(4)
O3—Mn1—O18	88.6(3)	O5—Co1—O6	176.6(4)
O7—Mn1—O18	91.4(3)	N2—Co1—O6	83.8(4)
O6—Mn1—O18	88.8(3)	O1—Co1—O6	94.3(4)
O11—Mn1—O18	98.0(3)	N1—Co1—O6	90.1(4)
O2—Mn1—O18	167.8(3)	O2—Co1—O6	87.1(3)
O15—Mn2—O11	172.4(3)	O9—Co2—N4	92.6(3)
O15—Mn2—O10	94.9(3)	O9—Co2—O13	89.1(3)
O11—Mn2—O10	92.6(3)	N4—Co2—O13	95.2(3)
O15—Mn2—O7	97.6(3)	O9—Co2—O10	178.4(3)
O11—Mn2—O7	74.8(3)	N4—Co2—O10	88.2(3)
O10—Mn2—O7	167.3(3)	O13—Co2—O10	92.2(3)
O15—Mn2—O14	90.7(3)	O9—Co2—N3	93.8(3)
O11—Mn2—O14	91.3(3)	N4—Co2—N3	172.2(4)
O10—Mn2—O14	78.3(3)	O13—Co2—N3	89.4(3)
O7—Mn2—O14	99.8(3)	O10—Co2—N3	85.3(3)
O15—Mn2—O17	90.4(3)	O9—Co2—O14	92.1(3)
O11—Mn2—O17	88.7(3)	N4—Co2—O14	85.2(3)
O10—Mn2—O17	92.9(3)	O13—Co2—O14	178.7(3)
O7—Mn2—O17	88.8(3)	O10—Co2—O14	86.5(3)
O14—Mn2—O17	171.1(3)	N3—Co2—O14	90.1(3)

Selected geometrical parameters (distances/Å and angles/º) for **11**

$[Co_2Mn_2(L^6)_4(dmf)_2]\cdot 2dmf$

Mn1—O6	1.844(5)	Co1—O1	1.889(5)
Mn1—O3	1.957(5)	Co1—O4	1.895(5)
Mn1—O3^{i}	2.012(5)	Co1—N2	1.899(5)
Mn1—O2	2.023(5)	Co1—O5	1.900(4)
Mn1—O5	2.138(5)	Co1—N1	1.913(5)
Mn1—O7	2.197(6)	Co1—O2	1.914(5)
O6—Mn1—O3	173.5(2)	O1—Co1—O4	90.0(2)
O6—Mn1—O3^{i}	96.3(2)	O1—Co1—N2	88.0(2)
O3—Mn1—O3^{i}	77.3(2)	O4—Co1—N2	95.7(2)
O6—Mn1—O2	94.0(2)	O1—Co1—O5	91.5(2)
O3—Mn1—O2	92.48(19)	O4—Co1—O5	178.4(2)
O3^{i}—Mn1—O2	168.81(19)	N2—Co1—O5	84.9(2)
O6—Mn1—O5	93.6(2)	O1—Co1—N1	95.8(2)
O3—Mn1—O5	88.19(19)	O4—Co1—N1	88.8(2)
O3^{i}—Mn1—O5	97.02(19)	N2—Co1—N1	174.1(2)
O2—Mn1—O5	77.89(18)	O5—Co1—N1	90.5(2)
O6—Mn1—O7	85.7(3)	O1—Co1—O2	178.0(2)
O3—Mn1—O7	94.4(2)	O4—Co1—O2	91.9(2)
O3^{i}—Mn1—O7	100.5(2)	N2—Co1—O2	91.2(2)
O2—Mn1—O7	84.7(2)	O5—Co1—O2	86.6(2)
O5—Mn1—O7	162.5(2)	N1—Co1—O2	84.8(2)

Symmetry code: ^{i} 2–*x*, 1–*y*, 2–*z*.

Selected geometrical parameters (distances/Å and angles/º) for **12**

$[Co_2Mn_2(L^9)_4(dmf)_2]\cdot 2dmf\cdot 7H_2O$

Mn1—O9	1.843(4)	Co1—O5	1.878(4)
Mn1—O10	1.964(4)	Co1—O6	1.890(4)
Mn1—O7	1.964(4)	Co1—O8	1.890(4)
Mn1—O11	2.162(8)	Co1—N1	1.898(4)
Mn1—O8	2.155(4)	Co1—N2	1.899(4)
Mn1—O12	2.358(13)	Co1—O7	1.910(4)
O9—Mn1—O10^{i}	174.30(17)	O5—Co1—O6	90.26(18)
O9—Mn1—O10	96.39(17)	O5—Co1—O8	91.82(18)
O9—Mn1—O7	92.97(17)	O6—Co1—O8	177.34(18)
O10^{i}—Mn1—O7	92.70(16)	O5—Co1—N1	96.38(18)
O10—Mn1—O7	168.56(18)	O6—Co1—N1	87.59(18)
O9—Mn1—O11	93.5(3)	O8—Co1—N1	90.55(17)
O10^{i}—Mn1—O11	84.8(3)	O5—Co1—N2	86.85(17)
O10—Mn1—O11	84.4(3)	O6—Co1—N2	96.28(18)
O7—Mn1—O11	101.6(3)	O8—Co1—N2	85.48(17)
O9—Mn1—O8	95.41(17)	N1—Co1—N2	174.97(18)
O10^{i}—Mn1—O8	86.29(18)	O5—Co1—O7	178.00(15)

O10—Mn1—O8	93.89(19)	O6—Co1—O7	90.98(18)
O7—Mn1—O8	78.66(15)	O8—Co1—O7	86.97(17)
O11—Mn1—O8	171.1(2)	N1—Co1—O7	85.23(19)
O9—Mn1—O12	84.6(3)	N2—Co1—O7	91.46(18)
O10—Mn1—O12	106.7(3)		
O7—Mn1—O12	80.6(3)		
O8—Mn1—O12	159.2(3)		

Symmetry code: ^{i} 1–*x*, 1–*y*,–*z*.

Selected geometrical parameters (distances/Å and angles/^{o}) for **13**

$[Co_2Mn_4(L^4)_4Cl_2(\mu_3\text{-}OH)_2(dmf)_4]\cdot 2dmf$

O3—Mn1	1.9824(13)	Mn1—O7^{i}	1.8448(13)
O4— Mn1	1.9585(13)	O8— Mn 2	2.1513(16)
O5— Mn1	1.9121(13)	O9— Mn 2	2.1644(14)
O6— Mn1	1.9053(13)	Mn2—Cl1	2.4079(6)
O7— Mn1	1.8384(13)	N2—Co1	1.9462(16)
O7— Mn1^{i}	1.8448(13)	O1—Co1	1.8760(14)
O5— Mn2	2.1357(13)	O2—Co1	1.8855(14)
Mn 2—O6^{i}	2.1009(13)	O3—Co1	1.9384(13)
O6— Mn2^{i}	2.1009(13)	O4—Co1	1.9259(13)
O7— Mn1—O7^{i}	85.24(6)	O5— Mn2—O8	164.68(7)
O7— Mn1—O6	97.35(6)	O6^{i}— Mn2—O9	152.49(6)
O7^{i}— Mn1—O6	87.16(6)	O5— Mn2—O9	96.16(5)
O7— Mn1—O5	86.31(6)	O8— Mn2—O9	82.40(6)
O7^{i}— Mn1—O5	99.39(6)	O6^{i}— Mn2—CL1	103.39(4)
O6— Mn1—O5	172.77(6)	O5— Mn2—CL1	97.67(4)
O7— Mn1—O4	168.45(6)	O8— Mn2—CL1	97.51(6)
O7^{i}— Mn1—O4	95.53(6)	O9— Mn2—CL1	103.00(4)
O6— Mn1—O4	94.20(6)	O1—Co1—O2	93.81(7)
O5— Mn1—O4	82.20(5)	O1—Co1—O4	91.13(6)
O7— Mn1—O3	99.03(6)	O2—Co1—O4	169.55(6)
O7^{i}— Mn1—O3	168.20(6)	O1—Co1—O3	168.55(6)
O6— Mn1—O3	81.41(5)	O2—Co1—O3	92.26(6)
O5— Mn1—O3	91.88(5)	O4—Co1—O3	84.51(5)
O4— Mn1—O3	82.50(5)	O1—Co1—N1	94.24(7)
O7— Mn1—CO1	139.27(4)	O2—Co1—N1	87.30(6)
O7^{i}— Mn1—CO1	135.48(4)	O4—Co1—N1	83.15(6)
O6— Mn1—CO1	87.28(4)	O3—Co1—N1	95.74(6)
O5— Mn1—CO1	85.90(4)	O1—Co1—N2	86.42(6)
O4— Mn1—CO1	41.03(4)	O2—Co1—N2	93.73(6)
O3— Mn1—CO1	41.47(4)	O4—Co1—N2	95.77(6)
O6^{i}— Mn2—O5	87.92(5)	O3—Co1—N2	83.50(6)
O6^{i}— Mn2—O8	86.59(6)	N1—Co1—N2	178.74(7)

Symmetry code: ^{i} 1–*x*, 1–*y*, 2–*z*.

Selected geometrical parameters (distances/Å and angles/º) for **14**

[CuL^{13}]·0.5CH$_3$OH

Cu1—O1	1.891(2)	Cu1—N1	1.956(2)
Cu1—O2	1.893(2)	Cu1—N2	1.941(2)
O1—Cu1—O2	87.73(9)	O1—Cu1—N1	94.14(10)
O1—Cu1—N2	177.88(9)	O2—Cu1—N1	177.62(10)
O2—Cu1—N2	94.05(10)	N2—Cu1—N1	84.11(10)

Selected geometrical parameters (distances/Å and angles/º) for **15**

[TBA]$_2$[{Ni(L^{13})$_2$}$_2$Ni]·6CH$_2$Cl$_2$

N1—Ni2	1.860(3)	Ni1—S2	2.1771(7)
N2—Ni2	1.869(3)	Ni1—S2^i	2.1772(8)
Ni1—S1^i	2.1571(7)	Ni2—O2	1.841(2)
Ni1—S1	2.1571(7)	Ni2—O1	1.853(2)
S1^i—Ni1—S1	180.000	O2—Ni2—O1	84.82(10)
S1^i—Ni1—S2	91.75(3)	O2—Ni2—N1	178.74(11)
S1—Ni1—S2	88.25(3)	O1—Ni2—N1	94.34(11)
S1^i—Ni1—S2^i	88.25(3)	O2—Ni2—N2	94.98(11)
S1—Ni1—S2^i	91.75(3)	O1—Ni2—N2	179.24(11)
S2—Ni1—S2^i	180.00(3)	N1—Ni2—N2	85.87(11)

Symmetry code: ^{i} 1–*x*, 1–*y*, 1–*z*.

Selected geometrical parameters (distances/Å and angles/º) for **16**

[TBA]$_2$[{Cu(L^{13})$_2$}$_2$Cu]$_2$·5CH$_2$Cl$_2$

Cu1—S1	2.2585(17)	Cu2—O2	1.899(5)
Cu1—S1^i	2.2585(17)	Cu2—O1	1.902(4)
Cu1—S2^i	2.2592(18)	Cu2—N1	1.958(5)
Cu1—S2	2.2592(18)	Cu2—N2	1.961(5)
S1—Cu1—S1^i	180.000	O2—Cu2—O1	88.44(19)
S1—Cu1—S2^i	90.01(6)	O2—Cu2—N1	173.0(3)
S1^i—Cu1—S2^i	89.99(6)	O1—Cu2—N1	93.8(2)
S1—Cu1—S2	89.99(6)	O2—Cu2—N2	93.1(2)
S1^i—Cu1—S2	90.01(6)	O1—Cu2—N2	178.0(2)
S2^i—Cu1—S2	180.000	N1—Cu2—N2	84.8(2)

Symmetry code: ^{i} 1–*x*, 1–*y*, 1–*z*.

Selected geometrical parameters (distances/Å and angles/º) for **17**

[PPh$_4$][{Ni(L^{13})$_2$}$_2$Ni]·4CH$_2$Cl$_2$

Ni1—S1	2.1549(6)	Ni1—S2	2.1431(7)
Ni1—S1^i	2.1548(6)	Ni1—S2^i	2.1431(7)

N1—Ni2	1.878(3)	O1—Ni2	1.846(2)
N2—Ni2	1.873(2)	O2—Ni2	1.851(3)
O1—Ni2—O2	85.13(11)	S2—Ni1—S2^{i}	180.000
O1—Ni2—N2	179.79(13)	S2—Ni1—S1^{i}	92.38(3)
O2—Ni2—N2	94.65(11)	S2^{i}—Ni1—S1^{i}	87.62(3)
O1—Ni2—N1	94.63(11)	S2—Ni1—S1	87.62(3)
O2—Ni2—N1	178.20(12)	S2^{i}—Ni1—S1	92.38(3)
N2—Ni2—N1	85.58(10)	S1^{i}—Ni1—S1	180.000

Symmetry code: ^{i} 1–*x*, 1–*y*, 1–*z*.

Selected geometrical parameters (distances/Å and angles/^{o}) for **18**

[PPh$_4$][{Cu(L^{13})$_2$}$_2$Cu]·4CH$_2$Cl$_2$

Cu1—S2	2.1725(12)	Cu2—O1	1.894(3)
Cu1—S2^{i}	2.1726(12)	Cu2—O2	1.915(4)
Cu1—S1^{i}	2.1761(10)	Cu2—N2	1.945(4)
Cu1—S1	2.1762(10)	Cu2—N1	1.966(4)
S2—Cu1—S2^{i}	180.00(6)	O1—Cu2—O2	88.45(16)
S2—Cu1—S1^{i}	87.51(4)	O1—Cu2—N2	177.39(17)
S2^{i}—Cu1—S1^{i}	92.49(4)	O2—Cu2—N2	93.64(17)
S2—Cu1—S1	92.49(4)	O1—Cu2—N1	93.87(16)
S2^{i}—Cu1—S1	87.51(4)	O2—Cu2—N1	176.45(18)
S1^{i}—Cu1—S1	180.000	N2—Cu2—N1	83.97(16)

Symmetry code: ^{i} –*x*, 1–*y*, 1–*z*.

Selected geometrical parameters (distances/Å and angles/^{o}) for **19**

[TBA]$_2$[{Cu(L^{13})$_2$}$_2$Ni]$_2$·2CH$_2$Cl$_2$

Cu1—O1	1.875(4)	Ni1—S1	2.1422(15)
Cu1—N1	1.900(4)	Ni1—S2	2.1575(17)
Cu1—N2	1.920(4)	Ni1—S1A	2.1625(17)
Cu2—O2A	1.892(4)	Ni1—S2A	2.1664(16)
Cu2—O1A	1.898(4)		
Cu2—N2A	1.925(5)		
Cu2—N1A	1.928(4)		
O2—Cu1—O1	86.44(16)	O2A—Cu2—N1A	172.9(2)
O2—Cu1—N1	177.1(2)	O1A—Cu2—N1A	92.79(19)
O1—Cu1—N1	94.36(17)	N2A—Cu2—N1A	84.2(2)
O2—Cu1—N2	95.04(17)	S1—Ni1—S2	92.29(6)
O1—Cu1—N2	177.83(19)	S1—Ni1—S1A	85.81(6)
N1—Cu1—N2	84.23(18)	S2—Ni1—S1A	177.98(7)
O2A—Cu2—O1A	88.73(19)	S1—Ni1—S2A	177.13(8)
O2A—Cu2—N2A	94.2(2)	S2—Ni1—S2A	90.03(6)
O1A—Cu2—N2A	176.80(19)		

Selected geometrical parameters (distances/Å and angles/º) for **20**

[Cu(Hfac)$_2$(HL^{14})]

O2—Cu1	2.2694(19)	Cu1—N1	1.9826(19)
O3—Cu1	1.9476(17)	Cu1—N2	2.5906(21)
O4—Cu1	1.9526(17)		
O1—Cu1—N1	90.76(7)	O4—Cu1—N1	91.51(7)
O3—Cu1—O4	91.16(7)	O3—Cu1—O2	88.10(7)
O3—Cu1—O1	86.44(7)	O4—Cu1—O2	93.21(7)
O3—Cu1—N1	170.67(8)	O1—Cu1—O2	87.32(7)
O4—Cu1—O1	177.53(7)	N1—Cu1—O2	100.67(8)

Selected geometrical parameters (distances/Å and angles/º) for **21**

[Cu$_2$(μ$_2$-Cl)(L^{14})$_2$]

N1—Cu1	2.0614(18)	N12—Cu2	2.0139(18)
N2—Cu1	1.9329(17)	Cl3—Cu2	2.4575(6)
N6—Cu2	1.9404(17)	Cl3—Cu1	2.4853(6)
N7—Cu1	1.9618(17)	Cu1—Cu2	2.4313(4)
N11—Cu2	1.9163(17)		
N2—Cu1—N7	155.72(7)	N11—Cu2—N6	146.48(7)
N2—Cu1—N1	82.91(7)	N11—Cu2—N12	84.01(7)
N7—Cu1—N1	105.83(7)	N6—Cu2—N12	103.53(7)
N2—Cu1—Cu2	86.86(5)	N11—Cu2—Cu1	88.31(5)
N7—Cu1—Cu2	86.50(5)	N6—Cu2—Cu1	88.90(5)
N1—Cu1—Cu2	167.36(5)	N12—Cu2—Cu1	166.62(5)
N2—Cu1—Cl3	102.24(5)	N11—Cu2—Cl3	106.05(5)
N7—Cu1—Cl3	94.53(5)	N6—Cu2—Cl3	101.69(5)
N1—Cu1—Cl3	115.09(5)	N12—Cu2—Cl3	110.64(5)
Cu2—Cu1—Cl3	59.966(15)	Cu1—Cu2—Cl3	61.108(15)

Selected geometrical parameters (distances/Å and angles/º) for **22**

[Cu$_2$(CF$_3$SO$_3$)(L^{14})$_2$]

Cu1—N2	1.892(4)	Cu2—N11	1.903(5)
Cu1—N7	1.930(5)	Cu2—N5	1.923(5)
Cu1—N1	2.028(4)	Cu2—N12	2.051(4)
Cu1—O1	2.372(4)	Cu2—O2	2.422(5)
Cu1—Cu2	2.5199(11)		
N2—Cu1—N7	161.1(2)	N11—Cu2—N5	162.0(2)
N2—Cu1—N1	83.19(18)	N11—Cu2—N12	83.04(18)
N7—Cu1—N1	105.22(18)	N5—Cu2—N12	105.3(2)
N2—Cu1—O1	108.31(19)	N11—Cu2—O2	94.0(2)
N7—Cu1—O1	88.44(19)	N5—Cu2—O2	102.5(2)
N1—Cu1—O1	93.10(17)	N12—Cu2—O2	85.31(18)

N2—Cu1—Cu2	86.96(13)	N11—Cu2—Cu1	86.39(14)
N7—Cu1—Cu2	85.96(13)	N5—Cu2—Cu1	86.18(15)
N1—Cu1—Cu2	168.49(13)	N12—Cu2—Cu1	168.44(13)
O1—Cu1—Cu2	84.33(11)	O2—Cu2—Cu1	90.79(12)

Selected geometrical parameters (distances/Å and angles/^{o}) for **23**

$[CuCl_2(HL^{14})_2]\cdot 2CH_3CN$

N1—Cu1	1.998(2)	Cu1—N1^{i}	1.998(2)
Cl1—Cu1	2.3080(6)	Cu1—Cl1^{i}	2.3080(6)
N1—Cu1—N1^{i}	180.000	N1—Cu1—Cl1	89.44(6)
N1—Cu1—Cl1^{i}	90.56(6)	N1^{i}—Cu1—Cl1	90.56(6)
N1^{i}—Cu1—Cl1^{i}	89.44(6)	Cl1^{i}—Cu1—Cl1	180.000

Symmetry code: ^{i} 1–*x*, 1–*y*, 1–*z*.

Selected geometrical parameters (distances/Å and angles/^{o}) for **24**

$[Cu(Hfac)_2(H_2L^{15})]$

N7—Cu1	1.973(3)	O2—Cu1	2.040(4)
N6—Cu1	2.318(3)	O3—Cu1	1.940(2)
O1—Cu1	2.212(4)	O4—Cu1	2.088(2)
O3—Cu1—N7	174.55(13)	O2—Cu1—O1	87.74(11)
O3—Cu1—O2	88.05(12)	O4—Cu1—O1	85.64(10)
N7—Cu1—O2	90.83(13)	O3—Cu1—N6	95.63(12)
O3—Cu1—O4	90.60(9)	N7—Cu1—N6	79.11(13)
N7—Cu1—O4	91.11(12)	O2—Cu1—N6	93.47(12)
O2—Cu1—O4	173.26(10)	O4—Cu1—N6	93.24(11)
O3—Cu1—O1	89.54(11)	O1—Cu1—N6	174.72(12)
N7—Cu1—O1	95.74(12)		

Selected geometrical parameters (distances/Å and angles/^{o}) for **25**

$[Ni(Hfac)_2(H_2L^{15})]$

N6—Ni1	2.170(2)	O2—Ni1	2.043(2)
N7—Ni1	2.030(2)	O3—Ni1	2.016(2)
O1—Ni1	2.0368(19)	O4—Ni1	2.0428(19)
O3—Ni1—N7	175.10(9)	O1—Ni1—O4	174.78(8)
O3—Ni1—O1	86.48(8)	O2—Ni1—O4	85.53(8)
N7—Ni1—O1	91.90(9)	O3—Ni1—N6	95.00(9)
O3—Ni1—O2	89.28(8)	N7—Ni1—N6	80.38(9)
N7—Ni1—O2	95.38(9)	O1—Ni1—N6	90.38(8)
O1—Ni1—O2	91.04(8)	O2—Ni1—N6	175.57(9)
O3—Ni1—O4	89.54(8)	O4—Ni1—N6	93.33(8)
N7—Ni1—O4	92.33(9)		

Selected geometrical parameters (distances/Å and angles/º) for **26**

[Co(Hfac)$_2$(H$_2$L^{15})]·CH$_3$CN

N6—Co1	2.255(4)	O2—Co1	2.061(4)
N7—Co1	2.083(4)	O3—Co1	2.061(4)
O1—Co1	2.061(4)	O4—Co1	2.043(4)
O4—Co1—O1	177.73(14)	O2—Co1—N7	175.70(16)
O4—Co1—O2	90.72(16)	O3—Co1—N7	94.36(17)
O1—Co1—O2	87.01(15)	O4—Co1—N6	86.39(15)
O4—Co1—O3	89.59(18)	O1—Co1—N6	94.01(16)
O1—Co1—O3	90.31(19)	O2—Co1—N6	97.80(16)
O2—Co1—O3	89.88(17)	O3—Co1—N6	171.37(15)
O4—Co1—N7	90.03(16)	N7—Co1—N6	78.02(15)
O1—Co1—N7	92.24(16)		

Selected geometrical parameters (distances/Å and angles/º) for **27**

[{Cu(Hfac)$_2$}$_2$(H$_2$L^{15})]·2CH$_3$OH

N1—Cu1	1.995(4)	O2—Cu1	1.962(4)
N2—Cu1	2.489(5)	O3—Cu1	1.961(4)
O1—Cu1	2.270(4)	O4—Cu1	1.960(3)
O4—Cu1—O3	91.16(15)	O2—Cu1—N1	90.30(16)
O4—Cu1—O2	176.42(14)	O4—Cu1—O1	96.19(13)
O3—Cu1—O2	90.43(16)	O3—Cu1—O1	92.29(14)
O4—Cu1—N1	87.66(15)	O2—Cu1—O1	86.95(14)
O3—Cu1—N1	171.31(15)	N1—Cu1—O1	96.39(15)

Selected geometrical parameters (distances/Å and angles/º) for **28**

[{Ni(Hfac)$_2$}$_2$(H$_2$L^{15})]·2CH$_3$CN

N1—Ni1	2.0399(19)	O2—Ni1	2.0373(15)
N2—Ni1	2.1810(18)	O3—Ni1	2.0309(16)
O1—Ni1	2.0230(17)	O4—Ni1	2.0320(15)
O1—Ni1—O3	87.59(7)	O4—Ni1—N1	90.48(7)
O1—Ni1—O4	88.33(7)	O2—Ni1—N1	91.02(7)
O3—Ni1—O4	90.18(6)	O1—Ni1—N2	95.60(7)
O1—Ni1—O2	89.94(7)	O3—Ni1—N2	176.62(7)
O3—Ni1—O2	92.49(6)	O4—Ni1—N2	91.04(6)
O4—Ni1—O2	176.76(6)	O2—Ni1—N2	86.40(7)
O1—Ni1—N1	175.10(7)	N1—Ni1—N2	79.67(7)
O3—Ni1—N1	97.17(7)		

Selected geometrical parameters (distances/Å and angles/°) for **29**

{[Co(Hfac)$_2$(H$_2$L^{15})]·[Co(Hfac)$_2$(CH$_3$OH)$_2$]}$_n$

Co1—O1^{ii}	2.0337(16)	Co2—O5^{iii}	2.050(2)
Co1—O2^{ii}	2.0616(16)	Co2—O3^{iii}	2.0551(17)
Co1—N4^{ii}	2.215(2)	Co2—O4^{iii}	2.0573(17)
O1^{ii}—Co1—O1	180.000	O5^{iii}—Co2—O5	180.000
O1^{ii}—Co1—O2	91.76(7)	O5^{iii}—Co2—O3^{iii}	86.18(8)
O1—Co1—O2	88.24(7)	O5—Co2—O3^{iii}	93.82(8)
O1^{ii}—Co1—O2^{ii}	88.24(7)	O5^{iii}—Co2—O3	93.82(8)
O1—Co1—O2^{ii}	91.76(7)	O5—Co2—O3	86.18(8)
O2—Co1—O2^{ii}	180.000	O3^{iii}—Co2—O3	180.000
O1^{ii}—Co1—N4^{ii}	92.16(7)	O5^{iii}—Co2—O4	89.93(8)
O1—Co1—N4^{ii}	87.84(7)	O5—Co2—O4	90.07(8)
O2—Co1—N4^{ii}	94.17(7)	O3^{iii}—Co2—O4	88.82(7)
O2^{ii}—Co1—N4^{ii}	85.83(7)	O3—Co2—O4	91.18(7)
O1^{ii}—Co1—N4	87.84(7)	O5^{iii}—Co2—O4^{iii}	90.07(8)
O1—Co1—N4	92.16(7)	O5—Co2—O4^{iii}	89.93(8)
O2—Co1—N4	85.83(7)	O3^{iii}—Co2—O4^{iii}	91.18(7)
O2^{ii}—Co1—N4	94.17(7)	O3—Co2—O4^{iii}	88.82(7)
N4^{ii}—Co1—N4	180.000	O4—Co2—O4^{iii}	180.0(1)

Symmetry code: ^{ii} 1–*x*, 1–*y*, 1–*z*; ^{iii} 1–*x*, –*y*, 2–*z*.

Selected geometrical parameters (distances/Å and angles/°) for **[Cu(HL^{12})$_2$]$_n$**

O1—Cu1	1.9414(14)	Cu1—N1^{i}	1.9962(15)
N1—Cu1	1.9962(15)	O2—Cu1^{ii}	2.4747(15)
Cu1—O1^{i}	1.9414(14)	O2—Cu1^{iii}	2.4747(15)
O1—Cu1—O1^{i}	180.000	O1—Cu1—N1	90.03(6)
O1—Cu1—N1^{i}	89.97(6)	O1^{i}—Cu1—N1	89.97(6)
O1^{i}—Cu1—N1^{i}	90.03(6)	N1^{i}—Cu1—N1	180.000

Symmetry code: ^{i} –*x*, 1–*y*, –*z*;
^{ii} –1–*x*, 1–*y*, –*z*;
^{iii} –1+*x*, *y*, *z*.

Selected geometrical parameters (distances/Å and angles/°) for **(TTF-sal)$_2$PF$_6$**

C1A—C2A	1.335(10)	C1—S4	1.728(7)
C1A—S4A	1.726(7)	C2—C1	1.331(10)
C2A—S3A	1.723(8)	C2—S3	1.722(8)
C3A—S3A	1.727(6)	C3—S3	1.740(6)
C3A—S4A	1.746(7)	C3—S4	1.744(7)
C4A—C3A	1.363(10)	C4—C3	1.361(10)
C4A—S2A	1.741(6)	C4—S2	1.737(6)
C4A—S1A	1.742(7)	C4—S1	1.737(7)
C5A—C6A	1.356(9)	C5—C6	1.334(9)
C5A—C7A	1.472(9)	C5—S1	1.726(7)

C5A—S2A	1.747(7)	C6—C7	1.473(9)
C6A—S1A	1.730(7)	C6—S2	1.757(7)
C7A—C8A	1.382(10)	C7—C12	1.386(9)
C7A—C12A	1.395(9)	C7—C8	1.401(9)
C8A—C9A	1.402(10)	C8—C9	1.37(1)
C9A—C10A	1.362(10)	C9—C10	1.388(10)
C10A—C11A	1.407(10)	C11—C10	1.403(10)
C12A—C11A	1.396(9)	C12—C11	1.405(10)
C13A—O2A	1.240(9)	C13—O2	1.226(9)
C13A—C11A	1.435(10)	C13—C11	1.463(10)
O1A—C10A	1.368(8)	O1—C10	1.342(9)

Selected geometrical parameters (distances/Å and angles/^{o}) for **(TTF-sal)$_2$AsF$_6$**

C1A—C2A	1.314(8)	C1—C2	1.326(8)
C1A—S4A	1.718(6)	C1—S4	1.718(6)
C2A—S3A	1.722(6)	C2—S3	1.736(6)
C3A—C4A	1.366(7)	C3—C4	1.352(7)
C3A—S4A	1.734(5)	C3—S3	1.737(4)
C3A—S3A	1.737(5)	C3—S4	1.739(5)
C4A—S2A	1.733(5)	C4—S1	1.738(4)
C4A—S1A	1.736(5)	C4—S2	1.739(5)
C5A—S1A	1.720(6)	C6—C5	1.343(7)
C6A—C5A	1.350(7)	C6—C7	1.473(7)
C6A—C7A	1.475(7)	C6—S2	1.744(5)
C6A—S2A	1.745(5)	C5—S1	1.724(5)
C7A—C12A	1.372(7)	C7—C12	1.388(6)
C7A—C8A	1.408(7)	C7—C8	1.398(7)
C9A—C8A	1.364(9)	C8—C9	1.361(8)
C10A—O1A	1.342(7)	C9—C10	1.385(8)
C10A—C9A	1.378(8)	C10—O1	1.351(7)
C11A—C10A	1.411(7)	C10—C11	1.401(7)
C11A—C13A	1.458(8)	C11—C12	1.385(7)
C12A—C11A	1.387(7)	C11—C13	1.460(7)
C13A—O2A	1.209(7)	C13—O2	1.212(7)

UNIVERSITE MATIERE BRETAGNE MOLECULES LOIRE ET MATERIAUX

université angers

Complexes homo- et hétero- métallique 3d avec des ligands N- et N,O donneurs : Synthèse, structure et propriétés.

Mots clés : Complexes métalliques, bases de Schiff, tétrazine, tétrathiafulvalène, dithiolène, ligands électroactifs, magnétisme

Résumé : Cette thèse est consacrée à la synthèse de complexes 3d homo et hétérométalliques avec des ligands bases de Schiff ou dérivés de la 1,2,4,5-tétrazine, à l'investigation de leur structure et de leurs propriétés physico-chimiques. Ce travail peut être divisé en trois parties.

Dans la première partie, nous nous sommes principalement concentrés sur les ligands bases de Schiff, dérivés du salicylaldéhyde et des aminoalcools, formés *in situ*. Treize complexes hétérométalliques ont été obtenus et entièrement caractérisés. Il a été montré que les composés synthétisés possèdent une activité catalytique dans la réaction de l'oxydation photochimique de l'eau, présentent des propriétés de photoconductive dans les polymères composites et peuvent être utilisés pour le développement de matériaux multifonctionnels.

La deuxième partie décrit la fonctionnalisation des ligands base de Schiff par l'introduction dans leur structure des unités tétrathiafulvalène et métaux dithiolènes électroactives. Deux nouvelles familles de ligands ont été synthétisées et caractérisées. La série de sels de radicaux cations et de complexes dithiolènes homo et hétérométalliques ainsi que leurs propriétés physiques ont été discutées.

La dernière partie est consacrée aux ligands à base de tétrazine. Les principaux avantages du noyau tétrazine ont été discutés. Deux nouveaux ligands dérivés de la picolylamine et leurs complexes 3d mono- et binucléaires ont été décrits.

Homo- and Heterometallic 3d-Metal Complexes with N- and N,O-donor Ligands: Synthesis, Structure and Properties

Keywords: Complex, Schiff base, Tetrazine, Tetrathiafulvalene, Dithiolene, Electroactive ligands, Magnetism

Abstract: The thesis is devoted to the synthesis of homo- and heterometallic 3d-metal complexes with Schiff base ligands or derivatives of 1,2,4,5-tetrazine, together with the investigation of their structural and physico-chemical properties. This work can be divided in three parts.

In the first part we have been mainly focused on the Schiff base ligands, derivatives of the salicylaldehyde and aminoalcohols. Thirteen heterometallic complexes were obtained and fully characterized. It has been shown that the synthesized compounds possess catalytic activity in the photochemical water oxidation, exhibit photoconducting properties in polymeric composites and can be used for the development of multifunctional materials of wide use.

The second part describes the functionalization of Schiff base ligands by the introduction into their structure of electroactive tetrathiafulvalene and dithiolate moieties. Two new families of ligands were synthesized and characterized. The series of radical-cation salts and homo- and heterometallic dithiolene complexes together with the investigation of their physical properties have been described.

The last part is devoted to the tetrazine based ligands. The main advantages of the tetrazine ring have been discussed. Two new ligands, derivative of picolylamine and their mono- and binuclear 3d-metal complexes are reported.

In conclusion, perspectives of further research related to the described results were highlighted.